UNIVERSITY OF MESSINA

DEPARTMENT OF ENGINEERING

DOCTORAL PROGRAM IN

"ENGINEERING AND CHEMISTRY OF MATERIALS AND CONSTRUCTIONS"

DEVELOPMENT OF Cu-BASED ELECTRODES AND CELL DESIGN FOR PHOTO- AND ELECTRO-CATALYTIC CO_2 REDUCTION

Doctoral Dissertation of:

Daniele Giusi

Supervisor:

Prof. Siglinda Perathoner

Co-supervisor:

Prof. Claudio Ampelli

The Chair of the Doctoral Program:

Prof. Giovanni Neri

2020/2021 – XXXIII Cycle

UNIVERSITA' DEGLI STUDI DI MESSINA

DIPARTIMENTO DI INGEGNERIA

CORSO DI DOTTORATO IN

"INGEGNERIA E CHIMICA DEI MATERIALI E DELLE COSTRUZIONI"

SVILUPPO DI ELETTRODI A BASE DI Cu E PROGETTAZIONE DI REATTORI PER LA RIDUZIONE FOTO- ED ELETTRO-CATALITICA DI CO_2

Tesi di dottorato di:

Daniele Giusi

Tutor:

Prof.ssa Siglinda Perathoner

Co-tutor:

Prof. Claudio Ampelli

Coordinatore del corso di Dottorato:

Prof. Giovanni Neri

2020/2021 – XXXIII Ciclo

UNIVERSITY OF MESSINA

DEPARTMENT OF ENGINEERING

DOCTORAL PROGRAM IN
"ENGINEERING AND CHEMISTRY OF MATERIALS AND CONSTRUCTIONS"
(S.S.D.: CHIM/04 Industrial Chemistry; ING-IND/25 Chemical Plants)

Supervisors	Institution	S.S.D.
Prof. Siglinda PERATHONER	**Università degli Studi di Messina** Dipartimento di Scienze Chimiche, Biologiche, Farmaceutiche e Ambientali	**CHIM/04** "Chimica Industriale"
Prof. Claudio AMPELLI	**Università degli Studi di Messina** Dipartimento di Scienze Chimiche, Biologiche, Farmaceutiche e Ambientali	**ING-IND/25** "Impianti Chimici"

Reviewers from Italy	Institution
Prof. Laura CALVILLO LAMANA	**Università degli Studi di Padova** Dipartimento di Scienze Chimiche
Prof. Serena ESPOSITO	**Politecnico di Torino** Dipartimento Scienza Applicata e Tecnologia (DISAT)

Reviewers from the European Union	Institution
Prof. Sixto GIMÉNEZ JULIÁ	**Universitat Jaume I, Castelló de la Plana (Spain)** Institute of Advanced Materials (INAM)
Prof. Elsje Alessandra QUADRELLI	**Université de Lyon, Lyon (France)** Institut de Chimie de Lyon, CNRS - Laboratoire de Chimie, Catalyse, Polymères et Procédés (C2P2), Equipe Chimie Organométallique de Surface

2020/2021 – XXXIII Cycle

INDEX

ABSTRACT (ENGLISH)

The process of carbon dioxide (CO_2) reduction has attracted a great attention in the scientific community in the last years. The development of materials and systems capable to convert H_2O and CO_2 into valuable products by using renewable and clean energy represents an attractive challenge for the next future.

In this context, the aim of the present PhD work is to explore different routes by photo- and electrocatalytic approaches to convert CO_2 into value-added chemicals and fuels. The research activity concerned both the synthesis of the catalytic materials used for the preparation/assembling of the electrodes and the design and engineering of the electrochemical devices.

Most of the activities were carried out at the laboratory CASPE/INSTM (Laboratory of Catalysis for Sustainable Production and Energy) of the University of Messina. Moreover, during the second year, one month was spent at the Institut Català d'Investigació Química (ICIQ Tarragona, Spain) and two months at the Institute for Chemical and Bioengineering (ETH Zürich, Switzerland) in the framework of H2020 A-LEAF Project and Research and Mobility ARCADIA Project.

The thesis is organized in six chapters, plus the conclusions. Chapter 1 focuses on CO_2 environmental issues, general implications and consequent opinions and strategies adopted by the scientific community in a long-term period to address these problems, with regard to the main common carbon capture and storage (CCS) strategies and photochemical, biochemical, photo- and electrocatalytic routes. Chapters 2 and 3 concern the theoretical basis on photo- and electro-chemical CO_2 reduction routes, including the state-of-the-art of the main photo- and electro-catalytic electrodes used so far and the engineering aspects of reactor design. In particular, the most promising photo-electro-chemical and photovoltaic devices are discussed, with emphasis on the advanced strategies concerning the coupling of these systems with different configurations and using different advanced materials, to achieve higher catalytic performances.

Chapters 4 and 5 refer to the experimental results obtained by photo- and electro-catalytic approaches. The states of the art for these two different approaches are presented,

together with the specific scope of each chapter, especially highlighting their differences but also the many common points in terms of reaction mechanism and kinetics. The catalysts used for the experimental investigation were nanostructured Cu_xO-based materials, prepared by different techniques, such as precipitation, solvothermal and electrodeposition methods, and then deposited on metallic, metal oxides or carbon-based substrates. Particularly, electrodeposition was a very versatile method allowing a direct controlled deposition of Cu_2O by modulating some parameters during the synthesis, such as time deposition, pH and type of electrolyte. Most of the study was focused on cuprous oxide (Cu_2O) semiconductor, for its interesting characteristics: it is an earth abundant material, non-toxic, showing a band gap of around 2.2 eV as bulk material. It has been widely used for solar cell sensitizers, sensors (see Chapter 6) and in CO_2 photocatalysis, especially for the formation of CO and CH_4.

Chapter 4 of this work shows that, due to a novel concept of gas flow-through photo(electro)catalytic reactor, the process selectivity can be shifted to more interesting carbon products, involving the formation of C-C bonds. This novel homemade device uses copper-functionalized nanomembranes, based on aligned TiO_2 nanotube arrays (prepared by controlled anodic oxidation) grown over a microperforated metallic substrate, acting as an electron collector and to provide the necessary robustness, which are then functionalized with Cu_xO by electrodeposition. This concept is quite different from the conventional CO_2 photocatalytic approaches. Due to the peculiar characteristics and conditions in the novel photoreactor (working under a cross-flow of gaseous CO_2 saturated with water crossing through the photocatalytic nanomembrane), it is possible to evidence for the first time the highly selective CO_2 conversion to C1-C2 carboxylic acids (formic, acetic and oxalic acids) without formation of H_2, CO, CH_4 or other hydrocarbons. Copper-oxide introduces an additional reaction pathway to C1-C3 alcohols (methanol, ethanol and isopropanol) or derived products (methyl formate). The best performances were obtained when Cu_2O nanoparticles (*p*-type) are deposited over *n*-type TiO_2 nanotubes, due to the creation of a *p-n* type heterojunction that improves visible light harvesting, giving an apparent quantum yield (ratio between electrons reacted and photons absorbed) with solar illumination of about 21 %. The Faradaic Efficiency on this photocatalyst was about 42 % to methanol and 44 % to acetic acid. Among the tested samples, Faradaic Efficiency up to 47 % to methanol or up to 73 % to acetic acid are observed. The relevance of these results on the mechanism of CO_2 photoreduction was also discussed along Chapter 4.

Chapter 5 focuses instead on the electrocatalytic reduction of CO_2. In this part of the work, Cu_2O was employed as pure oxide (at different oxidation states, I and II) or doped with other elements, such as S and In (CuS_x and Cu-In), for the design of composite electrodes able to address the process selectivity towards formic acid or carbon monoxide, respectively, through the modification of binding energy of the reaction intermediates with the catalytic active sites. Specifically, the research activities concerned preliminarily the optimization of the operating conditions in terms of reactor configuration, cathodic pH, applied potential at the working electrode (in the investigated range from -0.4 V to -1.0 V vs. RHE), CO_2 inlet flow and type of membrane (i.e. cationic, anionic or bipolar). A precise protocol was defined for carrying out each electrochemical test, ranging from cyclic voltammetry and capacitance determination to chronoamperometry steps, the latter including the determination of CO_2 reduction products. Testing with pure Cu_xO deposited on a carbon gas diffusion layer (GDL) in presence of a liquid electrolyte (0.1 M $KHCO_3$ aqueous solution) showed that i) the optimal catalyst loading on GDL was 10 mg cm^{-2}; ii) the best productivity and Faradaic efficiency (FE) to formic acid and carbon monoxide was obtained at -0.6 V vs. RHE (12.8 μmol h^{-1} and 5.5%, respectively); CuO/GDL behaved better than Cu_2O/GDL, with an increase of catalytic performance (i.e. FE = 12.6 %). The electrochemical behaviours of both the electrocatalysts were also investigated by Electrochemical Impedance Spectroscopy (EIS), evidencing a lower charge transfer resistance for CuO/GDL (6.5 Ω) with respect to Cu_2O/GDL (39.5 Ω).

The electrocatalytic activity strongly increased when advanced electrodes like CuS_x and Cu-In were used, providing a FE to formic acid of 58.5% and a FE % to carbon monoxide of 55.6%, respectively. Different cell configurations were investigated by using these catalysts, depending on the pathways of gas flow within the cell in three different compartments (a gas chamber, a liquid catholyte compartment, a liquid anolyte compartment). The best configuration in terms of maximum FE and minimization of H_2 formation (by proton reduction as side reaction) referred to the separation of gas and liquid products, collecting the gas products directly from the outlet of the gas chamber, thus overcoming issues related to the low solubility of CO_2 in aqueous solution. The behaviours of many commercial selective membranes were also evaluated, i.e. cationic (protonic), anionic and bipolar, also reinforced with Teflon. Results showed that Teflon reinforced protonic (Nafion N324) and bipolar (Fumasep FBM-PK) membranes provided the best activity; however, the reinforced Nafion allowed better to

minimize osmosis of electrolyte and cross-over of the reduction products, avoiding their oxidation at the anode side.

Finally, Chapter 6 focuses on strategies for the glucose detection in biofermentation processes and particularly on the amperometric methods based on the use of non-enzymatic glucose sensors. The most important biofermentation process is the alcoholic fermentation, which consists in the production of CO_2 and ethanol starting from several sugar substrates like glucose, sucrose and fructose. Industrial applications today are aimed to decrease the dependence of crude oil producing bioethanol, which is blended with the gasoline. In this context, Cu_2O nanocubes deposited on commercial screen printed carbon electrodes (SPCEs) with different particles size were developed as sensors. The performances of these Cu-modified SPCEs were evaluated in terms of glucose selectivity and sensitivity by cyclic voltammetry and chronoamperometry analysis and impedance resistance measurements. The developed electrodes showed a good sensitivity (1040μA/mM cm^{-2}) and selectivity towards the glucose detection with a high linear range response, without interference by other substrates, suggesting that the SPCE modification with Cu_2O could be a simple way to fabricate inexpensive and reliable sensors to monitor glucose in bio-fermentation processes.

ABSTRACT (ITALIAN)

Il processo di riduzione dell'anidride carbonica (CO_2) ha suscitato negli ultimi anni grande attenzione nella comunità scientifica. Lo sviluppo di materiali e sistemi in grado di convertire H_2O e CO_2 in prodotti ad alto valore utilizzando energia rinnovabile e pulita, rappresenta una sfida particolarmente attraente per il prossimo futuro.

In questo contesto, lo scopo del presente lavoro di Dottorato è stato quello di valutare diversi approcci, tra cui quelli foto- ed elettrocatalitici, per convertire la CO_2 in sostanze chimiche e combustibili a più alto valore aggiunto. L'attività di ricerca ha riguardato sia la sintesi dei materiali catalitici utilizzati per la preparazione/ assemblaggio degli elettrodi sia la progettazione e ingegnerizzazione dei dispositivi elettrochimici.

La maggior parte delle attività sono state svolte presso il laboratorio CASPE/INSTM (Laboratorio di Catalisi per la Produzione Sostenibile e l'Energia) dell'Università degli Studi di Messina. Durante il secondo anno, un mese è stato trascorso presso l'Institut Català d'Investigació Química (ICIQ Tarragona, Spagna) e due mesi presso l'Istituto di Chimica e Bioingegneria (ETH Zurigo, Svizzera) nell'ambito del Progetto H2020 A-LEAF e del Progetto di Ricerca e Mobilità ARCADIA.

La tesi è organizzata in sei capitoli, più le conclusioni. Il capitolo 1 si concentra sulle questioni ambientali derivanti dall'accumulo della CO_2, le implicazioni generali e le conseguenti opinioni e strategie adottate dalla comunità scientifica a lungo termine per affrontare queste problematiche, con riguardo alle principali strategie da attuare quali la cattura e stoccaggio del carbonio (CCS) e i vari metodi fotochimici, biochimici e foto ed elettrocatalitici. I capitoli 2 e 3 riguardano le basi teoriche dei metodi di riduzione foto ed elettrochimici della CO_2, e comprendono lo stato dell'arte dei principali elettrodi foto- ed elettro-catalitici utilizzati fino ad ora e gli aspetti ingegneristici della progettazione del reattore. In particolare vengono discussi i dispositivi fotoelettrochimici e fotovoltaici più promettenti, con particolare attenzione alle strategie avanzate riguardanti l'accoppiamento di questi sistemi con diverse configurazioni e utilizzando diversi materiali avanzati, per ottenere prestazioni catalitiche più elevate.

I capitoli 4 e 5 illustrano i risultati sperimentali ottenuti con gli approcci foto- ed elettrocatalitici di riduzione della CO_2. Viene presentato lo stato dell'arte per questi due diversi approcci, insieme allo scopo specifico di ogni capitolo, evidenziandone in particolare le differenze ma anche i molti punti comuni in termini di meccanismo di reazione e cinetica. I catalizzatori utilizzati per l'indagine sperimentale sono materiali nanostrutturati a base di Cu_xO, preparati con diverse tecniche, come metodi di precipitazione, solvo-termali ed elettrodeposizione, che sono stati depositati su substrati metallici, ossidi metallici o a base di carbonio. In particolare, l'elettrodeposizione è un metodo molto versatile che permette una deposizione controllata diretta di Cu_2O modulando alcuni parametri durante la sintesi, come il tempo di deposizione, il pH e il tipo di elettrolita. La maggior parte dello studio si è concentrata sul semiconduttore ossido rameoso (Cu_2O), per le sue caratteristiche interessanti: si tratta di un materiale terrestre abbondante, non tossico, che possiede un band gap di circa 2.2 eV come materiale in bulk. Viene ampiamente utilizzato per sensibilizzatori di celle solari, sensori (vedi Capitolo 6) e nella fotocatalisi della CO_2, in particolare per la formazione di CO e CH_4.

Il capitolo 4 di questo lavoro mostra che, grazie a un nuovo concetto di reattore foto (elettro) catalitico a flusso di gas, la selettività del processo può essere spostata verso prodotti a base di carbonio più interessanti, con la formazione di legami C-C. Questo nuovo dispositivo costruito nei nostri laboratori utilizza nanomembrane funzionalizzate con il rame, basate su una disposizione di nanotubi allineati di TiO_2 (preparati mediante ossidazione anodica controllata) cresciuti su un substrato metallico microforato, che agiscono sia come collettore di elettroni sia come supporto meccanico per fornire la necessaria robustezza; questi poi sono stati funzionalizzati con Cu_xO mediante elettrodeposizione. Questo concetto è molto diverso dagli approcci fotocatalitici CO_2 convenzionali. Per via delle caratteristiche e delle condizioni peculiari del nuovo fotoreattore (che lavora sotto un flusso di vapore saturato con CO_2 gassosa che attraversa la nanomembrana fotocatalitica), è possibile evidenziare per la prima volta la conversione altamente selettiva della CO_2 ad acidi carbossilici C1-C2 (formico, acetico e ossalico) senza formazione di H_2, CO, CH_4 o altri idrocarburi. L'ossido di rame introduce una via di reazione aggiuntiva alla formazione degli alcoli C1-C3 (metanolo, etanolo e isopropanolo) o ai prodotti derivati (formiato di metile). Le migliori prestazioni sono state ottenute quando le nanoparticelle di Cu_2O (tipo *p*) sono depositate su nanotubi di TiO_2 di

tipo *n*, grazie alla creazione di una eterogiunzione di tipo *p-n* che migliora la raccolta della luce visibile, fornendo una resa quantica apparente (rapporto tra elettroni reagiti e fotoni assorbiti) con illuminazione solare del 21% circa. L'efficienza faradica su questo fotocatalizzatore è stata di circa il 42% a metanolo e il 44% ad acido acetico. Tra i campioni testati, in generale si osserva un'efficienza faradica fino al 47% a metanolo o fino al 73% ad acido acetico. La rilevanza di questi risultati sul meccanismo della fotoriduzione della CO_2 è stata anche discussa nel Capitolo 4.

Il capitolo 5 si concentra invece sulla riduzione elettrocatalitica della CO_2. In questa parte del lavoro, Cu_xO è stato impiegato come ossido puro (a diversi stati di ossidazione, I e II) o drogato con altri elementi, come S e In (*CuS_x* e *Cu-In*), per la progettazione di elettrodi compositi in grado di indirizzare la selettività del processo verso l'acido formico o il monossido di carbonio, rispettivamente, attraverso la modifica dell'energia di legame degli intermedi di reazione con i siti attivi catalitici. Nello specifico, le attività di ricerca hanno riguardato preliminarmente l'ottimizzazione delle condizioni operative in termini di configurazione del reattore, pH catodico, potenziale applicato all'elettrodo di lavoro (nel range indagato da -0.4 V a -1.0 V vs. RHE), flusso di ingresso della CO_2 e tipo di membrana (cationica, anionica o bipolare). È stato definito un protocollo preciso per l'esecuzione di ogni test elettrochimico, che va dalla voltammetria ciclica e determinazione della capacità alle fasi di cronoamperometria, quest'ultima comprensiva della determinazione dei prodotti di riduzione della CO_2. Il test con Cu_xO puro depositato su uno strato di gas-diffusion-layer (GDL) in presenza di un elettrolita liquido (soluzione acquosa $KHCO_3$ 0,1 M) ha mostrato che i) il carico ottimale del catalizzatore su GDL era 10 mg cm^{-2}; ii) la migliore produttività ed efficienza faradica (FE) per acido formico e monossido di carbonio è stata ottenuta a -0,6 V vs. RHE (12.8 µmol h^{-1} e 5.5%, rispettivamente); il campione CuO/GDL si è comportato meglio di Cu_2O/GDL, con un aumento delle prestazioni catalitiche (FE=12.6%). I comportamenti elettrochimici di entrambi gli elettrocatalizzatori sono stati studiati anche attraverso la spettroscopia di impedenza elettrochimica (EIS), evidenziando una resistenza al trasferimento di carica inferiore per CuO/GDL (6.5 Ω) rispetto a Cu_2O/GDL (39.5 Ω).

L'attività elettrocatalitica è aumentata notevolmente quando venivano usati elettrodi avanzati come *CuS_x* e *Cu-In*, fornendo rispettivamente una FE ad acido

formico del 58.5% e una FE% al monossido di carbonio del 55.6%. Diverse configurazioni delle celle sono state studiate utilizzando questi catalizzatori, a seconda dei percorsi del flusso di gas all'interno della cella nei tre diversi compartimenti (una camera gassosa, un compartimento liquido per il catolita ed un compartimento liquido per l'anolita). La migliore configurazione in termini di elevata FE e bassa formazione di H_2 (mediante riduzione protonica come reazione collaterale) si è ottenuta separando l'evoluzione dei prodotti gassosi da quelli liquidi, ovvero raccogliendo i prodotti gassosi direttamente dall'uscita della camera gassosa, superando così le problematiche legate alla bassa solubilità della CO_2 in acqua. Sono stati valutati anche i comportamenti di molte membrane selettive commerciali, cationiche (protoniche), anioniche e bipolari, anche rinforzate con teflon. I risultati hanno mostrato che la membrana protonica rinforzata con Teflon Nafion N324 e la membrana bipolare Fumasep FBM-PK hanno fornito la migliore attività; tuttavia, il Nafion rinforzato ha permesso di minimizzare meglio l'osmosi dell'elettrolita e il cross-over dei prodotti di riduzione, evitandone l'ossidazione sul lato anodico.

Infine, il Capitolo 6 si concentra sulle strategie per la rilevazione del glucosio nei processi di biofermentazione e in particolare sui metodi amperometrici basati sull'utilizzo di sensori di glucosio non enzimatici. Il processo di biofermentazione più importante è la fermentazione alcolica, che consiste nella produzione di CO_2 ed etanolo a partire da diversi substrati zuccherini come glucosio, saccarosio e fruttosio. Le applicazioni industriali oggi mirano a diminuire la dipendenza del petrolio greggio producendo bioetanolo, che viene miscelato con la benzina. In questo contesto, sono stati sviluppati dei sensori a base di Cu_2O a forma di nanocubi, con particelle di dimensioni diverse, depositato su supporti commerciali di tipo "screen-printed carbon electrode" (SPCE). Le prestazioni di questi SPCE modificati con Cu sono state valutate in termini di selettività e sensibilità del glucosio mediante analisi di voltammetria ciclica e cronoamperometria e misure di impedenza. Gli elettrodi sviluppati hanno mostrato una buona sensibilità (1040µA/mM cm^{-2}) e selettività nei confronti del rilevamento del glucosio con una risposta ad alto range lineare, senza interferenze da parte di altri substrati, suggerendo che i SPCE modificati con Cu_2O potrebbe essere un modo semplice per fabbricare sensori economici e affidabili per monitorare il glucosio nei processi di biofermentazione.

1. INTRODUCTION

1.2 PROBLEM OF CO_2 ACCOMULATION

The spreading use of fossil fuels, as primary sources of energy, has led to a continue increasing in the amount of carbon dioxide released into the atmosphere (Figure 1.1). All data collected so far estimate the contribution of coal, fuel oil and gas at around 80 % of our energy portfolio until at least 2050[1]. The raise in the concentration of CO_2 in the atmosphere is also indicated as the main cause of the increase in temperature on the planet affecting the climate change. For these reasons, there is a wide technical-scientific effort, also felt at a political level, to control the accumulation of atmospheric CO_2[2-3].

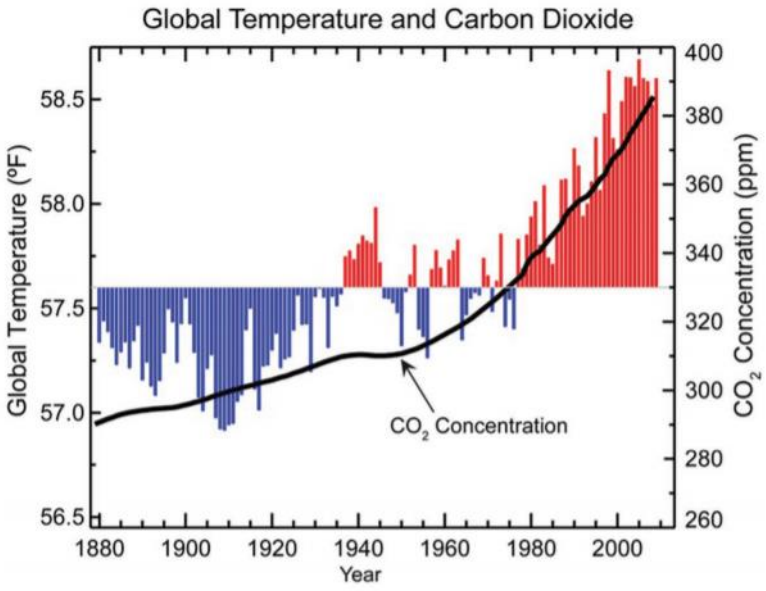

Figure 1.1 *CO_2 concentration variation and average temperature. Blue and red bars indicate the temperature respectively below and above the 1901-2000 temperature average. Reproduced with permission from ref.*[4]

An important study published in Nature by the Potsdam Institute for Climate Impact Research, named "*Residual fossil CO_2 emissions in 1.5-2°C pathways*[5], claimed how billions of tons of carbon dioxide should be removed from the atmosphere to have any chance of limiting global warming at least to 1.5-2 degrees by the end of the century, to observe the Paris climate agreements[6]. According to researchers of the Potsdam Institute, the amount of CO_2 that can be generated yet without overheating more the earth could be very small, around 200 billion tons of carbon

dioxide, to remain on a path of de-carbonization compatible with the objective of +1.5 degrees of temperature increase, compared to pre-industrial levels. The authors of the study highlight that, if we continue to emit CO_2 at the same rate of nowadays, we would reach about 4,000 billion cumulative tons at the end of this century. The Potsdam Institute asserts that it will be necessary to remove at least 600 Gt of CO_2 from the atmosphere in the coming decades, using technologies based on so called "negative emissions" on a large scale; they allow to capture and store the carbon emitted by man in the environment and offset the green house emissions produced by combustion processes.

1.2.1 CO_2 removal technologies and conversion strategies

1.2.1.1 Carbon dioxide removal technologies

According with the Intergovernmental Panel on Climate Change (IPCC), two main options for reducing the CO_2 in the atmosphere have been detected making use of the carbon dioxide removal technologies (CDRT):

i) reforestation;

ii) production of bio-energy combined with capture and storage of CO_2.

These set of strategies allow achieving lower CO_2 concentration stabilization objectives in the atmosphere compared to the situation in which these technologies are not used.

The first, takes advantages of some extended lands, as the forests. Reducing the deforestation and promoting reforestation allows increasing the absorption capacity of carbon dioxide by forests; these, represents two convenient mitigation options, but it's necessary to take in account the different application possibilities in the different parts of the world and the peculiarities of each territory. Thus, these strategies will acquire an important role, made up of emissions cutting actions through the reduction of deforestation and forest degradation, the conservation of forests and their sustainable management.

The second option involves the following planes:

i) allocate large land into crops to absorb CO_2 during the plant growth and then produce energy or fuels with the relative biomass;

ii) capture the related carbon dioxide emissions (CO_2 would be stored in underground deposits, as former gas fields);

Capture and separation technologies of CO_2, discussed in the next paragraph, are already well known, developed and applied in many contexts, and their introduction into the cycles for the production of electricity is mainly hindered by economic considerations. It is in fact known that, regardless of the technology used, cost of the produced electricity greatly increases compared to the plants lacking of any capture system. However, the adoption of efficient techniques for capturing CO_2 is essential for safeguarding the environmental balance. Laws of developed countries are now aimed towards an increasing restriction of the amount of carbon dioxide emitted into the atmosphere. Together with the capture of CO_2, technologies for its definitive storage have been developed, for example in geologically stable sites and this is currently the best solution proposed for the removal of huge quantities of gas. Therefore, it seems reasonable to ask the question whether there are possible technologies for a reuse, to our advantage, of this huge amount of carbon. Other interesting CDRT technologies include ocean fertilization, direct air capture, enhanced weathering and sequester of carbon through agricultural practices.

1.2.1.2 Carbon capture and conversion

As alternative to long-term storage, the captured CO_2 can be used directly, as a raw material, or indirectly through conversion into profitable products such as liquid fuels, chemicals, biodegradable polymers and construction materials. The term “carbon capture and conversion” (CCC) refers to a set of strategies in which the CO_2 is converted into useful chemical feedstocks, decreasing the fossil sources dependence and encouraging and enhancing the CO_2 capture. The energy of these processes is used to convert CO_2, in which carbon is in its highest oxidation state, into reduced forms of carbon, as it occurs in many organic molecules. The CO_2 can be used as energy storage and converted to various compounds like ethanol, methane, methanol, formic acid, ethylene, etc.[7] (Figure 1.2). These products are useful because they can be further used or as feedstock for the production of olefins like propylene and ethylene, which are subsequently turned to high hydrocarbons

or as excellent combustion engine fuels. Among these, the reduction of CO_2 to methanol is a great challenge because, beyond mitigating the global warming phenomena, it can also provide a great source of available carbon atoms[8]. From methanol, some derivatives like acetic acid[9], formaldehyde, dimethyl ether (DME), methyl tertiary-butyl ether (MTBE)[10] can in fact be obtained. The great versatility of methanol to be converted to many useful chemicals and the possibility to carry it on by means of the existent fuel distribution infrastructure, has laid the foundation of the so-called, "methanol economy"[11].

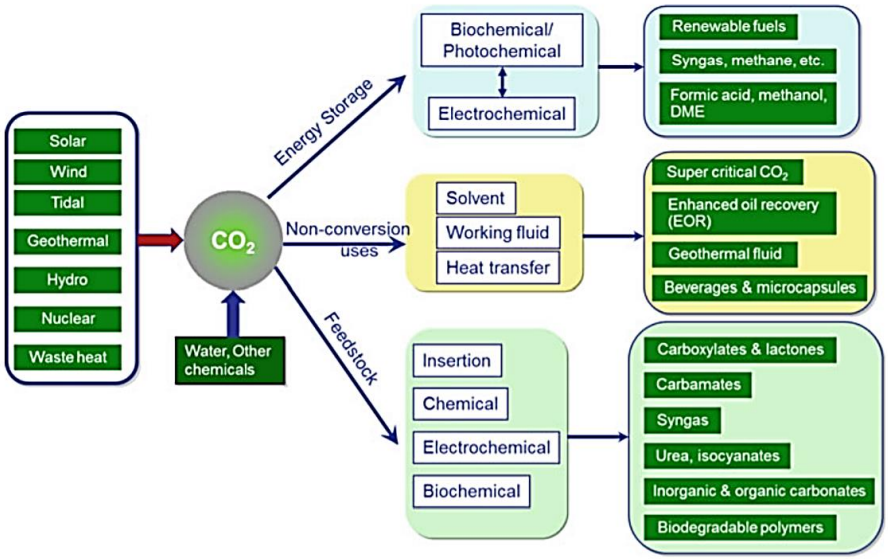

Figure 1.2 *Possible CO_2 reuse pathways. Reproduced with permission from ref.*[12]

The CO_2 can be converted by different techniques like electrochemical[13,14], thermochemical[15], biochemical[16], photochemical[17], chemical routes and all the possible combination of these. However, most of the work today is focused on electrochemical and photochemical route, because of their advantages over the others. A brief overview of the principles on which the previous technologies are based will be developed in the next paragraphs and will regard in order the following CO_2 storage/conversion routes; i) carbon capture and storage; ii) thermo and solar thermochemical conversion; iii) biochemical conversion and iv) photo-eletrochemical conversion. The main pros and cons of each category will also be described to justify the choices adopted in this thesis work.

1.3 CARBON CAPTURE AND STORAGE

The term "carbon capture and storage", known by the acronym "CCS", represents a set of strategies used to mitigate the impact of CO_2 on the atmosphere, and they are based on the following operations:

i) separation of carbon dioxide from the combustion plant exhausts;

ii) transport to the storage site, usually by compressing the gas under high pressure;

iii) storage and confinement at the destination site, avoiding and minimizing CO_2 emissions into the atmosphere.

The acronym BECCS, "bioenergy with carbon capture and storage", indicates the application of CCS strategies to biomass electric generators. The CCS and BECCS technologies allow to capture a greater amount of CO_2 emissions than that released during energy production, combining energy production biomass with CO_2 capture emitted by combustion and its storage in underground deposits. This occurs because it is supposed that biomass, once burned, releases the same amount of CO_2 absorbed during the growth of plants through photosynthesis into the atmosphere. The CCS system allows to capture and deposit extra CO_2 underground, making as results of the combination of bio-energy and CCS, a negative net emission[18]. In a simple CSS process (Figure 1.3), CO_2 is firstly captured in post-combustion (absorbed in a proper chemical solvent and subsequently separated), pre-combustion (the fuel is gasified with hydrogen and CO_2, which is separated) or through oxy-fuel combustion (involving the use of pure oxygen in a combustion chamber). Post-combustion chambers are usually employed in small-scale plants, and the process consists in separating the CO_2 after the combustion occurred. The main disadvantages regard the total cost associated with the storage and transport phases, which make not convenient following this route due to the small CO_2 concentration in the flue gas. The pre-combustion chamber is instead often integrated in the IGCC (integrated gasification combined cycle) power plants: the fuel, if in form of coal, is gasified to form syngas, namely a mix of H_2 and CO without other impurities (reaction 1). The obtained CO undergoes the water-gas shift reaction to form more H_2 and CO (reaction 2), while H_2 can be burned in air to obtain water vapour and N_2. If the fuel is CH_4, then it will be converted to H_2 and CO with the steam

reforming (reaction 3). The latter can undergo the gas water shift reaction production pushing the production of more H_2.

$$\text{Coal} \rightarrow CO + H_2 \qquad 1)$$

$$CO + H_2O \rightarrow H_2 + CO_2 \qquad 2)$$

$$CH_4 + H_2O \rightarrow CO + 3H_2 \qquad 3)$$

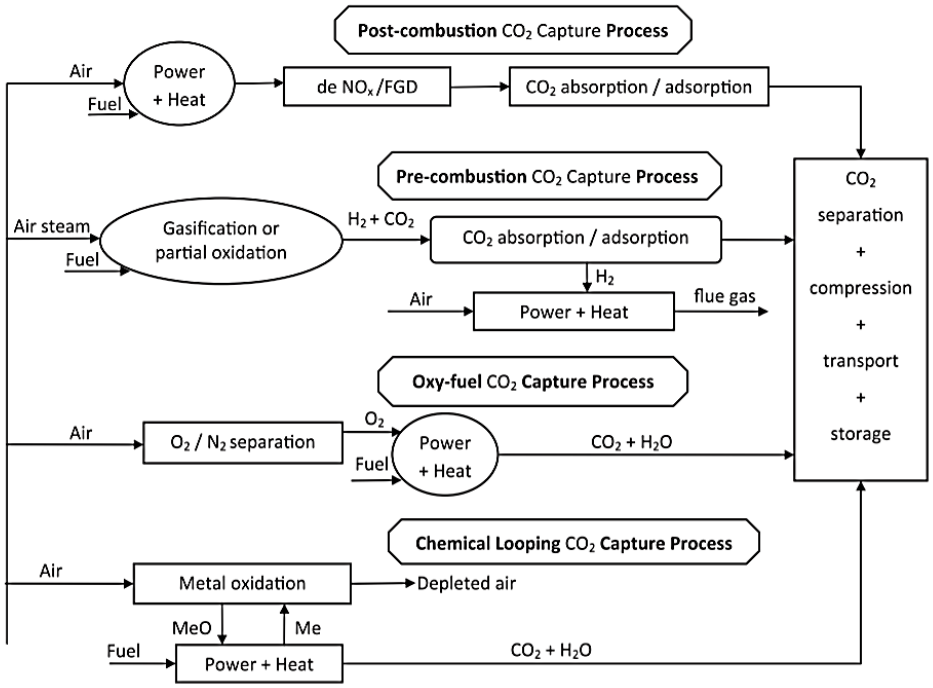

Fig. 1. CO_2 capture technologies.

Figure 1.3 *CO_2 carbon capture strategies. Reproduced with permission from ref.*[19].

The oxy-fuel combustion involves the use of pure oxygen and not air to burn the fuel. The main components of the flue gases are water, CO_2, SO_2 and particulate. The SO_2 can be removed by desulphatizing procedures, while electrostatic precipitator allows the particulate deposition. Despite this, the SO_2, due to its high concentration can cause severe corrosion problems. At the end, the flue gas is composed mainly of CO_2 in high concentration, but high-energy costs are required to separate it before storing and transport. The main separation techniques include absorption, adsorption, membrane separation, chemical looping combustion and cryogenic distillation. The confinement of CO_2 can lead to several problems, such as violent and unexpected emission from geological and containment sites due to structural site modifications or subsidence or to a prolonged and slow release into the atmosphere over a long time.

1.4 CARBON CAPTURE AND CONVERSION

1.4.1 Thermochemical conversion

Chemical fixation of CO_2 in useful organic compounds represents another attractive option for reducing its emissions in air. Its use as a raw material is however severely hindered by thermodynamic limitations. However, with the exception of CO, all products resulting from the chemical transformation of CO_2 require hydrogen as second reactant (Figure 1.4). These include: CO_2 catalytic hydrogenation, CO_2 dry reforming, CO_2 methanation and methanol and urea synthesis. Therefore, the problem of CO_2 conversion turns into a deeper problem related to the production and storage of hydrogen on a large scale[12].

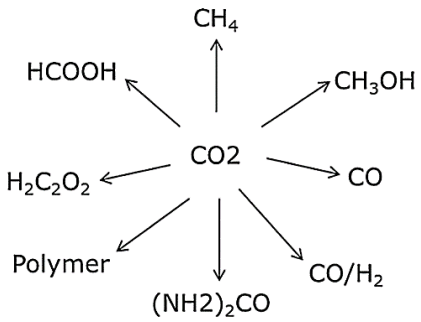

Figure 1.4 *Possible products from thermochemical CO_2 conversion. Reproduced with permission from ref.*[12]

Hydrogen is produced on a large scale thanks to steam reforming process (SMR), in which, at temperatures of 800-1000 °C and pressures of 20-30 bar, methane reacts with steam in the presence of a nickel-based catalyst to form CO and hydrogen.

$$O_2 + 2CH_4 \rightarrow 2CO + 4H_2 \qquad 4)$$

The production of hydrogen can be further pushed by the water-gas shift reaction (WGS), carried out at low temperatures, in which hydrogen and CO_2 are formed as a product of the reaction of steam with CO. Through the water-gas shift inverse reaction (RWGS), carried out with copper catalyst on alumina supports, it is possible to convert CO_2 in CO (reaction 5):

$$CO_2 + H_2 \rightarrow CO + H_2O \qquad 5)$$

Depending on the operating conditions in terms of temperature and pressure, it is possible to push the reaction equilibrium backward or forward. This reaction is important for the subsequent production of methanol, ammonia and in the Fischer-Tropsch synthesis, where it is necessary to ensure a precise H_2/CO ratio. In the CO_2 dry reforming (reaction 6), carbon dioxide acts as a weak oxidizer towards natural gas, in absence of steam, for the production of synthesis gas (mix of CO and H_2). This can be used later for the production of further chemical compounds and hydrocarbons.

$$CO_2 + CH_4 \rightarrow 2CO + 2H_2 \qquad 6)$$

However, at pressures above 5 atm, the RWGS becomes relevant, causing the H_2/CO ratio to decrease. Another disadvantage is the rapid deactivation of the catalyst due to coke formation. Catalytic hydrogenation of a CO and CO_2 mixture, carried out at temperatures of 210-290 °C and 50-80 bar of pressure, leads to the formation of various compounds, including methanol, whose consumption as an alternative fuel and chemical is in net increase (reactions 7-8):

$$CO + 2H_2 \rightarrow CH_3OH \qquad 7)$$

$$CO_2 + 3H_2 \rightarrow CH_3OH + H_2O \qquad 8)$$

Methane can be synthesized by strongly exothermic reaction of Sabatier, through the CO_2 and hydrogen reaction (reaction 9):

$$CO_2 + 4H_2 \rightarrow CH_4 + 2H_2O \qquad 9)$$

Another CO_2 possible conversion route is urea synthesis reaction, which involves an equilibrium of two different reactions. The first (reaction 10), rapid and exothermic, is carried out at high temperatures and pressures and leads to the formation of ammonium carbamate through the reaction of CO_2 with ammonia. The second (reaction 11), endothermic and slow, leads to the dehydration of ammonium carbamate, forming urea and water.

$$2NH_3 + CO_2 \rightleftarrows H_2N\text{-}COONH_4 \qquad 10)$$

$$H_2N\text{-}COONH_4 \rightleftarrows (NH_2)_2CO + H_2O \qquad 11)$$

The main disadvantage of these methods lies in the hard operating conditions, which often require high pressures and temperatures and can cause material

corrosion processes and accidental leaks. Table 1.1 shows the net CO_2 emissions considering the different sources of H_2.

	SMR	Biomass	Solar	Wind
Emissions (mol CO_2/mol H_2)	0.55	0.23	0.27	0.045
$CO_2 + H_2 \leftrightarrow CO + H_2O$	−0.45	−0.77	−0.73	−0.96
$CO_2 + 3H_2 = CH_3OH + H_2O$	0.65	−0.31	−0.19	−0.87
$CO_2 + 4H_2 = CH_4 + 2H_2O$	1.2	−0.08	0.08	−0.82

Table 1.1 *Net CO_2 emissions with different H_2 sources. Reproduced with permission from ref.*[12]

The data clearly show how the net CO_2 emission decreases (negative values) by using solar energy, wind energy and biomass as a source of production of hydrogen unlike the steam reforming process.

1.5 SOLAR TERMOCHEMICAL CONVERSION

Considering the growing demand for the use of renewable sources in the energy sector, great interest is increasingly covering the splitting of CO_2 obtained through concentrated sunlight, through a process like the "Solar thermochemical fuel production" (STFP). This process makes use of concentrated solar radiation, through the solar concentration technology (CST) necessary to reach the high temperatures of the process, to produce chemical fuels through the splitting of CO_2 into CO, a useful product leading to renewable hydrocarbons by subsequent transformation. One of the most used materials for this purpose is the CeO_2, which in 2010 was already considered a material with redox properties able to drive the thermochemical CO_2 splitting[20,21]. This process is achieved through two stages and the concentrated light is needed to reach the high temperatures required in the process, up to 1500 °C. In the first stage, CeO_2 is reduced at high temperature, while subsequently it is oxidized at low temperature by CO_2, leading to the formation of CO (Figure 1.5). In the first phase, the endothermic reduction reaction of the ceria is caused by a focused ray of sunlight, allowing the material to reach temperatures even higher than 1400 °C, also resulting in a release of oxygen. The reduced CeO_2 is then cooled below 1000 °C, in the absence of radiation, and then invested with a flow of CO_2 that oxidizes it, leading to the formation of CO as a by-product.

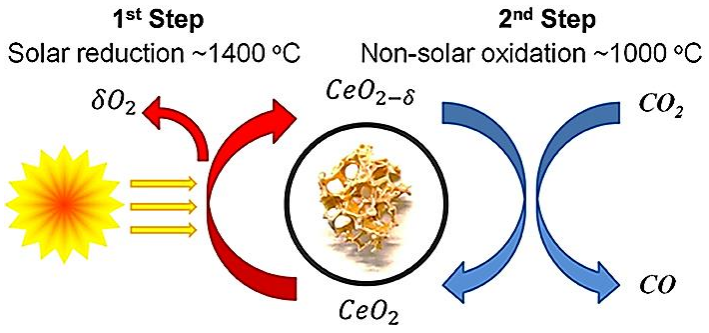

Figure 1.5 *Redox process for the CO production from the CO_2 splitting using CeO_2. Reproduced with permission from ref.*[21].

The ratio between the heating value of the produced CO and the energy of the incoming solar radiation represents the solar-to fuel energy conversion efficiency, which depends both on the characteristics of the thermochemical reactor and on the redox material. Its morphology has also an important impact as the reaction kinetics is directly linked to the surface area of the material. To allow a high efficiency of the process, it is necessary to identify materials characterized by stable redox properties capable of undergoing numerous cycles without deteriorating, and characterized by a morphology that is easily adaptable for integration with the thermochemical reactors[22,23]. Currently, there are various facilities around the world that use this technology. Among these, some of them operate with high flux solar furnaces (HSFF) using real, non-simulated solar energy, while others use high flux solar simulators (HFSS), with ovens powered by simulated sunlight. The largest solar power plant in France is able to offer a thermal power exceeding 1 MW.

1.6 BIOCHEMICAL CONVERSION

An innovative strategy for the conversion of CO_2 is represented by the use of biocatalysts; they are living organisms or their biological part, which speed up a chemical reaction. In respect to organic/inorganic species, they can be characterized by a high tolerance towards impurities, allowing the use of low purity reagents and reaching high efficiencies. Photosynthesis, using water, sunlight and CO_2, is a well-known biological process fixing inorganic carbon in the form of reduced organic compounds. Among the various biological species, autotrophs are organisms capable of synthesizing organic molecules starting from an inorganic carbon

substrate, while heterotrophs make use of organic carbon fixed by autotrophs for their development. A total of six pathways for inorganic carbon attachment were detected by forming C-C, C-H bonds and breaking C-O bonds through biomass cells. For example, plants and prokaryotes use a pentose-pathway cycle, which can be described in the following total reaction, the Calvin cycle[24]:

$$3CO_2 + 6NADPH + 5H_2O + 9ATP \rightarrow 3G3P + 6NADP + 9ADP + 8\ Pi \quad 12)$$

The Acetyl-CoA pathway is instead followed by microbes, such as methanogenic bacteria and archaea, for the formation of Acetyl-CoA from CO_2, through two steps in which CO_2 is reduced by dehydrogenase to formate and reduced to CO by CO dehydrogenase. Another way to reduce CO_2 involves the citric acid reduction cycle. Although numerous enzymes have been developed over time to carry out these conversions, the difficulty lies in carry on, in a controlled and repeatable way, these energetic transformations. An emerging tool to improve the whole process is the synthetic biology that allows engineering the microbes, modifying their properties in order to obtain different reaction paths and improve the selectivity towards the desired products, making the whole process economically advantageous. The use of native microbes has in fact the disadvantage of providing low efficiencies and the development of microorganisms can encounter obstacles due to unfavourable environmental conditions and can be characterized by low growth rates. Promising classes of organisms for the conversion of CO_2 into useful chemicals are photosynthetic organisms such as cyanobacteria and algae, although many challenges are in place today for optimizing their use in this field[25–28].

1.7 PHOTO-ELECTROCHEMICAL CONVERSION

In the optic of an integrated CO_2 capture and utilization strategy, an attractive and valuable way is the carbon dioxide reduction into synthetic fuels with electricity, under light irradiation or a combination of the two. This set of strategies comprises electroreduction, photoreduction and photo-electroreduction.

1.7.1 Electroreduction

Electroreduction is a very attractive strategy for the CO_2 conversion as i) it allows to operate at room temperature and atmospheric pressure, ii) it can be combined with renewable energy sources (such as solar cells for the production of the energy necessary for the reaction) and iii) the functionality and modularity are relatively simple[29-31]. Moreover, unlike chemical combustion processes, electrochemical processes can allow higher efficiencies as they are not affected by the limitations due to thermodynamic cycles. The electrocatalytic reduction of CO_2 can lead to the formation of high value-added products such as formic acid[32,33], carbon monoxide[34,35], ethylene[36], methane[37], etc. The distribution of the products is strongly dependent both on the reaction conditions (electrolytes and applied potential) and on the characteristics of the electrocatalyst[38]. However, many of these processes are characterized by low Faradaic efficiencies, high overpotentials, slow kinetics and low electrocatalyst stability[39].

1.7.2 Photoreduction

Photoreduction exploits the solar radiation for the CO_2 reduction into useful compounds, in the same way as glucose and oxygen are synthesized by green plants through natural photosynthesis. Numerous studies have been conducted in order to simulate this natural process. Ru and Re based complexes were initially employed through homogenous catalysis, with main formation of formate and CO[40-41]. Subsequently, studies moved towards heterogeneous catalysis through the use of oxide semiconductors (such as TiO_2, $SrTiO_3$, WO_3, etc) and metal sulphides for the photoreduction of CO_2 in the presence of water[42]. The basic principles of the so-called "artificial leaves" will be shown in more detail in the next paragraph.

1.7.3 Photo-electroreduction

Photo-electroreduction integrates both the electroreduction and photoreduction approach. The main advantages obtained through this strategy are:

i) required electrical voltage is lowered by solar energy, resulting in an overall electrical consumption decrease;

ii) applied external voltage drives the charge separation more effectively than in photocatalysis, which represents one of the most critical steps;

iii) use of two separate reaction half-cells prevents the products formed from undergoing reoxidation;

Photoreduction and photoelectroreduction are two highly attractive pathways for the conversion of CO_2 into organic compounds and artificial fuels through sunlight [43-46]. Although numerous advances have been made in this field in recent years, the catalytic performances are significantly lower than in photoelectrocatalytic water splitting. This is due to the fact that the activation of CO_2 is more difficult than H_2O, and the reduction process of CO_2 competes with the reduction of water for the formation of H_2. A further complication results in the reaction products, which are generally more complex than in water splitting, which produce only H_2, and require different technologies for their detection.

1.8 ARTIFICIAL LEAF

The photocatalytic reduction of CO_2 exploits solar radiation in the presence of a suitable photocatalytic material to produce synthetic fuels. Photoreduction can be thought as an artificial photosynthesis system (artificial leaf) in which a waste product such as CO_2 is recycled to produce energy, ideally closing the carbon cycle (Figure 1.6)[47,48]. However, the efficiency of this process does not exceed 45%, while an artificial photosynthesis process could be developed to exceed this value[49]. A natural leaf is a complex system composed of biostructures in the form of an efficient machine for photosynthesis in which the three basic steps, namely the capture of light, the separation of photogenerated charges and the surface reactions, allow to convert the solar into chemical energy by splitting water into O_2 and H_2; the latter reducing the adsorbed CO_2 into organic compounds.

Natural photosynthesis occurs in two phases, through reactions that make use of light and others that do not use it. As for the former, photosystems I and II allow the oxidation of water into O_2 and H^+ through sunlight (reaction 13) and the

reduction of $NADP^+$ in NADPH through protons and electrons produced by the first reaction (reaction 14).

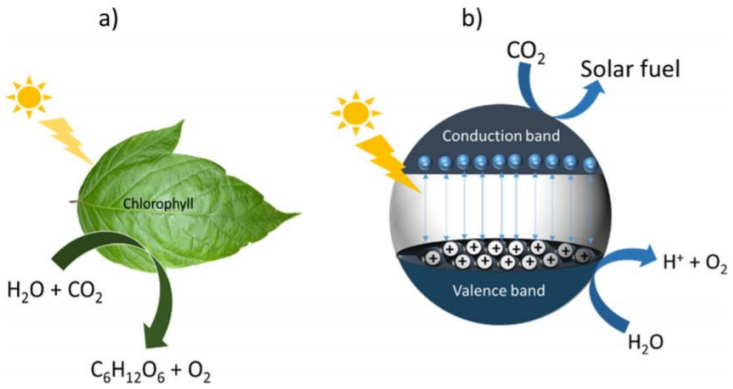

Figure 1.6 *Artificial and natural photosynthetic systems comparison. Reproduced with permission from ref.*[50]

The reactions not using light include the reactions between NADPH and CO_2 to form sugars and organic molecules[51].

$$2H_2O + 4hv \rightarrow O_2 + 4h^+ + 4e^- \qquad 13)$$

$$2NADP^+ + 2H^+ + 4e^- \rightarrow 2NADPH \qquad 14)$$

To mimic the natural photosynthesis produced by plants, artificial photosynthesis must use the "nascent" hydrogen, namely it uses the protons and hydrogen deriving from the water oxidation through solar energy. These reduce the CO_2 in the organic compounds but requires specific catalytic sites for these reactions. This technique has attracted attention over time as it does not require high temperatures and high-energy inputs, although it is generally necessary to operate at high pressures. In fact, the first two points make it more advantageous than chemical, electrochemical and biochemical transformations. The main drawback of this technique is the poor selectivity, but it can be improved by tailoring both the photocatalytic material and photoreactor design. A good catalyst for CO_2 must in fact lower the activation energy of reactions involving its reduction into carbon compounds, avoiding the reduction of H_2O in H_2. Numerous studies have been conducted over time to increase the efficiency and selectivity of the photocatalytic process through the improvement of the separation and transport of charges in the catalytic surface, the kinetics of CO_2 adsorption and the reaction intermediates. The hydrocarbons formed by the photoreduction of CO_2 are equivalent to traditional fossil hydrocarbons and can be used in mobile and stationary applications. The

photocatalytic route can be integrated in a carbon neutral cycle, to minimize the net CO_2 emissions (Figure 1.7).

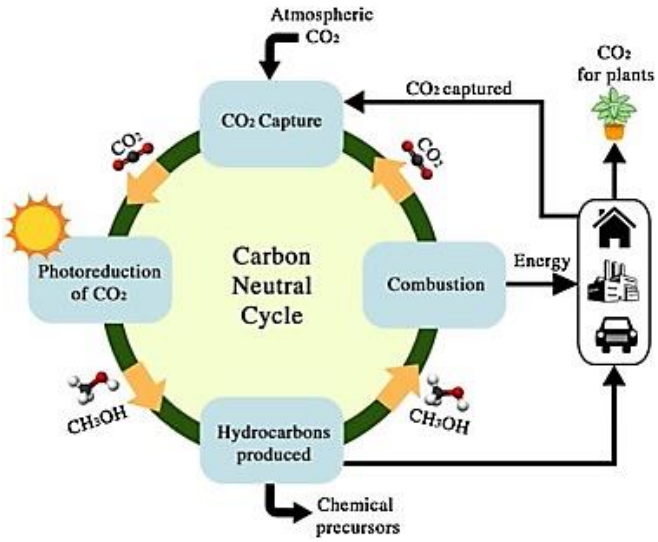

Figure 1.7 *Implementation of CO_2 photoreduction in a carbon neutral cycle. Reproduced with permission from ref.*[47]

The following equation represents the overall process by which gaseous and liquid products are formed by the artificial photosynthetic process (reaction 15):

$$2nCO_2 + 2nH_2O + hv \rightarrow 2(CH_2O)_n + 2nO_2 \quad 15)$$

The requirements that artificial leaves should possess compared to natural ones to be used massively, include a high efficiency of solar energy to chemical conversion, the possibility of using directly the fuels produced in an equipment for power production, a robustness of the system and an easy scalability[52].

Part of this thesis work has been carried out in collaboration with the ***European Consortium A-LEAF*** in order to create a platform for artificial photosynthesis through the capture and subsequent transformation of solar energy into chemical energy. The knowledge acquired through the consortium has made it possible to implement a bottom-up approach, in which all the acquired knowledge is scaled and transferred in the creation of a prototype of photoelectric cell, namely an artificial-leaf.

1.9 REFERENCES

1) Martha Ekkert. *Global Energy Transformation: A Roadmap to 2050*; **2018**.

2) *Global Energy & CO_2 Status Report 2018; International Energy Agency: Paris, France, **2019**.*

3) Ampelli, C.; Perathoner, S.; Centi, G. CO_2 Utilization: An Enabling Element to Move to a Resource- and Energy-Efficient Chemical and Fuel Production. *Philosophical Transactions of the Royal Society A: Mathematical, Physical and Engineering Sciences* **2015**, 373 (2037).

   https://doi.org/10.1098/rsta.2014.0177

4) Wu, J.; Huang, Y.; Ye, W.; Li, Y. CO_2 Reduction: From the Electrochemical to Photochemical Approach. *Advanced Science*. Wiley-VCH Verlag November 1, **2017**. https://doi.org/10.1002/advs.201700194.

5) Luderer, G.; Vrontisi, Z.; Bertram, C.; Edelenbosch, O. Y.; Pietzcker, R. C.; Rogelj, J.; de Boer, H. S.; Drouet, L.; Emmerling, J.; Fricko, O.; Fujimori, S.; Havlík, P.; Iyer, G.; Keramidas, K.; Kitous, A.; Pehl, M.; Krey, V.; Riahi, K.; Saveyn, B.; Tavoni, M.; van Vuuren, D. P.; Kriegler, E. Residual Fossil CO2 Emissions in 1.5-2 °c Pathways. *Nature Climate Change* **2018**, *8* (7), 626–633. https://doi.org/10.1038/s41558-018-0198-6.

6) *IRENA. Global Energy Transformation: A Road Map to 2050; International Renewable Energy Agency: AbuDhabi, UAE*; **2018**.

7) Ampelli, C.; Genovese, C.; Errahali, M.; Gatti, G.; Marchese, L.; Perathoner, S.; Centi, G. CO_2 Capture and Reduction to Liquid Fuels in a Novel Electrochemical Setup by Using Metal-Doped Conjugated Microporous Polymers. *Journal of Applied Electrochemistry* **2015**, 45 (7), 701–713. https://doi.org/10.1007/s10800-015-0847-7.

8) Tian, P.; Wei, Y.; Ye, M.; Liu, Z. Methanol to Olefins (MTO): From Fundamentals to Commercialization. *ACS Catalysis*. *American Chemical Society* March 6, **2015**, pp 1922–1938. https://doi.org/10.1021/acscatal.5b00007.

9) Genovese, C.; Ampelli, C.; Perathoner, S.; Centi, G. Mechanism of C-C Bond Formation in the Electrocatalytic Reduction of CO_2 to Acetic Acid. A Challenging Reaction to Use Renewable Energy with Chemistry. *Green Chem.* **2017**, 19 (10), 2406–2415. https://doi.org/10.1039/c6gc03422e.

10) Olah, G. A.; Goeppert, A.; Prakash, G. K. S. Chemical Recycling of Carbon Dioxide to Methanol and Dimethyl Ether: From Greenhouse Gas to Renewable, Environmentally Carbon Neutral Fuels and Synthetic Hydrocarbons. *Journal of Organic Chemistry* **2009**, 74 (2), 487–498. https://doi.org/10.1021/jo801260f.

11) Goeppert, A.; Czaun, M.; Jones, J. P.; Surya Prakash, G. K.; Olah, G. A. Recycling of Carbon Dioxide to Methanol and Derived Products-Closing the Loop. *Chemical Society Reviews*. *Royal Society of Chemistry* December 7, **2014**, pp 7995–8048. https://doi.org/10.1039/c4cs00122b.

12) Agarwal, A. S.; Rode, E.; Sridhar, N.; Hill, D. Handbook of Climate Change Mitigation and Adaptation; **2016**. https://doi.org/10.1007/978-1-4614-6431-0.

13) Martín, A. J.; Larrazábal, G. O.; Pérez-Ramírez, J. Towards Sustainable Fuels and Chemicals through the Electrochemical Reduction of CO_2: Lessons from Water Electrolysis. *Green Chemistry* **2015**, 17 (12), 5114–5130. https://doi.org/10.1039/c5gc01893e.

14) Costentin, C.; Robert, M.; Savéant, J. M. Catalysis of the Electrochemical Reduction of Carbon Dioxide. *Chemical Society Reviews*. March 21, **2013**, pp 2423–2436. https://doi.org/10.1039/c2cs35360a.

15) Steinfeld, A.; A.W. Weimer, A. W. Thermochemical Production of Fuels with Concentrated Solar Energy. Opt. Express **2010**, 18, A100–A111.

16) Sultana, S.; Chandra Sahoo, P.; Martha, S.; Parida, K. A Review of Harvesting Clean Fuels from Enzymatic CO_2 Reduction. *RSC Advances. Royal Society of Chemistry* **2016**, pp 44170–44194. https://doi.org/10.1039/c6ra05472b.

17) Li, K.; An, X.; Park, K. H.; Khraisheh, M.; Tang, J. A Critical Review of CO_2 Photoconversion: Catalysts and Reactors. *Catalysis Today* **2014**, 224, 3–12. https://doi.org/10.1016/j.cattod.2013.12.006.

18) Mander, S.; Anderson, K.; Larkin, A.; Gough, C.; Vaughan, N. The Role of Bio-Energy with Carbon Capture and Storage in Meeting the Climate Mitigation Challenge: A Whole System Perspective. *Energy Procedia* **2017**, 114 (November 2016), 6036–6043. https://doi.org/10.1016/j.egypro.2017.03.1739

19) Leung, D. Y. C.; Caramanna, G.; Maroto-Valer, M. M. An Overview of Current Status of Carbon Dioxide Capture and Storage Technologies. *Renewable and Sustainable Energy Reviews* **2014**, 39, 426–443. https://doi.org/10.1016/j.rser.2014.07.093.

20) Haussener, S.; Steinfeld, A. Effective Heat and Mass Transport Properties of Anisotropic Porous Ceria for Solar Thermochemical Fuel Generation. *Materials* **2012**, 5 (1), 192–209. https://doi.org/10.3390/ma5010192

21) Roy, S.; Ernst, J.; Kheradpour, P.; Bristow, C. A.; Lin, M. F.; Washietl, S.; Ay, F.; Meyer, P. E.; Stefano, L. di; Candeias, R.; Marbach, D.; Sealfon, R.; Kellis, M.; Landolin, J. M.; Carlson, J. W.; Chueh, W. C.; Falter, C.; Abbott, M.; Scipio, D.; Furler, P.; Haile, S. M.; Steinfeld, A. High-Flux Solar-Driven Thermochemical Dissociation of CO_2 and H2O Using Nonstoichiometric Ceria. *Science* **2010**, 330 (6012), 1797–1801.

22) Siegel, N. P.; Miller, J. E.; Ermanoski, I.; Diver, R. B.; Stechel, E. B. Factors Affecting the Efficiency of Solar Driven Metal Oxide Thermochemical Cycles. *Industrial and Engineering Chemistry Research* **2013**, 52 (9), 3276–3286. https://doi.org/10.1021/ie400193q

23) Lanzafame, P.; Abate, S.; Ampelli, C.; Genovese, C.; Passalacqua, R.; Centi, G.; Perathoner, S. Beyond Solar Fuels: Renewable Energy-Driven Chemistry. *ChemSusChem* **2017**, 10 (22), 4409–4419. https://doi.org/10.1002/cssc.201701507.

24) Yaashikaa, P. R.; Senthil Kumar, P.; Varjani, S. J.; Saravanan, A. A Review on Photochemical, Biochemical and Electrochemical Transformation of CO2 into Value-Added Products. Journal of CO_2 Utilization **2019**, 33 (March), 131–147. https://doi.org/10.1016/j.jcou.2019.05.017.

25) Zhang, A.; Carroll, A. L.; Atsumi, S. Carbon Recycling by Cyanobacteria: Improving CO_2 Fixation through Chemical Production. *FEMS Microbiology Letters* **2017**, 364 (16). https://doi.org/10.1093/femsle/fnx165.

26) Ryan Georgianna, D.; Mayfield, S. P. Exploiting Diversity and Synthetic Biology for the Production of Algal Biofuels. *Nature* **2012**, 488 (7411), 329–335. https://doi.org/10.1038/nature11479.

27) Berla, B. M.; Saha, R.; Immethun, C. M.; Maranas, C. D.; Moon, T. S.; Pakrasi, H. B. Synthetic Biology of Cyanobacteria: Unique Challenges and Opportunities. *Frontiers in Microbiology* **2013**, 4 (AUG), 1–14. https://doi.org/10.3389/fmicb.2013.00246.

28) Jiang, Y.; May, H. D.; Lu, L.; Liang, P.; Huang, X.; Ren, Z. J. Carbon Dioxide and Organic Waste Valorization by Microbial Electrosynthesis and Electro-Fermentation. *Water Research* **2019**, 149, 42–55. https://doi.org/10.1016/j.watres.2018.10.092.

29) Wang, Y.; Liu, J.; Wang, Y.; Wang, Y.; Zheng, G. Efficient Solar-Driven Electrocatalytic CO_2 Reduction in a Redox-Medium-Assisted System. *Nature Communications* **2018**, 9 (1). https://doi.org/10.1038/s41467-018-07380-x.

30) Huan, T. N.; Dalla Corte, D. A.; Lamaison, S.; Karapinar, D.; Lutz, L.; Menguy, N.; Foldyna, M.; Turren-Cruz, S. H.; Hagfeldt, A.; Bella, F.; Fontecave, M.; Mougel, V. Low-Cost High-Efficiency System for Solar-Driven Conversion of CO_2 to Hydrocarbons. *Proceedings of the National Academy of Sciences of the United States of America* **2019**, 116 (20), 9735–9740. https://doi.org/10.1073/pnas.1815412116.

31) Marepally, B. C.; Ampelli, C.; Genovese, C.; Saboo, T.; Perathoner, S.; Wisser, F. M.; Veyre, L.; Canivet, J.; Quadrelli, E. A.; Centi, G. Enhanced Formation of >C1 Products in Electroreduction of CO_2 by Adding a CO2 Adsorption Component to a Gas-Diffusion Layer-Type Catalytic Electrode. *ChemSusChem* **2017**, 10 (22), 4442–4446. https://doi.org/10.1002/cssc.201701506.

32) Han, N.; Wang, Y.; Yang, H.; Deng, J.; Wu, J.; Li, Y.; Li, Y. Ultrathin Bismuth Nanosheets from in Situ Topotactic Transformation for Selective Electrocatalytic CO_2 Reduction to Formate. *Nature Communications* **2018**, 9 (1), 1–8. https://doi.org/10.1038/s41467-018-03712-z.

33) Kwon, I. S.; Debela, T. T.; Kwak, I. H.; Seo, H. W.; Park, K.; Kim, D.; Yoo, S. J.; Kim, J. G.; Park, J.; Kang, H. S. Selective Electrochemical Reduction of Carbon Dioxide to Formic Acid Using Indium-Zinc Bimetallic Nanocrystals. *Journal of Materials Chemistry A* **2019**, 7 (40), 22879–22883. https://doi.org/10.1039/c9ta06285h.

34) He, S.; Ji, D.; Zhang, J.; Novello, P.; Li, X.; Zhang, Q.; Zhang, X.; Liu, J. Understanding the Origin of Selective Reduction of CO_2 to CO on Single-Atom Nickel Catalyst. *Journal of Physical Chemistry B* **2020**, 124 (3), 511–518. https://doi.org/10.1021/acs.jpcb.9b09730.

35) Wang, M.; Ren, X.; Yuan, G.; Niu, X.; Xu, Q.; Gao, W.; Zhu, S.; Wang, Q. Selective Electroreduction of CO_2 to CO over Co-Electrodeposited Dendritic Core-Shell Indium-Doped Cu@Cu_2O Catalyst. *Journal of CO_2 Utilization* **2020**, 37 (September 2019), 204–212. https://doi.org/10.1016/j.jcou.2019.12.013.

36) Chen, Y.; Fan, Z.; Wang, J.; Ling, C.; Niu, W.; Huang, Z.; Liu, G.; Chen, B.; Lai, Z.; Liu, X.; Li, B.; Zong, Y.; Gu, L.; Wang, J.; Wang, X.; Zhang, H.; Wang, J.; Wang, X.; Zhang, H. Ethylene Selectivity in Electrocatalytic CO_2 Reduction on Cu Nanomaterials: A Crystal Phase-Dependent Study. *Journal of the American Chemical Society* **2020**, 142 (29), 12760–12766. https://doi.org/10.1021/jacs.0c04981.

37) Wang, Z.; Yuan, Q.; Shan, J.; Jiang, Z.; Xu, P.; Hu, Y.; Zhou, J.; Wu, L.; Niu, Z.; Sun, J.; Cheng, T.; Goddard, W. A. Highly Selective Electrocatalytic Reduction of CO_2 into Methane on Cu-Bi Nanoalloys. *The journal of physical chemistry letters* **2020**, 11 (17), 7261–7266. https://doi.org/10.1021/acs.jpclett.0c01261.

38) Ampelli, C.; Genovese, C.; Cosio, D.; Perathoner, S.; Centi, G. Effect of Current Density on Product Distribution for the Electrocatalytic Reduction of CO_2. *Chemical Engineering Transactions* **2019**, 74 (December 2018), 1285–1290.

39) Ceballos, B. M.; Yang, J. Y. Highly Selective Electrocatalytic CO_2 Reduction by $[Pt(Dmpe)_2]^{2+}$ through Kinetic and Thermodynamic Control. *Organometallics* **2020**, 39 (9), 1491–1496. https://doi.org/10.1021/acs.organomet.9b00720.

40) Das, B.; Jia, C.; Ching, K.; Bhadbhade, M.; Chen, X.; Ball, G. E.; Colbran, S. B.; Zhao, C. Ruthenium Complexes in Homogeneous and Heterogeneous Catalysis for Electroreduction of CO_2. *ChemCatChem* **2020**, 12 (5), 1292–1296. https://doi.org/10.1002/cctc.201902020.

41) Kuramochi, Y.; Ishitani, O.; Ishida, H. Reaction Mechanisms of Catalytic Photochemical CO_2 Reduction Using Re(I) and Ru(II) Complexes. *Coordination Chemistry Reviews* **2018**, 373, 333–356. https://doi.org/10.1016/j.ccr.2017.11.023.

42) Thompson, W. A.; Olivo, A.; Zanardo, D.; Cruciani, G.; Menegazzo, F.; Signoretto, M.; Maroto-Valer, M. M. Systematic Study of TiO_2/ZnO Mixed Metal Oxides for CO_2 Photoreduction. *RSC Advances* **2019**, 9 (38), 21660–21666. https://doi.org/10.1039/c9ra03435h.

43) Xie, S.; Zhang, Q.; Liu, G.; Wang, Y. Photocatalytic and Photoelectrocatalytic Reduction of CO_2 Using Heterogeneous Catalysts with Controlled Nanostructures. *Chemical Communications* **2016**, 52 (1), 35–59. https://doi.org/10.1039/c5cc07613g.

44) Ampelli, C.; Passalacqua, R.; Genovese, C.; Perathoner, S.; Centi, G. A Novel Photo-Electrochemical Approach for the Chemical Recycling of Carbon Dioxide to Fuels. *Chemical Engineering Transactions* **2011**, 25, 683–688.

45) Ampelli, C.; Genovese, C.; Tavella, F.; Perathoner, S.; Centi, G. Nano-Engineered Electrodes for the Generation of Solar Fuels: Benefits and Drawbacks of Adopting a Photo-Electrocatalytic (PECa) Approach. *Chemical Engineering Transactions* **2017**, 57, 1597–1602. https://doi.org/10.3303/CET1757267.

46) Ampelli, C.; Genovese, C.; Centi, G.; Passalacqua, R.; Perathoner, S. Nanoscale Engineering in the Development of Photoelectrocatalytic Cells for

Producing Solar Fuels. *Topics in Catalysis* **2016**, 59 (8–9), 757–771. https://doi.org/10.1007/s11244-016-0547-5.

47) Tjandra, A. D.; Huang, J. Photocatalytic Carbon Dioxide Reduction by Photocatalyst Innovation. *Chinese Chemical Letters* **2018**, 29 (6), 734–746. https://doi.org/10.1016/j.cclet.2018.03.017.

48) Nguyen, V. H.; Nguyen, B. S.; Jin, Z.; Shokouhimehr, M.; Jang, H. W.; Hu, C.; Singh, P.; Raizada, P.; Peng, W.; Shiung Lam, S.; Xia, C.; Nguyen, C. C.; Kim, S. Y.; Le, Q. van. Towards Artificial Photosynthesis: Sustainable Hydrogen Utilization for Photocatalytic Reduction of CO_2 to High-Value Renewable Fuels. *Chemical Engineering Journal 2020*, 402, 126184. https://doi.org/10.1016/j.cej.2020.126184.

49) Xiao, Y.; Qian, Y.; Chen, A.; Qin, T.; Zhang, F.; Tang, H.; Qiu, Z.; Lin, B. L. An Artificial Photosynthetic System with CO_2-Reducing Solar-to-Fuel Efficiency Exceeding 20%. *Journal of Materials Chemistry A* **2020**, 8 (35), 18310–18317. https://doi.org/10.1039/d0ta06714h.

50) Adamu, A.; Russo-Abegão, F.; Boodhoo, K. Process Intensification Technologies for CO_2 Capture and Conversion – a Review. *BMC Chemical Engineering* **2020**, 2 (1), 1–18. https://doi.org/10.1186/s42480-019-0026-4.

51) Zhou, H.; Fan, T.; Zhang, D. An Insight into Artificial Leaves for Sustainable Energy Inspired by Natural Photosynthesis. *ChemCatChem* **2011**, 3 (3), 513–528. https://doi.org/10.1002/cctc.201000266.

52) Bensaid, S.; Centi, G.; Garrone, E.; Perathoner, S.; Saracco, G. Towards Artificial Leaves for Solar Hydrogen and Fuels from Carbon Dioxide. ChemSusChem **2012**, 5 (3), 500–521. https://doi.org/10.1002/cssc.201100661.

2. CO_2 PHOTO-ELECTRO-CATALYSIS

2.1 INTRODUCTION

Carbon dioxide (CO_2) is a linear, stable, non-polar molecule (Figure 2.1), being at the maximum potential state, and its conversion requires a very efficient catalyst to overcome kinetic and thermodynamic limitations.

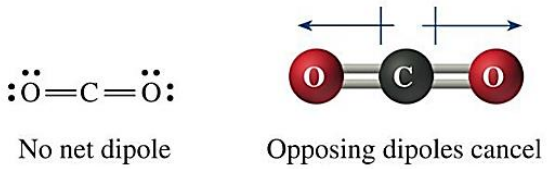

Figure 2.1 *Dipoles in CO_2.*

The C-O double bond has in fact an energy of 750 kJ mol^{-1}, which overcomes the C-C, C-H, C-O single bond having energies of 336, 441 and 327 kJ mol^{-1}, respectively. The studies of electrochemical conversion of CO_2 have been started more than 30 years ago, involving the use of metallic and non-metallic catalysts, and only electrons as energy input, to produce many fuels at different carbon number atoms including CO, HCOOH, CH_4, C_2H_4, CH_3OH, proceeding through two, four, six and eight multi-step electron reduction processes[1]. The distribution of these compounds depends on many factors ranging from the nature of the catalyst to the operating conditions and this makes the process generally poorly efficient and with limited selectivity. If light is used to promote these chemical reactions, the process is called photocatalytic or photo-electrocatalytic reduction of CO_2. This process is obtained employing semiconductor materials having band levels of appropriate energy to enable the expected reactions, coupled with an opportune co-catalyst to reach an adequate selectivity. Thus, the photo(electro)catalytic route combines materials able to harvest the light with electrocatalysts, allowing a fine-tuning and minimizing energy losses. In these composite electrodes, the key point is the interface engineering, namely the modification of the surface-active sites, for example through the insertion of atoms in order to form bimetallic systems, even considering that during a reaction they can suffer important surface modifications[2]. The required potential difference between cathode and anode imposes the use of different kinds of electrochemical devices, or a combination of them, made up of

photoanodes or photocathodes in series or, as alternative, coupled with an external energy supplier. Considering many units in series, the current density may be limited by the electrode with the higher resistance. A modular approach, consisting of a CO_2 electrolyser in the dark connected with a photovoltaic device, can overcome this problem[3]. Such a system, applied also to the water splitting, provided in this case a solar-to-hydrogen efficiency (STH) of 30%, the highest ever.

2.2 CO_2 ELECTROCATALYTIC REDUCTION

2.2.1 Thermodynamic and kinetic aspects

A single cathodic reaction in CO_2 electrocatalytic reduction process (CO_2ERR) can be written in this form:

$$xCO_2 + nH^+ + ne^- \rightarrow products + yH_2O$$

This half reaction is coupled with the anodic oxygen evolution reaction (OER), in which water provides electrons and protons needed for the process. There are several advantages of CO_2 conversion by the electrochemical route and they include i) the possibility of recycling the electrolyte minimizing the chemical wastes, ii) the control of the entire process only changing the operating conditions and the cathode potential. Moreover, the electricity needed to lead the process can be obtained by energy source not involving the generation of extra CO_2, like geothermal, thermoelectric, solar and windy processes. The electrochemical reactors are generally very compact, can be used in modular applications and are easy to scale-up for wider demands[4]. However, some severe limitations include:

i) the CO_2 energetic barrier and the reduction reactions slow kinetics, present even at high reduction potential and using an opportune electrocatalyst;

ii) the low efficiency of the process due to parallel electron-consuming reactions like the decomposition of the solvent and the stability of the catalyst, which can be compromised increasing the potentials;

iii) the low solubility of CO_2 in water (0.034 M at r.t.), which can be improved using a non-aqueous solvent, increasing the CO_2 partial pressure and/or working at low temperature.

Even pressure and CO_2 flow rate can affect the CO_2ERR reaction. Some metals, in fact, if exposed to high pressure can be activated and perform better than operating at low pressure, while if the flow rate is lower than 50 mL min^{-1} it strongly affects the Faradaic efficiency and selectivity. For a given electrochemical reaction, the total cell voltage (E_{cell}) required is the contribution of cathodic and anodic potentials, and is given by:

$$E_{cell} = E_{cathode} - E_{anode}$$

This represents only a theoretical thermodynamic value, because generally CO_2 reduction reactions require an overpotential exceeding several hundred mV to achieve acceptable kinetic rates. The possibility to lower this overpotential and select an efficient anode in the OER can make it possible to decrease the overall energy required for the process. The more positive the standard reduction potential (E°) of a given reduction reaction, the lower the Gibbs free energy (ΔG) is, making the reactions more favourable under the given conditions, as showed in the following equation:

$$\Delta G° = - nFE°$$

ΔG is proportional to n, the number of electrons involved in the process, and F, the Faraday constant.

The complexity of CO_2 reduction consists mainly in tuning properly the selectivity, because a large number of products can be obtained and these can further react together or with the CO_2. Considering that most reactions require a similar energy input, the only way to address the selectivity is by controlling the cathodic potential [5]. In terms of energy demand, the most interesting products like alcohols or methane require less energy but kinetic limitations, deriving from the high number of electrons and protons needed, exist. Thus, the use of high potentials can be more favourable for simpler and less attractive products like CO, or can enable undesired reactions like water reduction to H_2 (HER), the most important side-reaction consuming electrons and energy useful for the reduction of CO_2. From an electrochemical reaction, a mix of compounds (not only one product) can be produced, depending on the electrode potential applied in relation with the selectivity of the catalyst. Both the catalyst structure and the electrolyte are known to play an important role in catalysis, the first providing the active sites for the reduction and the latter by interacting with the intermediate species and reactants,

affecting then the overall reduction reaction path. The use of ionic liquid solvents, for example, can provide a favourable environment through the stabilization of the intermediate species and a tendency to form a complex with CO_2, improving the catalytic activity and driving selectivity [6,7]. Moreover, they are characterized by high stability, high conductivity and large electrochemical window. In order to tune finely the selectivity toward the desired products it is thus needed to understand the interaction mechanism between CO_2 and solvent. In order to drive the selectivity towards the desired products, many studies of CO_2 electrochemical reduction have been performed on metallic and non-metallic catalysts and different and novel reaction pathways have been proposed, as shown in Figure 2.2. The CO_2ERR involves multi-step reactions with different pathways, which occur at the electrode/electrolyte interface and require at least three main steps that can be described as follows[8]:

I) Adsorption of CO_2 at the electrode surface.

II) Migration of protons or electron transfer to break the C-O bonds to form C-H bonds.

III) Desorption of the as-rearranged products and diffusion into the electrolyte.

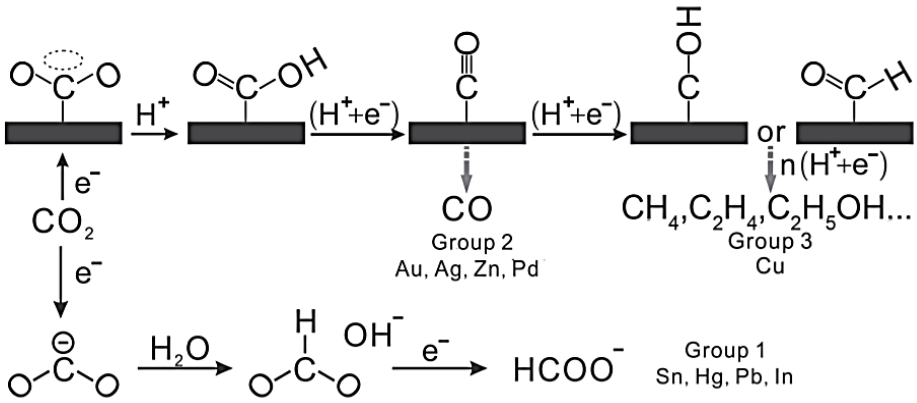

Figure 2.2 *Proposed reaction mechanism for CO_2 electrochemical reduction over metallic surface. Reproduced with permission from ref.*[9]

In the first step, the linear CO_2 molecule is turned to the bound $CO_2^{\bullet-}$ intermediate radical and, due to the geometrical rearrangement, this could represent the rate limiting step in the process. In order to reduce the kinetic limitations of this step, an overpotential of -1.9 V vs SHE (at pH=7) is in general required[10]. After this step, the reactive radical can promote more thermodynamically favourable proton-

electron transfer multi-step processes. A strategy to lower the total energy required is to bypass the formation of this radical, which requires a very high negative potential, with reductive multi-step process mediated by protons. Due to the wide complexity of interaction between electrode, electrolyte and CO_2, no single pathways that lead to a specific compound can be described. In fact, this depends on several factors like the specific morphology, type and nature of the catalyst, the number of electrons involved in the process and the energy barrier required. The standard reduction potentials (E° / V) of the half-cell reduction reactions for the main carbon products, obtained through electrocatalysis, are showed in Table 2.1. The values are reported for an aqueous media at pH=7.

Half-cell thermodynamic reaction	Name	E° vs SHE, at pH=7
$CO_2\,(g) + e^- = CO_2^{\bullet -}$	$CO_2^{\bullet -}$ anion radical	-1.90
$2H^+ + 2e^- = H_2$	hydrogen	-0.42
$CO_2\,(g) + 2H^+ + 2e^- = HCOOH_{(aq)}$	Formic acid	-0.61
$CO_2\,(g) + 2H^+ + 2e^- = CO_{(g)} + H_2O$	Carbon monoxide	-0.53
$CO_2\,(g) + 4H^+ + 4e^- = CH_2O_{(aq)} + H_2O$	Formaldehyde	-0.48
$CO_2\,(g) + 6H^+ + 6e^- = CH_3OH_{(aq)} + H_2O$	Methanol	-0.38
$CO_2\,(g) + 8H^+ + 8e^- = CH_{4(g)} + 2H_2O$	Methane	-0.24
$2CO_2\,(g) + 12H^+ + 12e^- = C_2H_{4\,(aq)} + 3H_2O$	Ethylene	0.06
$2CO_2\,(g) + 12H^+ + 12e^- = C_2H_5OH_{\,(aq)} + 3H_2O$	Ethanol	0.08

Table 2.1 *Half-electrochemical thermodynamic reaction potential (E°/V) vs SHE at pH=7.*[11]

The main parameters that can be used to estimate the performance of a CO_2ERR process are: I) current density, II) overpotential, III) Faradaic efficiency, IV) energetic efficiency.

I) Current density represents the current divided by the geometrical active area of the electrode.

II) *Overpotential* is the difference between the potential actually applied and the thermodynamically required potential.

III) Faradaic efficiency is a measure of the efficiency in which the total current is used directly to form a specific compound. It can be calculated as follows: $\frac{n\,F}{Q}$, namely the ratio of electrons moles involved for a specific reduction multiplied by

the Faraday constant (96486 C mol^{-1}), while Q is the total charge involved in the electrolysis.

IV) Energetic efficiency is a very useful parameter used to characterize low temperature electrolyzers. It expresses the ability to convert the electric potential applied (E°+μ) in the desired product, combining the polarization losses (μ) and the losses due to the ideal non-selectivity toward that product (FE<100%). It is given by $\frac{E^\circ\ FE}{E^\circ+\mu}$, where E° is the thermodynamic potential, FE the faradaic efficiency and μ the cell overpotential.

The CO_2ERR has been processed in many reactors with different design, like the *H-type cell*, the *flow cell system* and *microfluidic reactor* and they will be discussed in the next chapter.

2.2.2 Electrochemical influence of the double-layer on selectivity

The nature of the double-layer can be explained by dividing the electrochemical interface in five parts, as showed in Figure 2.3. The first part is the electrode, the solid conductive surface that allows the transfer of the charge carriers from the electrolyte, which is controlled by the applied potential. In the electrode/electrolyte interface, the Helmholtz plane can be recognized, which can be ideally divided into the Inner Helmholtz plane (IHP) and the Outer Helmholtz plane (OHP). The region of space in which the molecules are adsorbed belongs to the first plane, whether they are solvent, product, or intermediate species. All the solvated electrolyte ions, which are attracted by electrostatic forces, are placed in the OHP and then this region includes non-adsorbed particles. The electrode and the OHP have an opposite charge, because if the electrode is negatively charged, the OHP will be composed of ions with the solvation shell charged positively. Beyond the OHP, the diffuse layer extends by alternating layers of cations and anions, necessary to ensure the charge neutrality along all the double layer. The last part is the bulk, namely the region in which charge distribution is no longer affected by the electrode potential. This in fact undergoes an exponential decay from the electrode and along the entire double layer[12]. Structure and charge distribution in the double-layer are affected by several factors, such as the pH and the concentration gradient, close to the interface. It has been proved how a low pH can

break the water H-bond framework involved in the solvation spheres, making H_3O^+ attracted to the electrode in the IHP, increasing the effective electrode potential[13].

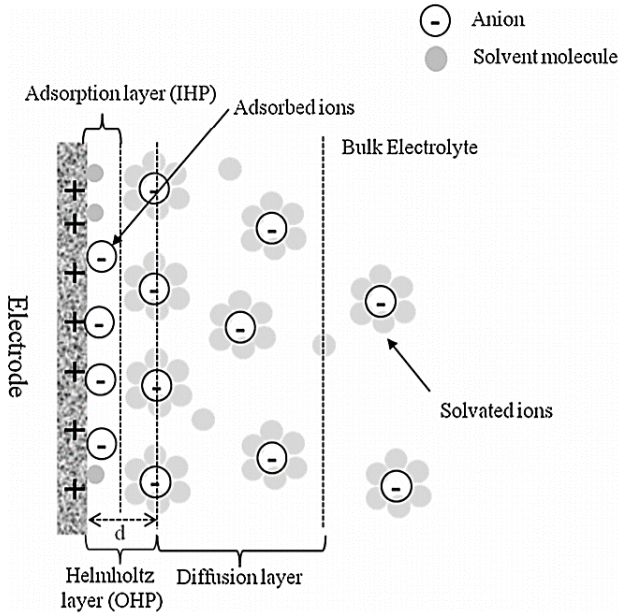

Figure 2.3 *Electrode/electrolyte interface mode. Reproduced with permission from ref.*[13]

The reaction rates of oxygen evolution reaction (OER), hydrogen evolution reaction (HER), or CO_2 electroreduction reaction (CO_2ERR) can be improved by modulating the electrolyte pH or the proton (H^+) concentration gradient, both affecting in different way the double-layer structure. In fact, it was found how a higher pH keeps a high order in the solvation shell and H-bond structure, decreasing the rate of HER with respect to working at lower pH. The concentration gradient near the electrode can strongly affect the kinetics of the processes due to mass transfer limitations. The overpotential of reactions involving the consumption and/or production of H^+ and OH^- can become larger than what expected, due to concentration gradients of these species. A study performed with a rotating electrode by Katsounaros et al.[14] reported how the interfacial pH can diverge from 3 units to 1 unit with respect to the bulk pH in neutral and acid/basic environment, respectively. Another study reported how working with high interfacial pH and with a Cu based electrode, HER can be limited in favour of CO_2ERR[15]. In a study involving Cu nanowires anchored to a Cu electrode support, Raciti et al.[16] proved how the selectivity towards C_2 products can be enhanced if a pH of 9-10 is kept near the electrode, without changing the CO_2 local concentration. The CO_2 local interface concentration is another key point, because if the overpotential is too high, CO_2 concentration can be depleted dropping to zero in the electrode surface.

2.3 CO_2 PHOTOREDUCTION

2.3.1 Basic principles

Since many years, researchers have attempted to emulate the natural photosynthesis with the aim to convert spontaneously the atmospheric CO_2 into water and other useful compounds using only sunlight like input energy. The efforts made so far highlight how the artificial photosynthesis can have a great potential although its efficiency is still very low. A first option is the use of photovoltaic cells to generate a voltage, which is then applied to a cathode to reduce CO_2; also in this case, the two electrodes should be properly designed to overcome the kinetic limitations of the reaction and move the selectivity toward the desired products. The main advantage of this approach is the flexibility in the design of both the PV modules and the two electrocatalysts, in order to optimize individually and then combine them to obtain the best performances. The second approach involves the use of light-harvesting semiconductors, often decorated with specific electrocatalysts (or co-catalyst) in a direct photocatalytic reaction. The main advantage of this route, with respect to the previous one, is the possibility to design more compact and easy scalable devices. These catalysts, which can be dispersed in aqueous solution, allow the following steps occurring all within the same catalyst particles, as showed in Figure 2.4.

I) Harvesting of photons

II) Charge separation in the electrode/electrolyte surface

III) CO_2 adsorption on the catalyst surface

IV) Charge transfer toward specific reaction pathways.

V) Product desorption

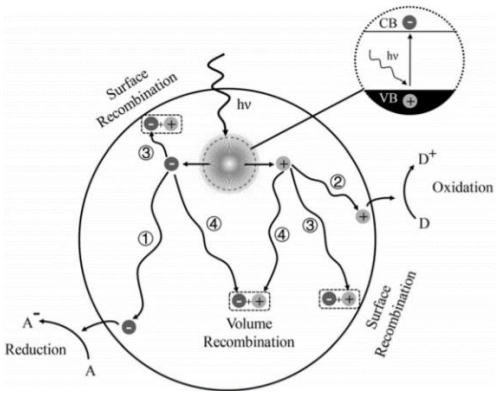

Figure 2.4 *Mechanism for the CO_2 photochemical reduction over a semiconductor particle. Reproduced with permission from ref.*[8]

In the first step, incident photons cause the formation of electron-hole pairs (h^+e^-) on the semiconductor (SC) surface, as described below:

$$SC + hv \rightarrow h^+e^-$$

$$h^+e^- \rightarrow h^+ + e^-$$

The electrons (e^-) are excited and the energy absorbed promotes them from the valence to the conduction band, while the holes (h^+) remain in equal number of the electrons excited, in the valence band. A CO_2 reduction process occurs if the electrons and holes generated possess enough energy to make possible the overall reaction, namely the reduction of CO_2 and/or oxidation of water, and to make this the bands must be energetically compatible with the reactions involved. In particular, the valence band edge must be more positive than the redox potential of the water oxidation reaction (0.817 V vs SHE at pH=7), while the conduction band must be more negative than the CO_2 reduction redox potential. On the other hands, it is necessary to take into account the overpotentials, associated with kinetic limitations, needed for the reactions. The band gap should be larger than that expected from the theoretical values, but it is important to make it also compatible with solar spectrum or in general with the incident photon energy. For example, TiO_2, one the most studied semiconductor, has a band gap of 3.2 eV and absorbs highly energetic photons in the region of ultraviolet (less than 400 nm), which are limited in the solar light spectrum to less than 5 %. Modifying the band structure of the photocatalyst involves strategies like the solid solution or doping.

The second step involves the separation, within the surface of the particle, of electrons and holes just generated, competing with the charge recombination

process. Lifetime of the photogenerated charges, charge recombination rate, crystallinity, surface properties are some factors making one process more dominant over the others. A charge recombination rate higher than the charge separation rate results in a significant free charge loss and consequently release in form of heat of the absorbed energy. Some surface treatments can modify the material properties and improve the charge separation to increment the resulting photocatalytic efficiency.

The CO_2 adsorption represents the third step and it is an important requisite to allow the electron transfer from the photocatalyst. A high surface area can in general represent a source of many active sites, but in other cases treatments like the alkali modification can modify the surface adsorption properties, exploiting the interaction of the Lewis acidity of CO_2 and the alkaline catalyst group. This can happen through the formation of intermediates like carbonate groups, which favour the activation and reaction of CO_2.

The surface reactions represent the fourth step, which is driven by the photogenerated electrons and holes, migrating along the particle surface. This is a pure electrocatalytic process and both the two charges operate different half reactions: in particular, the electrons reduce CO_2 to hydrocarbons, while the holes oxide water to O_2. This step can be enhanced by the introduction of an opportune co-catalyst, and in general the materials working well in pure electrocatalysis can be used with good results also coupled with a photocatalytic semiconductor.

The last step is the desorption, which involves the rapid release of the generated products from the catalyst surface. If it does not happen easily, the catalyst can be poisoned and efficiency can drop drastically. If the photocatalytic reactions are carried out in an aqueous media, they can involve either direct reaction of CO_2 with the e^- of the CB, or with other species formed from CO_2 such as bicarbonate, carbonate and hydrogen carbonate ions, whose distribution depends on pH and temperature, and acting with different reduction mechanisms. At pH<4 and pH>10 the main species are H_2CO_3/ HCO_3^- and CO_3^{2}, respectively, while at pH near 7 carbonic, hydrogen carbonic acid and carbonates are present[17].

$CO_2 + H_2O \leftrightarrow H_2CO_3 \leftrightarrow HCO_3^- + H^+$ $\quad pKa = 6.4$

$HCO_3^- \leftrightarrow CO_3^{2-} + H^+$ $\quad pKa = 10.3$

In literature, reaction mechanism hypotheses over different metal oxides like TiO_2, MgO and ZnO_2, have been reported involving several steps starting from the production of formic acid, from which subsequent reduction and hydrogenation provide the formation of methylene glycol, acetaldehyde, methanol, and methane. Carbon monoxide can be obtained by the reaction of CO_2 with the $CO_2^{\bullet -}$ anion radical or through its dissociation in the oxygen vacancy sites (V_O)[18].

$$CO_2 + e^-_{Cb} \rightarrow {}^{\bullet}CO_2^-$$

$${}^{\bullet}CO_2^- + H^+ \rightarrow HCOO^{\bullet}$$

$${}^{\bullet}CO_2^- + CO_2 \rightarrow CO + CO_3^{2-}$$

$$[V_O + SC] + {}^{\bullet}CO_2^- \rightarrow CO + SC$$

$${}^{\bullet}CO_2^- + {}^{\bullet}CO_2^- \rightarrow [O_2CCO_2]^{2-}$$

Methane can be obtained either by the reduction of carbon monoxide or by acetaldehyde, which turns to aceytl radical by oxidation, as shown by the following reactions:

$$CO + 6e^- + 6H^+ \rightarrow CH_4 + H_2O$$

$${}^{\bullet}CH_3 + H^+ \rightarrow CH_4$$

Hydrogen is the most important side-reaction product and its formation is thermodynamically more favourable with respect to CO_2 photoreduction, because the first is a two-electron transfer process, while the second requires 8 electrons and more. The steps that cause the formation of H_2 from water are described below and involve the formation of hydrogen radicals $H^{\bullet}$.

$$H_2O + h^+_{vb} \rightarrow H^+ + OH^-$$

$$H^+ + e^-_{Cb} \rightarrow H^{\bullet}$$

$$H^{\bullet} + H^{\bullet} \rightarrow H_2$$

Photocatalytic reactions can be performed also in gaseous media, and in this case the H_2O/CO_2 ratio is of great importance and needs to be optimized[19]. The feed ratio is a crucial element in addressing selectivity, due to the competitive adsorption of H_2O and CO_2 in the active sites of the catalyst, as demonstrated by Wu et al. in the

methanol synthesis with Cu/TiO_2 catalyst. Selectivity to methanol was high at low H_2O/CO_2 ratios and decreased at high ratio[20].

Many classes of materials, like metal oxides, metal sulphides, metal nitride and MOFs are employed in photocatalysis. The Figure 2.5 shows some common photocatalysts and their energy band structure. In the class of metal oxides, many d^0 transition metal cations, like Mo^{6+}, W^{6+}, Ta^{5+}, Ti^{4+}, Zr^{4+}, are commonly used for CO_2 reduction. Their band gap can generally allow the two half reactions of CO_2 reduction and water oxidation because their CB, made up of O $_{2p}$ orbitals, is more positive than 3 eV, while their VB, made up of d empty orbital, are more negative than 0 V. However, one limitation in these materials is the need to exploit the solar spectrum for the most part in the ultraviolet region.

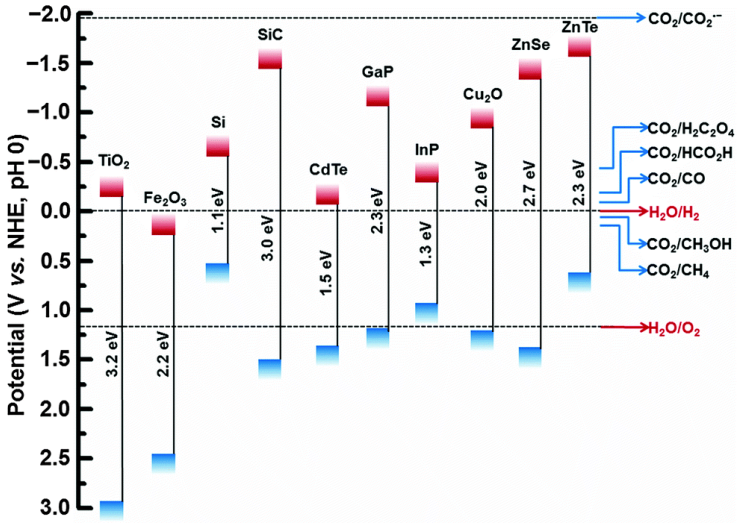

Figure 2.5 *Band energy levels for different photocatalysts compared with the main energy band for CO_2 reduction. Reproduced with permission from ref.*[21]

Other transition metal oxides, like titanates, niobates, tungstate, tantalates, vanadate, as well as other metal oxides with d^0 configurations, like Sb^{5+}, Sn^{4+}, Ge^{4+}, Ga^{3+}, In^{3+}, are active as photocatalysts. For the latter, sp hybridized orbitals form their conduction band at high energy, but this means a large band gap as well, thus needing higher energy photon, namely UV light[22]. Platinum (Pt), selective for the reduction of water to hydrogen, is not usually used for CO_2 reduction because it becomes poisoned due to strong CO bond[23], while Ag for the reverse reason shows a better activity[24]. It has been shown how bimetallic systems loaded on a matrix, like $Cu\text{-}Pt/TiO_2NTs$, offer good selectivity for the production of C_2H_4, CH_4, C_2H_6[25]. Use of heterostructures, coupling with different semiconductor types, can provide higher surface area and better light absorption. $CdSe/Pt/TiO_2$ heterostructures were

used successfully for the photoreduction of CO_2, with predominant activity towards the formation of CH_4, methanol, and H_2 and CO in traces[26]. The co-doping, realized with different combinations like metal/metal, metal/non-metal, could affect the properties of a photocatalyst; metals can facilitate the migration of the photogenerated electrodes limiting the recombination, while non-metals can improve light absorbance due to a red shift, making the band gap narrower.

A very important class is represented by the Metal-organic Framework (MOF) materials, consisting of metal atoms or clusters included in a framework of organics ligands resulting in a complex and versatile open and porous structure that can combine the advantages of different materials[27]. Including TiO_2 particle in an organic framework can combine the photocatalytic activity of the first with the visible light absorption of the second. Several Ti-based MOFs with amine functionality decorated with substituted alkyl groups were recently proposed[28].

The metal sulphides have also been used in the photocatalytic conversion of CO_2. In comparison with metal oxides, they are more susceptible of auto-photocorrosion because they possess a more negative VB than the metal oxides, but not enough to catalyse the oxidation of water; thus, there is the need to add hole scavengers to increase the oxidation capacity. CdS and ZnS are two very used photocatalysts for CO_2 reduction. Eggins et al.[29] showed that CdS was able to produce as the main products methanol formaldehyde, formate, acetate, and glyoxylate, while ZnS produced mainly CO and formate when doped with Ru[30].

About the metal nitrides, their VB is made up of N_{2P} orbitals and this ensures them a narrow band gap with a wide light absorption, but in contrast it was recognized a low photoactivity for the d^0 configuration nitride-based metals, like TaON, Ta_3N_5 and the class of $MTaO_2N$ (M=Sr,Ba, La), due to their low energetic conduction band[31]. Most promising in the CO_2 photoreduction are also the metals with d^{10} configuration, as the GaN, reported for the CO and CH_4 production[32] and for its high photostability (making not necessary the use of hole scavengers) and zinc-based metal nitrides, like ZnGaNO and ZrGeO[33].

A useful parameter to estimate the conversion efficiency of photons into electrons is apparent quantum yield (AQY).

It is calculated by dividing the number of reacted electrons by the number of incident photons, as the following equation shows:

AQY% = (Number of reacted electrons) / (Number of incident photons) x 100

The number of incident photons (N) is calculated by:

N = (Light absorbed by the photocatalyst) / (Average photon energy) x t

Where *t* is the reaction time; the average photon energy can be calculated as hc/λ where *h* is the Planck's constant ($6.626\ 10^{-34}$ J s), *c* the speed of light ($3\ 10^{8}\ m\ s^{-1}$) and λ can be estimated as the average wavelength of the broadband light source.

2.4 REFERENCES

1) Hori, Y.; Murata, A.; Yoshinami, Y. Adsorption of CO, Intermediately Formed in Electrochemical Reduction of CO, at a Copper Electrode. *J. CHEM. SOC. FARADAY TRANS* **1991**, *87* (1), 125–128.

2) Pan, F.; Yang, Y. Designing CO_2 reduction Electrode Materials by Morphology and Interface Engineering. *Energy and Environmental Science* **2020**, 13 (8), 2275–2309. https://doi.org/10.1039/d0ee00900h.

3) Jia, J., Seitz, L., Benck, J. Huo, Y., Desmond Ng, J., Bilir, T., Harris, J., Jaramillo, T. Solar water splitting by photovoltaic-electrolysis with a solar-to-hydrogen efficiency over 30%. *Nat Commun* 7 **2016**, 13237. https://doi.org/10.1038/ncomms13237

4) Agarwal, A. S.; Zhai, Y.; Hill, D.; Sridhar, N. The Electrochemical Reduction of Carbon Dioxide to Formate/Formic Acid: Engineering and Economic Feasibility. *ChemSusChem* **2011**, 4 (9), 1301–1310. https://doi.org/10.1002/cssc.201100220.

5) Spinner, N. S.; Vega, J. A.; Mustain, W. E. Recent Progress in the Electrochemical Conversion and Utilization of CO_2. *Catalysis Science and Technology*. January **2012**, pp 19–28. https://doi.org/10.1039/c1cy00314c.

6) Feng, J.; Zeng, S.; Feng, J.; Dong, H.; Zhang, X. CO_2 Electroreduction in Ionic Liquids: A Review. *Chinese Journal of Chemistry* **2018**, 36 (10), 961–970. https://doi.org/10.1002/cjoc.201800252.

7) Faggion, D.; Gonçalves, W. D. G.; Dupont, J. CO_2 Electroreduction in Ionic Liquids. *Frontiers in Chemistry* **2019**, 7 (MAR), 1–8. https://doi.org/10.3389/fchem.2019.00102.

8) Wang, L.; Chen, W.; Zhang, D.; Du, Y.; Amal, R.; Qiao, S.; Wu, J.; Yin, Z. Surface Strategies for Catalytic CO_2 Reduction: From Two-Dimensional Materials to Nanoclusters to Single Atoms. Chemical Society Reviews. *Royal Society of Chemistry* November 7, **2019**, pp 5310–5349. https://doi.org/10.1039/c9cs00163h.

9) Zhu, D. D.; Liu, J. L.; Qiao, S. Z. Recent Advances in Inorganic Heterogeneous Electrocatalysts for Reduction of Carbon Dioxide. *Advanced Materials.* Wiley-VCH Verlag May 11, **2016**, pp 3423–3452. https://doi.org/10.1002/adma.201504766.

10) Li, X.; Wen, J.; Low, J.; Fang, Y.; Yu, J. Design and Fabrication of Semiconductor Photocatalyst for Photocatalytic Reduction of CO_2 to Solar Fuel. *Science China Materials* **2014**, 57 (1), 70–100. https://doi.org/10.1007/s40843-014-0003-1.

11) Wu, J.; Huang, Y.; Ye, W.; Li, Y. CO_2 Reduction: From the Electrochemical to Photochemical Approach. *Advanced Science* **2017**, 4 (11), 1–29. https://doi.org/10.1002/advs.201700194.

12) Bockris, j. O.; Devanathan, m. A. V.; Müller, k. On the structure of charged interfaces. *In Electrochemistry*; Elsevier, **1965**; pp 832–863. https://doi.org/10.1016/b978-1-4831-9831-6.50068-0.

13) Kang, J.; Wen, J.; Jayaram, S. H.; Yu, A.; Wang, X. Development of an Equivalent Circuit Model for Electrochemical Double Layer Capacitors (EDLCs) with Distinct Electrolytes. *Electrochimica Acta* **2014**, 115, 587–598. https://doi.org/10.1016/j.electacta.2013.11.002.

14) Katsounaros, I.; Meier, J. C.; Klemm, S. O.; Topalov, A. A.; Biedermann, P. U.; Auinger, M.; Mayrhofer, K. J. J. The Effective Surface pH during Reactions at the Solid-Liquid Interface. *Electrochemistry Communications* **2011**, 13 (6), 634–637. https://doi.org/10.1016/j.elecom.2011.03.032.

15) Varela, A. S.; Kroschel, M.; Reier, T.; Strasser, P. Controlling the Selectivity of CO_2 Electroreduction on Copper: The Effect of the Electrolyte Concentration and the Importance of the Local pH. *Catalysis Today* **2016**, 260, 8–13. https://doi.org/10.1016/j.cattod.2015.06.009.

16) Raciti, D.; Mao, M.; Wang, C. Mass Transport Modelling for the Electroreduction of CO_2 on Cu Nanowires. *Nanotechnology* **2018**, 29 (4). https://doi.org/10.1088/1361-6528/aa9bd7.

17) Yuan, L.; Xu, Y. J. Photocatalytic Conversion of CO_2 into Value-Added and Renewable Fuels. *Applied Surface Science* **2015**, 342, 154–167. https://doi.org/10.1016/j.apsusc.2015.03.050.

18) Karamian, E.; Sharifnia, S. On the General Mechanism of Photocatalytic Reduction of CO_2. *Journal of CO_2 Utilization* **2016**, 16, 194–203. https://doi.org/10.1016/j.jcou.2016.07.004.

19) Roy, S. C.; Varghese, O. K.; Paulose, M.; Grimes, C. A. Toward Solar Fuels: Photocatalytic Conversion of Carbon Dioxide to Hydrocarbons. *ACS Nano.* March 23, **2010**, pp 1259–1278. https://doi.org/10.1021/nn9015423.

20) Wu, J. C. S.; Lin, H. M.; Lai, C. L. Photo Reduction of CO_2 to Methanol Using Optical-Fiber Photoreactor. *Applied Catalysis A: General* **2005**, 296 (2), 194–200. https://doi.org/10.1016/j.apcata.2005.08.021.

21) Chang, X.; Wang, T.; Gong, J. CO_2 Photo-Reduction: Insights into CO2 Activation and Reaction on Surfaces of Photocatalysts. *Energy and Environmental Science. Royal Society of Chemistry* July 1, **2016**, pp 2177–2196. https://doi.org/10.1039/c6ee00383d.

22) Inoue, Y. Photocatalytic Water Splitting by RuO2-Loaded Metal Oxides and Nitrides with D0- and D10 -Related Electronic Configurations. *Energy and Environmental Science* **2009**, 2 (4), 364–386. https://doi.org/10.1039/b816677n.

23) Umeda, M.; Niitsuma, Y.; Horikawa, T.; Matsuda, S.; Osawa, M. Electrochemical Reduction of CO_2 to Methane on Platinum Catalysts without Overpotentials: Strategies for Improving Conversion Efficiency. *ACS Applied Energy Materials* **2020**, 3 (1), 1119–1127. https://doi.org/10.1021/acsaem.9b02178.

24) Kočí, K.; Matějů, K.; Obalová, L.; Krejčíková, S.; Lacný, Z.; Plachá, D.; Čapek, L.; Hospodková, A.; Šolcová, O. Effect of Silver Doping on the TiO_2 for Photocatalytic Reduction of CO_2. *Applied Catalysis B: Environmental* **2010**, 96 (3–4), 239–244. https://doi.org/10.1016/j.apcatb.2010.02.030.

25) Wang, Y.; Cao, L.; Libretto, N. J.; Li, X.; Li, C.; Wan, Y.; He, C.; Lee, J.; Gregg, J.; Zong, H.; Su, D.; Miller, J. T.; Mueller, T.; Wang, C. Ensemble Effect in Bimetallic Electrocatalysts for CO_2 Reduction. *Journal of the American Chemical Society* **2019**, 141 (42), 16635–16642. https://doi.org/10.1021/jacs.9b05766.

26) Wang, C.; Thompson, R. L.; Baltrus, J.; Matranga, C. Visible Light Photoreduction of CO_2 Using CdSe/Pt/TiO_2 Heterostructured Catalysts. Journal of Physical *Chemistry Letters* **2010**, 1 (1), 48–53. https://doi.org/10.1021/jz9000032.

27) Luo, X. L.; Yin, Z.; Zeng, M. H.; Kurmoo, M. The Construction, Structures, and Functions of Pillared Layer Metal-Organic Frameworks. Inorganic Chemistry Frontiers. *Royal Society of Chemistry* October 1, **2016**, pp 1208–1226. https://doi.org/10.1039/c6qi00181e.

28) Logan, M. W.; Ayad, S.; Adamson, J. D.; Dilbeck, T.; Hanson, K.; Uribe-Romo, F. J. Systematic Variation of the Optical Bandgap in Titanium Based Isoreticular Metal-Organic Frameworks for Photocatalytic Reduction of CO_2 under Blue Light. *Journal of Materials Chemistry* A **2017**, 5 (23), 11854–11863. https://doi.org/10.1039/c7ta00437k.

29) Eggins, B. R.; Irvine, T. S.; Eileen P. Murphy E.P.; Grimshawb, J. Formation of Two-Carbon Acids from Carbon Dioxide by Photoreduction on Cadmium. *J. Chem. Soc., chem. Commun.* **1988**.

30) Baran, T.; Dibenedetto, A.; Aresta, M.; Kruczała, K.; MacYk, W. Photocatalytic Carboxylation of Organic Substrates with Carbon Dioxide at Zinc Sulfide with Deposited Ruthenium Nanoparticles. *ChemPlusChem* **2014**, 79 (5), 708–715. https://doi.org/10.1002/cplu.201300438.

31) Sato, J.; Kobayashi, H.; Inoue, Y. Photocatalytic Activity for Water Decomposition of Indates with Octahedrally Coordinated D10 Configuration. II. Roles of Geometric and Electronic Structures. *Journal of Physical Chemistry* B **2003**, 107 (31), 7970–7975. https://doi.org/10.1021/jp030021q.

32) Alotaibi, B.; Fan, S.; Wang, D.; Ye, J.; Mi, Z. Wafer-Level Artificial Photosynthesis for CO_2 Reduction into CH_4 and CO Using GaN Nanowires. *ACS Catalysis* **2015**, 5 (9), 5342–5348. https://doi.org/10.1021/acscatal.5b00776.

33) Zhang, N.; Ouyang, S.; Kako, T.; Ye, J. Mesoporous Zinc Germanium Oxynitride for CO_2 Photoreduction under Visible Light. *Chemical Communications* **2012**, 48 (9), 1269–1271. https://doi.org/10.1039/c2cc16900b.

3. MATERIALS AND CELL DESIGN FOR CO_2 REDUCTION

3.1 COPPER BASED CATALYSTS

3.1.1 Electrochemical behaviour of Cu in CO_2 reduction

Products like CH_4, CO, formate and other hydrocarbons were detected from electroreduction of CO_2 in $KHCO_3$ electrolyte solution by Hori et al. in a work published in 1994[1]. They reported how a strong bond with the CO_2•- intermediate, together with the break of the C-O bond and the desorption of the subsequent CO formed, can be obtained with elements like Ga, Ag, Au, Zn, Pd; others like In, Sn, Pb, Bi allow the desorption of this radical, which can be converted to formic acid as the most predominant product, while Fe, Ni, Ti, Pt provide H_2 as the major product, because they strongly adsorb the CO, being poisoned. Among these, copper (Cu) is one of the most attractive catalysts for the conversion of CO_2 into useful compounds with reasonable current density. In total, it has been proved that copper is capable to generate up to 18 different carbon compounds. It is in fact well known that Cu is the only metal that can produce, apart from CO and formic acid, compounds involving the transfer of more than two electrons, like ethane, methane, ethyne, ethylene, ethanol, methanol. As minor products, in some cases olefins, paraffins, aldehydes, and ketones composed of carbon atoms with more than six carbon, were also detected and it was proposed that these products can result from the conversion of enol-like intermediates. Cu catalysts can easily reduce CO adsorbed on its surface, derived by the activation of CO_2, to *CO intermediate groups which can finally be converted to alcohols and other hydrocarbons by a coupling reaction with other *CO groups or, if only a protonation occurs, into methane and methanol.

The surface properties like the crystallinity strongly affect activity and selectivity over a Cu catalyst and this was proved on a single Cu crystal, in which the predominance of Cu (111) planes can drive the selectivity to methane, while Cu (100) to ethylene[2]. As discussed, it is well known that these two compounds are formed via CO intermediate, but in the case of ethylene it is supposed that two CO

molecules adsorbed are converted through electron assisted dimerization, like proposed by Koper and co-workers, while in a Cu (111) surface the formation of CHO via protonation of CO, with final production of methane, is more favourable[3].

Novskov and co-workers proposed, after DFT analysis, the chemical dimerization of the CHO instead of two CO[4]. Despite the kind of active sites present along the grain boundaries and active for the generation of products was not shown, Kanan and co-workers proved how the grain boundaries morphology can affect in some way the formation of C_{3+} products[5]. Several efforts have been aimed to understand the electronic mechanism that drives the selectivity toward specific products in the photoreduction of CO_2 over copper oxide-derived catalysts, for example for the production of methanol, which is one of the more valuable products as described in the first chapter. With a model made up of $Cu_{32}O_{16}$ and $Cu_{14}O_7$ nanoclusters (Cu^I), it was proposed a mechanism in which in the first steps H_2O (source of hydrogen) and CO_2 adsorb on the nanoclusters surface, through a break of the Cu-Cu bond; H_2O dissociates and forms hydroxylate groups ($OH•_{surf}$), which can activate other CO_2 molecules and provide hydrogen species for the next CO_2 reduction steps, while CO_2 can be adsorbed in linear form or bend to form surface carbonated species. The first intermediate is the carboxyl group –CO(OH), strongly bonded to the surface, derived by the hydrogenation of the O atoms of the CO_2, which follows the production of formic acid HCO(OH), also strongly bonded to the surface, through a second step of hydrogenation. The last hydrogenation of the formic acid leads to formaldehyde and methanol, the latter less bonded to the surface with respect to the previous intermediate, as reported in the following mechanism[6]:

$$CO_2 + H• \rightarrow CO(OH)$$

$$CO(OH)• + H • \rightarrow HCO(OH)_{surf}$$

$$HCO(OH)_{surf} + H \rightarrow H_2CO_{surf} + OH•_{surf}$$

$$H_2CO_{surf} + H• \rightarrow H_3CO_{surf}$$

$$H_3CO• + H• \rightarrow H_3C(OH)_{surf}$$

3.1.2 Electrochemical behaviour of copper-based bimetallic systems

Several strategies, involving creation of nanostructures and control of morphology, have been developed to increase the Cu activity in CO_2ERR. Nanoengineering of the surface to contain multiple sites for binding the key intermediate and driving selectivity, can be obtained through the synthesis of bimetallic systems or alloys[7-9]. In the case of Cu, it was suggested how the formation of its alloys with other metals can improve kinetics and selectivity with an alteration of the Cu atoms in the neighbor chemical environment. The properties of the second metal added to Cu have a strong influence on modelling the binding energy of the key intermediate, as shown in the Figure 3.1[10]. The second metal can bind a hydrogen atom (green mark) or an oxygen atom (red mark) stronger than Cu atoms through the formation of *CHO species with two different configurations and this is the key point to determine the further reaction pathways. The selectivity toward hydrocarbons and alcohols depends on the M-O bond strength, which affects the formation of *CH_2O and *CH_3O adsorbed species.

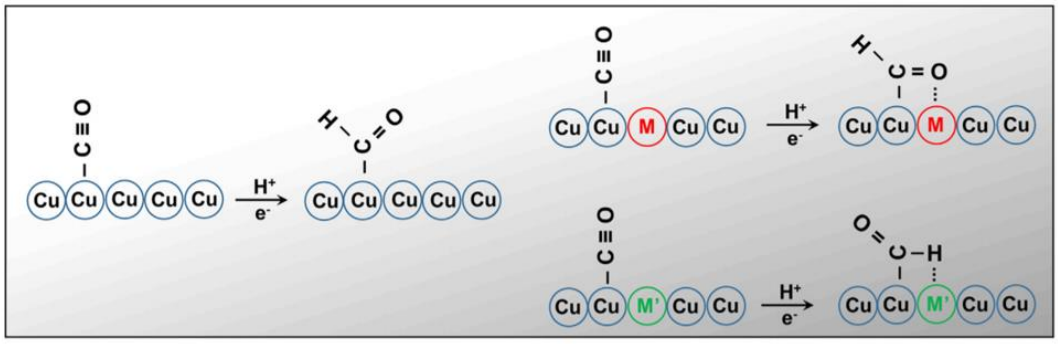

Figure 3.1 *Oxygen and hydrogen binding mechanism over bimetallic surface. Reproduced with permission from ref.*[10]

In Figure 3.2, the metals added to copper, divided in the four categories based on the relative H-M and O-M bond strength, are reported. The strongest O-M bond associated with the weaker H-M bond can be obtained through metals of the groups II like Sn and In, while the strongest H-M bond and the weakest O-M bond are related to Pd. The selectivity for compounds like hydrogen, carbon monoxide and formic acid is determined by the affinity of the metal to hydrogen and oxygen with respect to copper. Figure 3.3 reports the energy binding differences between *H and *COOH species versus the H* species. This plotting is split in three different zones,

which represent H_2, CO and HCOOH as main products. Hydrogen is the main product in the metals in which the H-M bond is strong, while carbon monoxide and formic acid are formed as primary products when this bond is moderate and weak, respectively, shifting to the right zone of the graph. Then, comparing to other metals, copper has a relative weaker *H and stronger *CO affinity making it a good candidate for the selective reduction toward hydrocarbons and alcohols, as shown in Figure 3.4.

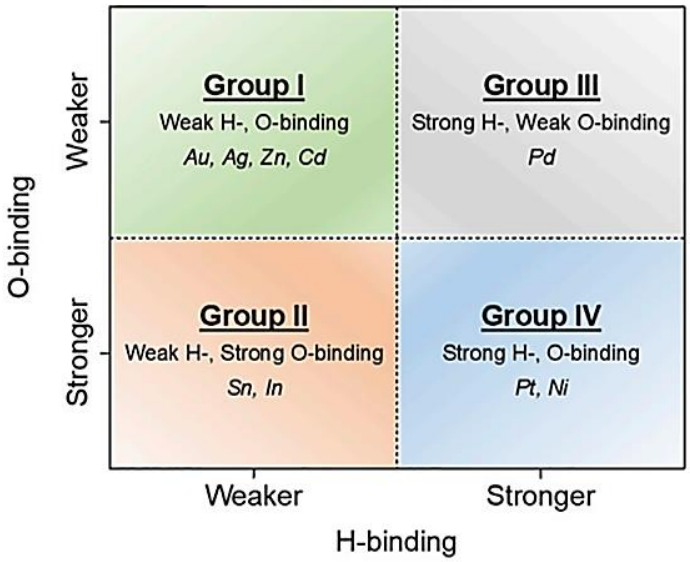

Figure 3.2 *Metal categories based on H and O bond streght. Reproduced with permission from ref.*[10]

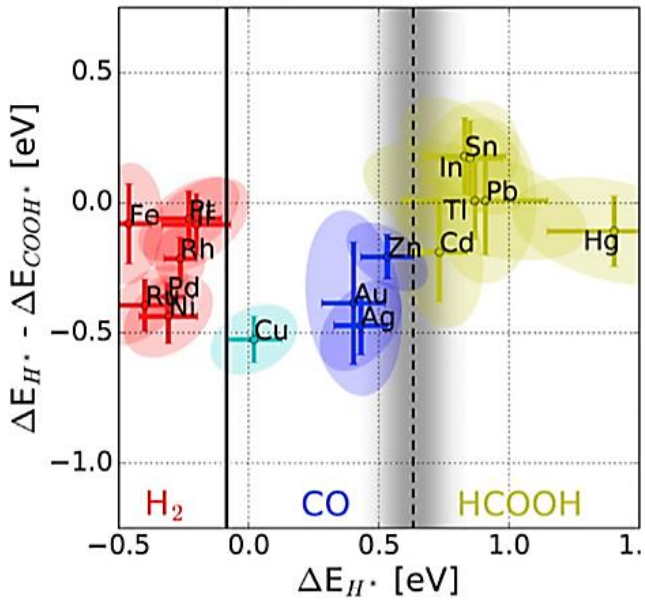

Figure 3.3 **H and *COOH energy binding versus H* energy bindings. Reproduced with permission from ref.*[10]

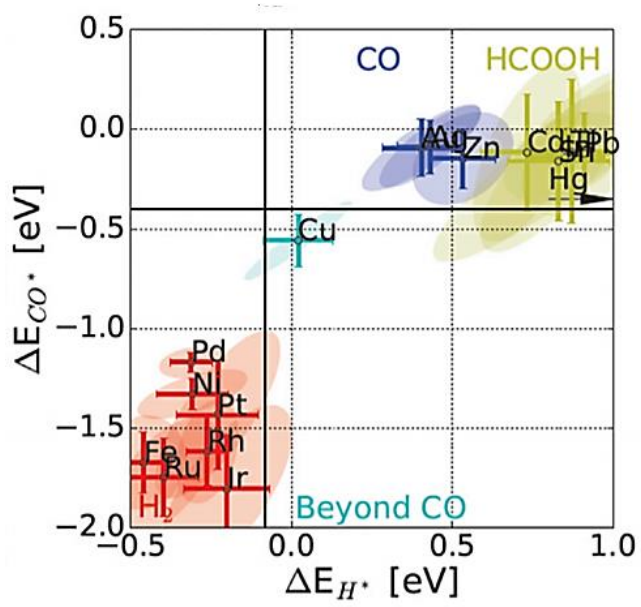

Figure 3.4 **CO and *H binding energies for different metals. Reproduced with permission from ref.*[10]

Thus, CO selectivity can also be related to CO heat adsorption (ΔH_{CO}) associated with the M-CO bond; a high value involves a strong bond with the metal, allowing hydrogen and hydrocarbon evolution, while a low value makes easier the HCOOH formation. ΔH_{CO} values lower than 10 kcal mol^{-1} are reported to encourage CO formation.

3.1.3 Selectivity to CO and HCOOH

Despite it was proven how 100% selectivity to CO can be obtained over noble metals, like Ag, Au, Pd, the high cost of these materials has not allowed a scale implementation. Consumption of these precious materials can be reduced by doping Cu with other metals like In, Au, Sn, which help to improve CO selectivity. The Cu-Au alloys push the selectivity toward CO, which can be further improved by changing the alloy composition, as shown for the Au_3Cu composite by Kim et al[11].

Recently, Takanabe et al.[12] reported Cu-Sn and Cu-In alloys, obtained through Sn and In electrodeposition on a copper oxide (I) substrate, showed a 85% CO FE at -0.6 V. The high selectivity toward CO was obtained because the copper alloys, as mentioned above, promote a modification in the binding strength of the CO intermediate, namely the H* and COOH* species. In particular, DFT studies

showed how the bimetallic structures can affect the ensemble effect of the catalytic centers of the metals and, in general, the electronic structure associated with the d-band centers. In the case of Cu-In (reported in the $Cu_{11}In_9$ form) these studies suggest how, despite the bulk properties are not altered with the introduction of In atoms, the occupation of certain Cu sites is prevalent, in major amount the edge sites; the adsorption properties are also altered due to the Cu atoms near In on the (110) face. Moreover, the presence of In increases the H* adsorption energy barrier, stabilizing the *HCOO intermediate, while it does not affect the stabilization of *CO species. It was observed how in a M_xIn_{1-x} system, the hydrogen evolution is favoured with these metal order: Zn < Cu < Ni < Co < Fe, while the order becomes: Fe < Co < Zn < Ni < Cu in the case of CO evolution, as reported in Figure 3.5[13].

The pathway of a reaction can be controlled by the H^+ interaction with the two metal centers, promoting the selective CO_2 reduction on one or both. However, it should be taken in account that properties such as morphology, atomic structure and composition, can drastically modify the reaction pathways toward different products. For example, it was reported how the modification of the atomic order of the Cu-Au alloy, highly selective to CO, turns it to a H_2 selective catalyst[14], while the tuning of the Cu-In composition can push its selectivity to formate instead of CO, as show by Hoffman et al[15].

Another issue affecting selectivity regards the bimetallic surface segregation, caused by the electrolysis overpotential applied, which can induce a deactivation of the catalyst. Moreover, to reduce the total catalytic cost, there is the need to increase the number of surface-active centers with respect to the bulk, considering that the first contribute to the catalytic performances.

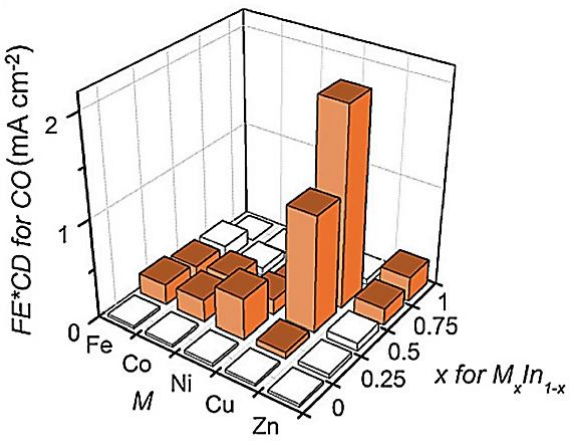

Figure 3.5 *CO Faradaic efficiency and current density plotted versus metal composition. Reproduced with permission from ref.*[13]

Comparing to copper and its oxides, which favour the production of hydrocarbons, alcohols and CO, high formate FE production was instead detected with Cu-S_x catalysts. An 85% formate FE was in fact reported by Zhu et al. with a catalyst prepared by Cu_2S electroreduction on a Cu foam support, showing a flower-like pattern morphology[16]. The explanation about the HCOOH selectivity was attributed to the particular morphology. The suppression of the CO intermediates, and the derived alcohols and hydrocarbons, can also be explained by the presence of S dopants remained on the catalyst and not by the material morphology, as proved by Operando Raman Spectroscopy and Density Functional Theory calculations. The HCOO* and COOH* adsorption energies in fact decreased due to the sulfur atoms, causing the conversion of HCOO* to formate, suppressing instead the conversion of the COOH* to CO[7].

3.1.4 Photocatalytic properties of copper oxide

Copper oxide catalysts are mostly used in photovoltaics application. Cuprous oxide (Cu_2O), alone or coupled with other semiconductors in multi-junction layers, is one of the most present in literature. It has a cubic crystalline structure, in which the O atoms organize in bcc sublattice with a coordination number double than the copper atoms, and the latter organize in fcc sublattice (Figure 3.6).

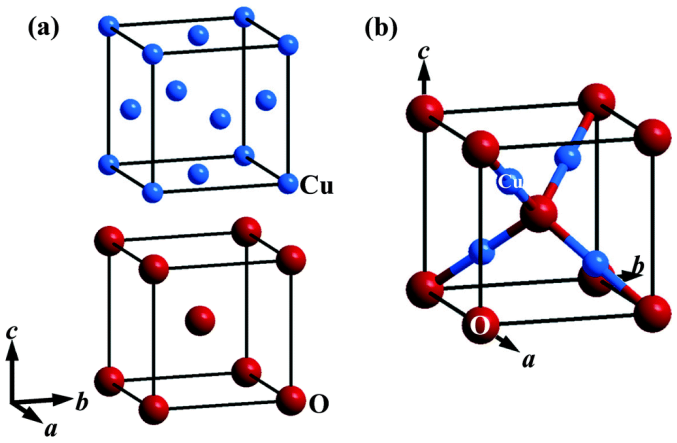

Figure 3.6 *Unit cells for Cu_2O. Reproduced with permission from ref.*[18].

Cu_2O, being an oxide in its stoichiometric composition, should be an insulator, but intrinsic defects in the material, like cation deficiency, vacant or interstitial oxygen, Schottky barrier, make possible the *p*-type conductivity. It is a semiconductor with a band gap of 2.1-2.6 eV, which provide one the most reducing conduction band (CB) between the most commonly used semiconductors with a value of CB = -1.4 eV vs NHE at pH=7, exhibiting a high absorption coefficient in the visible spectrum.

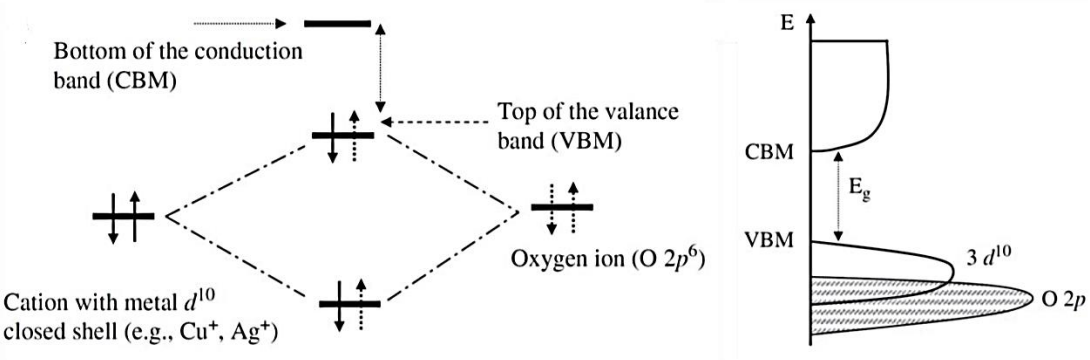

Figure 3.7 *Band energy levels of Cu_2O. Reproduced with permission from ref.*[19]

The electronic structure of Cu^+ ion is $3d^{10}4s^0$, thus the $3d^{10}$ level is slightly less energetic than $4s^0$, making the holes less localized and improving their mobility. This makes also possible to reduce the band gap of Cu_2O by increasing the interaction of Cu-Cu bond of the upper valence band (VB). This situation is different comparing with most common semiconductors, in which the VB top is made up of O_2p orbitals and the most electronegative oxygen atoms allow a strong localized VB edge, which makes possible to reduce the band gap only acting with doping with other elements (Figure 3.7).

Cuprous oxide can be obtained in different morphologies, like sheets, spheres, octahedra, hexapods, rhombic-dodecahedra, and can be synthesized through different methods like electrodeposition, hydrothermal and solvothermal ways. Lattice properties, morphology and relative different surface energies, can affect the way in which some crystallographic planes, or quantum confinement, modify the photochemical activity. This material is promising for photocatalytic and photoelectrochemical application because of low toxicity, low cost, natural abundance, and semiconductor properties. Some limitations concern its stability, due to natural oxidation phenomena, and its photostability during photocatalysis, due to the photo-generated charges in the surface. The wide application of Cu_2O in the redox reactions is due to its high chemical activity, because its oxidation states can be forced from Cu^{1+} of the original form to Cu^0 in a reduction process or Cu^{2+}; this can be considered also as a problem because it means that Cu_2O can be easily oxidized into other forms, like CuO and Cu_4O_3. A great challenge involves the synthesis of pure Cu_2O phase and also the retaining of its photostability during the photocatalysis, avoiding the oxidation to cupric oxide, which is less active. It was proved that copper vacancies in Cu_2O structure represent the most stable defect states, and how they are advantageous in photocatalysis, as they limit charge carrier recombination[20]. Cu_2O was also used in several oxidative applications like oxidation of methyl orange (MO) with a mechanism explained with the formation of strong oxidant OH• radicals; their formation is promoted by reduction reactions made up by the O_2•- ions, which in turn are obtained by the reduction of molecular O_2 by the photogenerated electrons. In general, the oxidant species include H_2O_2, O_2•- OH• and the photogenerated holes (h^+)[21]. Moreover, Cu (I) based materials have poor stability due to photocorrosion. Although their stability in photocatalysis is poor due to corrosion phenomena, its coupling with a wide band n-type semiconductor as TiO_2 can modify the surface generating a type II semiconductor (figure 4). The absorbed photons induce in the center of the two components a photo-induced electron-hole pair, and the following charge migration can be explained with two main mechanism, A and B (Figure 3.8)[22].

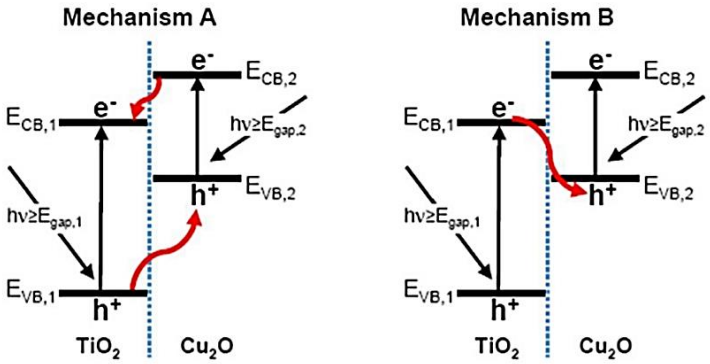

Figure 3.8 *Supposed mechanisms for light-induced photocatalysis for heterostructured materials. Reproduced with permission from ref.*[22]

The A scheme is a double charge mechanism and involves the migration of electrons from the CB of Cu_2O to the CB of TiO_2 while the holes move from the VB of the TiO_2 to VB of Cu_2O. In this case, the potential energy of the carries decreases with limitations in the reducing power. Charge separation is improved but the massive transfer of the holes to Cu_2O VB can lead, in absence of an opportune electron donor, to a photocorrosion that can affect the photocatalytic response. The B is a Z-scheme mechanism, in which the holes of VB of Cu_2O are scavenged by the TiO_2 CB electrons. This results in a not limited reducing power due to decreasing in the carries potential energy, and the photocorrosion of Cu_2O is thus minimized. The better performances of the heterostructured materials with respect to the single components, can be explained by the combination of these two mechanisms.

3.2 TITANIA NANOTUBE ARRAYS

3.2.1 Titanium oxide properties

Titanium oxide (TiO_2) is an *n*-semiconductor mostly used in photocatalysis due to its chemical stability, low cost, chemical resistance and availability. However, its activity is limited in the UV spectrum region, which make this compound not much effective in sunlight-based applications, considering that only 4% of the sunlight spectrum is made up of UV light. Moreover, it shows a high electron-hole pair recombination if compared with the surface-adsorbed species reaction kinetics. Many techniques have been employed to modify TiO_2 in order to

minimize the electron-hole pair recombination and shift the absorption to the visible region. These include the doping, co-doping, incorporation of organic compounds and coupling with other semiconductors to form heterojunctions. TiO_2-based photocatalysts are widely used in the environmental and energy sector, in air and water cleaning systems, for self-cleaning surfaces and in photocatalytic processes such as the H_2 evolution and organic molecules degradation such as methyl orange and methylene blue. Its properties and photocatalytic performances can be varied, modifying its dimensionality. The 1D-TiO_2 nanostructures (such as nanobelts, nanowires, nanotubes and nanorods) are of particular interest in the photocatalytic field, showing high surface-to-volume ratio that allows a decrease in the electron-hole recombination rate and a high interfacial charge transfer. For example, some applications of TiO_2 nanotubes (TiO_2NTs) include photocatalysis, photovoltaics, photoelectrolysis, batteries, gas sensing, and biomedical implants[23-26]. Introduction of black TiO_2, produced by Chen et al. in 2011[27], allowed to overcome the problem relative to the absorption limited to the ultraviolet region of the TiO_2. Black TiO_2 higher ability to absorb the visible light is due to the introduction of oxygen vacancies and Ti^{3+} ions into TiO_2 or even through the introduction of a disordered layer on the surface of a highly crystalline TiO_2. Since then, black TiO_2 has been widely used in many fields, for dye sensitized solar cells, for the manufacture of lithium batteries and photoelectrochemical applications including the CO_2 reduction.

3.2.2 Controlled anodic oxidation preparation

The synthesis of TiO_2NTs through the anodic oxidation process of Ti sheets in a F^- ion-based solution was first reported in 2001 by Grimes' group[28]. The anodization of thin films of Ti is generally carried out using an electrochemical cell with two electrodes and applying a constant potential between them. The key processes responsible for titania formation can be summarized in three phases (Figure 3.9):

I) The growth of the oxide on the metal surface occurs through the interaction of the metal with O_2^- and OH^- ions. After the formation of an initial oxide layer, these anions migrate reaching the metal/oxide interface where they react with the metal.

II) Migration of Ti^{4+} metal ions from metal to the metal/oxide interface. Ti^{4+} cations are expelled from the metal/oxide interface under the application of an electric field that causes them to move towards the oxide/electrolyte interface.

III) Assisted dissolution of the oxide at the oxide/electrolyte interface. Due to the electric field applied, the Ti-O bond is polarized and a slight dissolution of the Ti^{4+} cations occurs. These are solubilized by the electrolyte while the free anions O^{2-} migrate towards the metal/oxide interface to interact with the metal (see step 1). The chemical dissolution of TiO_2 in the HF^- based electrolyte plays a key role in the formation of nanotubes. When the anodization process starts, the interaction of Ti^{4+} surface ions with O^{2-} ions in the electrolyte leads to the formation of the first uniform oxide layer. The overall reaction for the anodic oxidation of titanium can be represented as:

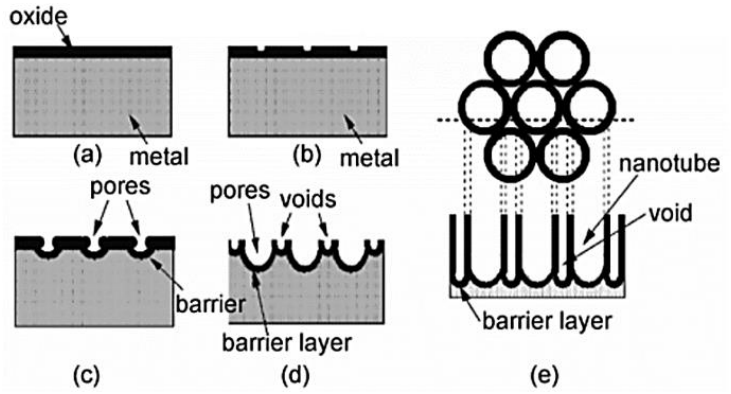

$$2H_2O \rightarrow O_2 + 4e^- + 4H^+$$

$$Ti + O_2 \rightarrow TiO_2$$

Figure 3.9 *TiO_2 nanotubes formation steps. Reproduced with permission from ref.*[29]

In the initial steps of the anodizing process, localized dissolution processes occur due to the high electric field present along the thin oxide layer, leading to the formation of small cavities that act as pores. This can be represented by the following equation:

$$TiO_2 + 6F^- + 4H^+ \rightarrow TiF_6^{2-} + 2H_2O$$

Therefore, these cavities are converted into large pores that spread evenly over the surface, leading to an increase in the density of the pores. Pore growth occurs due to the internal movement of the oxide layer on the bottom of the pores due to the processes just described. The Ti^{4+} ions that migrate from the metal to the oxide/electrolyte interface then dissolve in the HF^- based electrolyte. High anodizing voltages increase oxidation and dissolution assisted by the electric field, from which a greater thickness of the nanotube layer can be obtained. Due to the

localized dissolution described above, small cavities originate in the oxide road making the layer at the interface between the oxide and the metal increasingly thin, thus intensifying the electric field along this barrier leading to further growth of the pores. When this phenomenon becomes deep, the electric field inside these protruding metal regions becomes greater thus increasing the growth of the oxide layer and its dissolution, with the simultaneous growth of the voids leading to the formation of defined tubes. An equilibrium condition will then be reached in which the rate of formation of the oxide on the barrier layer (metal/oxide interface) equals the rate of chemical dissolution at the interface with the electrolyte; dissolution is determined by the concentration of F^- ions and the pH of the solution.

3.3 ELECTROLYZER

The main CO_2 reduction setups can be divided into batch, semi-batch and continuous flow reactors.

3.3.1 H-type cell

Figure 3.10 shows a batch (or semi-batch) configuration, namely an H-type cell. This has a three-electrode configuration (working, reference and counter electrodes) and consists of two half-cells separated by a protonic or anionic conductive membrane. The cathode compartment can be connected directly to a gas chromatograph (GC) or mass spectrometer (MS) to analyse in real-time the products. This setup allows the ionic conductivity through the two chambers (H^+ or OH^-) and avoids the transfer of the cathodic products to the anode, preventing their oxidation. This configuration is useful for screening new catalysts due to its practicality and easy setup, but it is not adequate for processing large CO_2 gas volumes due to CO_2 slow mass transfer transport, which limits to 100 mA cm^{-2} the maximum current density. Increasing temperature, pressure and gas and liquid flow rate in the cell causes the increment of mass transport phenomena, which are also dependent from solubility, density and viscosity. The use of 3D materials like the gas diffusion electrodes (GDE) helps to increase the interfacial contact area and minimize the bubble dimension[30].

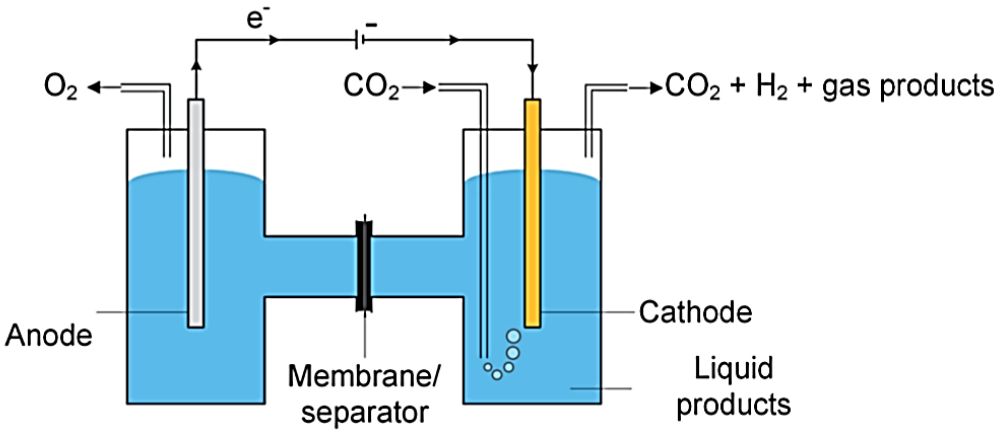

Figure 3.10 *H-type cell electrolyzer. Reproduced with permission from ref.*[31]

3.3.2 Flow cell systems

Flow cell systems are inspired by water splitting devices and can be assembled in three basic configurations: gas phase electrolyzer, solid phase electrolyzer and liquid phase electrolyzer.

In the gas phase electrolyzer (reported in Figure 3.11), the cathode is fixed with an ion exchange membrane (usually polymeric solid) forming a MEA (membrane-electrode assembly).

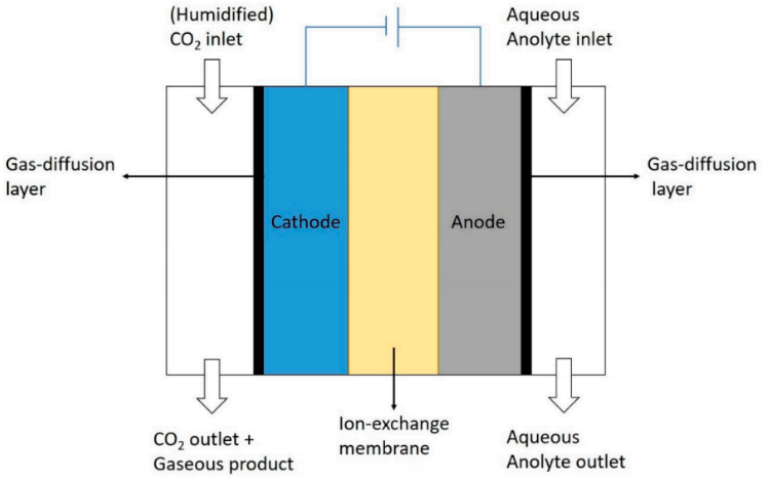

Figure 3.11 *Gas phase flow cell. Reproduced with permission from ref.*[32]

To allow the flow of ionic charges through the membrane, it is necessary to ensure the presence of water, either by humidifying the membrane or by ensuring the presence of a liquid anolyte near the MEA. CO_2 flow through the cathode is allowed using a gas diffusion layer (GDL), which provides a triple phase boundary of electrolyte, catalyst and CO_2. Higher CO productions[33] and better formate

selectivity[34] were obtained using a gas flow electrolyzer without any catholyte flow, also improving the stability and reaching higher currents.

In the solid-phase electrolyzer (reported in Figure 3.12), the electrodes and the electrolyte are in solid form, the latter usually as solid oxide. CO_2 reduction is activated at high temperatures (from 300 up to 600°C), while the membrane can be oxygen or proton conductive. The main advantage of this type of configuration is given by the increase in the reaction kinetics due to the high temperatures and minor problems of CO_2 diffusion in liquid electrolysers. The main disadvantages concern cell degradation, carbon deposition, low Faradaic efficiencies, sealing problems and excessive selectivity towards CO[35].

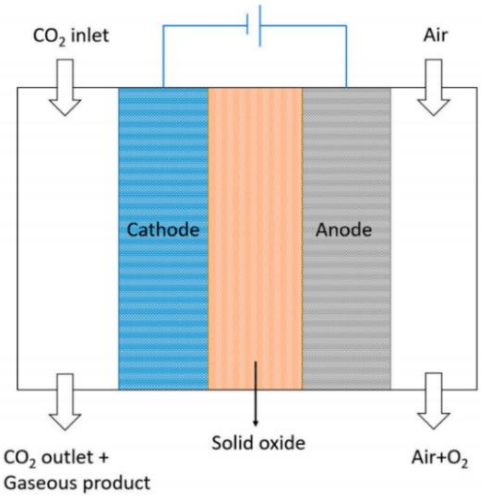

Figure 3.12 *Solid state flow cell. Reproduced with permission from ref.*[32]

Liquid-phase electrolyzer, the most common used systems, consists of two liquid electrolytes, two gas diffusion layers on both electrodes, and an ion exchange membrane to allow ion charge transport (see Figure 3.13). This system allows to keep the membrane humidified with respect of the gas phase setup and can be used for pressurized applications.

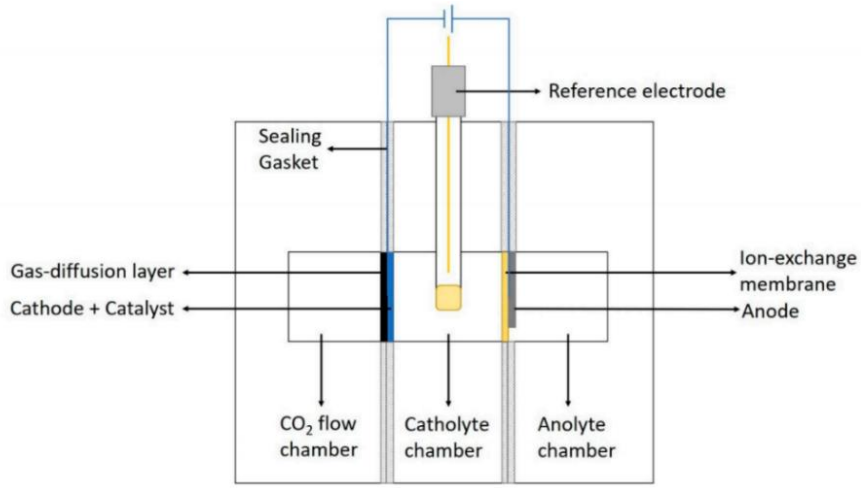

Figure 3.13 *Liquid phase flow cell. Reproduced with permission from ref.*[32]

In the microfluidic reactors, a thin layer of liquid electrolyte separates the cathode and anode, exploiting the capacity of the laminar flow to reduce mixing and making not necessary the presence of a membrane. Gas diffusion electrodes can be used to improve the phase contact, with an external reference electrode. Li et al. obtained 91% of efficiency using a two-phase catholyte in a trickle bed reactor[36].

3.3.3 Half-cells separator

The two half-cells of the H-type cell are separated in order to achieve the following scopes:

i) reduce risk of mixing the products with relative gas leakages forming unsafe mixture (H_2/O_2),

ii) avoid short circuits between the electrodes,

iii) avoid the reoxidation of the products at the anode,

iv) keep the local pH,

v) provide transport of protons or anions.

Porous separator and ion exchange membrane (IEM) can provide most of these requirements. Microporous diaphragms with pore size from 0.1 to 50 µm and plastic mesh, like polyolefin, are included in the first category. The semi-permeable IEM allows the selective transport of certain ions and charge species. In the class of the monopolar IEM belong the ion exchange membranes - IEM (e.g. Nafion®) and the

anion exchange membranes - AEM (e.g. Sustanion®). Another class includes the bipolar membranes (BEM), which are used in many applications sandwiching the catalyst between two layers made each of IEM and AEM. These membranes were reported to be able to keep a more stable pH difference in the two compartments.

The choice of membrane type should be made in base of CO_2 reduction products target and the overall configuration in terms of electrolytes and electrodes. For example, if a protonic exchange membrane is used, the electrolytes acidity should be taken into account because an excess of protons can push the selectivity towards the HER (hydrogen evolution reaction). Furthermore, the pH can limit the range of catalysts available to avoid corrosion problems, forcing the use of expensive noble metals. It was reported how an AME in some cases increases the faradaic efficiency towards carbon products, due to the OH^-, HCO_3^- CO_3^{2-} transport to the anode part[37].

However, this kind of membrane can be affected by several problems:

i) these anions can be oxidized to CO_2 in the anode compartment, reducing the overall efficiency;

ii) exposure to an alkaline environment can poison the membrane, reducing the ions mobility and increasing the overall cell resistance;

iii) degradation due to OH^- ions can occur, specially if the membrane is low hydrated[38].

3.4 PHOTOVOLTAIC/ELECTROLYZER INTEGRATION

3.4.1 PEC cell

Coupling of photovoltaic and electrochemical systems has so far attracted great attention. One of the advantages is the possibility to optimize separately the two apparatuses. In CO_2 reduction process, the photovoltaic system is necessary to supply holes and electrons to the electrochemical cell in order to carry out the two reactions of CO_2 reduction and water oxidation. The potential value of 2 V needed for CO_2 electro-reduction, due to the overpotentials required for the reaction, can easily be obtained by connecting several electrochemical cells in series, but

considerable current limitations can occur in this case. The use of multi-junction catalysts in PV cell has made possible to increase the "solar to electricity efficiency" from 20 to over 30% in the last years[39]. The coupled systems created so far in most cases have led to the formation of CO and formate and only a few have led to the formation of longer carbon chains. In the Figure 3.14a is showed a configuration in which the photovoltaic device, which can consist in more modules connected together, is connected to an electrolyzer by ohmic contact. One of the major disadvantages of this configuration is the need to use noble metals in both electrodes in order to achieve high efficiencies. One study reported the use of three perovskites connected in series coupled with an Au cathode and IrO_2 anode electrolyzer based, which provided a STF toward CO of 6.5%[40]. STF (solar-to-fuel energy conversion) is the ratio of the energy stored in a fuel and the solar energy required for its production. Figures 3.14b,c show two configurations in which the photovoltaic module is not separated but directly integrated with the cathode and the anode of the electrolyzer, to improve both reduction or oxidation reactions, respectively. A similar system was recently reported, in which the photovoltaic unit, composed of a silicon multijunction connected in series with a Ni electrode, in the form of foam, with Zn decorated Cu as the electrocathode, has led to a 16% CO Faradaic efficiency[41]. However, an integrated high efficiency and cheap PV/EC system requires many prerequisites, such as the use of earth-abundant-metals with low overpotential-based electrodes, the use of electrolytes operating at moderate pH to avoid corrosion problems, the integration of these components in the electrochemical cell avoiding energy losses and easy coupling with the PV system. Iridium oxide-based anodes coupled to a III-V/Si tandem cell allowed to obtain 3% solar to hydrogen conversion efficiency, while the use of photovoltaic cells based on GaInP/GaInAs/Ge allowed to obtain a solar to CO conversion efficiency of 13.4%[42].

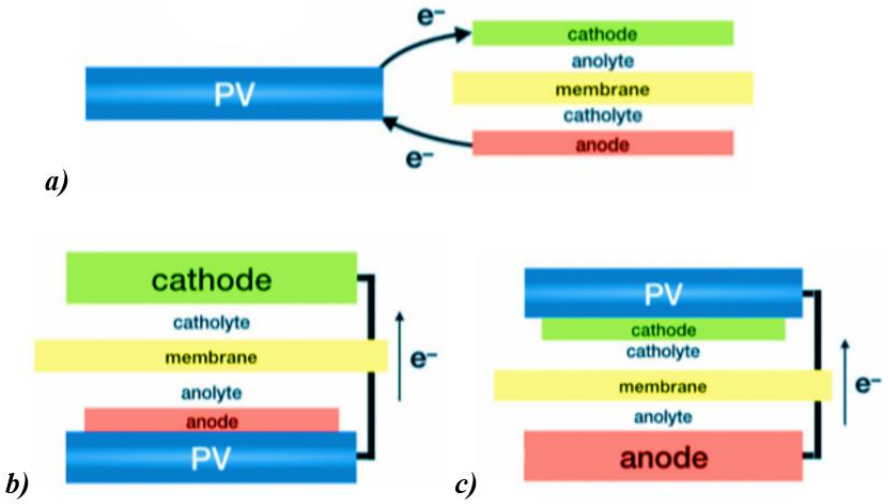

Figure 3.14 *Possible PV/EC combinations. Adapted from ref.*[43]

Apart from these base configurations, it is possible to integrate the anodic or the cathodic function directly with the photovoltaic units, through their decoration with co-catalysts necessary to drive the reactions.

The photoelectrochemical systems (PEC) are based on this concept and exploit the use of photoelectrodes instead or in combination of separated PV and EC modules. These systems emulate the natural photosynthesis employing the photoelectrons generated by the photocatalyst to perform a couple or redox reactions. This kind of cell is an extension of an electrochemical device with the difference that a part of energy is provided by light. When the semiconductor absorbs the photons, the electrons are excited to a higher energy level of the CB and, in combination with the relative holes in their VB, they carry out the desired reactions. In general, the process is not usually performed in a one-compartment cell (Figure 3.15), but in a two-chamber cell in which CO_2 reduction and water oxidation reactions take places separately. This allows to increase the separation of products, minimizing charge recombination and in general increasing the efficiency. To allow an efficient transport of electrons through the electrodes and of protons in the electrolyte, the two electrodes are made of a thin layer of material deposited on a conductive substrate while the two chambers are separated by a proton conductive membrane (PEMs) or an anionic exchange membrane (AEM). The first allows an efficient transport of protons from the anode to the cathode and are in generally favoured over the AEM, which involves the transport of the anions from the cathode to the anode. However, the choice depends on the general conditions and cell configuration. A PEC system is then basically composed of i) a photoelectrode, ii)

an electrolyte, iii) a membrane and iv) an electrocatalyst or another photoelectrode. The semiconductor, of which is composed the photoelectrode, is in direct contact with the electrolyte, and interacts with it when exposed to light, through the generation of electron-hole pairs, which subsequently drive the reductive/oxidative reactions in the liquid media to generate the products[44]. The first PEC was designed by Halmann in 1978, who used a *p*-type gallium phosphide photocathode to generate mainly formic acid, methanol and formaldehyde[45].

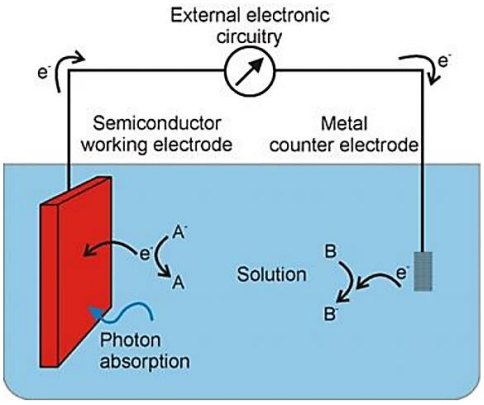

Figure 3.15 *Photoelectrochemical one-compartment prototype. Reproduced with permission from ref*[46]

To perform a reaction in a PEC system many factors should be taken into account for increasing the overall performances, such as the light source, the reactor materials, mixing, heat exchange and operation mode. The light irradiation should be distributed in a homogeneous way along the entire semiconductor surface not to lose energy; Xenon arc-lamps are generally employed, simulating the natural sunlight. About the photoreactor materials, the Pyrex glass is mostly used in literature due to its high light transmission in the UV region (<300 nm). The thickness of the window is of great importance because it can limit light transmission and in general provides size reactor limitations. Mixing favours the contact between all the species in the heterogeneous catalysis, while systems like a water jacket between the PEC cell and the light source can minimize the heating of the electrolyte.

Today, three different basic PEC configurations are used: i) the photoanode-driven cell, ii) the photocathode-driven cell and iii) the so-called Z-scheme, namely a photocathode-photoanode driven cell, whose configurations are represented in Figure 3.16 and discussed in the next paragraphs.

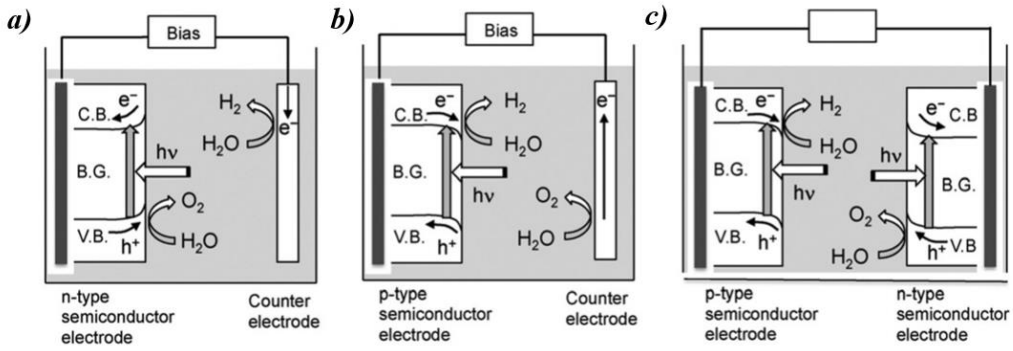

Figure 3.16 *PEC configurations with* ***a)*** *n-tpye,* ***b)*** *p-type photoelectrodes* ***c)*** *and their conbination. Reproduced with permission from ref.*[47]

However, a PEC system can be more complex than the basic configurations mentioned above, and in fact can integrate one or two photoelectrodes, can be biased or not and can incorporate an external PV cell to provide extra voltage. Single-photoelectrode based system using a $CuFeO_2$/CuO as photocathode and a Pt anode was reported to obtain 1% formate efficiency[48]. A formate STF efficiency of 10% was instead obtained using a Ni/TiO_2/InGaP/GaAs photoanode with a Pd/C/Ti cathode[49]. Some examples of photocathode-photoanode driven cells include the combination of a Ru-metal complex/Zn-doped InP photocathode combined in parallel with TiO_2 photoanode, giving a very low 0.04% formate STF efficiency, raised to 0.14% when connected to a $SrTiO_3$ photoanode[50]. Another system consists in a tandem configuration in which two photocathodes are coupled with an external PV device. A Faradaic efficiency to C_{2+} of 60% and a 3.5% total STF were reached using two Cu/Ag/TiO_2 photocathodes, in which the oxidation reaction is performed combining these two electrodes with a series of PV perovskites[51]. So far, all the most efficient PEC systems produce CH_3OH, CHOOH, CO, C_2H_5OH, and CH_4, but due to the complex mechanism involved in CO_2 reduction into fuels, low efficiency and selectivity characterize most of PEC systems. Comparing with photocataysis, in a PEC system a wide variety of semiconductors to harvest light can be used, because of the possibility of applying an external electrical bias, thus lowering the energy needed[52-53]. Furthermore, in a PEC system the semiconductor charge transfer is important, while this is less relevant in a photocatalytic application in which there is no the need of semiconductors with high charge transfer because they are suspended in solution. This results in the fact that a semiconductor with low charge transfer may not be used with the same efficiency in a PEC system. The photoelectrodes can be *p* or *n* semiconductors, or based on *p*-*n* multilayer

heterojunctions; the basic mechanism involving the band energy level doping modification, which affects charge transfer, will be described in the following section.

3.5 PHOTOELECTRODE CONFIGURATION

3.5.1 p-type

A *p*-type driven semiconductor PEC cell is composed of i) a *p*-type semiconductor photocathode coated on a support, ii) an electrolyte and iii) a counter electrode with the electrocatalyst. The IV, III-V, II-VI semiconductors, together with few metal oxides, are mostly used as photocathodes. When light photons are harvested by a photocathode, the electric field near the semiconductor/electrolyte interface, due to a band bending, is enough to break the formed electron-hole pairs, and this charge separation can be improved by the application of an external bias. The photogenerated electrons reduce CO_2 at the semiconductor interface and the holes oxidize water moving to the counter electrode. The presence of impurities and electron or hole trap defects can produce charge recombination, with the release of energy as heat.

p-type semiconductors are generated when a semiconductor is doped with impurities, which can accept electrons from the VB, leaving an excess of holes in the lattice. When a *p*-type semiconductor is placed in an electrolyte, a flow of electrons occurs from the latter to the semiconductor, if the redox potential of the electrolyte is within the semiconductor energy band gap and different from its Fermi level, thus increasing the Fermi level of the semiconductor until reaching the equilibrium (Figure 3.17). A space-charge region near the two sides of the semiconductor/electrolyte interface is generated; these two regions are known as depletion and Helmholtz layers for the semiconductor and the electrolyte sides, respectively. The latter consists of charge ions adsorbed on the semiconductor surface. A band bending effect, resulting from the upward bending of the VB and CB near the interface, is generated, but in general, due to the formation of the Helmholtz layer, this difference is not equal to the Fermi level/redox potential difference. Aspects such as chemical corrosion resistance, suitable band energy, good absorption in the visible solar spectrum and CB band with a more negative

energy than the reduction potential of CO_2, are the most important characteristics of an ideal *p*-type semiconductor. A negative CB band is also important to overcome the kinetic limitations[54].

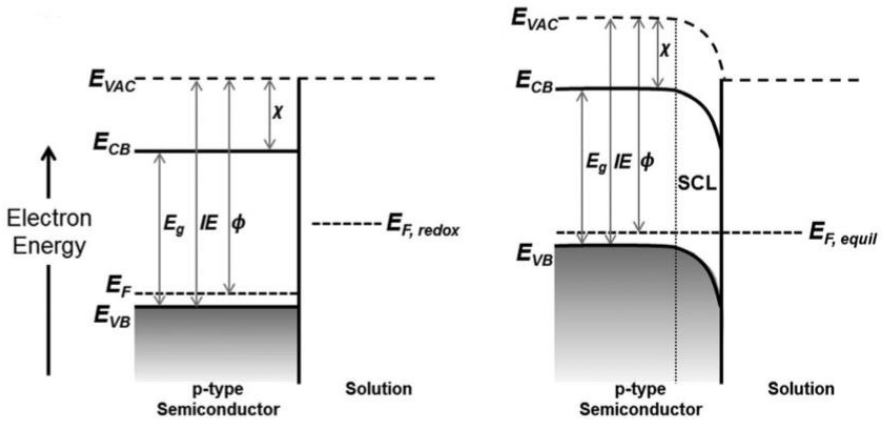

Figure 3.17 *Band bending for p-type semiconductor after contact with the electrolyte. Reproduced with permission from ref.*[55]

3.5.2 n-type

An *n*-type semiconductor driven PEC cell is composed of i) a photoanode semiconductor, ii) an exchange membrane and iii) a counter electrode with the electrocatalyst. Once absorbed the photons, the respective electron-hole pairs generated are dissociated and the holes migrating to the interface oxidize water, while the electrons through an external circuits make the reduction reactions happen. The photoanode, beyond absorbing light, can act to lower the energy required to the CO_2 reduction reactions, and so the total PEC performance requires an equilibrium from the contribution of anode and cathode, which can be tailored to control the selectivity.

n-type semiconductors are generated when a semiconductor is doped with impurities, which can donate electrons to the CB. This make the Fermi level of the semiconductor closer to the CB. When a *n*-type semiconductor is placed in an electrolyte, a flow of electrons occurs from the semiconductor to the liquid, if its redox potential is close to semiconductor energy levels, until their Fermi levels are equilibrated (Figure 3.18). The semiconductor Fermi level energy drops and a downward band occurs pushing the holes toward the semiconductor/electrolyte interface. This is the reason why *n*-type semiconductors are employed in the photo-

oxidation reactions. The first investigation with this kind of configuration was made by Ogura and co[56].

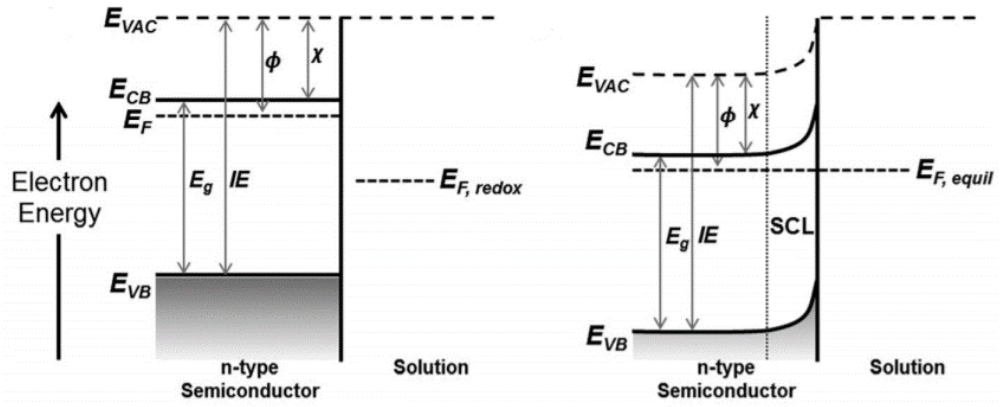

Figure 3.18 *Band bending for n-type semiconductor after contact with the electrolyte. Reproduced with permission from ref.*[55]

3.5.3 Z-scheme PEC cell

Recently, new systems combining a photocathode and a photoanode in a single apparatus have been studied; they seem very promising because they can combine two photoactive elements as electrodes, making the cell working without the application of an external bias, simulating the photosynthetic mechanism of the plants. In this configuration, known as Z-scheme, the photoanode and the photocathode are wired together, and when they harvest the light, they produce electron-hole pairs (Figure 3.19). A minor part of the charge carries drive the reaction at the photocathode and the oxidation at the photoanode, while the most part is recombined along the ohmic-connection.

This system can be divided into two main categories: direct[57] and indirect Z-schemes[58]. The indirect Z-scheme can be split in other two categories, the conventional the traditional Z-scheme and all-solid state Z-scheme; in the first, species acting like electron mediators guarantee the transport route of the electrons, while in the second charge transport is provided by an electric conductor, like Au or Ag NPs. These systems have been investigated in the CO_2 photo-electro-reduction because i) they provide strong photogenerated charge carrier redox ability, ii) oxidative and reductive compartments are separated, iii) they give high light harvesting and iv) it is possible to use a large range of combination of photocatalysts. In the traditional setup, two semiconductors, in which one has VB

and CB higher than those of the other, a couple of electron mediators are required. The redox mediator should have good recyclability, appropriate potential band energies and good light absorbance transparency. Fe^{3+}/Fe^{2+} and IO^{3-}/I^{-} are usually some redox ionic couples used as electron mediators.

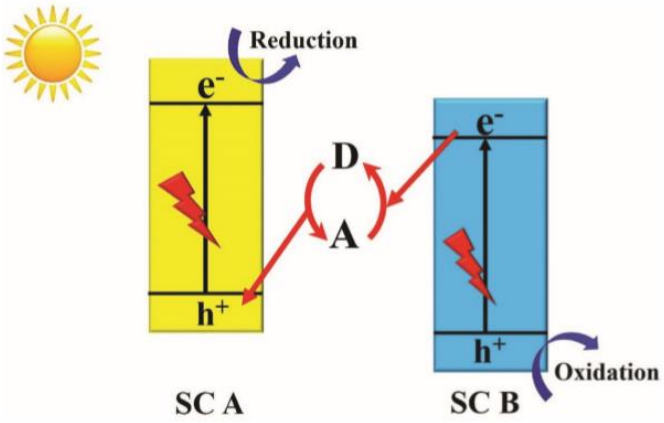

Figure 3.19 *Traditional Z-scheme. Reproduced with permission from ref.*[59]

When the photocatalys absorb the incident photons, electron-hole charge carries are formed; the electrons of the CB of the PCI reduce the oxidized form of the electron mediator (A - Acceptor), while the holes of the VB of the PCII are reduced by the reduced form the electron mediator (D - Donor); the electrons and holes in CB and VB of PCII and PCI, respectively, with the stronger redox potential are free to operate for the reduction of CO_2 and oxidation of water. These are the direct reactions, which are thermodynamically not favoured with respect to the backward reactions that involves consumption of the stronger photogenerated electrons and holes by the redox mediator. Other problems include the possible deactivation of the redox couple, the slow charge carrier transfer, pH sensitivity, and light shielding effect. In an all-solid Z-scheme (Figure 3.20), as just mentioned, a solid conductor, instead of redox couples, allows charge transfer. Conductive materials like graphene, CuNPs and noble metals like Au or Ag, are mostly used for the solid conductors and their role is not only to provide the conductibility of the photogenerated electron-hole pairs, but also to improve the stability of the photocatalysts. The main advantages over the redox couple are less problem of reverse reactions (which consume charge carriers with strong redox power), possibility of working both in liquid and gas phase and faster charge carrier, while the main drawback concerns the high cost of the conductors.

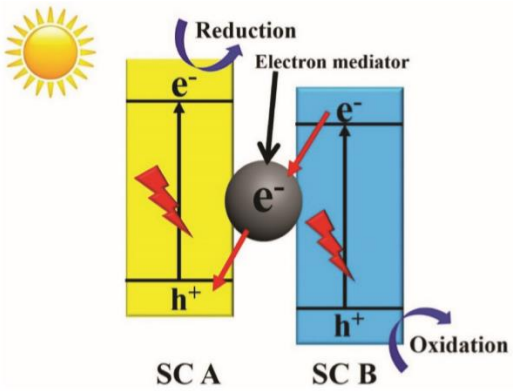

Figure 3.20 *All-solid Z-scheme. Reproduced with permission from ref.*[59]

In a direct Z-scheme (Figure 3.21), the two photocatalysts are in intimate contact without any mediator and with respect to the traditional Z-scheme, light shielding, photocorrosion and backward reactions are minimized. In this system, the carrier separation and the charge carrier transfer are dependent by the electric field generated and so it is necessary a work function difference between the two photocatalysts.

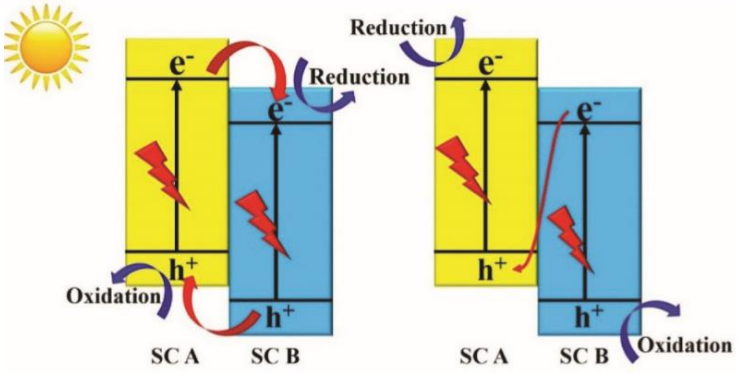

Figure 3.21 *Direct Z-scheme. Reproduced with permission from ref.*[59]

Two typical configurations are used; in the first the PCI has higher CB and CV of the PCII and smaller work function (Mechanism A), while in the second case a *p-n* junction (Mechanism B); in the first case (Figure 3.22), electrons move from PCI to PCII, until their Fermi level is equilibrated causing a band energy bending. When the two photocatalysts absorb the light, due to this band energy, the electrons from the CB of the PCII react with the holes of the VB of the PCI, leaving free the photogenerated electrons and holes of the CB and VB of PCI and PCII, respectively [44].

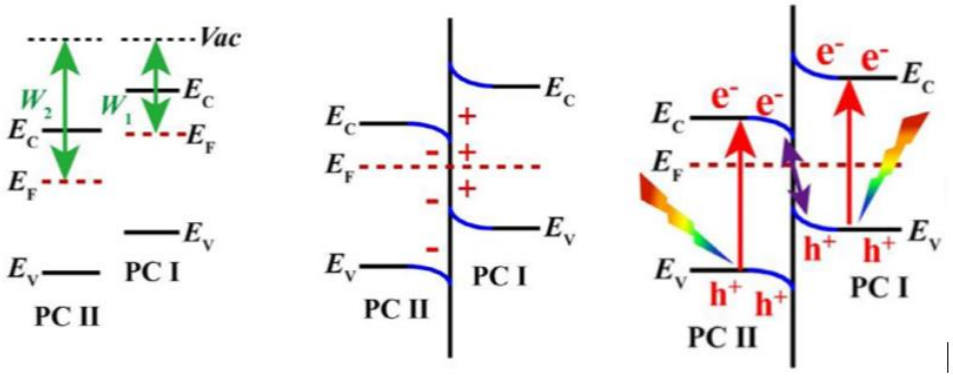

Figure 3.22 *Charge carrier transfer with Mechanism A. Reproduced with permission from ref.*[57]

In the mechanism B (Figure 3.23), the free electrons move from the *n*-type to *p*-type semiconductor, causing an internal electric field that causes band bending and a transfer of the photogenerated electrons from the CB of CPI to CPII, and photogenerated holes from VB of CPII to VB of CPII, not favouring the Z-scheme transfer mode.

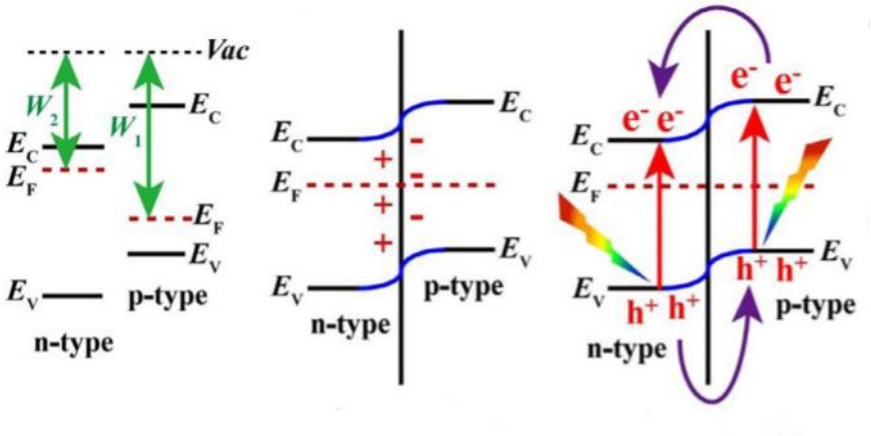

Figure 3.23 *Charge carrier transfer with Mechanism B. Reproduced with permission from ref.*[57]

3.6 REFERENCES

1) Hori, Y.; Wakebe, H. H. I.; Tsukamoto, T.; Koga, O. Electrocatalytic Process of CO Selectivity in Electrochemical Reduction of CO_2 at Metal Electrodes in Aqueous Media. *Electrochimica Acta* **1994**, 39 (11–12), 1833–1839.

2) Hori, Y.; Takahashi, I.; Koga, O.; Hoshi, N. Electrochemical Reduction of Carbon Dioxide at Various Series of Copper Single Crystal Electrodes. *Journal of Molecular Catalysis A: Chemical* **2003**, 199 (1–2), 39–47. https://doi.org/10.1016/S1381-1169(03)00016-5.

3) Schouten, K. J. P.; Kwon, Y.; van der Ham, C. J. M.; Qin, Z.; Koper, M. T. M. A New Mechanism for the Selectivity to C1 and C2 Species in the Electrochemical Reduction of Carbon Dioxide on Copper Electrodes. *Chemical Science* **2011**, 2 (10), 1902–1909. https://doi.org/10.1039/c1sc00277e.

4) Peterson, A. A.; Abild-Pedersen, F.; Studt, F.; Rossmeisl, J.; Nørskov, J. K. How Copper Catalyzes the Electroreduction of Carbon Dioxide into Hydrocarbon Fuels. *Energy and Environmental Science* **2010**, 3 (9), 1311–1315. https://doi.org/10.1039/c0ee00071j.

5) Feng, X.; Jiang, K.; Fan, S.; Kanan, M. W. A Direct Grain-Boundary-Activity Correlation for CO Electroreduction on Cu Nanoparticles. *ACS Central Science* **2016**, 2 (3), 169–174. https://doi.org/10.1021/acscentsci.6b00022.

6) Uzunova, E. L.; Seriani, N.; Mikosch, H. CO_2 Conversion to Methanol on Cu(i) Oxide Nanolayers and Clusters: An Electronic Structure Insight into the Reaction Mechanism. Physical Chemistry Chemical Physics **2015**, 17 (16), 11088–11094. https://doi.org/10.1039/c5cp01267h.

7) Birhanu, M. K.; Tsai, M. C.; Chen, C. T.; Kahsay, A. W.; Zeleke, T. S.; Ibrahim, K. B.; Huang, C. J.; Liao, Y. F.; Su, W. N.; Hwang, B. J. Electrocatalytic Reduction of Carbon Dioxide on Gold–Copper Bimetallic Nanoparticles: Effects of Surface Composition on Selectivity. *Electrochimica Acta* **2020**, 356, 136756. https://doi.org/10.1016/j.electacta.2020.136756.

8) Yin, Z.; Gao, D.; Yao, S.; Zhao, B.; Cai, F.; Lin, L.; Tang, P.; Zhai, P.; Wang, G.; Ma, D.; Bao, X. Highly Selective Palladium-Copper Bimetallic Electrocatalysts for the Electrochemical Reduction of CO_2 to CO. *Nano Energy* **2016**, 27, 35–43. https://doi.org/10.1016/j.nanoen.2016.06.035.

9) Shao, J.; Wang, Y.; Gao, D.; Ye, K.; Wang, Q.; Wang, G. Copper-Indium Bimetallic Catalysts for the Selective Electrochemical Reduction of Carbon Dioxide. *Chinese Journal of Catalysis* **2020**, 41 (9), 1393–1400. https://doi.org/10.1016/S1872-2067(20)63577-X.

10) Vasileff, A.; Xu, C.; Jiao, Y.; Zheng, Y.; Qiao, S. Z. Surface and Interface Engineering in Copper-Based Bimetallic Materials for Selective **CO_2** Electroreduction. *Chem. Elsevier Inc August 9*, **2018**, pp 1809–1831. https://doi.org/10.1016/j.chempr.2018.05.001.

11) Kim, D.; Resasco, J.; Yu, Y.; Asiri, A. M.; Yang, P. Synergistic Geometric and Electronic Effects for Electrochemical Reduction of Carbon Dioxide Using Gold-Copper Bimetallic Nanoparticles. *Nature Communications* **2014**, 5 (May), 1–8. https://doi.org/10.1038/ncomms5948.

12) Rasul, S.; Anjum, D. H.; Jedidi, A.; Minenkov, Y.; Cavallo, L.; Takanabe, K. A Highly Selective Copper-Indium Bimetallic Electrocatalyst for the

Electrochemical Reduction of Aqueous CO_2 to CO. *Angewandte Chemie - International Edition* **2015**, 54 (7), 2146–2150. https://doi.org/10.1002/anie.201410233.

13) He, J.; Dettelbach, K. E.; Salvatore, D. A.; Li, T.; Berlinguette, C. P. High-Throughput Synthesis of Mixed-Metal Electrocatalysts for CO_2 Reduction. *Angewandte Chemie* **2017**, 129 (22), 6164–6168. https://doi.org/10.1002/ange.201612038.

14) Kim, D.; Xie, C.; Becknell, N.; Yu, Y.; Karamad, M.; Chan, K.; Crumlin, E. J.; Nørskov, J. K.; Yang, P. Electrochemical Activation of CO_2 through Atomic Ordering Transformations of AuCu Nanoparticles. Journal of the American Chemical Society **2017**, 139 (24), 8329–8336. https://doi.org/10.1021/jacs.7b03516.

15) Hoffman, Z. B.; Gray, T. S.; Moraveck, K. B.; Gunnoe, T. B.; Zangari, G. Electrochemical Reduction of Carbon Dioxide to Syngas and Formate at Dendritic Copper-Indium Electrocatalysts. ACS Catalysis **2017**, 7 (8), 5381–5390. https://doi.org/10.1021/acscatal.7b01161.

16) Zhu, Q. G.; Sun, X. F.; Kang, X. C.; MA, J.; Qian, Q. L.; Han, B. X. Cu_2S on Cu Foam as Highly Efficient Electrocatalyst for Reduction of CO_2 to Formic Acid. Wuli Huaxue Xuebao/ Acta Physico - *Chimica Sinica* **2016**, 32 (1), 261–266. https://doi.org/10.3866/PKU.WHXB201512101.

17) Deng, Y.; Huang, Y.; Ren, D.; Handoko, A. D.; Seh, Z. W.; Hirunsit, P.; Yeo, B. S. On the Role of Sulfur for the Selective Electrochemical Reduction of CO_2 to Formate on CuSx Catalysts. ACS Applied Materials and Interfaces **2018**, 10 (34), 28572–28581. https://doi.org/10.1021/acsami.8b08428.

18) Chen, K.; Sun, C.; Song, S.; Xue, D. Polymorphic Crystallization of Cu2O Compound. CrystEngComm **2014**, 16 (24), 5257–5267. https://doi.org/10.1039/c4ce00339j.

19) Avelas Resende, J. Copper-Based p-Type Semiconducting Oxides: From Materials to Devices, **2017**.

20) Singh, M.; Jampaiah, D.; Kandjani, A. E.; Sabri, Y. M.; della Gaspera, E.; Reineck, P.; Judd, M.; Langley, J.; Cox, N.; van Embden, J.; Mayes, E. L. H.; Gibson, B. C.; Bhargava, S. K.; Ramanathan, R.; Bansal, V. Oxygen-Deficient Photostable Cu_2O for Enhanced Visible Light Photocatalytic Activity. *Nanoscale* **2018**, 10 (13), 6039–6050. https://doi.org/10.1039/c7nr08388b.

21) Zhang, F.; Dong, G.; Wang, M.; Zeng, Y.; Wang, C. Efficient Removal of Methyl Orange Using Cu_2O as a Dual Function Catalyst. *Applied Surface Science* **2018**, 444, 559–568. https://doi.org/10.1016/j.apsusc.2018.03.087.

22) Aguirre, M. E.; Zhou, R.; Eugene, A. J.; Guzman, M. I.; Grela, M. A. Cu_2O/TiO_2 Heterostructures for CO_2 Reduction through a Direct Z-Scheme:

Protecting Cu_2O from Photocorrosion. *Applied Catalysis B: Environmental* **2017**, 217, 485–493. https://doi.org/10.1016/j.apcatb.2017.05.058.

23) Lee, K.; Mazare, A.; Schmuki, P. One-Dimensional Titanium Dioxide Nanomaterials: Nanotubes. *Chemical Reviews* **2014**, 114 (19), 9385–9454. https://doi.org/10.1021/cr500061m.

24) Ampelli, C.; Genovese, C.; Tavella, F.; Favaro, M.; Agnoli, S.; Granozzi, G.; Perathoner, S.; Centi, G. Assembling of TiO_2 Nanotube Photoelectrodes with Enhanced Visible Properties for a Sustainable Production of H_2. *Chemical Engineering Transactions* **2015**, 43 (2001), 667–672. https://doi.org/10.3303/CET1543112.

25) Ampelli, C.; Tavella, F.; Perathoner, S.; Centi, G. Engineering of Photoanodes Based on Ordered TiO_2-Nanotube Arrays in Solar Photo-Electrocatalytic (PECa) Cells. *Chemical Engineering Journal* **2017**, 320, 352–362. https://doi.org/10.1016/j.cej.2017.03.066.

26) Ampelli, C.; Tavella, F.; Genovese, C.; Perathoner, S.; Favaro, M.; Centi, G. Analysis of the Factors Controlling Performances of Au-Modified TiO_2 Nanotube Array Based Photoanode in Photo-Electrocatalytic (PECa) Cells. *Journal of Energy Chemistry* **2017**, 26 (2), 284–294. https://doi.org/10.1016/j.jechem.2016.11.004.

27) Chen, X. Liu, L. Yu, P. Y. Mao, S. S. Increasing Solar Absorption for Photocatalysis with Black Hydrogenated Titanium Dioxide Nanocrystals. *Science* **2011**, 331 (6018), 746-50. https:// 10.1126/science.1200448

28) Grimes, C. A. Synthesis and Application of Highly Ordered Arrays of TiO_2 Nanotubes. *Journal of Materials Chemistry* **2007**, 17 (15), 1451–1457. https://doi.org/10.1039/b701168g.

29) Shi, H. Formation Mechanism of Anodic TiO_2 Nanotubes. *Advances in Engineering Research* **2017**, 123.

30) Song, J. T.; Song, H.; Kim, B.; Oh, J. Towards Higher Rate Electrochemical CO_2 Conversion: From Liquid-Phase to Gas-Phase Systems. Catalysts. MDPI AG March 1, **2019**. https://doi.org/10.3390/catal9030224.

31) Garg, S.; Li, M., Weber, A. Z.; Ge, L.; Li, L.; Rudolph, V.; Wang, G.; Rufford, T. E. Advances and challenges in electrochemical CO_2 reduction processes: an engineering and design perspective looking beyond new catalyst materials. *Journal of Materials Chemistry A*, **2020** ,8, 1511-1544. https://doi:10.1039/c9ta13298h

32) Lin, R.; Guo, J.; Li, X.; Patel, P.; Seifitokaldani, A. Electrochemical Reactors for CO_2 Conversion; **2020**; Vol. 10. https://doi.org/10.3390/catal10050473.

33) Salvatore, D. A.; Weekes, D. M.; He, J.; Dettelbach, K. E.; Li, Y. C.; Mallouk, T. E.; Berlinguette, C. P. Electrolysis of Gaseous CO_2 to CO in a

Flow Cell with a Bipolar Membrane. *ACS Energy Letters* **2018**, 3 (1), 149–154. https://doi.org/10.1021/acsenergylett.7b01017.

34) Lee, W.; Kim, Y. E.; Youn, M. H.; Jeong, S. K.; Park, K. T. Catholyte-Free Electrocatalytic CO_2 Reduction to Formate. *Angewandte Chemie - International Edition* **2018**, 57 (23), 6883–6887. https://doi.org/10.1002/anie.201803501.

35) Xu, C.; Zhen, S.; Ren, R.; Chen, H.; Song, W.; Wang, Z.; Sun, W.; Sun, K. Cu-Doped Sr2Fe1.5Mo0.5O6-: δ as a Highly Active Cathode for Solid Oxide Electrolytic Cells. *Chemical Communications* **2019**, 55 (55), 8009–8012. https://doi.org/10.1039/c9cc03455b

36) Li, H.; Oloman, C. Development of a Continuous Reactor for the Electro-Reduction of Carbon Dioxide to Formate - Part 2: Scale-Up. *Journal of Applied Electrochemistry* **2007**, 37 (10), 1107–1117. https://doi.org/10.1007/s10800-007-9371-8.

37) Hori, Y.; Ito, H.; Okano, K.; Nagasu, K.; Sato, S. Silver-Coated Ion Exchange Membrane Electrode Applied to Electrochemical Reduction of Carbon Dioxide. *Electrochimica Acta* **2003**, 48 (18), 2651–2657. https://doi.org/10.1016/S0013-4686(03)00311-6.

38) Hagesteijn, K. F. L.; Jiang, S.; Ladewig, B. P. A Review of the Synthesis and Characterization of Anion Exchange Membranes. Journal of Materials Science. *Springer New York LLC August 1*, **2018**, pp 11131–11150. https://doi.org/10.1007/s10853-018-2409-y.

39) Kang, U.; Park, H. A Facile Synthesis of $CuFeO_2$ and CuO Composite Photocatalyst Films for the Production of Liquid Formate from CO2 and Water over a Month. *Journal of Materials Chemistry A* **2017**, 5 (5), 2123–2131. https://doi.org/10.1039/c6ta09378g.

40) Schreier, M.; Curvat, L.; Giordano, F.; Steier, L.; Abate, A.; Zakeeruddin, S. M.; Luo, J.; Mayer, M. T.; Grätzel, M. Efficient Photosynthesis of Carbon Monoxide from CO_2 Using Perovskite Photovoltaics. *Nature Communications* **2015**, 6. https://doi.org/10.1038/ncomms8326.

41) Urbain, F.; Tang, P.; Carretero, N. M.; Andreu, T.; Gerling, L. G.; Voz, C.; Arbiol, J.; Morante, J. R. A Prototype Reactor for Highly Selective Solar-Driven CO2 Reduction to Synthesis Gas Using Nanosized Earth-Abundant Catalysts and Silicon Photovoltaics. *Energy and Environmental Science* **2017**, 10 (10), 2256–2266. https://doi.org/10.1039/c7ee01747b.

42) Schreier, M.; Héroguel, F.; Steier, L.; Ahmad, S.; Luterbacher, J. S.; Mayer, M. T.; Luo, J.; Grätzel, M. Solar Conversion of CO_2 to CO Using Earth-Abundant Electrocatalysts Prepared by Atomic Layer Modification of CuO. *Nature Energy* **2017**, 2 (7). https://doi.org/10.1038/nenergy.2017.87.

43) Galan-Mascaros, J. R. Photoelectrochemical Solar Fuels from Carbon Dioxide, Water and Sunlight. *Catalysis Science and* Technology **2020**, 10 (7), 1967–1974. https://doi.org/10.1039/c9cy02606a.

44) Dias, P.; Mendes, A. Hydrogen Production from Photoelectrochemical Water Splitting. *Encyclopedia of Sustainability Science and Technology* **2018**, 1–52. https://doi.org/10.1007/978-1-4939-2493-6_957-1.

45) Halmann, M. Photoelectrochemical Reduction of Aqueous Carbon Dioxide on P-Type Gallium Phosphide in Liquid Junction Solar Cells. *Nature* **1978**, 115–116.

46) Castro, S.; Albo, J.; Irabien, A. Photoelectrochemical Reactors for CO_2 Utilization. *ACS Sustainable Chemistry and Engineering* **2018**, 6 (12), 15877–15894. https://doi.org/10.1021/acssuschemeng.8b03706.

47) Awad, N. K.; Ashour, E. A.; Allam, N. K. Recent Advances in the Use of Metal Oxide-Based Photocathodes for Solar Fuel Production. *Journal of Renewable and Sustainable Energy* **2014**, 6 (2). https://doi.org/10.1063/1.4871899.

48) Zhou, X.; Liu, R.; Sun, K.; Chen, Y.; Verlage, E.; Francis, S. A.; Lewis, N. S.; Xiang, C. Solar-Driven Reduction of 1 Atm CO_2 to Formate at 10% Energy-Conversion Efficiency by Use of a TiO_2 -Protected III-V Tandem Photoanode in Conjunction with a Bipolar Membrane and a Pd/C Cathode Electrocatalyst. *ECS Transactions* **2017**, 77 (4), 31–41. https://doi.org/10.1149/07704.0031ecst.

49) Arai, T.; Sato, S.; Kajino, T.; Morikawa, T. Solar CO_2 Reduction Using H_2O by a Semiconductor/Metal-Complex Hybrid Photocatalyst: Enhanced Efficiency and Demonstration of a Wireless System Using $SrTiO_3$ Photoanodes. *Energy and Environmental Science* **2013**, 6 (4), 1274–1282. https://doi.org/10.1039/c3ee24317f.

50) Gurudayal; Beeman, J. W.; Bullock, J.; Wang, H.; Eichhorn, J.; Towle, C.; Javey, A.; Toma, F. M.; Mathews, N.; Ager, J. W. Si Photocathode with Ag-Supported Dendritic Cu Catalyst for CO_2 Reduction. *Energy and Environmental Science* **2019**, 12 (3), 1068–1077. https://doi.org/10.1039/c8ee03547d.

51) Gurudayal; Beeman, J. W.; Bullock, J.; Wang, H.; Eichhorn, J.; Towle, C.; Javey, A.; Toma, F. M.; Mathews, N.; Ager, J. W. Si Photocathode with Ag-Supported Dendritic Cu Catalyst for CO_2 Reduction. Energy and *Environmental Science* ***2019***, 12 (3), 1068–1077. https://doi.org/10.1039/c8ee03547d.

52) de Brito, J. F.; Genovese, C.; Tavella, F.; Ampelli, C.; Boldrin Zanoni, M. V.; Centi, G.; Perathoner, S. CO_2 Reduction of Hybrid Cu_2O–Cu/Gas Diffusion Layer Electrodes and Their Integration in a Cu-Based Photoelectrocatalytic Cell. *ChemSusChem* **2019**, 12 (18), 4274–4284. https://doi.org/10.1002/cssc.201901352.

53) Ampelli, C.; Genovese, C.; Marepally, B. C.; Papanikolaou, G.; Perathoner, S.; Centi, G. Electrocatalytic Conversion of CO_2 to Produce Solar Fuels in

Electrolyte or Electrolyte-Less Configurations of PEC Cells. *Faraday Discussions* **2015**, 183, 125–145. https://doi.org/10.1039/c5fd00069f.

54) Kalamaras, E.; Maroto-Valer, M. M.; Shao, M.; Xuan, J.; Wang, H. Solar Carbon Fuel via Photoelectrochemistry. *Catalysis Today* **2018**, 317, 56–75. https://doi.org/10.1016/j.cattod.2018.02.045.

55) Tan, H. L.; Abdi, F. F.; Ng, Y. H. Heterogeneous Photocatalysts: An Overview of Classic and Modern Approaches for Optical, Electronic, and Charge Dynamics Evaluation. Chemical Society Reviews. *Royal Society of Chemistry March 7*, **2019**, pp 1255–1271. https://doi.org/10.1039/c8cs00882e.

56) Ogura, K.; Takagi, M. Electrocatalytic Reduction of Carbon Dioxide to Methanol Part III. Use of an Electrochemical Photocell. *J Electromal. Chow* **1986**, 201, 359.

57) Xu, Q.; Zhang, L.; Yu, J.; Wageh, S.; Al-Ghamdi, A. A.; Jaroniec, M. Direct Z-Scheme Photocatalysts: Principles, Synthesis, and Applications. Materials *Today. Elsevier B.V. December 1*, **2018**, pp 1042–1063. https://doi.org/10.1016/j.mattod.2018.04.008.

58) Shehzad, N.; Tahir, M.; Johari, K.; Murugesan, T.; Hussain, M. Fabrication of Highly Efficient and Stable Indirect Z-Scheme Assembly of AgBr/TiO_2 via Graphene as a Solid-State Electron Mediator for Visible Light Induced Enhanced Photocatalytic H_2 Production. *Applied Surface Science* **2019**, 463, 445–455. https://doi.org/10.1016/j.apsusc.2018.08.250

59) Low, J.; Jiang, C.; Cheng, B.; Wageh, S.; Al-Ghamdi, A. A.; Yu, J. A Review of Direct Z-Scheme Photocatalysts. *Small Methods* **2017**, *1* (5), 1700080. https://doi.org/10.1002/smtd.201700080

4. PHOTOCATALYTIC CO_2 REDUCTION

4.1 STATE OF THE ART

Photocatalytic reduction of CO_2 has been performed in different ways over different catalytic materials, including organic and inorganic semiconductors[1–3]; great efforts have been given to the study of i) thermodynamics of the reactions involved in order to suppress the side hydrogen evolution reaction (HER), ii) activation and reduction mechanisms on semiconductor surface through heterogeneous catalysis, and iii) capacity to harvest light to generate electron/hole charges, which can interact with CO_2 converting it into a variety of interesting compounds useful in the fuel industry, and avoiding the major issue, namely the charge recombination, which results in low quantum yield[4]. Among the semiconductors, titanium oxide (TiO_2) has widely been employed due to its important features like the large availability, environmental safety, chemical resistance and strong photocatalytic activity in oxidation and reduction processes[5,6]. However, the main disadvantages of this material are related to i) the poor capacity of exploiting the visible light range without the addition of dyes, sensitizers, dopants (like incorporation of nitrogen atoms) or the incorporation of noble metals[7], and ii) the high charge recombination rate. Moreover, CH_4 and CO are generally the main products obtained in a significant amount by CO_2 photocatalytic reduction, but no formation of $>C_1$ compounds[8] is usually reported. From the economic perspective, acetic acid (i.e. a C2 product) has for example a market value 3–4 times higher than CO or CH_4, and its direct synthesis from CO_2 may greatly reduce the number of process steps and energy intensity with respect to the actual process starting from fossil fuels.

Regarding the photocatalytic materials, Cu_2O has widely been employed in CO_2 photocatalysis in the recent years, because of their excellent characteristics like non-toxicity, heart abundance, high absorbance coefficient and low preparation costs. The most important features that make it an excellent candidate in the photocatalytic conversion of CO_2 are i) the absorption in the visible light range ($\lambda < 620$ nm), which represents 45% of the solar spectrum due to its the narrow band

gap (around 2 eV) and ii) the valence and conduction band positions, the latter energetic enough to make CO_2 reduction occur. Due to copper ion vacancies, Cu_2O behave like a *p*-type semiconductor; its ability to promote multi-electron processes makes it an advantageous candidate in the photoreduction of CO_2 due to its capacity to accept and accumulate electrons from the absorption of visible radiation[9]. The true potential of Cu_2O can be obtained by limiting some problems and obtaining; i) more photo-stable materials; ii) more stable materials during synthesis and storage; iii) oxygen-deficient structures (reported to be more active). Cu_2O is present in the +1 oxidation state, and can be oxidized to CuO (2+) or reduced to Cu (0). This allows this material to be used efficiently to carry out many redox reactions, but on the other hand the main disadvantage is the easy photo-oxidation to CuO, which is reported to be less photo-active[10-12]. Moreover, it is possible to drive the reaction selectivity towards more interesting products by tailoring the morphology of Cu_2O through the adoption of different preparation techniques. It was proved, in fact, how the Cu_2O film thickness can drive CO_2 reduction selectivity towards compounds like hydrogen, carbon monoxide, ethylene, ethane, methane and methanol, inducing also a different local pH[13]. CO_2 photocatalytic reduction can also be affected by the 3D spacial organization of the Cu_2O semiconductor particles[14]. One of the major drawbacks of the photocatalytic application of Cu_2O is the photocorrosion, induced by the electrons and holes formed in its surface when irradiated. However, the formation of Type II band alignment heterostructures, coupling *p*-type Cu_2O with *n*-type wide band semiconductors (like TiO_2), may avoid the photocorrosion[15,16]. Of great importance is the choice of the reactor where the CO_2 photoreduction reaction is carried out. Some authors reported their studies in pressurized reactors at low temperature to increase the CO_2 solubility, and in these cases the selectivity was strongly electrolyte-dependent[17-19]. In this work, an innovative gas-phase flow-through photoreactor was used, operating at room temperature and atmospheric pressure, the details of which will be illustrated below.

4.2 SCOPE OF THE CHAPTER

In the following sections, the photocatalytic tests of CO_2 reduction, carried out both in a conventional slurry reactor and in a novel photo-device operating in gas phase, will be reported. The latter allows to perform the process at room temperature and

atmospheric pressure, contrary to most of the work reported in literature that was focused on the photoreduction of CO_2 in liquid phase[20-23]. In the adopted novel gas-phase reactor configuration, reactions occur at a gas-solid interface, and the photocatalytic surface, based on photo-active nanomembranes, was crossed by a mixture of vapor saturated with CO_2, avoiding with the use of electrolytes[24]. This avoids the preferential absorption of water on the photocatalytic surface, with respect to liquid/solid configurations, minimizing the hydrogen production and increasing the local CO_2 concentration. This novel configuration shows notable differences compared to conventional reactors operating in liquid or gas phase, or even photoelectrochemical cells (PECs). In the latter, the photocatalyst is in direct contact with the electrolyte, and the two chambers are separated by a membrane, which allows the passage of protons[25-26]. In our case, the CO_2 saturated vapor-inlet flow crosses directly the catalyst (in form of nanomembrane deposited over perforated substrate). This allows to obtain the following advantages: i) there are no limitations due to the solubility of CO_2 in the electrolyte and diffusion phenomena in the electrode/electrolyte double-layer; ii) the chemisorption of water is severely limited. These characteristics led to a substantial difference in terms of productivity compared to conventional reactors.

As photocatalysts, nanostructured photoactive materials based on copper and prepared by electrodeposition (under different conditions in terms of pH, time deposition and electrolyte) were employed, depositing them on different microperfored supports like titanium, copper or aligned titania nanotube supports (the latter prepared by anodic oxidation). Electrodeposition technique was chosen as it allows to carry out synthesis at low temperature obtaining materials with high purity and by using low-cost devices. Moreover, in order to control thickness, morphology and stoichiometry of the resulting photocatalytic film, the electrodeposition technique was very useful as it allows to modulate synthesis parameters like time and applied voltage[27].

The use of different supports allowed to prepare multilayer photocatalytic materials with different electronic and interfacial charge-carrier transport properties, and to evaluate their influence on selectivity toward more valuable products (i.e. >C1 chemicals). Specifically, the preparation of a Cu_2O thin layer on aligned titania nanotube arrays allowed to create a heterojunction (*p*-type Cu_2O/*n*-type TiO_2 nanotubes) with the scope of further improving charge separation. The

crystallographic, optical and photochemical investigation on these multilayer photocatalytic materials provided valuable information to explain the different production rates of the prepared photocatalysts, in order to find a correlation of their morphological and structural properties with their photocatalytic activity.

4.3 EXPERIMENTAL

4.3.1 Photocatalyst fabrication

4.3.1.1 p-type Cu_2O deposition

p-type Cu_2O was deposited on Ti (or Cu) metallic support (acting as working electrode) by an electrodeposition process, using a three-electrode cell setup made up by a Ag/AgCl reference electrode and a platinum counter electrode. The deposition was carried out using an Amel 2049 potentiostat model (see Figure 4.1).

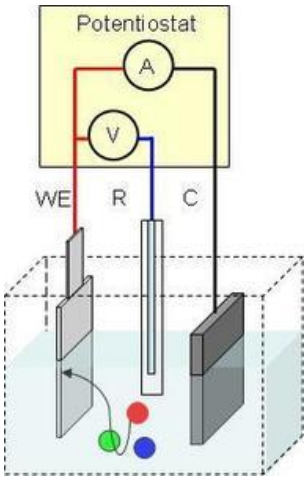

Figure 4.1 *Three electrode setup for Cu_2O electrodeposition on metal support.*

All the supports were previously cleaned by sonication with isopropanol for 30 minutes, and then oven-dried at 100°C. The electrolyte consists in a solution based on 0.1 M $CuSO_4 \cdot 5H_2O$ and 0.75 M lactic acid and, after stirring for 5 hours to stabilize the complex equilibrium and let temperature drop, by adjusting pH to 9 with a few drops of 5 M NaOH solution[28]. The electrodeposition was performed at 60°C. The reaction involved is the following:

$$Cu^{2+} + e^- \rightarrow Cu^+ \qquad 1)$$

A basic electrolyte (pH>7) favours the precipitation of Cu^+ over the electrode, in according to the following reaction:

$$2Cu^+ + 2OH^- \rightarrow Cu_2O + 2H_2O \qquad 2)$$

Prior to deposition, a linear sweep voltammetry -LSV- (see Figure 4.2a) from 0 to -1.5 V (vs Ag/AgCl) was conducted to select the potential range in which only Cu_2O selectively is formed, avoiding the deposition of metallic copper.

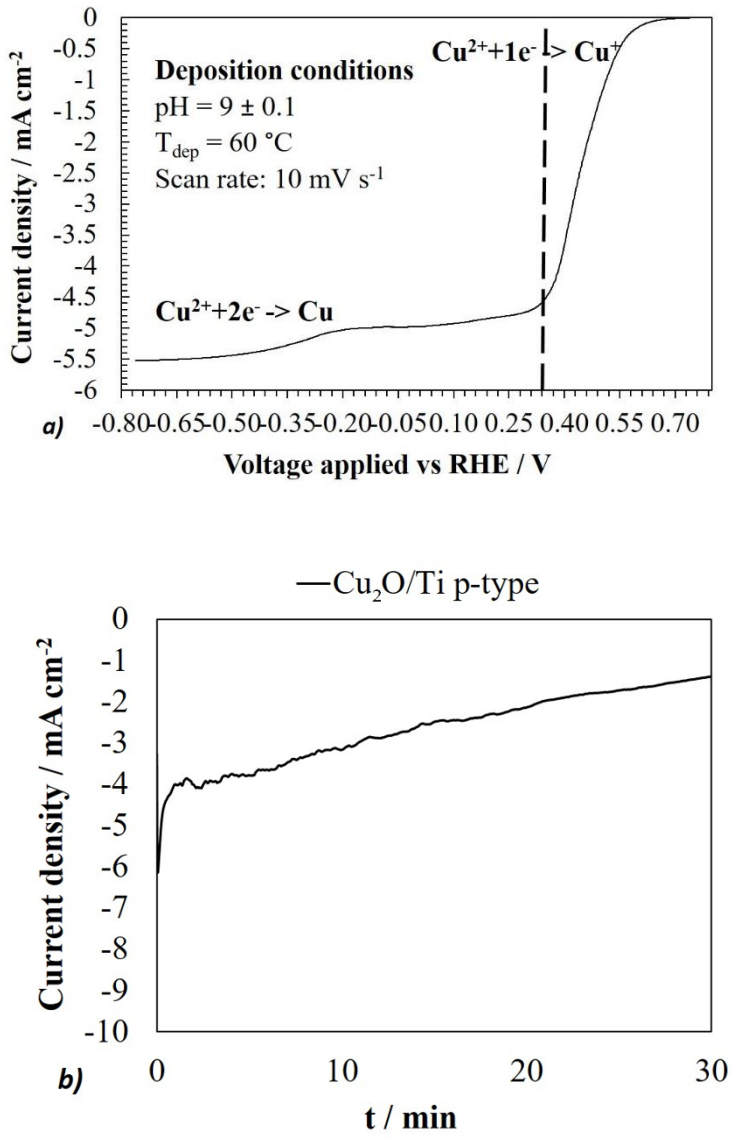

Figure 4.2 a) *LSV for deposition of p-type Cu_2O on Ti support by using a basic electrolyte;* ***b)*** *relative current density in the chronoamperometry at 0.34 V (vs. RHE).*

Thus, electrodepositions on Ti (*Cu_2O/Ti ptype*), on Cu (*Sample Cu_2O/Cu*) and on TiO_2 nanotube substrates (*TiO_2NTs/Cu_2O*) were carried out by applying a potential of -0.4 V (vs Ag / AgCl) (0.34 V vs. RHE) for different times. Figure 4.2b reports

the relative current density (vs. time) during Cu_2O electrodeposition on Ti at this applied voltage.

4.3.1.2 n-type Cu_2O deposition

n-type Cu_2O was deposited using the same set-up described for the *p*-type Cu_2O deposition on Ti and Cu metallic substrates (*Cu_2O/Ti ntypeA*, *Cu_2O/Cu ntypeA*, respectively), but starting from an acid solution based on 0.08 M sodium acetate and 0.02 M copper acetate[29]. The pH of the electrolyte was adjusted to 5 with a few drops of glacial acetic acid (Figure 4.3).

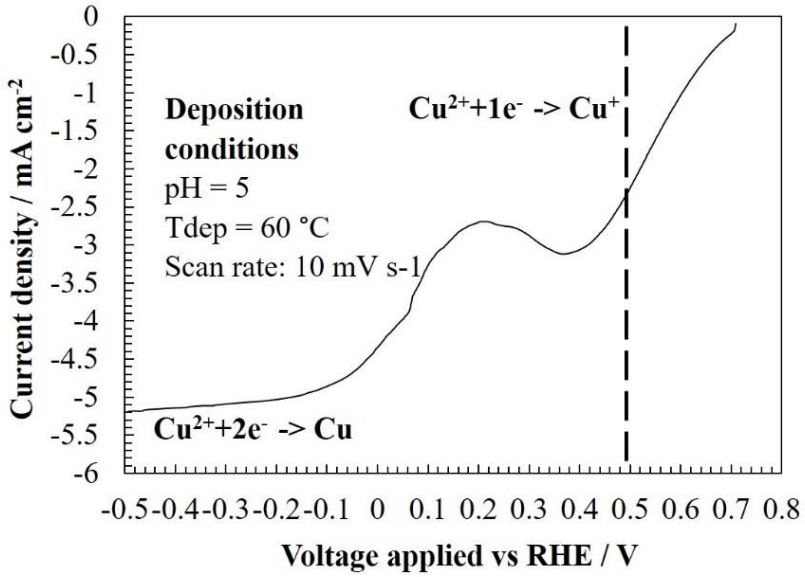

Figure 4.3 *LSV for deposition of n-type Cu_2O on Ti support by using an acid electrolyte.*

In this case, a potential of 0.49 V vs. RHE was chosen in order to avoid reduction to metallic Cu also due to hydrogen evolution process, which is favourite in a proton rich environment. In acid electrolyte, the following reaction occurs:

$$Cu_2O + 2e^- + 2H^+ \rightarrow 2Cu + H_2O \qquad 3)$$

4.3.1.3 CuO from Cu_2O conversion

The *n*-type Cu_2O (*Cu_2O/Ti n-typeA*) was annealed to obtain two different samples, the characteristics of which will be explained later.
The first sample was obtained by annealing at 450 °C for 1 hour to obtain a CuO phase (*Ti/CuO p-type*). The second sample was obtained by annealing at 250 °C for the same time (this sample was named *Ti/Cu_2O ntypeB*). The conversion to CuO phase is described by the following reaction:

$$Cu_2O + 1/2\ O_2 \rightarrow CuO \qquad 4)$$

4.3.1.4 *Cu_2O/TiO_2NTs p-n junction*

A controlled anodization process was employed to synthesize arrays of titanium nanotubes (*TiO_2NTs*) on a Ti metallic disk (supplied by Alfa Aesar, 99.6% purity), 0.025 mm thick and 35 mm in diameter; Before oxidation, the plate was sonicated in isopropanol at a temperature of about 50 °C for 30 min and subsequently dried in air to remove any organic residue present on the surface. The electrolyte was based on 2 wt.% of water and 0.33 wt.% of NH_4F in ethylene glycol, while the potential was set to 50 V for 45 min, reached with a ramp of 5 V min^{-1}. The so obtained sample was annealed at 450°C for 3 hours with a ramp of 2°C min^{-1} then sonicated with HCl for 30 seconds to polish the surface. The anodic oxidation set-up consists of a Teflon cell and a magnetic stirrer. The anode consists of a special Teflon support to hold the metal titanium plate, while the cathode consists of a standard platinum electrode supplied by the Amel company (see Figure 4.4).

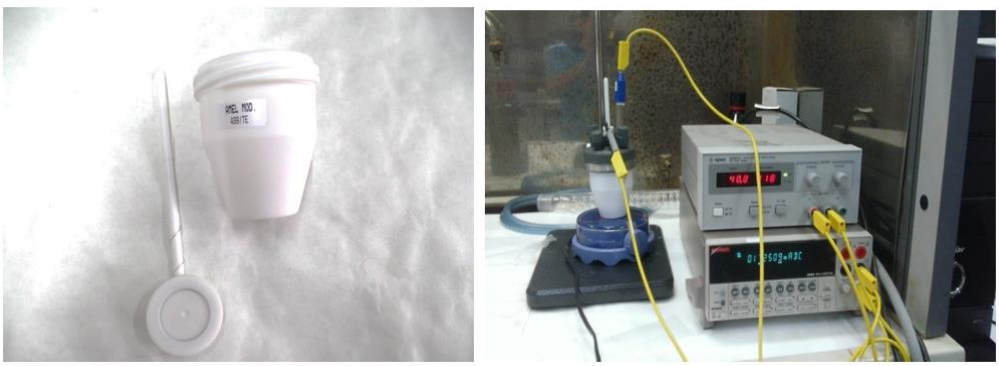

Figure 4.4 *Anodic oxidation Teflon support and complete setup.*

The *TiO_2NTs* sample was processes in CO_2 photocatalytic reaction without and with the deposition of a layer of Cu_2O (*TiO_2NTs/Cu_2O p-n*), through the electrodeposition method and under the operating conditions mentioned in the previous paragraphs.

4.3.1.5 Cu_2O prepared by wet precipitation

Cuprous oxide nanocubes, *Cu_2O NC-25*, was synthesized by a wet precipitation process in which 0.85 g of $CuCl_2 \cdot 2H_2O$ was dissolved in 500 mL of distilled water under stirring at the temperature of 60°C. After that, 50 mL of 2 M NaOH was added. This solution was stirred for 30 min and then 50 mL of a 0.6 M ascorbic acid solution were added. The formation of a red copper oxide precipitate was noticed and the precipitation was stopped after a stirring of 3 h at 60°C. After cooling the solution, the as-obtained precipitate was washed several times with distilled water and ethanol, collected by centrifugation and dried in a vacuum oven at 60°C for 12 h. Another Sample, *Cu_2O NC-60*, was synthesized by the same procedure with the only difference that 2 M NaOH was added at room temperature and not at 60 °C[30].

4.3.2 Setup

4.3.2.1 Photocurrent setup

The photocurrent behaviour was evaluated by chronoamperometry and cyclic voltammetry methods, through ON-OFF light cycles long 3 s each.
The setup used consists in a cell filled with 170 mL of a 0.5 M Na_2SO_4 solution, in which the working electrode, a Pt counter electrode and a 3M Ag/AgCl reference electrode (supplied by Amel Company) are immersed (see Figure 4.5). The reaction cell consists in a Pyrex flask equipped with a quartz window, with input and output lines for the flow of inert gas (N_2), while the incident light is generated by a solar simulator (Lot-Oriel, lamp at Xe, 300 W), with a set of lenses needed to collect and focus the light beam; a water filter eliminates infrared radiation. The voltage and the generated photocurrent were controlled and measured by an Amel 2049 potentiostat/galvanostat. The measurements made at fixed potential (chronoamperometry - CA) were recorded by using various filters to evaluate the

wavelength response in the following order: solar simulator filter, UVC blocking filter, UVB/C blocking filter, Vis/IR blocking filter (see Table 4.1).

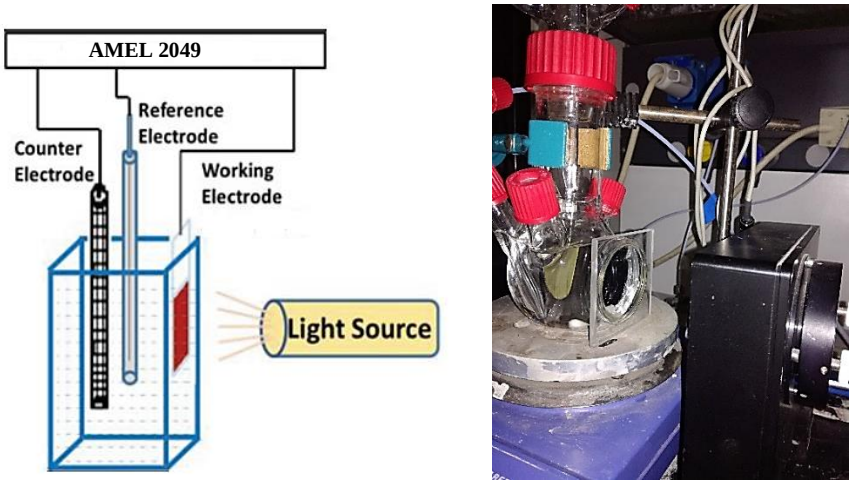

Figure 4.5 *Photocurrent setup.*

All the potential values are converted into RHE (Reversible Hydrogen Electrode) voltages through the following equation:

$$E_{(RHE)} = E_{Ag/AgCl} + 0.05916\ pH + 0.21$$

Filter Code	Description
AM 1.5 G	**Air Mass 1.5-global (direct light diffused through the atmosphere), 48°**
LSZ 178	**Anti UVC filter, 280-400 nm**
LSZ 179	**Anti UVB/UVC, filter 320-400 nm**

Table 4.1*. Filter-code (by Quantum Design) with relative cut-off wavelengths.*

Figure 4.6 shows how the irradiance varies with the wavelength for the various cut-off filters applied.

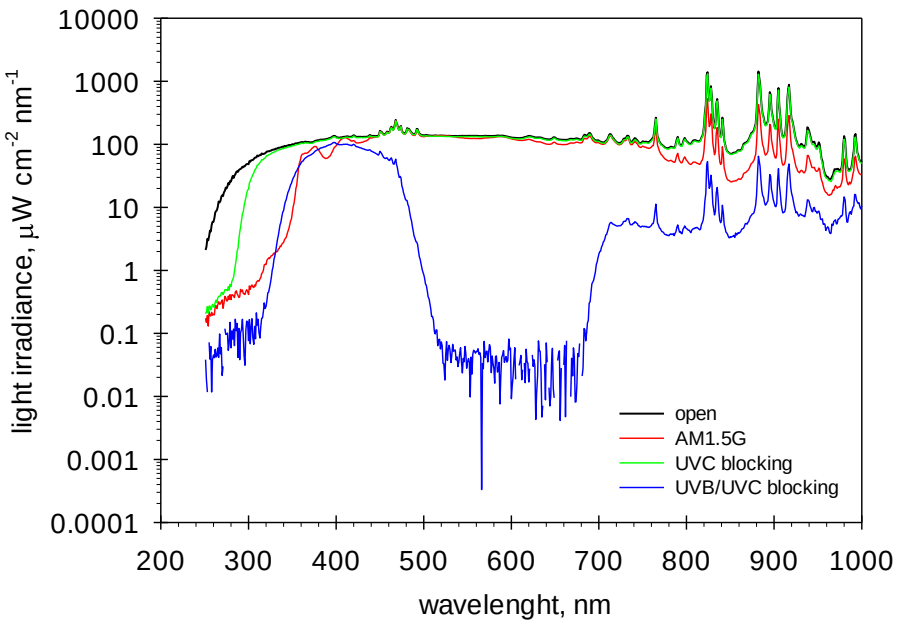

Figure 4.6 *Light irradiance vs wavelength for various cut-off filters.*

4.3.2.2 Photocatalytic setup

Slurry reactor

The reactor used for slurry photocatalytical tests is showed in Figure 4.7. The slurry reactor concept is similar to a fluidized bed reactor, in which the suspended phase is the gas reacting itself; in a slurry reactor, instead, the catalyst particles are suspended in a liquid (typically a $KHCO_3$ water solution) under stirring, while the gas phase (CO_2) flows continuously through the catalyst.

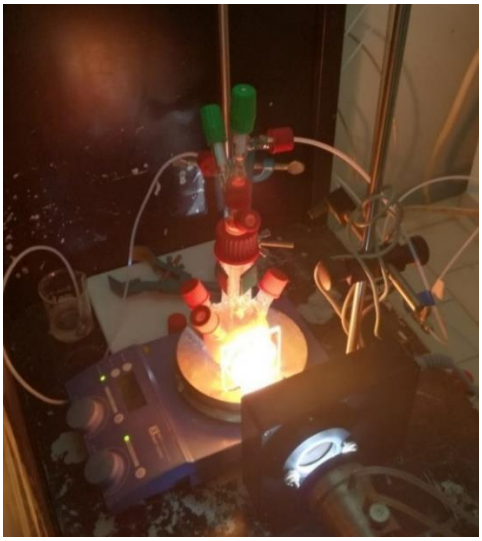

Figure 4.7 *Liquid phase system reaction.*

Gas phase reactor

A homemade photoreactor operating in gas phase, involving gas-solid interfacial reactions, was employed for CO_2 photoreduction.

All the CO_2 photocatalytic tests were carried out at atmospheric pressure and room temperature, except for the inlet gas phase flow, which was heated at 60°C.

The photoreactor, equipped with a quartz window for light transmission, is made in Plexiglas®, with the photocatalyst placed within it in the form of thin multilayer film, as showed in Figure 4.8.

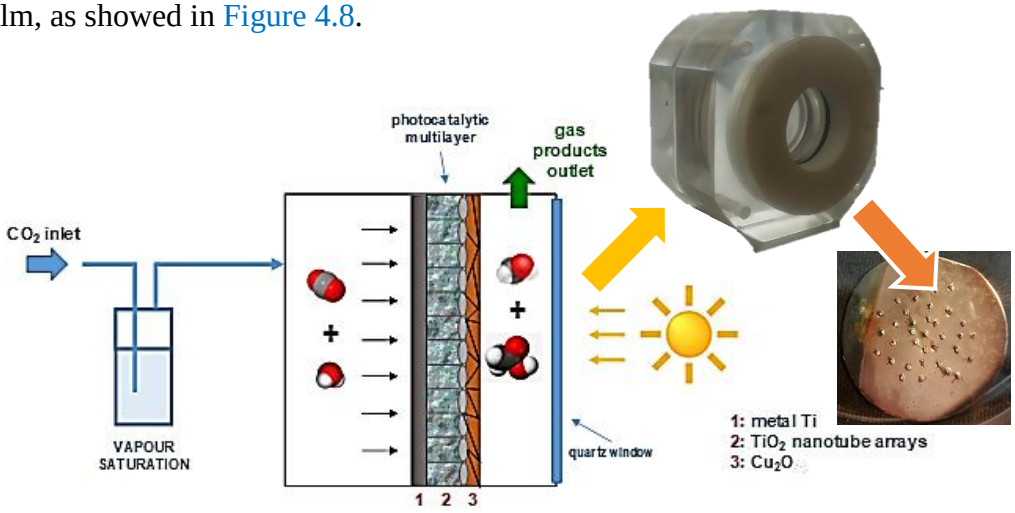

Figure 4.8 *Overall Photocatalytic setup and focus on the thin film multi-layered photocatalyst inside the photoreactor.*

A Xe-arc lamp, Lot Oriel, 300 W, is the light source and includes a series of lenses to collect and focus the light, while the infrared contribution is removed by a water filter, and the solar irradiance is simulated by an AM 1.5G filter.

As showed in Figure 4.8, a water-saturated CO_2 flow was obtained introducing a CO_2 gas flow of 33 mL min^{-1} into heated water (vapour saturator), generating at 60°C a saturation humidity of 0.10 Kg_{vapour}/kg_{CO2}. This flow diffuses through the metallic substrate due to small holes of 0.1 mm diameter made on its surface, and through the photocatalytic thin film due to the mesoporosity of TiO_2 NTs and Cu_xO. The outlet gas phase was condensed in a cold trap to make easier the absorption of liquid products such as ethanol, methanol, isopropanol, methylformiate, detectable by a Gas Chromatography-Mass Spectrometry (GC-MS), and acetic acid, formic acid, oxalic acid through an Ion-Chromatography (IC). A Gas Chromatograph (MicroGC GCX Pollution Analytic Equipment), with a sensitivity of ~2 ppm, was used to detect gases compounds like H_2, CH_4, CO, C_2H_4, C_2H_6.

A spectroradiometer, Lot Oriel, model ILT950, was used to measure the irradiance, which resulted to 135 mW cm^{-2} (for an irradiated area of 5 cm^{-2}). The irradiance measures light energy incident to the photocatalyst surface.

4.3.3 Characterization

Linear sweep voltammetry was used to characterize the *Cu_2O/Ti p-type* sample, under ON/OFF cycles of pulsed light in a range from 0.22 to 0.62 V vs RHE. The lower potential value of 0.22 V vs RHE was chosen to avoid and minimize the reduction to metallic Cu, which can modify the catalytic behaviour of these semiconductors. As observed in Figure 4.9, the current becomes more negative when light is ON, indicating a typical *p*-type behaviour, due to the transfer of electrons from the electrolyte to the electrode/electrode interface involving the photoreduction of the protons. During a single ON/OFF cycle when light is ON, the current decays (in absolute value) due to electron-hole recombination. Moving to the more positive potentials, the photocurrent decreases and becomes negligible at 0.62 V vs RHE, showing a less significant charge separation.

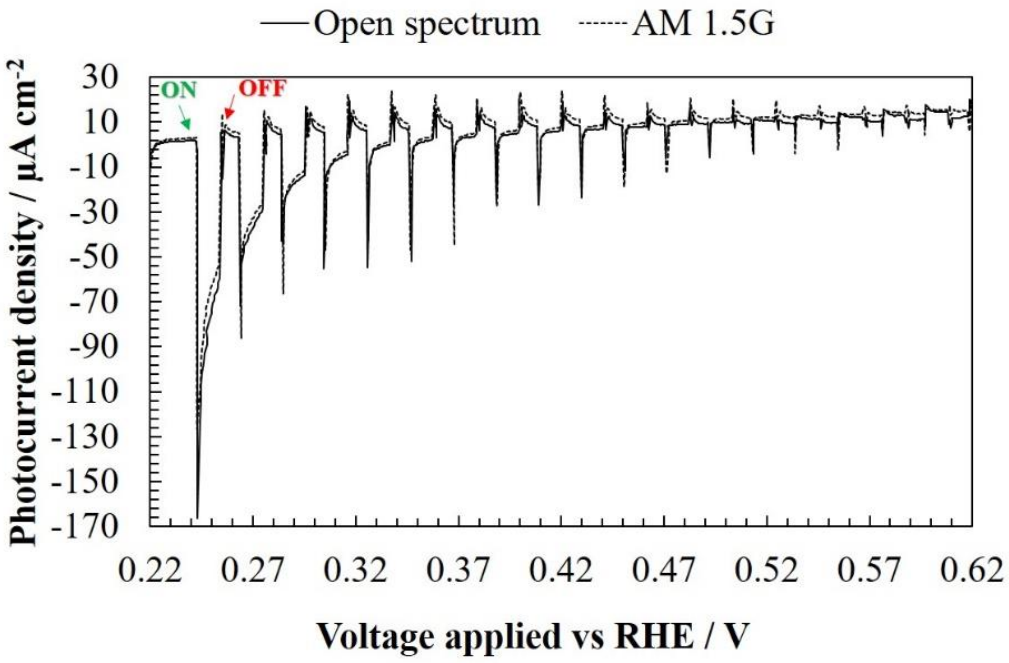

Figure 4.9 *Cu_2O/Ti p-type linear sweep voltammetry profile.*

The LSV analysis was performed both at open spectrum and with an AM 1.5 G filter, which simulates the solar spectrum; it can be observed how the measurements are superimposable, indicating that the Cu_2O thin layer absorbs in prevalence in the

visible light region. Figure 4.10 shows the photocurrent behaviour of the sample, obtained imposing a potential of 0.024 V vs RHE (-0.6 V vs Ag/AgCl).
This potential was chosen because it provides a good electron-hole pair separation and consequently a higher photocurrent compared to cathodic potential.

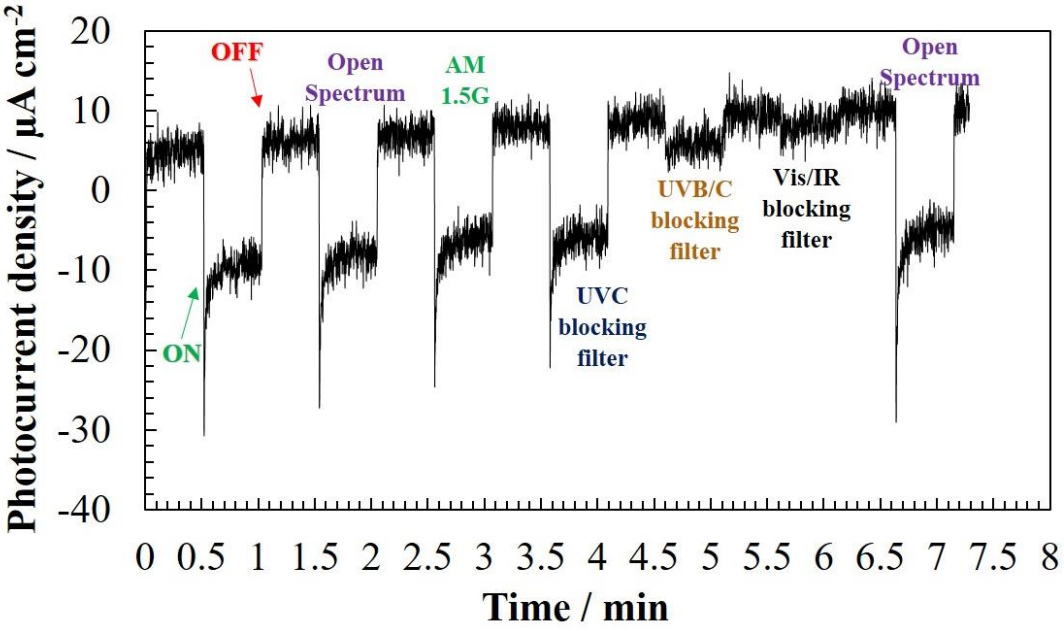

Figure 4.10 *Cu_2O/Ti p-type photocurrent response with various filters.*

Under a light ON/OFF cycle, the current increases in absolute value (as shown by the green and red arrows in the graph) and the magnitude is dependent on the light filter applied and thus on the light wavelength of exposure. Even in this case, the photocurrent increment in presence of the AM 1.5 G filter is very similar to that obtained in absence of any filter, highlighting again that Cu_2O works most in the visible light region. The Figures 4.11a,b show the LSV responses of the *n*-type Cu_2O (*Cu_2O/Ti n-typeA)* compared with *CuO/Ti p-type* and *Cu_2O/Ti n-typeB* samples, respectively, annealed at different temperatures; in particular, from 0.22 to 0.31 V vs RHE the *Cu_2O/Ti n-typeA* sample acts as a *p*-type semiconductor, while it shifts to *n*-type behaviour at potentials higher than 0.31 V. When this sample is annealed at 450°C, due to a total conversion of Cu_2O to CuO (*CuO/Ti p-type),* the photoresponse turns from *n* to a total *p*-behaviour (blue line in Figure 4.11a), evidencing a negative photocurrent difference when light is turned ON. However, this difference decays moving toward higher potentials.

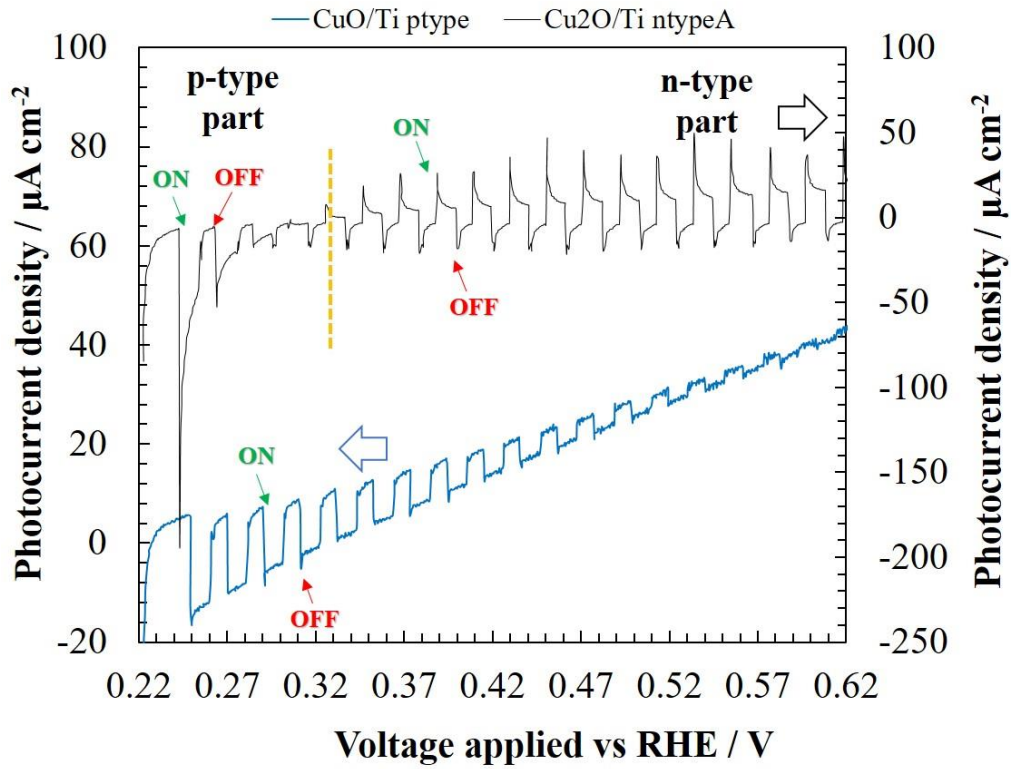

a)

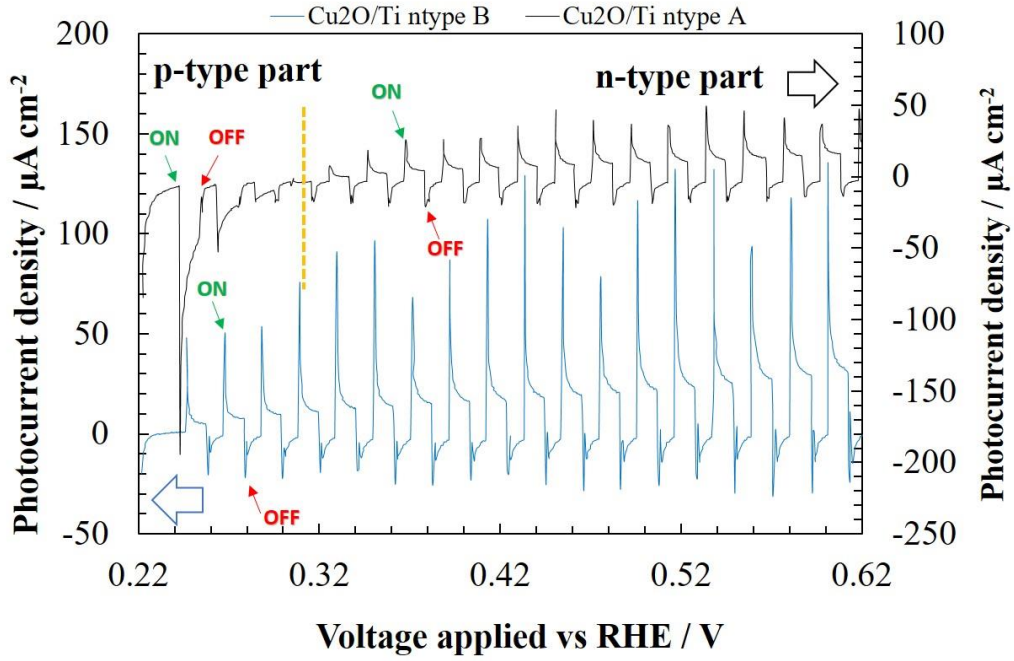

b)

Figure 4.11 *Photocurrent comparison between a) Cu_2O/Ti n-type A and CuO/Ti p-type and b) Cu_2O/Ti n-type A and Cu_2O/Ti b-type B.*

The annealing of the *n*-type Cu_2O to 250°C causes a change in the photocurrent behaviour and in this case the catalysts acts as an *n*-type semiconductor in all the potential range investigated, evidencing a positive photocurrent difference when light is turned ON (Figure 4.11b). In an *n*-type semiconductor, with respect to a *p*-

semiconductor, the holes (and not the electrons) move toward the electrode/electrolyte interface, ripping off electrons from the electrode and causing the anodic photocurrent. In Figure 4.12, the linear sweep voltammetry profiles of *Cu_2O/Cu p-type and Cu_2O/Ti p-type* samples (synthesized by the same procedure) are compared. Overlapping the two curves, a similar *p*-type behaviour can be observed, which is characterized by a first spike and then a decay of the current, with light cathodic increments of approximately 1.74 times higher for *Cu_2O/Ti p-type* with respect to the *Cu_2O/Cu p-type* current.

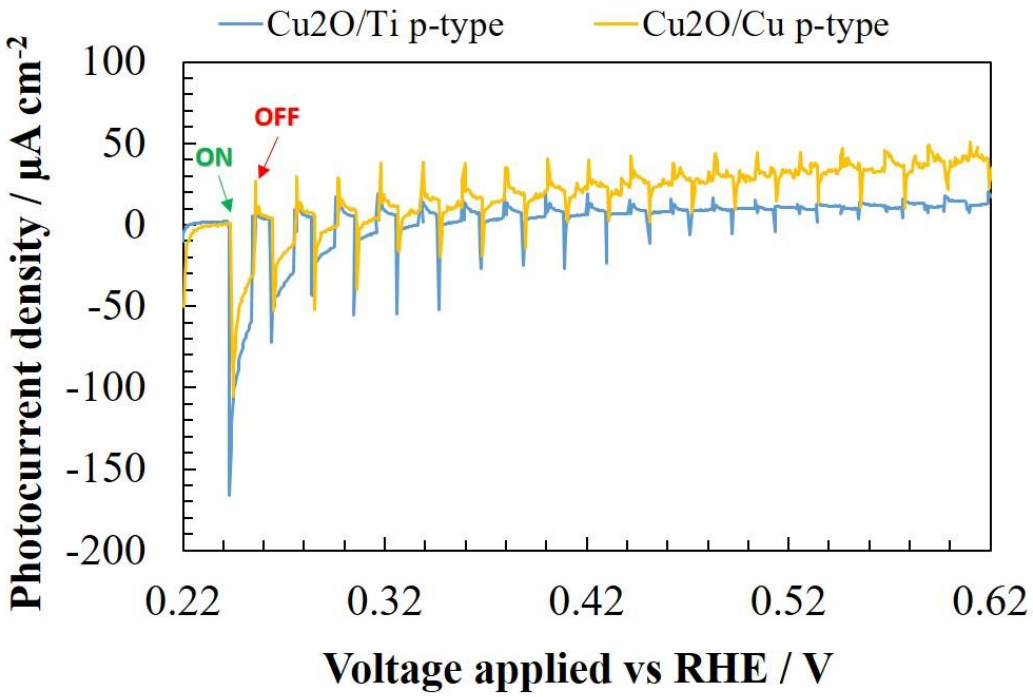

Figure 4.12 *Cu_2O/Cu p-type linear sweep voltammetry profile.*

Figure 4.13 shows the photocurrent comparison of titania nanotube arrays (*n-type TiO_2NTs, black line)* and the same sample in which a thin layer of *p*-type Cu_2O was deposited through electrodeposition. These measurements were obtained applying a potential of 0 V vs Ag/AgCl (0.62 V vs RHE) in a 0.5 M Na_2SO_4 water solution. Results show how the bare *TiO_2NTs* behave like an *n*-type semiconductor, with a predominance of absorption in the UV-visible light region, as indicated by the photoanodic current density increment at open spectrum in comparison with the signal when the AM 1.5G filter was used (in the latter case the current increment is significantly lower for *TiO_2NTs*). Moreover, as shown by the first three peaks, the photocurrent was stable under several ON/OFF light cycles. A fast recombination process is clearly showed by the current spikes present when the light is turned ON and a rapid decay of the current density is observed after a few seconds until

reaching a stable value, while dark and illuminated photocurrent density difference turns from 0.34 to 0.14 mA cm^{-2}. With the deposition of a thin layer of *p*-type Cu_2O, the difference between the dark and illuminated photocurrents resulted, at open spectrum, 15% higher than that of the bare *n-type* TiO_2NTs (with an increment of about 0.18 mA cm^{-2}). However, the most promising results regard the significant increment in the photoanodic current when AM 1.5G filter is applied (see the yellow circle in the graph of Figure 4.13). This shows the ability of Cu_2O deposited on TiO_2NTs to absorb light in the visible range more efficiently than the bare TiO_2NTs sample, which is instead more active in the UV-Visible region. As the *p*-type Cu_2O alone was not able to provide a positive anodic current at this applied voltage (see LSV in Figure 4.9), the good light absorption of Cu_2O/TiO_2NTs sample is to ascribe to the formation of a *p-n* heterojunction at the interface between Cu_2O and TiO_2 NTs. Note on the contrary that, by using a Vis/IR blocking filter, the Cu_2O/TiO_2NTs sample showed a photocurrent density lower than that of bare *n*-type TiO_2 NTs, because the presence of copper slightly reduced (about 15%) the fraction of UV radiation absorbed by the TiO_2 layer. Thus, the increment of the photocurrent at 0.62 V vs RHE for this sample is not due to Cu_2O separated contribution, but to a formation of a *p-n* junction, which modifies substantially the semiconductor properties.

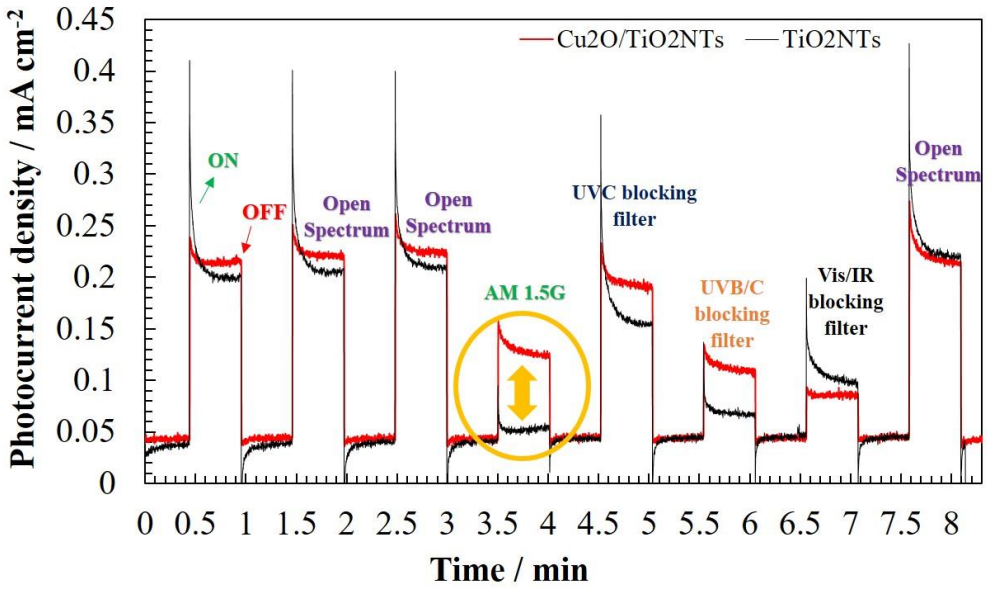

Figure 4.13 *Photocurrent comparison between TiO_2NTs and Cu_2O/TiO_2NTs. In the yellow circle the difference in photocurrent under the AM.1.5 filter is showed.*

The optical properties were evaluated by UV-visible Diffuse Reflectance Spectroscopy measuring the spectra in the range of 1100-200 nm. UV-visible

spectra of the *Cu₂O/Ti p-type*, *TiO₂NTs*, *Cu₂O/TiO₂NTs* samples were showed in the Figure 4.14.

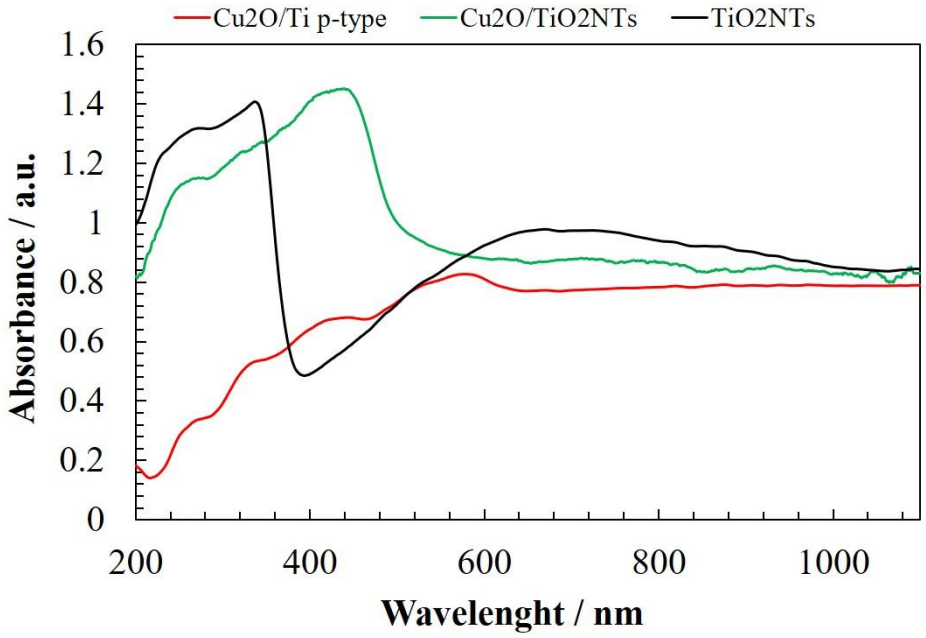

Figure 4.14 *UV-Vis comparison between Cu₂O/Ti p-type, TiO₂NTs, Cu₂O/TiO₂NTs samples.*

The red line refers to the *Cu₂O/Ti p-type* sample and shows an absorption in the 550-600 nm region with a series of resonance bands present in the ultraviolet region. The *TiO₂NTs* sample (black line) presents a strong absorption below 400 nm in the UV region, confirming the results obtained through the photocurrent tests, and a broad band, visible from 500 to 1200 nm, which includes a peak located at 700 nm. However, the latter peak can mainly be addressed to scattering and plasmonic phenomena. The photoanodic current increment when the titania is exposed to light is due mainly to the strong UV absorption in this region. The *Cu₂O/TiO₂NTs* (green line) shows a UV-visible onset at 500 nm with a peak at 450 nm and its red-shift with respect to the *TiO₂NTs*, is due to the formation of a *p-n* junction that, changing the electron-hole band energy levels, allows a light absorption in the visible region. In Figure 4.15 the UV-vis spectra of *Cu₂O/Ti n-typeB*, *CuO/Ti p-type*, *Cu₂O/Cu p-type*, *Cu₂O/Ti p-type* are showed. Among these, the *Cu₂O/Ti n-typeB* (yellow line) shows a very simile profile to the *Cu₂O/Ti p-type* (light blue line), while the *CuO/Ti p-type* sample (black line) shows an onset at 858 nm, evidencing a broad band extended to the visible region, while the *Cu₂O/Cu p-type* shows an onset at 670 nm and a peak centred at 580 nm.

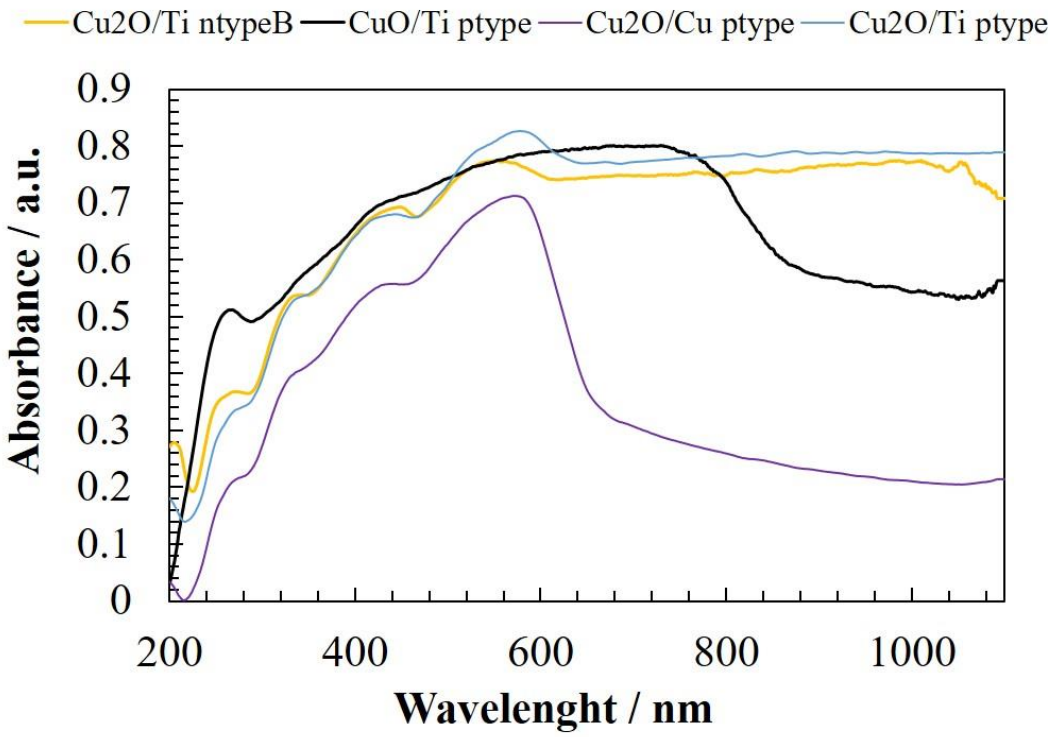

Figure 4.15 *UV-visible spectra comparison of Cu-based samples*

Through X-ray Diffraction (XRD) of powders, the crystallographic structure and the purity of various samples were investigated (Figure 4.16). The analysis was performed from 10° to 80° through a continuous PSD (position sensitive detector) fast scan mode, a step size of 0.040° and a time per step of 165 s. The detector used was a Lynxeye (1D mode), with these parameters: PSD opening 5.008°, lower discriminator 0.110 V and lipper discriminator 0.250 V. Other settings were Ka2 ratio 0.5 and kβ 1.39222 Å. The X-ray generator works at 30 kV and 10 mA. For the various samples in which the Cu_2O was deposited by electro-deposition (*Cu_2O/Ti p-type*, *Cu_2O/Ti n-typeA*, *Cu_2O/Ti n-type B*, *Cu_2O/Cu p-type*) the presence of impurities was excluded and the reflection planes present at 29.7°, 36.6°, 42.5°, 52.5°, 61.6°, 73.7° and 77.5° refer to the planes (110), (111), (200), (211), (220), (311) and (222), respectively, belonging to the cuprous oxide. The sample *Cu_2O/Ti ntypeB* was obtained by annealing at 250°C the *Cu_2O/Ti ntypeA*, but no CuO peaks were detected, indicating an eventual oxidation in the surface of particles and not in the bulk, while in the *CuO/Ti p-type sample*, obtained from the same precursor but with an annealing at 450°C, the Cu_2O peaks disappear and the characteristic peaks of CuO were detected showing the total conversion of the sample. The characteristic Cu_2O and TiO_2 peaks, the latter present in form of anatase, were detected for the sample *Cu_2O/TiO_2NTs.*

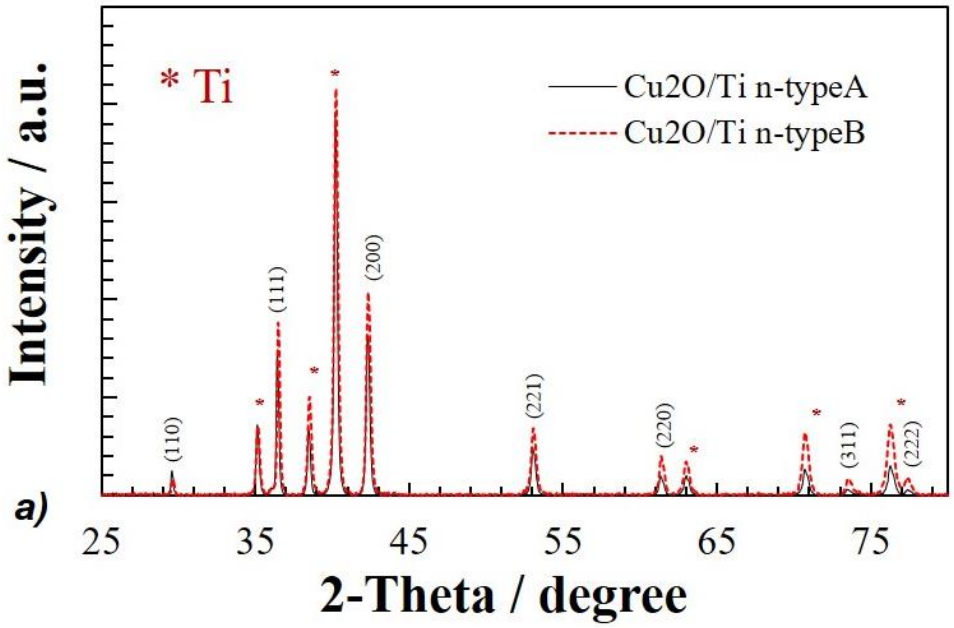
* Ti
Cu2O/Ti n-typeA
Cu2O/Ti n-typeB
Intensity / a.u.
(110)
(111)
(200)
(221)
(220)
(311)
(222)
a)
25
35
45
55
65
75
2-Theta / degree

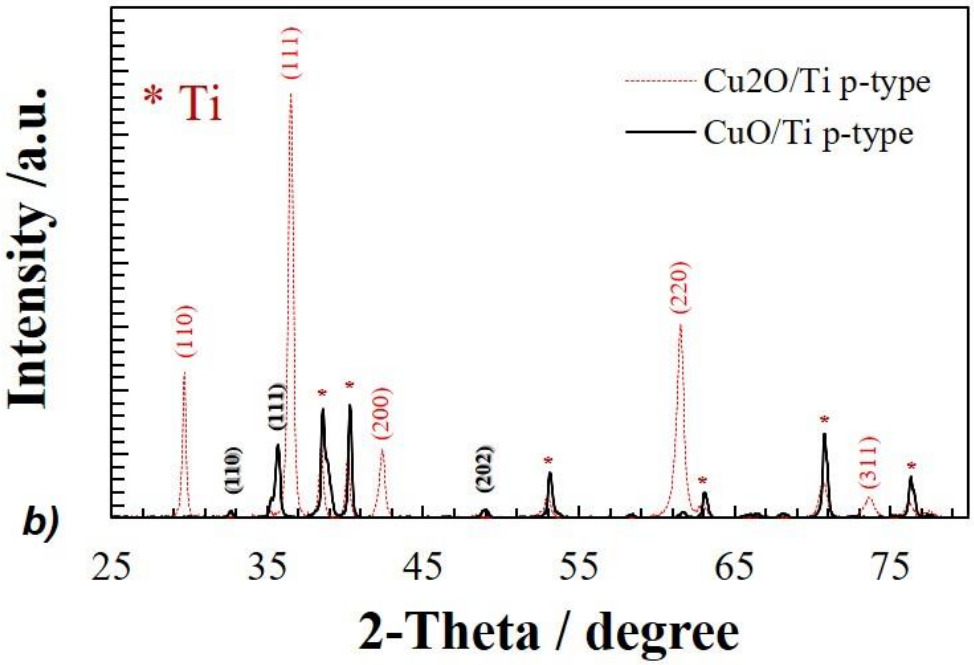
* Ti
Cu2O/Ti p-type
CuO/Ti p-type
Intensity /a.u.
(110)
(111)
(200)
(220)
(110)
(111)
(202)
(311)
b)
25
35
45
55
65
75
2-Theta / degree

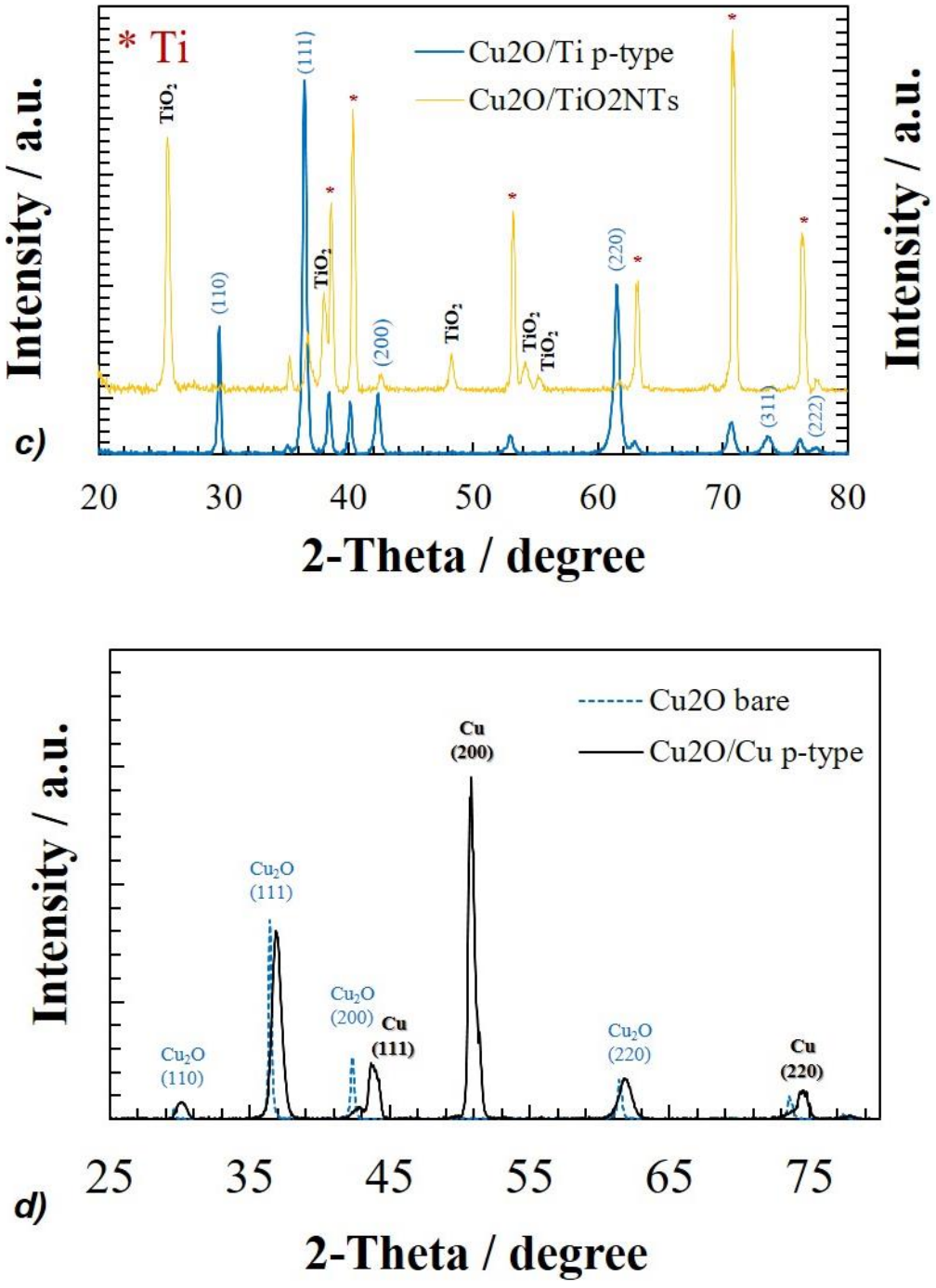

Figure 4.16 *XRD patterns of a) Cu_2O/Ti n-type A and Cu_2O/Ti n-type b and b) Cu_2O/Ti p-type and CuO/Ti p-type.*

Morphological analysis of the samples was performed by a scanning electron microscopy (SEM) using a Phenom ProX Scanning Electron Microscope equipped with an energy-dispersive detector (EDS). The SEM images are reported in Figure 4.17.

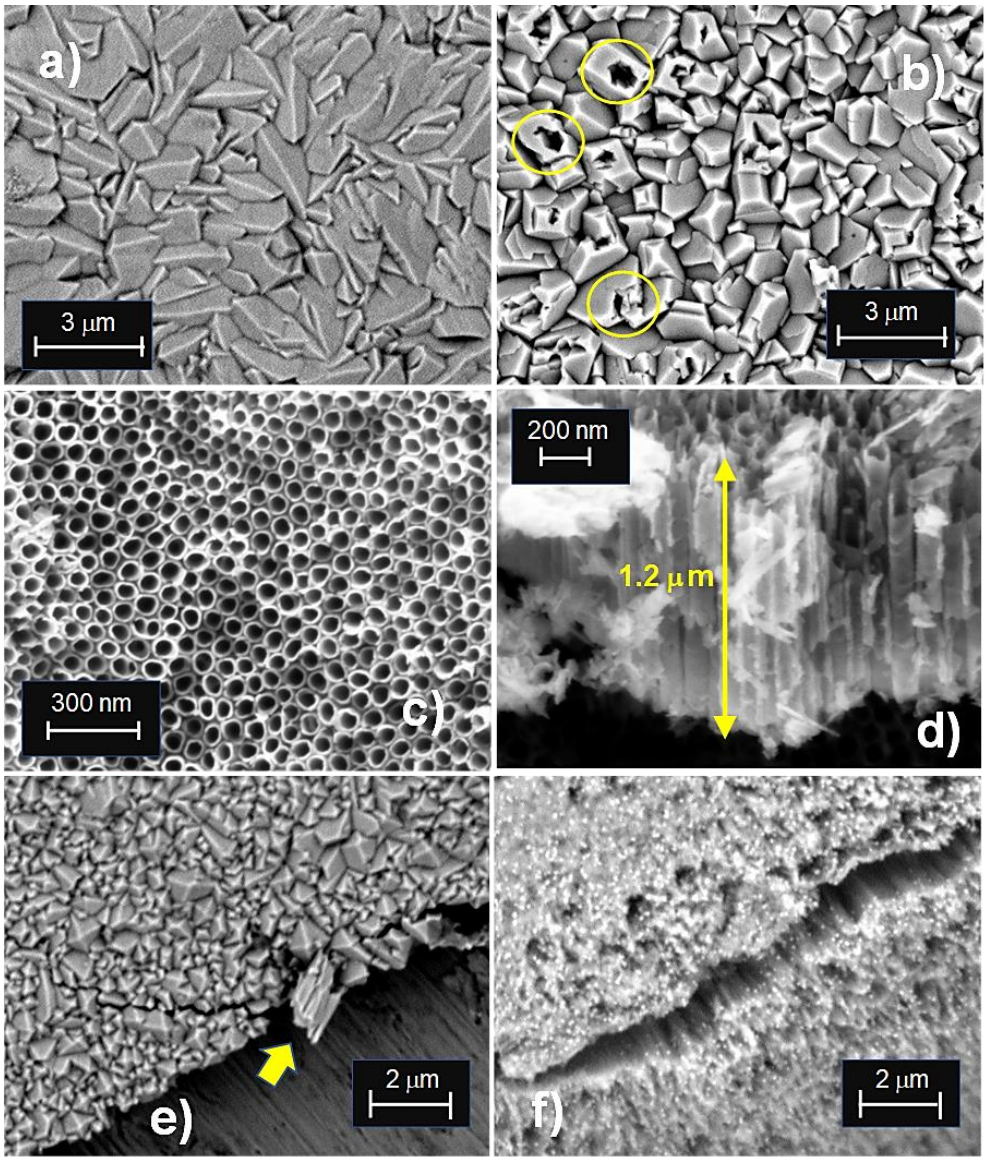

Figure 4.17 *SEM images of a) Cu_2O/Cu p-type; b) Cu_2O/Ti n-typeA; c) TiO_2NTs; d) cross section of nanotubes arrays of the TiO_2NTs sample; e) f) Cu_2O/TiO_2NTs.*

SEM analysis shows how the *Cu_2O/Cu p-type*, obtained through a basic lactate electrolyte based procedure on a Cu metallic support, has a pyramidal-like shape with an edge distribution size of the particles varying from 1.2 to 2.7 μm and a similar morphological pattern can be recognized in the *Cu_2O/Ti p-type*, which was synthesized by the same procedure but on a titanium support; in this case, the particle size ranges from 700 to 900 nm. The SEM image of *Cu_2O/Ti n-typeA*, synthesized in an acidic medium of acetic acid and sodium acetate, shows a similar pattern mentioned above for the other samples, but with the difference that the particles are slightly smaller and a consistent presence of holes are recognized; the latter can be attributed to a mechanical action performed by the H_2 formation side-reaction, which can be more relevant working at acid pH. The SEM image of

TiO_2NTs, prepared by the anodic oxidation of a Ti disk in an ammonium fluoride based electrolyte, shows the presence of a package of ordered arrays of 1D nanotubes, round shaped, with thickness of 8-9 nm and mean diameter of 54 nm. The morphology of *Cu_2O/TiO_2NTs* sample, obtained by the electrodeposition of Cu_2O particles of TiO_2NTs with the same method used for *Cu_2O/Cu p-type*, is shown in Figures 4.17e,f. In presence of TiO_2NTs, the particles size of Cu_2O is smaller with respect to the same deposition on a Cu or Ti substrate, and also the pyramidal-like shape is less evident. All the analyses reported here are related to samples then used for the gas-phase CO_2 photoreduction tests with a monochamber reactor, as it will be described in the next paragraphs.

In Figures 4.18, 4.19, 4.20, the EXD analyses for the sample *Cu_2O/Ti p-type*, *Cu_2O/TiO_2NTs* and CuO/Ti *p*-type are reported. For the *Cu_2O/Ti p-type*, only copper and oxygen atoms were detected with an atomic concentration of 62.7 and 37.3, respectively. For the *Cu_2O/TiO_2NTs*, titanium, oxygen and copper were found with 12.7, 89.9 and 4.4 atomic concentrations. In this case, the higher amount of oxygen is due to its incorporation in TiO_2 and Cu_2O oxides. In the case of *CuO/Ti p-type*, the concentrations of atomic copper, titanium, oxygen were respectively 32, 9.7 and 58.3.

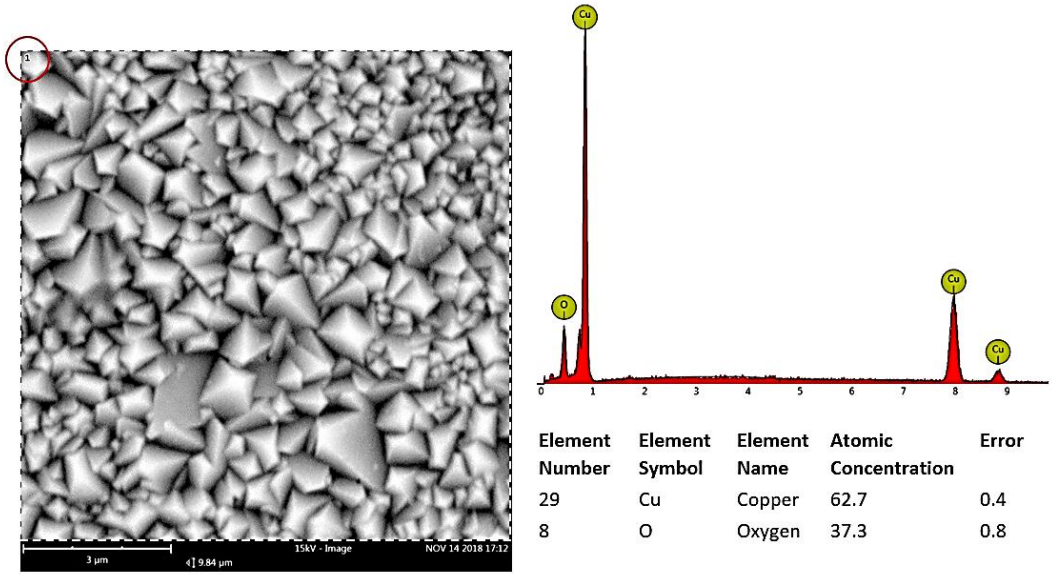

Element Number	Element Symbol	Element Name	Atomic Concentration	Error
29	Cu	Copper	62.7	0.4
8	O	Oxygen	37.3	0.8

Figure 4.18. *EXD Cu_2O/Ti p-type*

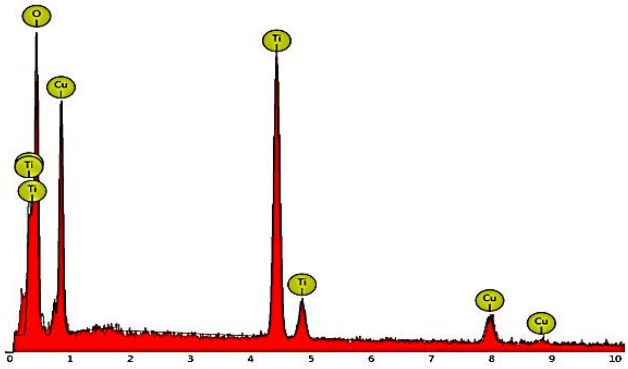

Element Number	Element Symbol	Element Name	Atomic Concentration	Error
22	Ti	Titanium	12.7	0.2
8	O	Oxygen	82.9	1.1
29	Cu	Copper	4.4	0.6

Figure 4.19 *EXD Cu_2O/TiO_2NTs*

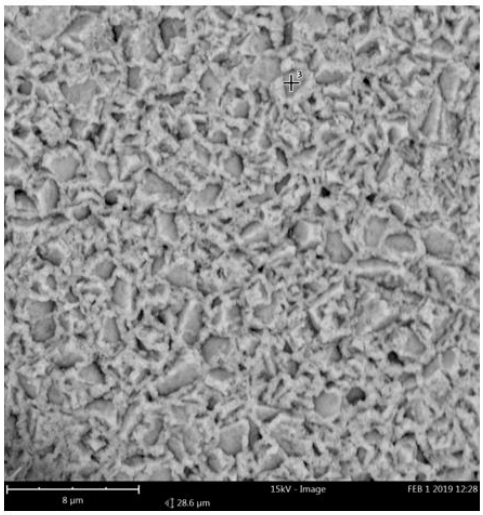

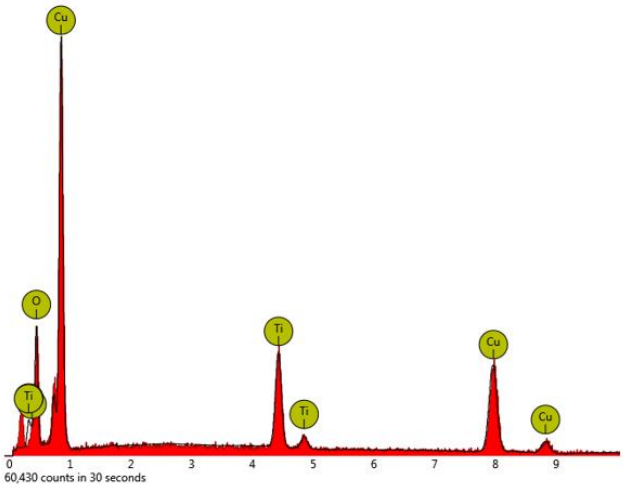

Element Number	Element Symbol	Element Name	Atomic Concentration	Error
29	Cu	Copper	32.0	0.3
22	Ti	Titanium	9.7	0.2
8	O	Oxygen	58.3	0.7

Figure 4.20 *EXD CuO/Ti p-type*

Copper (I)- based catalysts synthesized by a facile wet-precipitation method were also used for preliminary CO_2 photoreduction tests in slurry. Their synthesis will be described in detail in paragraph 5.3.1, as they were also used for CO_2 electrocatalytic reduction (chapter 5) and for glucose amperometric detection

(chapter 6). The characterization of these samples (named as *Cu_2O NC-25* and *NC-60*), is instead reported below.

The presence of Cu (I) in these samples was confirmed by the XRD analysis, aimed to exclude the presence of impurities and to check the presence of their characteristic peaks; the reflection planes present at 29.7°, 36.6°, 42.5°, 52.5°, 61.6°, 73.7° and 77.5° referring to the planes (110), (111), (200), (211), (220), (311) and (222), confirm the presence of cuprous oxide in both the samples, with some differences in the peaks intensity (see Figure 4.21); the peak related to (111) plane results higher in the NC-60. Optical properties were evaluated by a UV-visible Diffuse Reflectance Spectroscopy measuring the spectra in the range of 1200-200 nm and comparing the different catalysts in terms of band-gap through the Tauc plot measure (Figures 4.22a and b). The semiconductor bandgap, in according to the literature, is given by the following formula[31]:

$$\boldsymbol{\alpha h\nu = A\left(h\nu - E_g\right)^{\eta}}$$

where *α, h, ν* represent the absorption coefficient, the Plank constant and the frequency, respectively, and *hν* is the incident photon energy.

In according to the nature of electronic transition, the *n* exponent can take the values 1/2 and 3/2 for direct allowed and forbidden transitions and 2 and 3 for indirect allowed and forbidden transitions. Considering that Cu_2O is a direct bandgap semiconductor, the *n* exponent is assumed to be 1/2 and the E_g can be evaluated using the Tauc Plot, plotting $(\alpha h\nu)^2$ versus *hν* and extrapolating the linear region of the y axis to intercept the abscissa representing the photon energy *hν*. The absorption coefficient was evaluated by the Kubelka-Munk function (K-M), which represents the correlation between the absorption and the reflectance (R) of the sample and can be applied for optically dense systems.

$$\boldsymbol{F = \frac{(1 - R^2)}{2R} \approx \alpha}$$

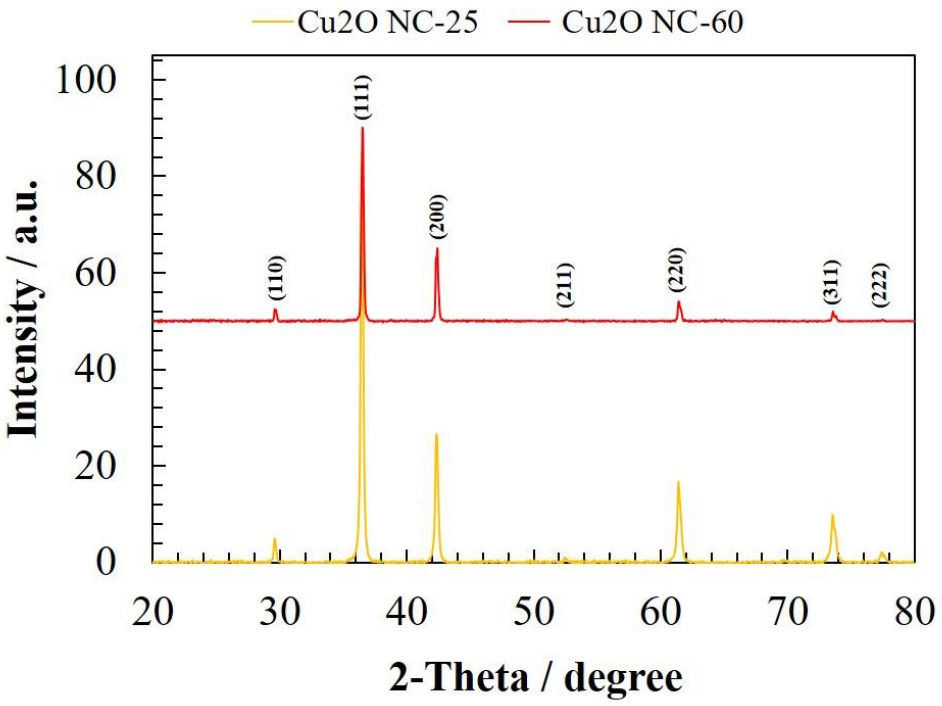

Figure 4.21 *XRD analysis for the samples Cu_2O NC-25 and N-C60.*

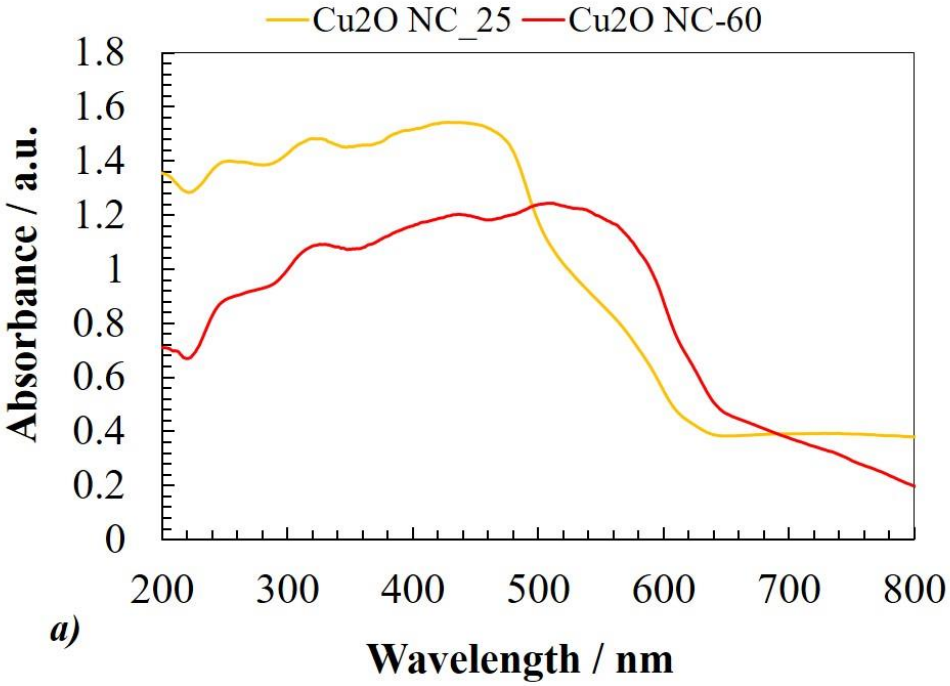

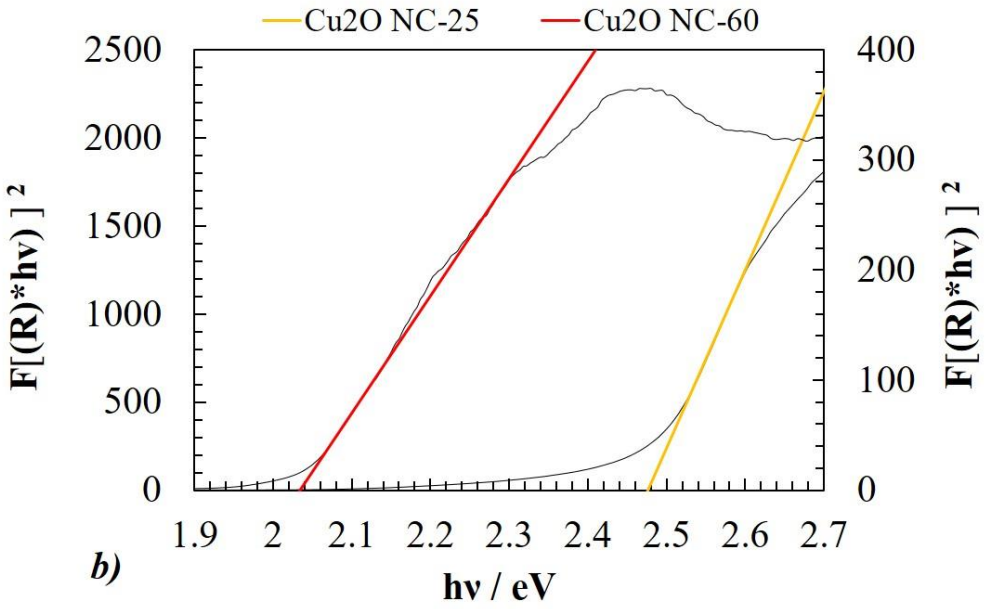

Figure 4.22 a) *UV/vis spectrum and* ***b)*** *Tauc Plot for band gap determination.*

The blue shift of the sample *Cu_2O NC_25* (Eg ≈ 2,47 eV) compared to samples *Cu_2O NC_60* (Eg ≈ 2,03 eV) is due to the smaller particle size causing a quantum confinement size effect[32]. As confirmed by UV-visible spectra and bandgap values calculated through the Tauc plot, the SEM analysis shows that *Cu_2O NC_25* has a particle distribution ranging from 150 nm to 200 nm (Figure 4.23a), whereas *Cu_2O NC_60* from 200 to 900 nm (Figure 4.23b).

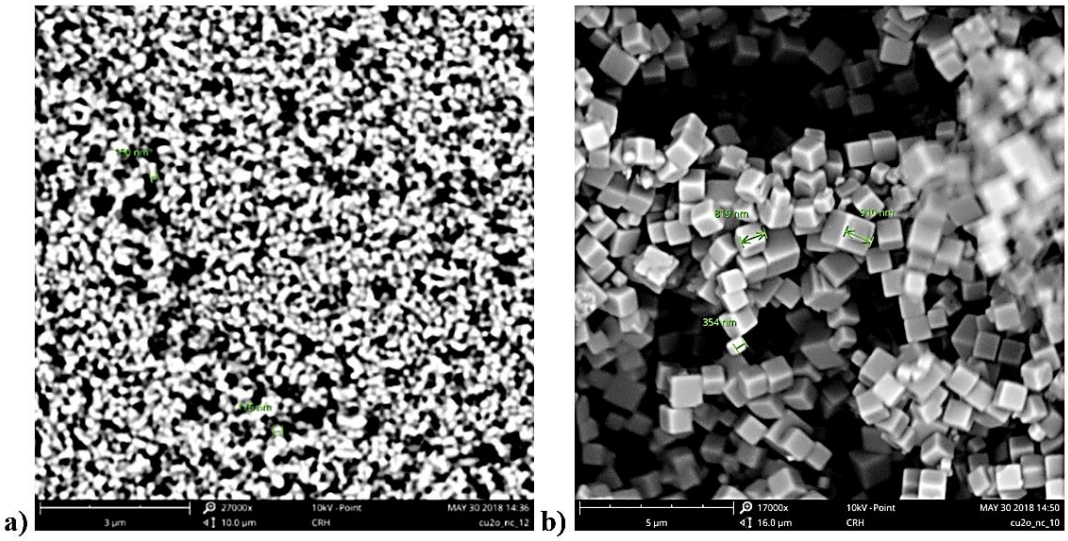

Figure 4.23 *SEM analysis for a) Cu_2O NC-25 and b) Cu_2O NC-60.*

4.3.4 Testing

4.3.4.1 CO_2 reduction in slurry

Initially, we performed some tests using a conventional slurry reactor, as described in the experimental part (see Figure 4.7). The photocatalyst for this kind of reactor must be in the form of a powder in suspension by a magnetic stirring in an aqueous solution. For these tests, we prepared two samples (*Cu_2O NC-25* and *Cu_2O NC-60*) by wet precipitation method, which allowed to synthesise selectively Cu(II) oxides at different particle size depending on temperature used for dissolution of the copper precursor (25 or 60 °C, respectively); this was aimed to decrease the particle size as much as possible (compatibly also the limitations of our characterization techniques). CO_2 photoreduction tests were thus performed in slurry, suspending the *Cu_2O NC-25* (characterized by particles with smaller dimensions, therefore more attractive for photocatalysis) powder under stirring in the reactor flask and flowing CO_2 into the solution under illumination. Specifically, a certain amount of catalyst (i.e. 100 mg) was immersed in 120 mL of a 0.2 M $KHCO_3$ water solution under stirring. The outlet gas phase from the reactor was analysed online through a gas chromatograph, while the liquid phase was sampled during the tests (after 2.5 and 5 hours) and then analysed by ionic chromatography. The tests were performed with a reaction time of 5 hours and lighting was guaranteed by a solar simulator (Lot-Oriel, lamp at Xe, 300 W).

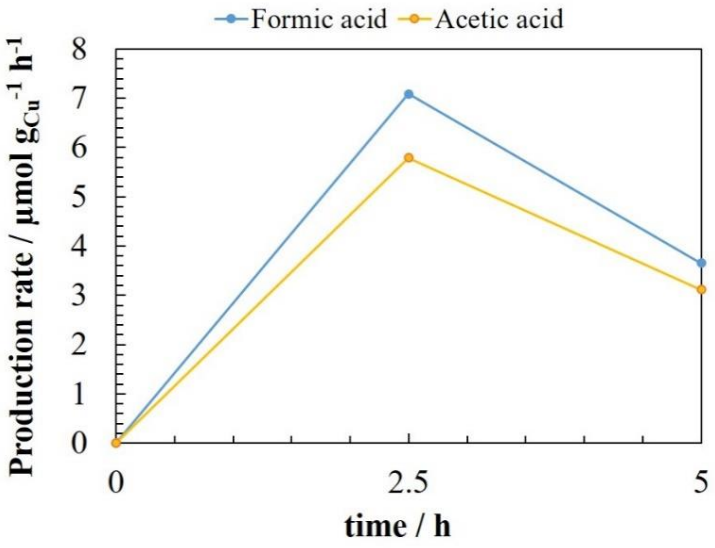

Figure 4.24 *Formic and acetic acid production rates with Cu_2O NC-25 photocatalyst.*

Figure 4.24 reports the production rate (µmol g_{Cu}^{-1} h^{-1}) for the two products detected, namely formic acid and acetic acid. No other products, i.e. gas products or carbon products involving the formation of C-C bond, were detected by using the conventional slurry photoreactor.

It can be observed how both products reach a plateau at 2.5 h and then decrease after 5 hours. The formic acid and acetic acid production rates were 7.1 and 3.6 µmol g_{Cu}^{-1} h^{-1}, respectively, at 2.5 h, and 3.6 and 3.1 µmol g_{Cu}^{-1} h^{-1}, respectively, at 5 h. The catalyst at the end of the reaction was extracted in water, and 1.25 and 1.88 µmol g_{Cu}^{-1} of formic and acetic acid, respectively, were detected from the analysis of the extract. This result shows a major selectivity for the formic acid detected in liquid phase, while the decrease of productivity with time for the two compounds, may be ascribed to competitive reactions involving the two compounds or to a deactivation of the photocatalyst. However, further analysis is needed to confirm these hypotheses. Moreover, a metallic copper catalyst was also tested under the same conditions, and results showed a formic acid production rate of only 0.146 µmol g_{Cu}^{-1} h^{-1}, almost 49 times lower than the production rates over Cu_2O catalyst. This result can be explained with the consideration that metals are not able to provide an efficient charge-carrier separation like semiconductors, making them more interesting in electrochemical applications.

4.3.4.2 CO_2 reduction in the novel gas-phase flow-through reactor

In this section, the results of CO_2 photoreduction reactions, obtained by the new gas-flow through photo-electrocatalytic reactor based on nanomembranes functionalized with copper, will be described. The experiments were carried out by electrodepositing different Cu_xO forms on various microperforated substrates, including nanotubes TiO_2 aligned arrays (grown by anodic oxidation on Ti metal supports); their purpose is to serve as electron collectors and to provide robustness. These nanomembranes therefore represent an integral part of the entire photoreactor. As mentioned in the section "scope of the chapter", the new gas phase photo-reactor shows significant differences compared to conventional reactors, such as PECs or slurry reactors. A stream of vapor saturated with CO_2 passes through the micro-perforations of the substrate and the mesoporosity of the photocatalyst and interacts with the active sites exposed to the illuminated side of

the plate. The high local CO_2 concentration and its low solubility in water (leading to less diffusion limitations in the double layer) cause a distribution of the reaction products, different from what obtained from conventional reactors. Furthermore, a slurry reactor shows the following limitations: i) the active sites of the photocatalyst, stirred in the aqueous media in the form of suspended powders, are not constantly irradiated during the whole reaction; ii) charge recombination phenomena are more frequent, leading to decrease in the photocatalytic yield; iii) larger quantities of photocatalyst are needed. Another difference concerns the fact that a liquid medium dissipates better the heat lowering the temperature of the photocatalyst. In our case, the photocatalyst reaches temperatures of 120 °C (measured with a thermocouple).

Preliminarily, several tests were carried out to confirm that the products obtained solely derived from the photocatalytic reduction of CO_2 and not from other unknown sources of carbon. The apparatus used for photocatalytic reduction tests, using CuO_x-based samples as photocatalysts, is shown in Figure 4.8. This novel photoreactor working in gas phase requires a photocatalyst in the form of a multilayer, quite different from the powders used in conventional slurry photoreactors. As described in the previous paragraphs, electrodeposition technique is very suitable for deposition of semiconductor layer on metallic substrates. Table 4.2 reports the types of catalysts prepared and tested in the flow-through photoreactor.

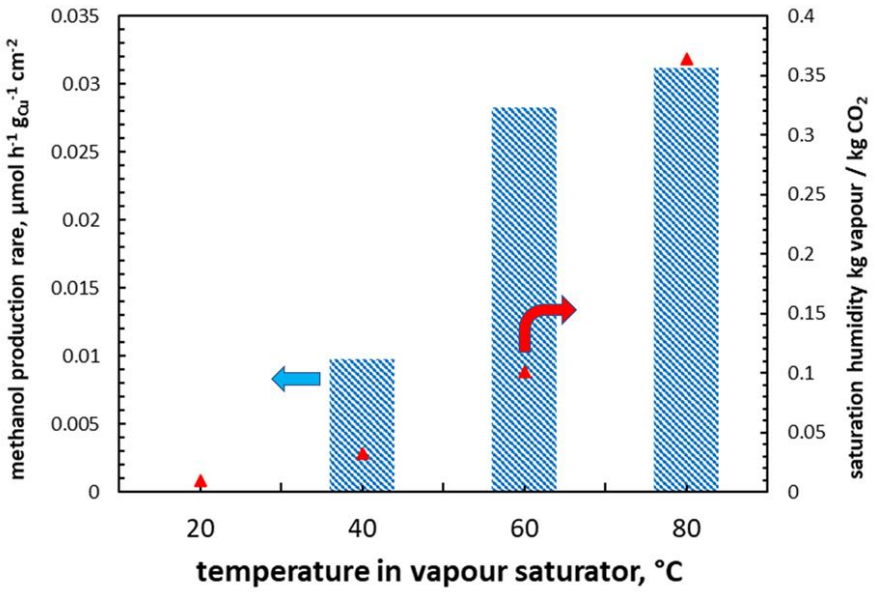

Figure 4.25 *Methanol production rate and saturation humidity (inlet gas flow) vs. vapour saturator temperature for Cu_2O/Ti p-type catalyst.*

Before starting the photocatalytic test, it was evaluated how the saturation humidity (kg vapour/kg CO_2) and the temperature of the vapour saturator can affect the productivity (Figure 4.25). Considering as the reference one of the main reaction products in the tests (i.e. methanol), it can be observed that at 20 °C it is only present in traces. A maximum production rate of methanol is instead obtained at 80 °C (0.0312 µmol h^{-1} g_{Cu}^{-1} cm^{-2}). Considering that this value is slightly higher than that obtained at 60 °C (0.0283 µmol h^{-1} g_{Cu}^{-1} cm^{-2}), all the tests were therefore carried out with a saturator temperature of 60 °C to avoid problems deriving from the instability of the photocatalytic setup.

Table 4.3 shows the results of the various tests in terms of apparent turnover-frequency – TOF (per cm^2 of exposed surface area) as µmol of products formed per atoms of Cu. Taking into account that the number of active sites does not correspond to the number of Cu atoms, this is only an apparent TOF, and it allows comparing different catalysts containing different amount of copper.

Acronym	*Substrate **	*Electrodeposited copper*	*Intermediate titania film #*	*Semiconductor type*
Cu_2O/Ti p-type	Ti	Cu_2O	-	p
Cu_2O/Cu p-type	Cu	Cu_2O	-	p
Cu_2O/Ti n-type A	Ti	Cu_2O	-	n
CuO/Ti p-type	Ti	Cu_2O, then annealing 450°C	-	p
Cu_2O/Ti n-type B	Ti	Cu_2O, then annealing 250°C	-	n
TiO_2 NTs/Ti	Ti	-	NT	n
Cu_2O/TiO_2 NTs/Ti p-n	Ti	Cu_2O	NT	p (Cu_2O), n TiO_2 NTs

* microperforated metallic foil
# NT: ordered arrays of vertically-aligned TiO_2 nanotubes made by anodic oxidation.

Table 4.2 *List of the photocatalysts tested in CO_2 photoreduction and their acronyms.*

	TOF, µmol·mol_{Cu}^{-1}·h^{-1}·cm^{-2}				
	Cu_2O/Ti p-type	**Cu_2O/Cu p-type**	**Cu_2O/Ti n-typeB**	**CuO/Ti p-type**	**Cu_2O/TiO_2NTs p-n junction**
methanol	4.0	5.6	80.8	20.0	1390.8
formic acid	4.2	4.4	40.5	-	3.2
methyl formate	0.7	0.9	9.9	23.5	0.7
acetic acid	1.4	1.6	36.1	41.7	7.6
oxalic acid	5.7	4.4	40.5	13.8	3.3
ethanol	-	-	39.2	-	-
isopropanol	-	-	3.5	0.7	-

Table 4.3 *Apparent TOF for CuOx based catalysts.*

Methanol, oxalic acid and formic acid were the main products for *Cu_2O/Cu p-type and Cu_2O/Ti p-type* catalysts, which also showed very low TOF numbers. While the formation of methanol and formic acid is relatively well-known in the literature for CO_2 photoreduction, the oxalic acid has been less commonly detected. One hypothesis to explain the mechanism is the activation of two formic acid molecules and their dehydrogenative coupling[33]. Acetic acid and methyl formate were also detected, although in small amounts, as CO_2 photoreduction products. Acetic acid mechanism formation can be explained assuming that the -CH_3 adsorbed species, the presence of which is favourite at high CO_2 concentrations, react with the radical CO_2^{-}• generated in the first step of CO_2 photoreduction. In these tests, the local high concentration of CO_2 is guaranteed by the novel design of the photoreactor working in gas phase and having a pure CO_2 flow directly through the photocatalytic nanomembrane.

The *Cu_2O/Cu p-type* sample was the only catalyst providing amounts of CH_4, even if only in traces, the formation of which can be justified by the metallic copper acting both as support and co-catalyst. *Cu_2O/Ti n-typeB* and *CuO/Ti p-type* samples provided a photoreduction rate more than one order of magnitude higher with respect of *p-type Cu_2O* sample. *Cu_2O/Ti n-typeB* if compared to *Cu_2O/Ti p-type*, showed new products like isopropanol and ethanol were detected. Acetic acid becomes the major product when Cu_2O is replaced with CuO (see *CuO/Ti p-type vs Cu_2O/Ti p-type)* and this also causes an increasing in the methyl formate production, while ethanol and formic acid were not detected. In Figure 4.26 is reported the Faradaic Efficiency (FE, left axis) for every catalyst deposited over metallic substrates, taking in account the number of electrons needed for every reaction (2 for formic acid and oxalic acid, 6 for methanol, 8 for acetic acid and methyl formate, 12 for methanol and 18 for isopropanol); in the same Figure, in the right axis the ratio between the sum of C2+C3 products FE and the sum of C1 products FE and the Coulombs per hour, normalized for cm^2 of photoelectrode and moles of copper, are reported.

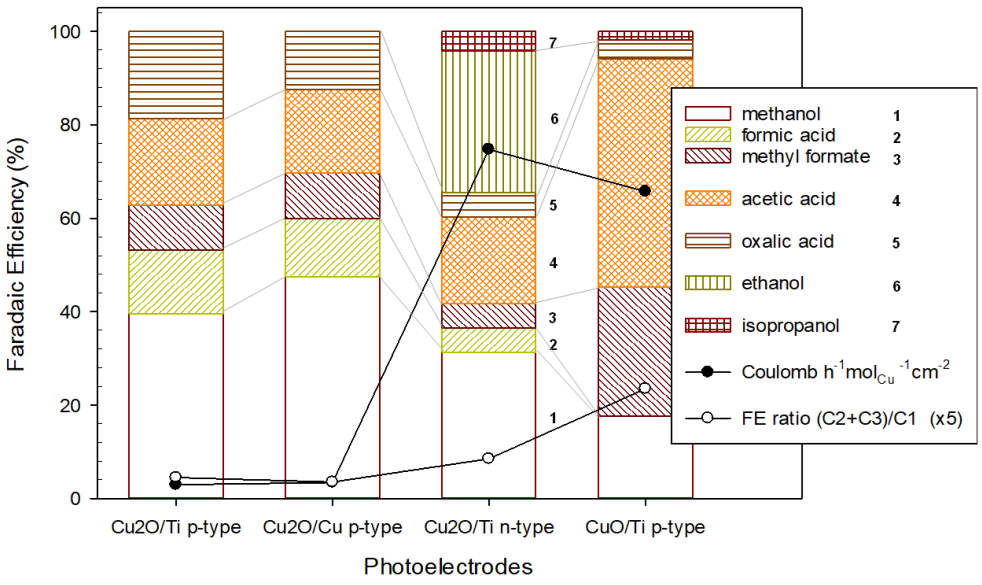

Figure 4.26 *Faradaic Efficiency (FE) to different products, ratio of the Sum of C2-C3 FE products and the sum of C1 FE products and Coulomb per hour (normalized per moles of Cu and cm^2 exposed area).*

As showed in Figure 4.26, the sample *Cu_2O/Ti n-typeB* was recognized as the catalyst providing the maximum photocurrent (Coulomb/h converted to chemicals), leading to the longer carbon chain among the others, while the *Cu_2O/Ti p-type* and *Cu_2O/Cu p-type* showed low photocurrents and the lowest (C2+C3)/C1 ratio, lower than 1. Replacing Cu_2O with CuO allowed to obtain the highest acetic acid and methyl formate FE, both involving 8 electrons. A FE of about 20% to oxalic acid was obtained with the Cu_2O/Ti photoelectrode, while a FE of nearly 50% to methanol (the highest) was obtained with the *Cu_2O/Cu p-type*. Products like CH_4 and CO, most commonly observed in the most of the photocatalytic tests reported in literature, are here absent or present in traces in some cases; this can be related to the different adsorbed population on the catalyst surface, due to the fact that in this case CO_2 diffusion to the surface of the photocatalyst is not limited by the competition of water chemisorption and by the presence of a double layer. These aspects are due to the novel configuration of the gas-phase photoreactor, indicating that the same photocatalyst can provide different reduction products with different production rates if processed in a device with a novel design quite different from a conventional slurry photoreactor.

Moreover, these results show how the nature of copper and the presence of different heterojunctions, may affect the product distribution in CO_2 reduction. To prove how the support can influence the catalytic behaviour, Cu_2O was also deposited over a thin oxide layer (thickness of 1.2 μm) of ordered arrays of TiO_2 NTs, obtained by

anodic oxidation of a Ti substrate, as described in the experimental part. In Figure 4.27, the behaviours of *$Cu_2O/TiO_2NTs/Ti$ (p-n type)* and bare *TiO_2NTs/Ti* (without copper deposition), and in addition the most active catalyst of Figure 4.26 (*Cu_2O/Ti n-typeB*), are compared. Considering that in the case of the *TiO_2NTs/Ti* no copper was deposited, the results were here normalized per mg of catalyst instead of copper moles.

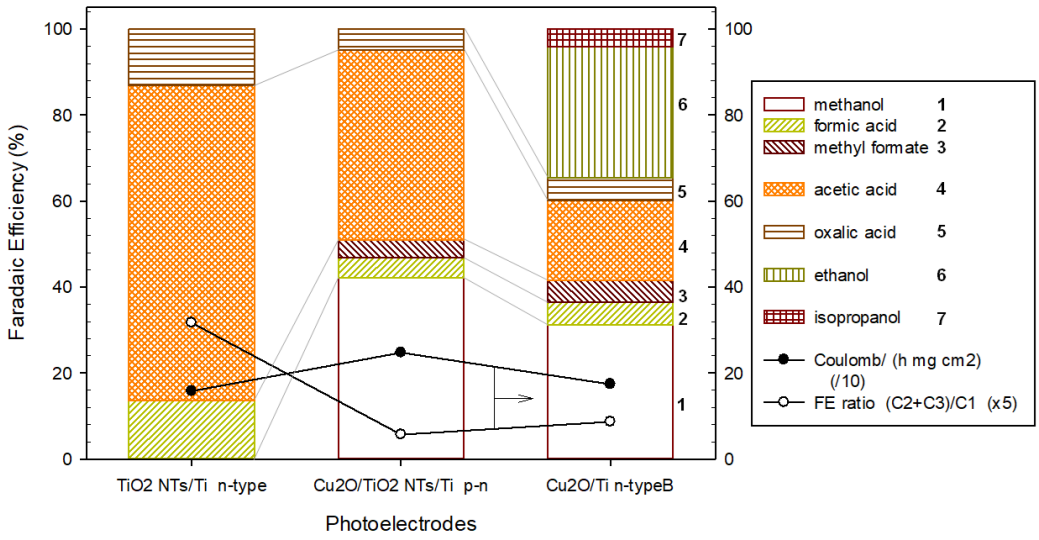

Figure 4.27 *Faradaic Efficiency (FE) to different products, ratio of the sum of C2-C3 FE products and the sum of C1 FE products and Coulomb per hour (normalized to moles Cu and cm^2 exposed area).*

In the case of *$Cu_2O/TiO_2NTs/Ti$ (p-n type)*, the activity should be considered approximately as the sum of the *Cu_2O/Ti n-type* and *Ti_2O NTs/Ti n-type* activities, taking in account about 15% light absorption drop in the titania when the Cu_2O is deposited over in (as shown in the photocurrent test, see Figure 4.13). Using the bare *TiO_2NTs/Ti* catalyst, only carboxylic acids were detected with a selectivity of about 100% to these products; a FE of about 73% was detected for acetic acid, and 13 and 14% for formic acid and oxalic acid, respectively. Considering that formic acid is the only C1 product obtained, it can be observed that the FE to >C1 products resulted 6 times higher than the FE to C1. Formation of methanol and methyl formate is instead observed when the *Cu_2O* is deposited over the TiO_2NTs; it is to take into account that methyl formate formation does not involve any C-C bond formation, as it only derives from coupling of C1 products, e.g. from the reaction of formaldehyde with methanol, the first obtained by oxidative dehydrogenation of methanol.

Figure 4.28 shows a hypothesis of a mechanism for the formation of formic acid, acetic acid and methanol for the Cu_xO-TNT samples. It is hypothesized how acetic acid is formed by reaction of the -CH_3 surface groups and the $CO_2^{-\cdot}$ radical anion, while methanol is formed by reduction of the -CH_2O^- groups, obtained by following reductions starting from -CO_2^- intermediate.

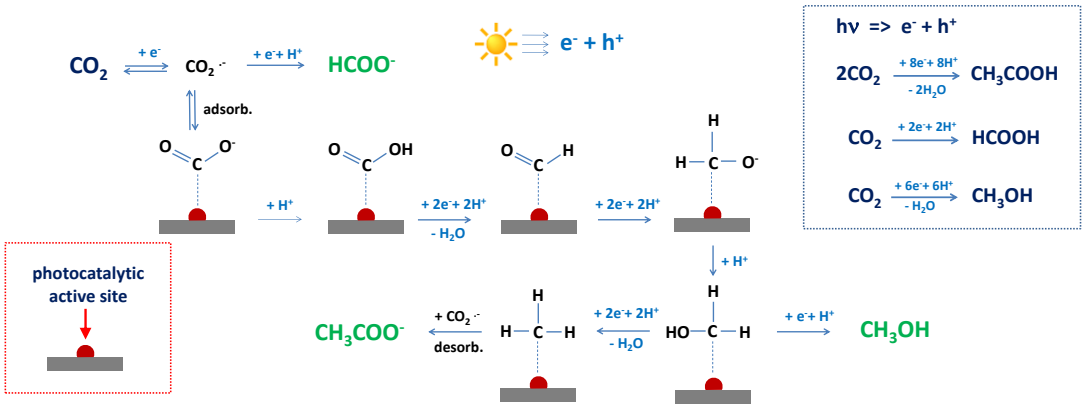

Figure 4.28 *Proposed formation mechanisms for acetic acid, formic acid and methanol on the Cu_xO-TNT samples.*

Methanol and methyl formate were also detected with Cu_2O/Ti photocatalysts, evidencing how their formation is related to the presence of copper oxide, while isopropanol and ethanol were only detected with the catalyst *Cu_2O/Ti n-typeB*, thus they are peculiar for this sample. If we exclude these two products, we can notice how the product distribution for *$Cu_2O/TiO_2NTs/Ti$* is a combination of *Cu_2O/Ti n-type* and *Ti_2ONTs/Ti n-type* distributions, as showed before. To explain these results, it is useful to take into account the *n*-type semiconductor/interface transfer charge mechanism, in which the photogenerated holes, moving toward the electrode interface, oxidize both the species adsorbed on the catalyst surface and water. One hypothetical mechanism to describe what happens at the photocatalyst surface is something similar to a short-circuit in which both the photogenerated electrons and holes act like in a micro electrochemical cell, catalysing the reduction and oxidation of the carbon species, respectively.

The *Cu_2O/Ti n-typeB* sample was the only *n*-type catalyst providing the formation of ethanol, while *Cu_2O/Ti n-typeB* an *CuO/Ti p-type* samples, which are the only containing Cu(II), led to the formation of isopropanol.

The *$Cu_2O/TiO_2NTs/Ti$* obtained through the electrodeposition of *p*-type Cu_2O on the *n*-type TiO_2 nanotubes, provided the best photoreduction performances and this

effect is due to the creation of a *p-n* heterojunction, which modifies the optical and photocatalytic properties of the catalyst.

In Figure 4.29, a model for the titania nanotubes (TNT) and Cu_2O bands structure and their relative energy levels are proposed; the energy levels for the two reactions involved, namely the formation of methanol by reduction of CO_2 (E_{CO_2/CH_3OH}) and OH^- from O_2 (E_{O_2/OH^-}) are showed. The TNT sample (*n*-type semiconductor) has a Fermi energy level (E_F) close to its conduction band (CB), while the Cu_2O sample (*p*-type semiconductor) has a (E_F) close to its valence band (VB). When the two materials are placed in contact, their E_F lines go up together with the E_F of the electrons involved in the reactions. Whereas the described reactions must occur simultaneously, this can be calculated as $(E_{CO_2/CH_3OH} + E_{OH^-/O_2})/2$.

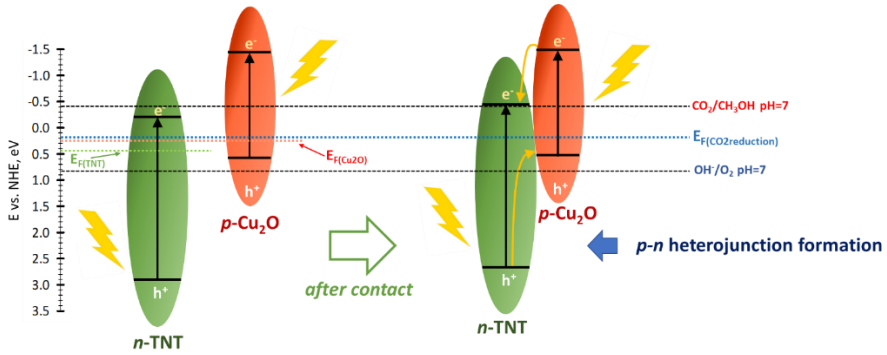

Figure 4.29 *Proposed interaction of Cu_2O and TNT bands, with p-n heterojunction formation.*

Methanol, with a production rate of 71.0 μmol g_{Cu}^{-1} h^{-1}, was the main product, followed by acetic and oxalic acid with 55.8 and 24.4 μmol g_{Cu}^{-1} h^{-1}, respectively. The apparent quantum yield (AQY - ratio between electrons reacted and photons absorbed) was estimated as 21.5% for the *Cu_2O/TiO_2NTs* catalyst and this can be considered as one of the higher AQY for the production of methanol and acetic acid ever reported fore CO_2 photoreduction. It is well known that the methanol yield can be improved by adding OH^- ions in the photocatalytic suspension, because they improve the CO_2 dissolution and act like hole-scavengers, favouring the oxidation reactions. With water as the suspension medium, like in CO_2 photoreduction, this effect is less relevant because of the lower OH^- concentration.

4.4 CONCLUSION

By the electrodeposition technique, *p*- and *n*-type Cu_xO based catalysts were prepared depositing them on different metallic substrates like Ti, Cu discs and ordered TiO_2 nanotube arrays (TiO_2NTs), and testing them in CO_2 photoreduction.

By the SEM analysis, a pyramidal-like shape structure for Cu_2O-based catalysts was observed, with a particle size ranging from 1.2 to 2.7 μm; in some cases, the presence of holes was detected, depending on the synthetic procedure adopted. About the Cu_2O/TiO_2NT sample obtained through the deposition of *p*-type Cu_2O on the *n*-type TiO_2NTs, it was noticed how Cu_2O, characterized by a particle size ranging from 0.1-0.5 μm, covered homogeneously the top surface of the nanotubes. The TiO_2NTs sample (prepared by anodic oxidation of a Ti foil) showed TiO_2 nanotube arrays with a length of 1.2 μm, corresponding to the oxide thickness.

Linear sweep voltammetry (LSV) and chronoamperometry (CA) measurements were performed to characterize the catalysts in terms of photo-response, in order to investigate the semiconductor nature (*p* or *n*-type) under ON/OFF light pulsations. The Cu_2O/Ti *n*-typeA, prepared in acidic solution, shifted his behaviour from mixed *n*-/*p*-type to totally *n*-type when annealed at 250°C (Cu_2O/Ti *n*-typeB) while turned to p-type when annealed at 450°C (CuO/Ti p-type). In this case, in fact, a CuO phase with different characteristics was synthesized, as confirmed by XRD analysis. The Cu_2O/TiO_2NT/Ti *p*-*n* sample showed a *n*-type behaviour with an increment of the cathodic current of 1.8 mA cm^{-2} under illumination with respect to dark. The higher increment of the photocurrent in the visible region of the spectrum with respect to the bare TiO_2NT, as well as the absorption shifted to the visible light zone with an absorption peak at 500 nm and a maximum at 450 nm (as confirmed by the UV/visible analysis) suggest the formation of a *p*-*n* junction between the *p*-type Cu_2O and n-type TiO_2 layer. The band gap of 3.2 eV of TiO_2 shifted to around 2.0 eV when coupled with the Cu_2O. The CO_2 photocatalytic tests were carried out in a novel compact homemade flow-through photoreactor operating in gas phase. The CO_2/H_2O flow was forced to cross the catalyst, due to the presence of small holes in the metallic substrate and the mesoporosity of Cu_2O and TiO_2NTs photocatalysts. This novel design of the photoreactor allowed to minimize the presence of adsorbed water on the catalyst surface, as usually occurs in conventional slurry photoreactors working in liquid/solid interface mode.

By processing the *$Cu_2O/TiO_2NT/Ti$ p-n* sample, the detected products were methanol, acetic acid and oxalic acid. For the acetic acid, a Faradaic efficiency (FE) of 44% was calculated, which is the highest FE ever reported in our knowledge. The apparent quantum yield (AQY) was equal to 21.5% for CO_2 reduction to methanol and acetic acid, also one of the highest reported, while the irradiance was measured as 135 mW cm^{-2}. Considering that: i) coupling of *p*-type Cu_2O and *n*-type TiO_2NT allowed the formation of actives site for the selective reduction to more value added products, ii) these reactions were carried out at room temperature and atmospheric pressure and without the addition of OH^- scavengers and in the absence of H_2 due to side-reactions, we can conclude that these results are quite appealing and interesting for future developments in CO_2 photocatalytic topic. In our experimental conditions, the products distribution was very different with respect to mostly of works reported in literature, and there are some explanations that can justify this. As it was highlighted in this chapter, the outlet gas stream from the reactor was sent before to a diluted cold trap made of diluted sulfuric acid (0.001M), to capture methyl formate, alcohols and carboxylic acids and after analysed to detect the non-condensable products (like CH_4, CO, H_2 and light hydrocarbons). Furthermore, the catalyst after reaction was treated by soaking for about 15 min with some drops of sulfuric acid (0.001M) and then washing a defined amount of water, to extract carbon based compounds remained adsorbed on the catalytic surface.

The formation of C2-C3 products can be explained by the fact that in our system no aqueous solution was present, and the presence of a low water partial pressure in the CO_2 flow (nearly 4% water concentration), caused a high local adsorbed concentration of CO_2, which does not result limited by the solubility in water and minimizing all the reaction that involves high levels of H* coverage. Another interesting aspect is the role of copper in the photocatalytic CO_2 reduction. The experiments presented in this chapter showed how alcohols, like methanol and derived products (i.e. methyl formate) formed only in presence of copper while the TOF to methanol is dependent from the catalyst preparation, showing a relationship with the photocurrent. The sum of methyl formate and methanol FE resulted about 50% for Cu_2O deposited on Cu and Ti, while 40% when deposited on *TiO_2 NTs/Ti n-type* or in the case of *CuO/Ti p-type*, which provided higher selectivity for methyl formate over methanol. In the case of *CuO/Ti p-type*, the higher redox properties of Cu^{2+} with respect of Cu^+ can favour the methyl formate path instead of methanol,

justifying also the formation of acetic acid. For the *Cu_2O/TiO_2 NTs/Ti p-n*, the lower methanol FE can be explained by the formation of other products like ethanol and isopropanol and this can be addressed to the presence of different interfacial sites that enable different reaction paths. The formation of a *p-n* junction can be relevant to understand this behaviour, but further investigations are needed to confirm this hypothesis.

4.5 REFERENCES

1) Mao, J.; Li, K.; Peng, T. Recent Advances in the Photocatalytic CO_2 Reduction over Semiconductors. *Catalysis Science and Technology*. **October 2013**, pp 2481–2498. https://doi.org/10.1039/c3cy00345k.

2) Aurian-Blajeni, B.; Halmannjf, M.; Manassen, J. Photoreduction of Carbon Dioxide and Water into Formaldehyde and Methanol on Semiconductor Materials. *Solar Energy* **1980**, 25 (2), 165–170.

3) Zhang, L.; Wang, W.; Wang, H.; Ma, X.; Bian, Z. Design of Inorganic–Organic Hybrid Photocatalytic Systems for Enhanced CO_2 Reduction under Visible Light. *Chemical Engineering Science* **2019**, 207, 1246–1255. https://doi.org/10.1016/j.ces.2019.07.049.

4) L.; Xu, S. M.; Wang, Z.; Xu, Y.; Wang, X.; Hao, X.; Bai, S.; Ning, C.; Wang, Y.; Zhang, W.; Jo, Y. K.; Hwang, S. J.; Cao, X.; Zheng, X.; Yan, H.; Zhao, Y.; Duan, H.; Song, Y. F. Highly Selective Photoreduction of CO_2 with Suppressing H_2 Evolution over Monolayer Layered Double Hydroxide under Irradiation above 600 Nm. *Angewandte Chemie - International Edition* **2019**, 58 (34), 11860–11867. https://doi.org/10.1002/anie.201904246.

5) Moustakas, N. G.; Strunk, J. Photocatalytic CO_2 Reduction on TiO_2-Based Materials under Controlled Reaction Conditions: Systematic Insights from a Literature Study. *Chemistry - A European Journal* **2018**, 24 (49), 12739–12746. https://doi.org/10.1002/chem.201706178.

6) Abdullah, H.; Khan, M. M. R.; Ong, H. R.; Yaakob, Z. Modified TiO_2 Photocatalyst for CO_2 Photocatalytic Reduction: An Overview. *Journal of CO_2 Utilization*. Elsevier Ltd December 1, **2017**, pp 15–32. https://doi.org/10.1016/j.jcou.2017.08.004.

7) al Jitan, S.; Palmisano, G.; Garlisi, C. Synthesis and Surface Modification of TiO_2-Based Photocatalysts for the Conversion of CO_2. *Catalysts. MDPI AG February 1*, **2020**. https://doi.org/10.3390/catal10020227.

8) Shehzad, N.; Tahir, M.; Johari, K.; Murugesan, T.; Hussain, M. A Critical Review on TiO_2 Based Photocatalytic CO_2 Reduction System: Strategies to Improve Efficiency. *Journal of CO_2 Utilization*. Elsevier Ltd July 1, **2018**, pp 98–122. https://doi.org/10.1016/j.jcou.2018.04.026.

9) Bi, F.; Ehsan, M. F.; Liu, W.; He, T. Visible-Light Photocatalytic Conversion of Carbon Dioxide into Methane Using Cu_2O/TiO_2 Hollow Nanospheres. *Chinese Journal of Chemistry* **2015**, 33 (1), 112–118. https://doi.org/10.1002/cjoc.201400476.

10) Singh, M.; Jampaiah, D.; Kandjani, A. E.; Sabri, Y. M.; della Gaspera, E.; Reineck, P.; Judd, M.; Langley, J.; Cox, N.; van Embden, J.; Mayes, E. L. H.; Gibson, B. C.; Bhargava, S. K.; Ramanathan, R.; Bansal, V. Oxygen-Deficient Photostable Cu_2O for Enhanced Visible Light Photocatalytic Activity. *Nanoscale* **2018**, 10 (13), 6039–6050. https://doi.org/10.1039/c7nr08388b.

11) Zheng, Z.; Huang, B.; Wang, Z.; Guo, M.; Qin, X.; Zhang, X.; Wang, P.; Dai, Y. Crystal Faces of Cu_2O and Their Stabilities in Photocatalytic Reactions. *Journal of Physical Chemistry C* **2009**, 113 (32), 14448–14453. https://doi.org/10.1021/jp904198d.

12) Ovcharov, M. L.; Mishura, A. M.; Shcherban, N. D.; Filonenko, S. M.; Granchak, V. M. Photocatalytic Reduction of CO_2 Using Nanostructured Cu_2O with Foam-like Structure. *Solar Energy* **2016**, 139, 452–457. https://doi.org/10.1016/j.solener.2016.10.010.

13) Handoko, A. D.; Tang, J. Controllable Proton and CO_2 Photoreduction over Cu_2O with Various Morphologies. In *International Journal of Hydrogen Energy*; **2013**; Vol. 38, pp 13017–13022. https://doi.org/10.1016/j.ijhydene.2013.03.128.

14) Ovcharov, M. L.; Mishura, A. M.; Shcherban, N. D.; Filonenko, S. M.; Granchak, V. M. Photocatalytic Reduction of CO_2 Using Nanostructured Cu_2O with Foam-like Structure. *Solar Energy* **2016**, 139, 452–457. https://doi.org/10.1016/j.solener.2016.10.010.

15) Wei, T.; Zhu, Y. N.; An, X.; Liu, L. M.; Cao, X.; Liu, H.; Qu, J. Defect Modulation of Z-Scheme TiO_2/Cu_2O Photocatalysts for Durable Water Splitting. *ACS Catalysis* **2019**, 9 (9), 8346–8354. https://doi.org/10.1021/acscatal.9b01786.

16) Aguirre, M. E.; Zhou, R.; Eugene, A. J.; Guzman, M. I.; Grela, M. A. Cu_2O/TiO_2 Heterostructures for CO_2 Reduction through a Direct Z-Scheme: Protecting Cu_2O from Photocorrosion. *Applied Catalysis B: Environmental* **2017**, 217, 485–493. https://doi.org/10.1016/j.apcatb.2017.05.058.

17) Galli, F.; Compagnoni, M.; Vitali, D.; Pirola, C.; Bianchi, C. L.; Villa, A.; Prati, L.; Rossetti, I. CO_2 Photoreduction at High Pressure to Both Gas and Liquid Products over Titanium Dioxide. *Applied Catalysis B: Environmental* **2017**, 200, 386–391. https://doi.org/10.1016/j.apcatb.2016.07.038.

18) Varela, A. S.; Kroschel, M.; Reier, T.; Strasser, P. Controlling the Selectivity of CO_2 Electroreduction on Copper: The Effect of the Electrolyte Concentration and the Importance of the Local pH. *Catalysis Today* **2016**, 260, 8–13. https://doi.org/10.1016/j.cattod.2015.06.009.

19) Song, J. T.; Song, H.; Kim, B.; Oh, J. Towards Higher Rate Electrochemical CO_2 Conversion: From Liquid-Phase to Gas-Phase Systems. *Catalysts. MDPI AG* March 1, **2019**. https://doi.org/10.3390/catal9030224.

20) Olivo, A.; Ghedini, E.; Signoretto, M.; Compagnoni, M.; Rossetti, I. Liquid vs. Gas Phase CO_2 Photoreduction Process: Which Is the Effect of the Reaction Medium? *Energies* **2017**, 10 (9), 1–14. https://doi.org/10.3390/en10091394.

21) Asai, Y.; Katsuragi, H.; Kita, K.; Tsubomura, T.; Yamazaki, Y. Photocatalytic CO_2 Reduction Using Metal Complexes in Various Ionic Liquids. *Dalton Transactions* **2020**, 49 (14), 4277–4292. https://doi.org/10.1039/c9dt04689e.

22) Gao, Y.; Qian, K.; Xu, B.; Li, Z.; Zheng, J.; Zhao, S.; Ding, F.; Sun, Y.; Xu, Z. Recent Advances in Visible-Light-Driven Conversion of CO_2 by Photocatalysts into Fuels or Value-Added Chemicals. *Carbon Resources Conversion* **2020**, 3 (February), 46–59. https://doi.org/10.1016/j.crcon.2020.02.003.

23) Olivo, A.; Trevisan, V.; Ghedini, E.; Pinna, F.; Bianchi, C. L.; Naldoni, A.; Cruciani, G.; Signoretto, M. CO_2 Photoreduction with Water: Catalyst and Process Investigation. *Journal of CO_2 Utilization* **2015**, 12, 86–94. https://doi.org/10.1016/j.jcou.2015.06.001.

24) Giusi, D.; Ampelli, C.; Genovese, C.; Perathoner, S.; Centi, G. A Novel Gas Flow-through Photocatalytic Reactor Based on Copper-Functionalized Nanomembranes for the Photoreduction of CO_2 to C1-C2 Carboxylic Acids and C1-C3 Alcohols. *Chemical Engineering Journal* **2020**, 127250. https://doi.org/10.1016/j.cej.2020.127250.

25) Li, C.; Wang, T.; Liu, B.; Chen, M.; Li, A.; Zhang, G.; Du, M.; Wang, H.; Liu, S. F.; Gong, J. Photoelectrochemical CO_2 Reduction to Adjustable Syngas on Grain-Boundary-Mediated a-Si/TiO_2/Au Photocathodes with Low Onset Potentials. *Energy and Environmental Science* **2019**, 12 (3), 923–928. https://doi.org/10.1039/c8ee02768d.

26) Chu, S.; Ou, P.; Ghamari, P.; Vanka, S.; Zhou, B.; Shih, I.; Song, J.; Mi, Z. Photoelectrochemical CO_2 Reduction into Syngas with the Metal/Oxide Interface. *Journal of the American Chemical Society* **2018**, 140 (25), 7869–7877. https://doi.org/10.1021/jacs.8b03067.

27) Laidoudi, S.; Bioud, A. Y.; Azizi, A.; Schmerber, G.; Bartringer, J.; Barre, S.; Dinia, A. Growth and Characterization of Electrodeposited Cu_2O Thin Films. *Semiconductor Science and Technology* **2013**, 28 (11). https://doi.org/10.1088/0268-1242/28/11/115005.

28) Chen, T.; Kitada, A.; Seki, Y.; Fukami, K.; Usmanov, D. T.; Chen, L. C.; Hiraoka, K.; Murase, K. Identification of Copper(II)–Lactate Complexes in Cu_2O Electrodeposition Baths: Deprotonation of the α-Hydroxyl Group in Highly Concentrated Alkaline Solution. *Journal of The Electrochemical Society* **2018**, 165 (10), D444–D451. https://doi.org/10.1149/2.0831810jes.

29) Wang, P.; Wu, H.; Tang, Y.; Amal, R.; Ng, Y. H. Electrodeposited Cu_2O as Photoelectrodes with Controllable Conductivity Type for Solar Energy Conversion. *Journal of Physical Chemistry C* **2015**, 119 (47), 26275–26282. https://doi.org/10.1021/acs.jpcc.5b07276.

30) Espro, C.; Marini, S.; Giusi, D.; Ampelli, C.; Neri, G. Non-Enzymatic Screen Printed Sensor Based on Cu_2O Nanocubes for Glucose Determination in Bio-Fermentation Processes. *Journal of Electroanalytical Chemistry* **2020**, 873, 114354. https://doi.org/10.1016/j.jelechem.2020.114354.

31) Makuła, P.; Pacia, M.; Macyk, W. How To Correctly Determine the Band Gap Energy of Modified Semiconductor Photocatalysts Based on UV-Vis Spectra. *Journal of Physical Chemistry Letters* **2018**, 9 (23), 6814–6817. https://doi.org/10.1021/acs.jpclett.8b02892.

32) Edvinsson, T. Optical Quantum Confinement and Photocatalytic Properties in Two-, One- and Zerodimensional Nanostructures. *Royal Society Open Science* **2018**, 5 (9). https://doi.org/10.1098/rsos.180387.

33) Mele, G.; Annese, C.; D'Accolti, L.; de Riccardis, A.; Fusco, C.; Palmisano, L.; Scarlino, A.; Vasapollo, G. Photoreduction of Carbon Dioxide to Formic Acid in Aqueous Suspension: A Comparison between Phthalocyanine/TiO_2 and Porphyrin/TiO_2 Catalysed Processes. *Molecules* **2015**, 20 (1), 396–415. https://doi.org/10.3390/molecules20010396

5. ELECTROCATALYTIC CO_2 REDUCTION

5.1 STATE OF THE ART

The process of CO_2 electrocatalytic reduction, particularly if associated with renewable energy sources and/or carbon-capture storage strategies, represents an attractive way to produce carbon-based chemicals and fuels useful for many purposes, despite it is still characterized by the lack of active and selective electrocatalysts[1–3].

If metals like Cu, Ag and Au are used as electrocatalysts, hydrogen evolution reaction (HER) is limited by the weak $^*H$ bond, while CO_2 reduction reaction (CO_2RR) kinetics is favoured by the large activation energy required for the formation of *COOH intermediate[4-6]. Carbon monoxide, instead, strongly binds with the surface of metals like Pd, Pt and Ni, which are also able to activate CO_2[7]. However, this strong bond leaves only interstitial sites for the evolution of hydrogen, which results favoured rather than the carbon reduction reactions.

Among the catalysts mostly present in literature[8-9], copper (Cu) presents unique features because it is capable to produce alcohols and hydrocarbons[10-11], despite its selectivity in general is low due to a wide range of products generated in parallel reactions[12-15]. This poor selectivity can be explained with a low intermediate binding energy. Copper catalysts allow reactions involving from 2 to 8 electrons, leading in the first case to the production of carbon monoxide and formic acid, and in the latter case to methane. It has been shown that copper oxidation before the reaction can improve the selectivity to C_2 products, like ethylene and ethanol, otherwise produced in low amount[16–19]. Morphology and film thickness have also been reported to be relevant in addressing selectivity; carbon monoxide and formic acid are mainly formed over thick electrocatalytic films at low overpotential, while methanol is formed over thin films[20]. The presence of a nanostructure in the electrodes and in general the control of morphology may improve the selectivity and reduce the overall CO_2RR overpotential, but often it is not enough to address the reaction pathways towards the desired products. One way to improve and tune

the selectivity of Cu toward a specific compound consists in engineering the electrode surface through the use of bimetallic components or alloys, which strongly modify the electronic properties and the environment of copper atoms[21,24].

5.2 SCOPE OF THE CHAPTER

Scope of the chapter is to evaluate the activity of Cu-based electrodes processed in a homemade compact electrocatalytic device designed on purpose to minimize overpotential inside the cell. The electrodes were prepared by depositing Cu_xO on a gas diffusion layer (GDL), to allow a better adsorption of CO_2 on the metal oxide active phase. The technique of synthesis adopted for the preparation of Cu_xO (precipitation method) allowed to prepare selectively cuprous oxide (Cu I, Cu_2O), which can easily be converted into CuO (Cu II) by calcination.

The influence of the state of Cu (Cu I or Cu II) on the electrocatalytic activity, together with the Cu loading on the GDL, was explored at different applied potential for the process of CO_2 reduction. The results obtained were then used to optimize the behaviour of more complex composite electrocatalysts (*CuS_x, Cu-In*) prepared in the framework of the European Project A-LEAF for the realization of a prototype mimicking a leaf-type system. The aim was to define the optimum working conditions (i.e. voltage, current density, electrolyte, pH) towards the desired selectivity/efficiency and to obtain useful elements to adjust the cell/electrode configuration to these relevant findings. The electrodes were prepared by spraying homogeneously the Cu-based materials on the GDL (i.e. spray coating technique).

5.3 EXPERIMENTAL

5.3.1 Synthesis of electrocatalysts

5.3.1.1 Cu_2O synthesis

Cuprous oxide (Cu_2O) nanocubes were synthesized by a wet precipitation process in which 0.85 g of $CuCl_2 \cdot 2H_2O$ was dissolved in 500 mL of distilled water under stirring at 60°C. Keeping the same temperature (60 °C), 50 mL of 2 M NaOH solution was added. Then, the resulting solution was stirred for 30 min before

adding 50 mL of a 0.6 M ascorbic acid solution. The formation of a red copper oxide precipitate was noticed and the precipitation was stopped after 3 h stirring. After cooling the solution, the as-obtained precipitate was washed several times with distilled water and ethanol, collected by centrifugation and dried in a vacuum oven at 60°C for 12 h[25]. This sample was named *Cu_2O NC-60*. Another sample was synthesized by the same procedure with the difference that 2 M NaOH was added at room temperature and not at 60 °C, named *Cu_2O NC-25*.

The Preparation of more complex Cu-based electrodes is now illustrated.

5.3.1.2 CuS_x

CuS_x (20:1) based catalysts were synthesized following the procedure reported by ETH et al.[26]. Specifically, 0.134 mmol of S and 8 mmol of $Cu(NO_3)_2 \cdot 3H_2O$ were dissolved in 40 mL of ethylene glycol under stirring at room temperature for 30 min. This solution, transferred into a 50 mL autoclave, was firstly heated for 10 hours at 140°C with a ramp of 5°C min^{-1} and then cooled at room temperature. The precipitate was cleaned with water for three times and then vacuum-dried at 50 mBar overnight at 80°C.

5.3.1.3 Cu-In

Cu-In (20:1) based catalysts were synthesized following the procedure reported by ETH et al.[27]. Specifically, 0.2 mmol of $InCl_3$ and 4 mmol of $Cu(NO_3)_2 \cdot 3H_2O$ were dissolved in 40 mL of ethylene glycol under stirring at room temperature for 30 min. This solution, transferred into a 50 mL autoclave, was firstly heated for 10 hours at 140°C with a ramp of 5°C min^{-1} and then cooled at room temperature. The precipitate was cleaned with water for three times and then vacuum-dried at 50 mBar overnight at 80°C.

5.3.1.4 Deposition of catalysts on carbon diffusion layer electrodes

Spray-coating technique was used to deposit the catalyst in the form of an ink (a stable suspension of the catalytic powder in an organic solvent) on a carbon-based gas diffusion layer (GDL, Sigracet® 29BCE, supplied by Ion Power) heated to allow the evaporation of the solvent. The inks were prepared as follows: the powders were mixed, under stirring, with 50 mL of isopropanol and 50 µL of

Nafion^{TM} 5 wt. %, perfluorinated solution; after 20 min stirring, the suspension was sprayed on the GDL obtaining a loading of 1 mg cm^{-2}.

5.3.2 Electrochecamical setup

The electrocatalytic tests were carried out in a compact homemade electrochemical device, made of Plexiglas and working in a three-electrode configuration (see pictures in Figure 5.1).

The copper-based electrode (working electrode, 1x1 cm) was immersed in 0.1 M $KHCO_3$ aqueous electrolyte, while a platinum ring was used as the counter-electrode, located at the anode compartment separated from the cathode by a Nafion® membrane (N324, supplied by Ion Power) and working in 0.1 or 3.6 M $KHCO_3$ aqueous electrolyte. The higher $KHCO_3$ concentration at the anode (3.6 M, corresponding to its solubility in water) was used only for the electrocatalytic tests at higher voltage (-0.8 V vs. RHE) when a higher availability of OH^- was necessary for water oxidation. A 3M Ag/AgCl electrode (supplied by AMEL) was used as reference electrode and located very closed to the working electrode to minimize overpotential (series resistance). The potential values were then translated into RHE (Reversible Hydrogen Electrode) voltages by using the following equation:

$$E_{(RHE)} = E_{Ag/AgCl} + 0.059\ pH + 0.21$$

A continuous recirculation of catholyte/anolyte between each half-cell (cathode and anode, respectively) and an independent reservoir container was guaranteed by means of a peristaltic pump working at a liquid flow rate of 50 mL min^{-1}.

Electrochemical CO_2 reduction tests were initially conducted in a double-chamber liquid-phase cell using pure copper oxides (+1 and +2 as oxidation states) as electrocathodes; subsequently, more advanced materials were produced (by doping the copper oxide with S and In) and tested in a more complex electrochemical cell, obtained by modifying the first type by introducing an additional gas-chamber (to improve the separation of liquid and gaseous products) together with the other two liquid compartments already present.

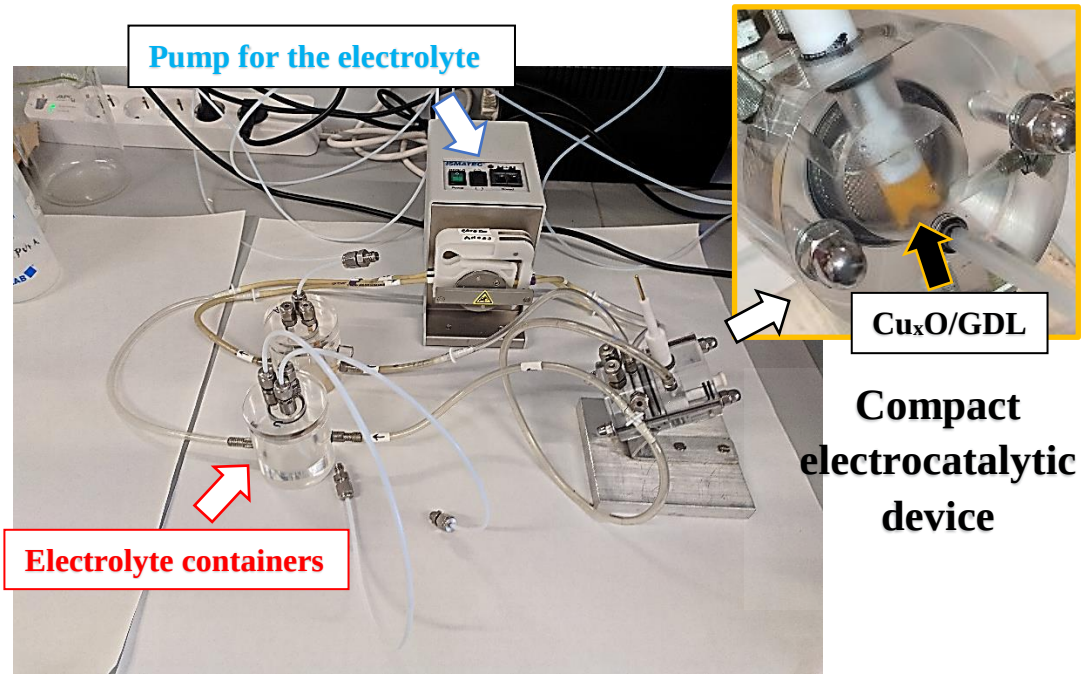

Figure 5.1 *Electrochemical setup with a focus on the cathodic chamber*

5.3.3 Testing

5.3.3.1 Detailed protocol for a single electrochemical test

Every electrochemical test consists in performing a series of operations in a defined order, which were adapted as the routine protocol. Before starting, the $KHCO_3$ catholyte solution was saturated with a vigorous flow of CO_2, and this allowed to run every test with a stable and defined pH value (6.8 in the case 0.1 M concentration).

i) The first operation consists in running of a series of chrono-voltammetry measurements (CV), with a speed of 20 mV m^{-1}, from the open circuit voltage (OCP) to a defined value, will be the one used in the subsequently step of the chrono-amperometry test (CA). The OCP represents the working-reference voltage difference evaluated when no current flows in the circuit. The CVs were stopped when the current/voltage profiles overlap each other, indicating that the system has reached a steady-state equilibrium, and then catalyst/electrolyte interface does not undergo further modifications (Figure 5.2).

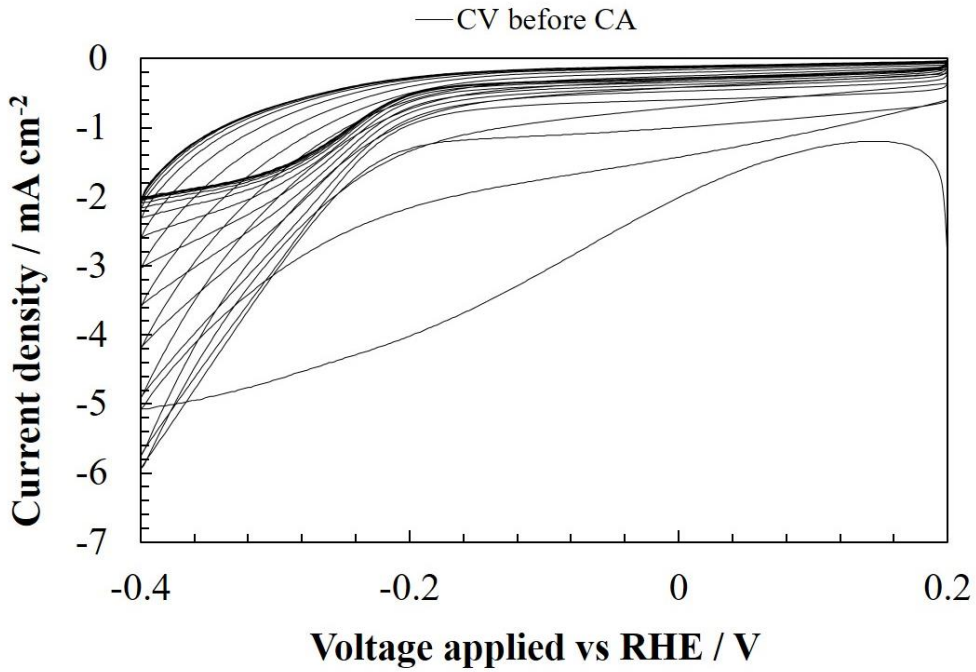

Figure 5.2 *Example of CV performed until steady-state.*

ii) The second operation consists in the determination of the double-layer capacitance, and the double-layer technique (DL) was used for this scope. The nature and the influence of the double layer will be discussed later. It consists in the running of several subsequent CVs, each one performed at a different rate (from 2 to 50 mV s^{-1}) in a limited potential range, in general a few mV around the OCP, which is evaluated before the CV, to provide a very low current (Figure 5.3).

The double-layer capacitance values were then estimated by a mathematical approach: the values of current (mA) corresponding to a fixed potential value (mV) for every scan were plotted versus the CV rate (X-axis) of the relative scan, obtaining a curve. Its linear first order regression and relative straight-line slope provide the capacitance, measured in μF cm^{-2}. To perform a more accurate measurement, two current values for a given potential value were plotted, and the capacitance average finally was calculated[24] (Figure 5.4).

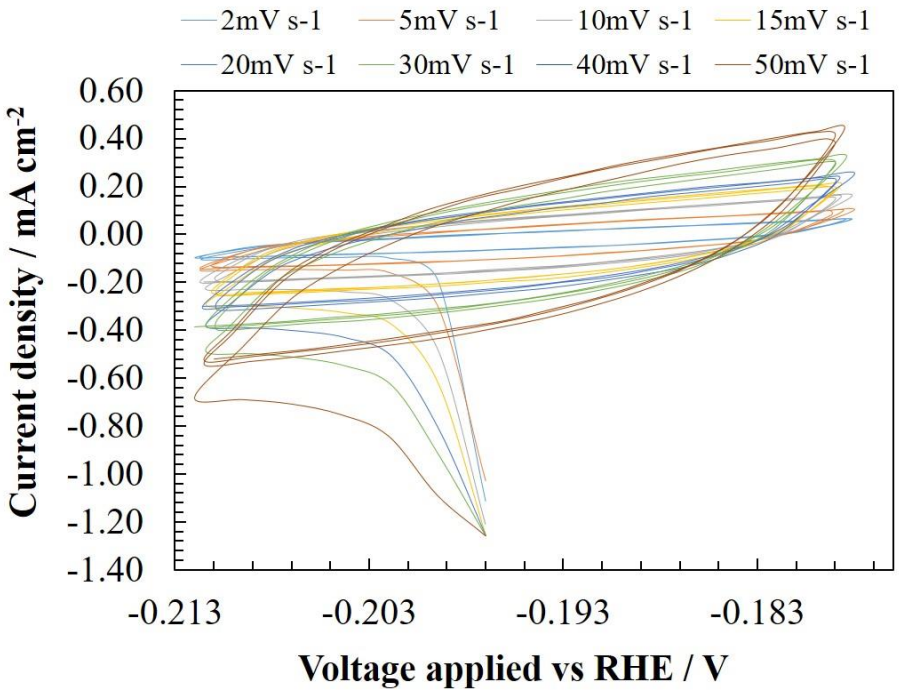

Figure 5.3 *Series of CV for DL capacitance*

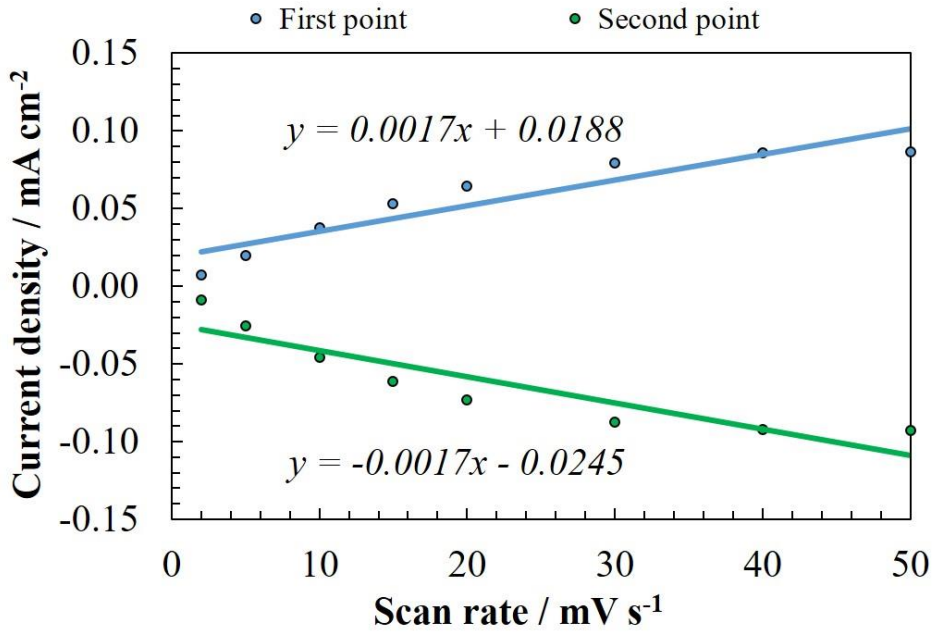

Figure 5.4 *Current density/Scan rate plot for capacitance determination.*

iii) The following step consists in running a CA, at the same potential of the highest value used previously in the CV. This represents the most important part of the whole protocol, because the CA step represents the actual CO_2 reduction process (coupled with oxygen evolution by water oxidation at the anode) used to calculate the carbon productivity and Faradaic efficiency. The gas-phase going out from the gas chamber, after flowing to a silica absorber to remove the water and the CO_2,

was collected and analysed through gas chromatography (MicroGC GCX Pollution Analytic Equipment), at constant time intervals (ten minutes).

iv) At the end of the CA step, double-layer capacitance and chrono voltammetry (with the same potential excursion of the first one, see figure 45, red line) were performed again to check if any change happened at the electrode interface. Finally, part of the liquid phase in the catholyte and anolyte were collected in sealed sample-holders and analysed through ionic-cromatography (IC, Metrohm 940 Professional, column Metrohm Organic Acids).

5.3.4 Testing in CO_2 reduction

The tests using the cell reported in figure 5.1 were carried out using Cu_2O (*Cu_2O NC-25* sample) as the cathodic material deposited over a carbon gas diffusion layer at 1, 5 and 10 mg cm^{-2} catalyst loading. The calcined sample (CuO/GDL) was also tested. These tests were performed with 0.1 M $KHCO_3$ solution as catholyte saturated with CO_2 (pH 6.8) and 0.1 M or 3.6 M $KHCO_3$ water solutions as anolyte (both with Mili-Q water). The latter concentration (which refers to the solubility of $KHCO_3$ in water at 25°C) was employed at higher potentials, in order to avoid the complete depletion of OH^- ions and the relative dropping of the working-reference voltage at high current densities. In Figure 5.5, the CVs before and after the CA (from 0.2 to -0.4 V vs RHE), and the current profile of CA at -0.4 V vs RHE, for a Cu_2O/GDL catalyst with 10 mg cm^{-2} loading are reported. In the plot, only the latest CV profile (obtained after many stabilization cycles) was reported. The CA profile shows how the current increases with time, up to -1.25 mA, and this indicates the activation of the catalyst. This can be confirmed by the CV profile performed after the CA, which shows higher currents than the one measured in the first CV. This behaviour is also showed for the Cu_2O/GDL with 5 mg cm^{-2} loading, but not for the one with a loading of 1 mg cm^{-2} and for the CuO/GDL catalyst (Figure 5.6). This activation may be due to the formation of core-shell type particles with surface at different oxidation state than bulk, but further investigation is needed to confirm this hypothesis.

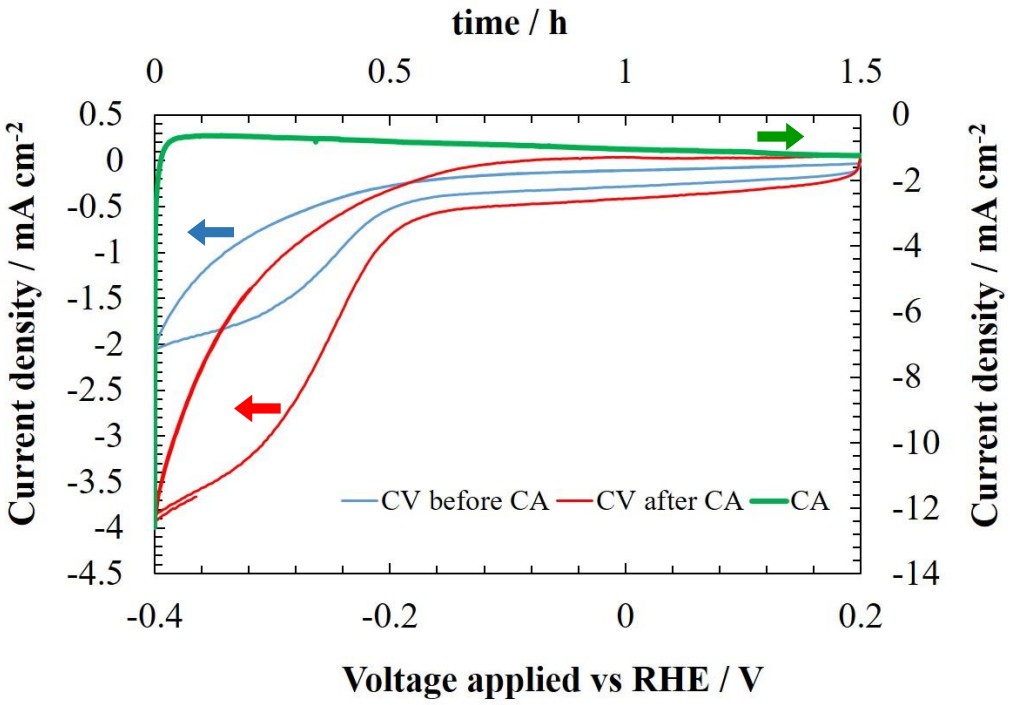

Figure 5.5 *Chronoamperometry (green line) and cyclic voltammetry profiles before (blue line) and after (red line) the CA.*

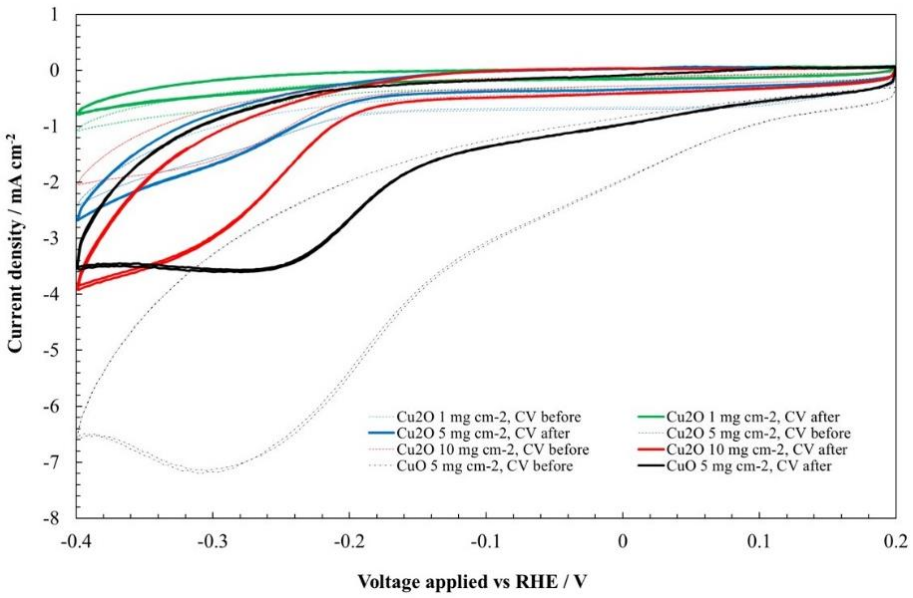

Figure 5.6 *CV profiles (before and after the CA) for Cu_2O/GDL and CuO/GDL catalysts at different loadings.*

5.3.4.1 Effect of Cu_2O loading

In Figure 5.7, the current densities (in mA cm^{-2}), in the -0.4/-0.8 V (vs RHE) range for the three catalysts loading are reported.

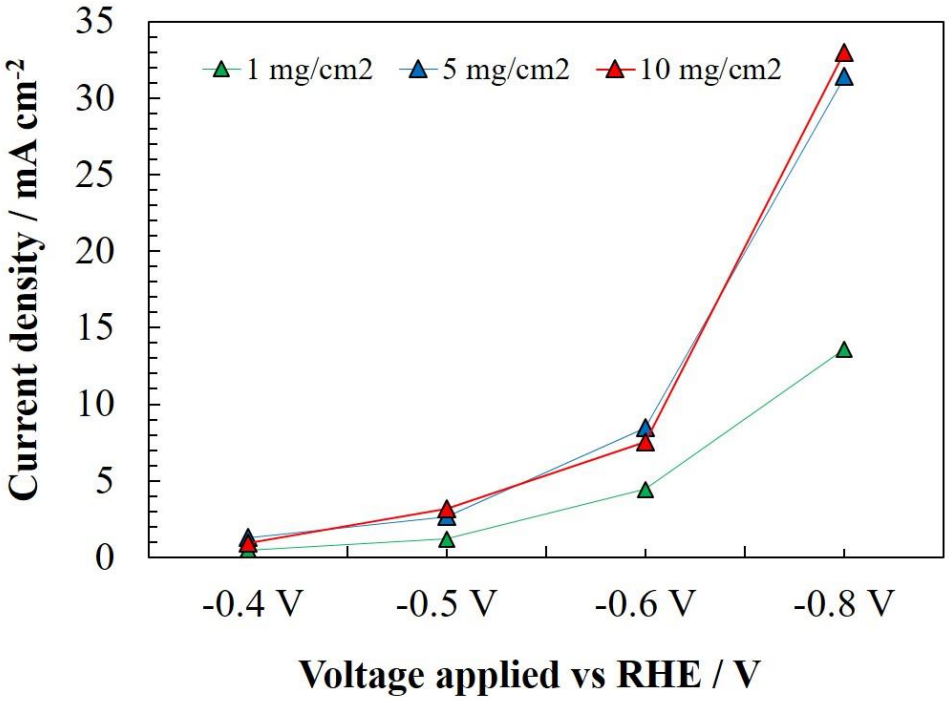

Figure 5.7 *Current densities in function of applied voltage at different catalyst loading.*

Increasing the Cu_2O loading from 1 to 5 mg cm^{-2} causes an increment of the current density, while from 5 to 10 mg cm^{-2} current density variations are negligible and the two curves result overlapped.

On Carbon Productivity

In Figure 5.8, carbon monoxide and formic acid productivity and current densities for the *Cu_2O/GDL* catalysts at different loading versus the voltage applied, are reported. It can be noticed how the productivity increases with the catalyst loading and, at the same loading, increases with the potential, showing a maximum value in any case at -0.6 V vs RHE. With 1 mg cm^{-2} loading, the productivity is 3.33 µmol h^{-1}, while for the intermediate loading (5 mg cm^{-2}) and for the maximum loading (10 mg cm^{-2}), it is 8.71 and 12.83 µmol h^{-1}, respectively. The tests were also carried out at a higher potential, -0.8 V vs RHE, and the results, in terms of FE and carbon productivity, compared to the GDL are shown in Figure 5.9.

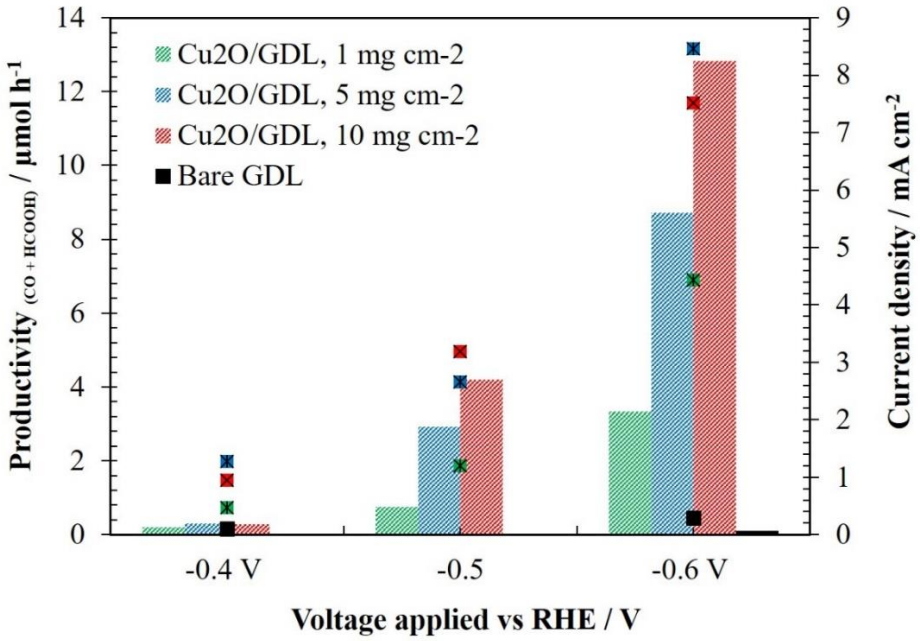

Figure 5.8 *Productivity and Current density vs Voltage applied plot.*

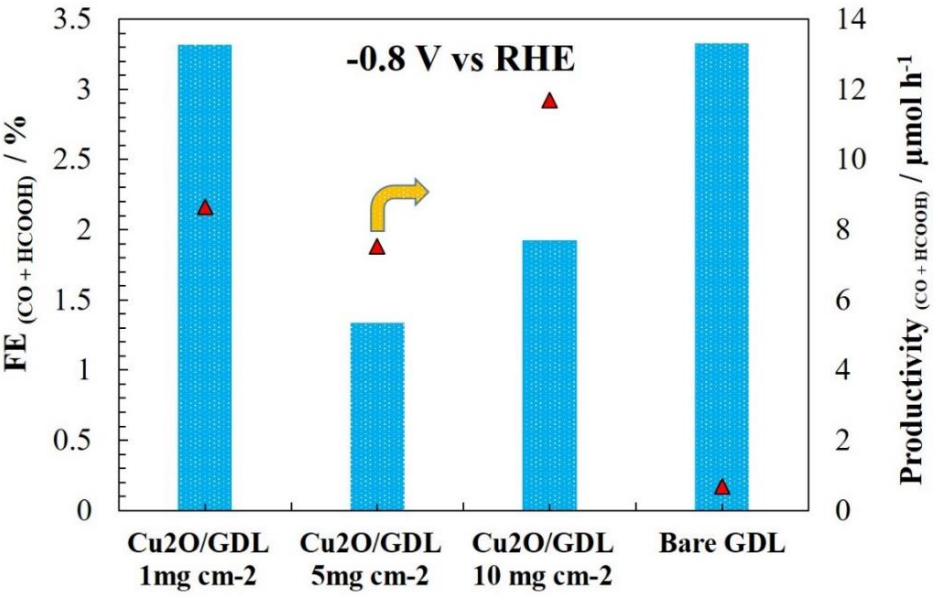

Figure 5.9 *Faradaic efficiency (to CO and HCOOH and current density at -0.8 V vs RHE for Cu_2O/GDL at different loadings.*

At -0.8 V, the FE to CO and HCOOH is lower, due to the side-reaction of hydrogen evolution. It can be noticed that, especially for higher catalyst loading, Cu_2O loses partially its catalytic activity, although higher currents were obtained. As results, Faradaic efficiency of bare GDL resulted higher than of 5 and 10 mg cm^{-2} loading Cu_2O/GDL at -0.8 V vs RHE. Note that the current density for GDL is very low (Figure 5.8), but GDL shows some activity in CO_2 reduction as the commercial bare GDL used in this work has an additional microporous carbon layer, useful for

improving adherence with the sprayed Cu-based layer. It is also to take into consideration that the tests at -0.8 V vs RHE were carried out on the same catalyst that was processed in series by increasing the set applied potential, consequently the catalyst was affected by the previous tests.

On Carbon Monoxide Selectivity

The selectivity towards carbon monoxide is shown in Figure 5.10. It increases with potential, reaching a plateau at -0.6 V and then decreasing at higher potentials.

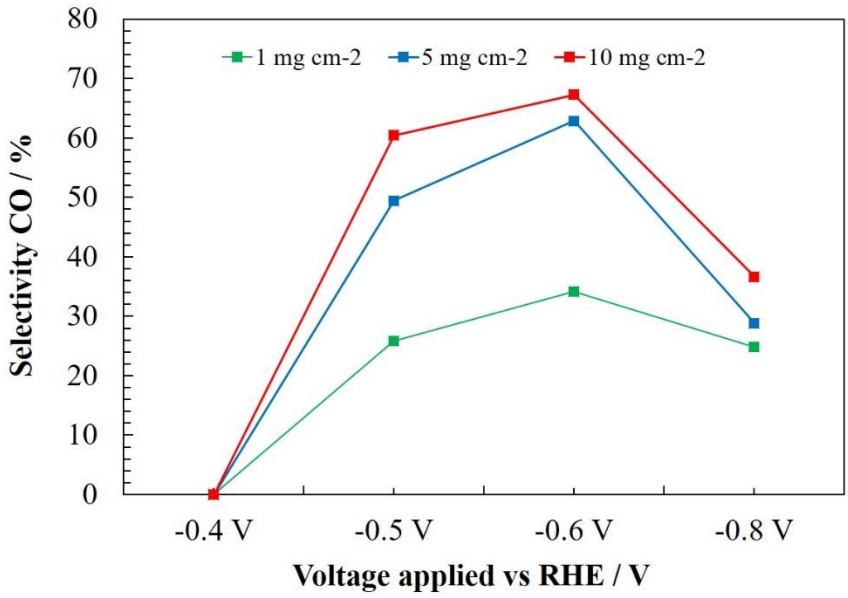

Figure 5.10 *CO selectivity vs Voltage applied.*

No carbon monoxide was detected at potentials lower than -0.4 V vs RHE, at least under the sensitivity of the analytic system (around 1-2 ppm). A maximum of 67% selectivity to carbon monoxide at -0.6 V vs RHE was detected for the *Cu_2O/GDL* electrode with 10 mg cm^{-2} loading, while due to deactivation of the catalyst at -0.8 V, the value drops to 24-25%, favouring the formation of formic acid. These results suggest the possibility of tuning the formation of CO concentration (in relation with the production of H_2), by varying the applied voltage and/or the catalyst loading, in order to produce syngas with a controlled CO/H_2 ratio[28-31]. However, this is out of the scope of this work.

On final pH of the electrolyte

The catholyte and anolyte pH values, measured at the end of the tests, are reported in Figure 5.11.

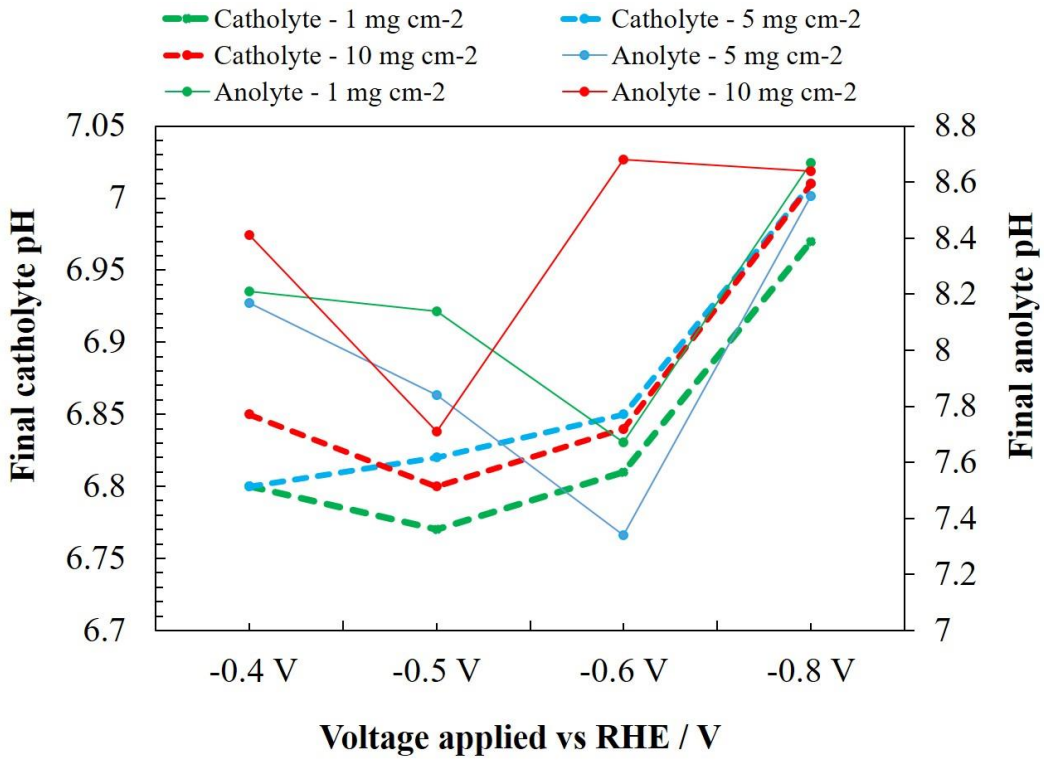

Figure 5.11 *Final catholyte and anolyte pH values for different potentials and catalyst loading.*

The higher the cathodic potential, the more the catholyte pH increases at the end of the electrocatalytic test, changing from 6.8 before the test to nearly 7 measured at the end of the test at -0.8 V vs RHE (figure 5.13, broken lines), with a variation limited to 0.23 pH points; this can be explained with the H^+ depletion in the cathode, due to their consumption in all the occurring reduction half reactions, namely involving the formation of H_2 or carbon based products. However, the pH at the cathode side can be considered as quite constant, at least for the time of the electrocatalytic test.

On the contrary, in the anolyte a decreasing of the final pH values was recorded due to the OH^- depletion by oxygen evolution reaction (figure 5.13, solid lines). It should be taken into account that in some cases (e.g. high current densities) a 3.3 M $KHCO_3$ solution was used as the anolyte with a starting pH higher than 0.1 M $KHCO_3$.

5.3.4.2 Cu_2O and CuO performance comparison

The Cu_2O was annealed at 450°C for 1 hour at 10 °C min^{-1} turning it into CuO, highlighted with a change of colour from the orange to black, as described in the experimental part. In Figure 5.12, the comparison in terms of carbon monoxide and formic acid FE% and current density of the *Cu_2O-NC25* and the derived *CuO*, both with a loading of 5 mg cm^{-2}, is reported.

The FE to CO and HCOOH of the CuO sample resulted higher than that of Cu_2O at any applied potential, with a maximum FE at -0.6 V vs RHE potential. In this case, the CuO allowed to obtain a FE almost 2 times higher with respect to Cu_2O (i.e. almost 12%), evidencing how both the state of oxidation and the morphological modification due to annealing at high temperature, allowed more favourable conditions for CO_2 reduction over the CuO-based electrocatalyst. The maximum selectivity to CO for the CuO sample resulted 74.5, obtained at -0.6 V vs RHE (Figure 5.13).

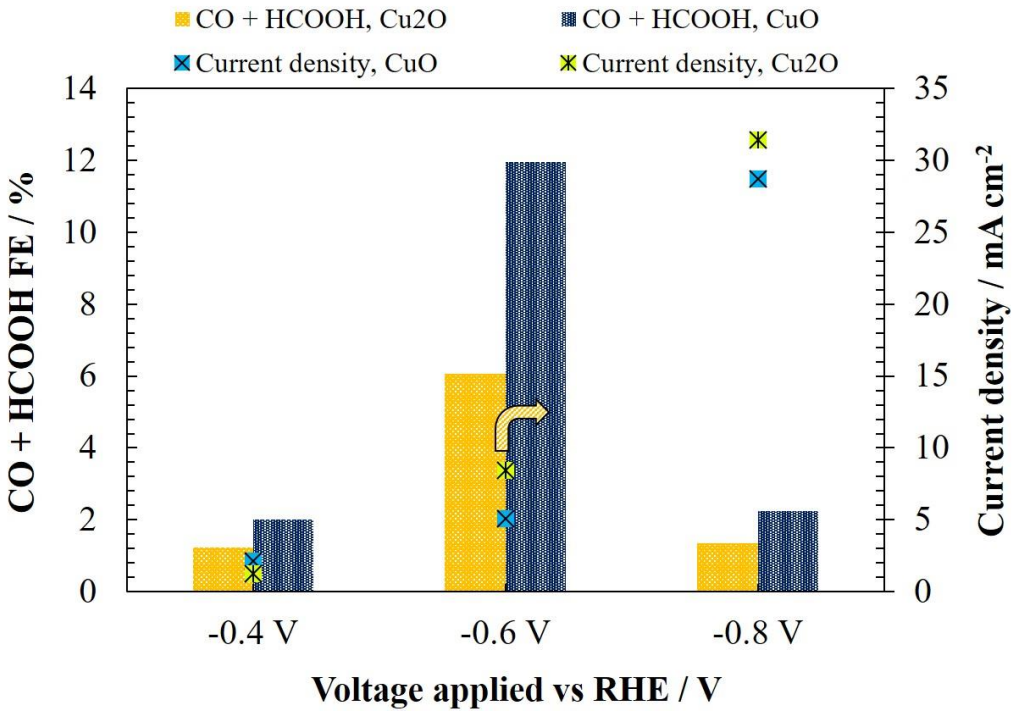

Figure 5.12 *Carbon monoxide and formic acid FE and current density vs applied voltage for Cu_2O NC-25 and CuO samples.*

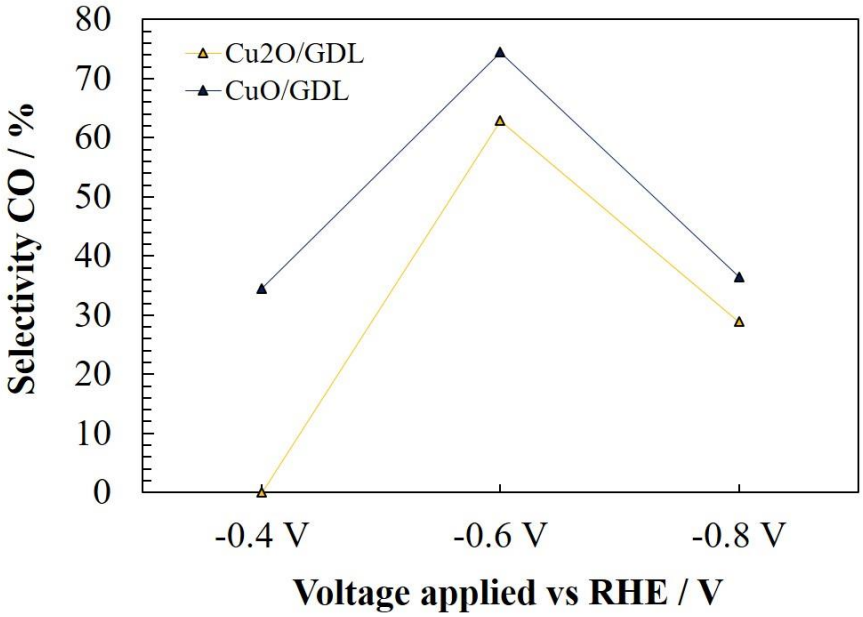

Figure 5.13 *CO selectivity for Cu_2O/GDL and CuO catalysts.*

5.3.4.3 Electrochemical Impedance Spectroscopy (EIS)

The Cu_2O and CuO samples were subjected to Electrochemical Impedance Spectroscopy (EIS) measurements, to evaluate their ability in charge transfer and diffusion limitation, which can strongly influence the electro catalytic behaviour. In particular, the measurements were carried out in two different reaction environments, namely:

System A) 1 M PBS solution and 5 mM potassium ferrocyanide. In this case, the measurements were carried out in a small beaker (5 mL) under slight stirring at room temperature, depositing the catalytic powder in a screen printed carbon electrode;

System B) in the same electrochemical device and under the same operating conditions of the electrocatalytic CO_2 reduction tests (see previous paragraphs);

The first measurements (system A) were adopted with the aim of studying the behaviour of the samples in a reaction environment used as a standard in the literature, especially as regards the sensor field, in a way to allow reproducibility and an easy comparison with the behaviour of other electrocatalytic materials. In the second case (System B), the measurements were instead aimed at evaluating not only the materials but also the system used in the electroreduction tests, to

understand how the various resistance to charge transfer or other parameters related to overpotential can be correlated to the experimental results.

For the tests carried out in the first reaction environment (System A), modified screen printed carbon electrodes (SPCEs), supplied by DropSens, were used (Figure 5.14).

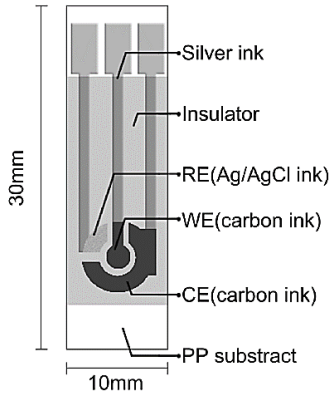

Figure 5.14 *Screen printed carbon electrode (SPCE).*

The commercial SPCEs consist of three parts: a planar carbon surface with a diameter of 4 mm, a pseudo reference electrode and a carbon counter electrode. The samples were therefore deposited in the SPCEs through the drop-casting technique. Specifically, 5 mg of powder (Cu_2O or CuO) were dissolved in 100 µL of distilled water, under stirring, until a homogeneous dispersion was formed. Subsequently, in three steps, 5 µL of this dispersion was cast onto the surface of the SPCE, and then drying at room temperature.

The samples used in system B were instead made by spray coating, as already described in the previous sections.

Preliminarily to the EIS measurements, the samples in both reaction systems were subjected to pre-CVs, in order to stabilize the system and work in a steady state, an indispensable condition for the good reliability of the results. The CVs were conducted in a potential range of 0 to 0.3 V for system A, and 0.2 to -0.6 V for system B. The parameters for EIS analysis, carried out using the "Autolab" potentiostat and "NOVA" software, were the following: Frequency range: from 10^5 Hz to 0.1 Hz and 0.01 V_{RMS} of amplitude (RMS stands for root-mean-square, namely the square root of the time-average of the squares of voltages).

Pre-CVs for the bare SPCE, Cu_2O/SPCE and CuO/SPCE samples (System A) and bare GDL, Cu_2O/GDL and CuO/GDL electrodes (System B) are reported in Figure 5.15a,b respectively.

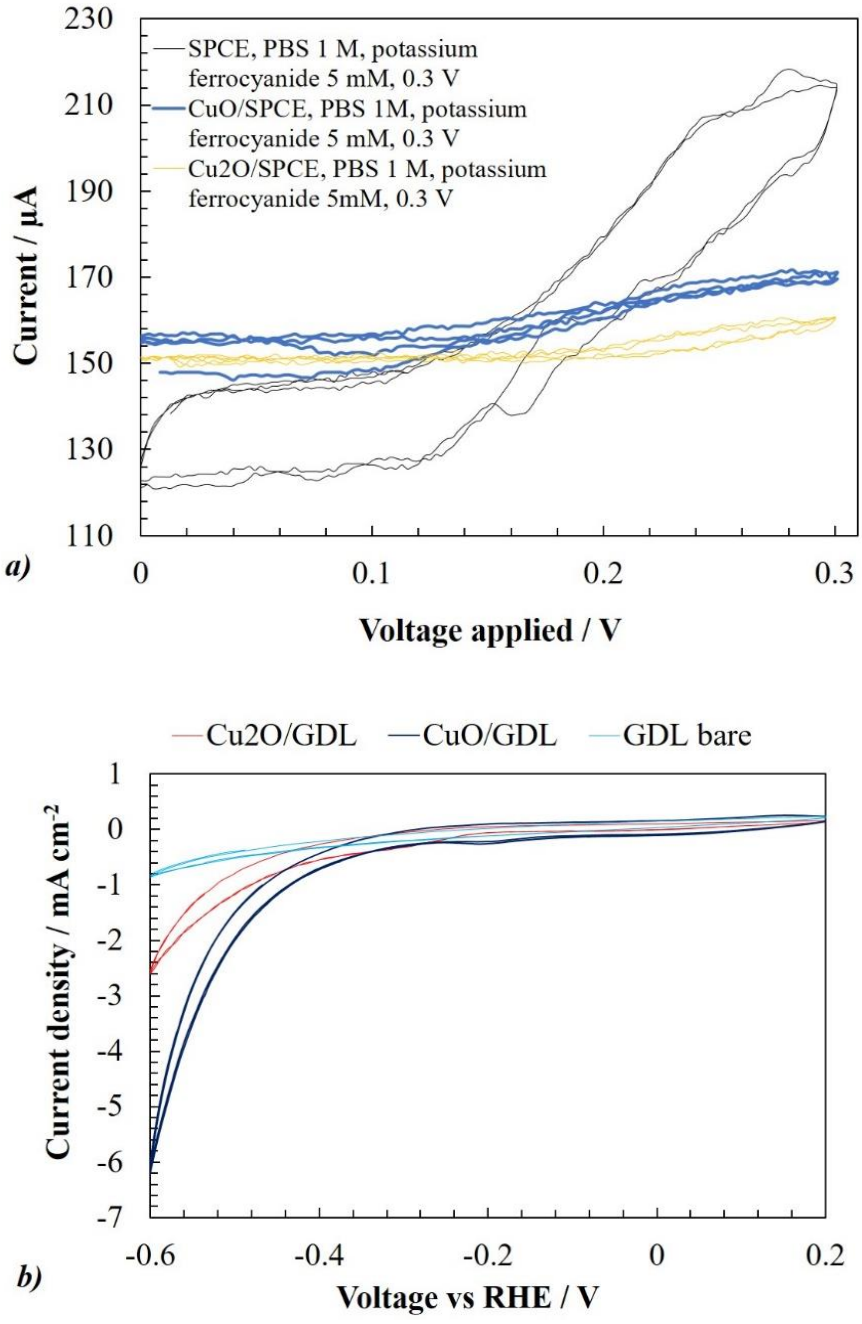

Figure 5.15 *CVs performed prior to EIS analysis for a) System A; b) System B*

The CVs in Figure 5.15b show how the onset of CO_2 reduction occurs at lower (less negative) potential than the other two electrodes, confirming results of FE and productivity reported in the previous paragraphs.

System A

Figure 5.16a shows the Nyquist plot for the measurements reported with system A. The experimental data are represented by points, while the solid lines refer to the fitting curves processed through software simulation of an appropriate equivalent circuit (reported in the same figure). These circuits have been elaborated in order to represent at best the described physical system, minimizing χ^2 (chi-square, this statistical test offers a measurement of the discrepancies between a model distribution and real data set). This diagram shows the real impedance on the x-axis and the imaginary impedance on the y-axis. The impedance represents the analog of the resistance and its measurement takes place in the case of alternating current systems (AC). Impedance is therefore a measure of resistance to the flow of electrons, and is often presented as a complex number that takes into account a real component (resistance) and an imaginary component (represented by capacitance and inductances). Each point in the Nyquist diagram can be represented by a vector starting from the origin; its length represents the impedance.

The bare SPCE was represented by a simple Randles circuit. It consists of a resistor, R_s, in series with the parallel between the resistor R_{ct} and the CPE element. R_s represents the resistance of the solution and is a function of the ions present at a given concentration in the cell. R_{ct} is the charge transfer resistance and is due to the redox reactions occurring at the electrode/solution interface. CPE (constant phase element) is an element, representing the double electrode/solution layer, which does not have an ideal capacitive character. For defined situations, CPE identifies a capacitor or resistor. The *Cu_2O/SPCE* and *CuO/SPCE* samples are instead represented by the resistance R_s in series with a double parallel between the CPE element and the series between the resistance R_{ct} and the element Ws. The latter, Warburg element, represents the resistance due to diffusion phenomena at the electrode/solution interface. This configuration is usually adopted in the case in which the Nyquist diagram shows a double semicircle, characteristic of the presence of a double time constant. In our case, this configuration was adopted as it allows to obtain the best fitting. The two semicircles could be fused or partially overlapped due to corrosive phenomena or due to the adsorption of reaction intermediates.

All the parameters obtained by EIS analysis are summarized in Table 5.1. The Cu_2O/SPCE and CuO/SPCE R_{ct} values are 3.62 vs 3.98 Ω, respectively, while the

R_{ct}' values are 11.8 vs 28.2 Ω, respectively. The R_{ct}' of CuO/SPCE is therefore higher than Cu_2O/SPCE and this can be seen from the Nyquist plot in which after the first semicircle (almost overlapped) the curve for the first deviates to a greater extent. The R_{ct} values are similar, only slightly higher for the CuO/SPCE, as also evidenced by the very similar CV curves reported in Figure 5.15a.

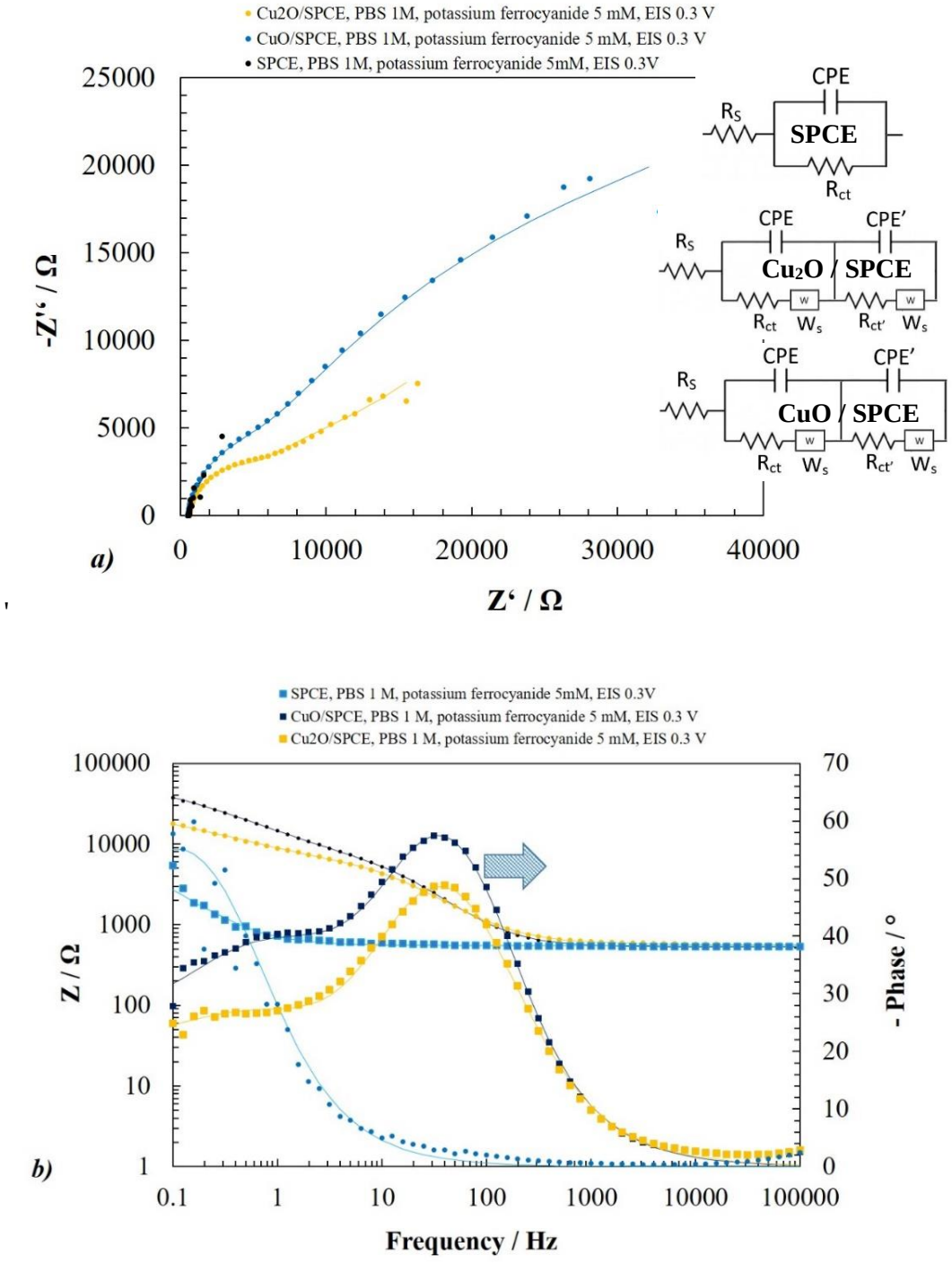

Figure 5.16 *a) Nyquist plots, equivalent circuits and b) Bode plot for SPCE, Cu_2O/SPCE and CuO/SPCE modified electrodes acquired from EIS measurements in the System A.*

On the contrary, the R_{ct} values of the Cu-based SPCEs are lower than the bare SPCE sample, probably due to the fact that the latter shows a lower conductivity. A further difference of the copper-based electrodes compared to the bare SPCE is evident in the Bode plot (Figure 5.16b). This diagram plots the logarithm of the impedance (lg Z) versus the logarithm of the frequency (lg f) and also the phase shift (ϕ) versus the frequency (lg f). The phase diagram is shifted towards low frequencies by about 39 Hz, due to different effective capacitors.

	R_s (Ω)	R_{ct} (kΩ)	CPE		W_s	R_{ct} ' (kΩ)	CPE'		W_s'
			$Yo*10^{-6}$ ($\Omega^{-1}*s^N$)	N	$Yo*10^{-3}$ ($\Omega^{-1}*s^{1/2}$)		$Yo*10^{-6}$ ($\Omega^{-1}*s^{1/2}$)	N	$Yo*10^{-6}$ ($\Omega^{-1}*s^{1/2}$)
Bare SPCE	550	10.5	578	0.875	-	-	-	-	-
CuO/SPCE	524	3.98	2.67	1.01	$79.4*10^{-3}$	28.2	36.7	0.707	$1.10*10^{18}$
Cu_2O/SPCE	566	3.62	5.33	0.918	$29.4*10^{3}$	11.8	36.4	0.704	141

Table 5.1 *Equivalent electric circuit elements acquired from Nyquist fit and simulation.*

System B

Figures 5.17a,b show the Nyquist and Bode plots respectively, for the bare *GDL*, *Cu_2O/GDL* and *CuO/GDL* electrodes obtained by EIS analysis in the electrocatalytic device used for CO_2 reduction tests (System B). For the bare *GDL*, the equivalent circuit is represented by a resistor R_s in series with the parallel R_{ct} and CPE. An inductance L was added in series with the resistance R_s, which allows overall to improve the fitting with the experimental data. The equivalent circuit of the *Cu_2O/GDL* and *CuO/GDL* samples is an extension of the GDL bare circuit, with a further parallel group consisting of the elements R_{ct}' and CPE'. Inductive effects that could justify the insertion of the element L may be due to geometrical factors of the electrochemical device, or even to the electrical connections.

Table 5.2 summarized all the parameters obtained by EIS measurements on the testing electrochemical cell (System B). Compared to the measurements carried out in system A, it is possible to note substantial differences regarding the charge transfer resistance values between the GDL and the samples containing *Cu_2O/GDL* and *CuO/GDL*. The R_{ct} of the *GDL* is 299 Ω, considerably higher than the *Cu_2O/GDL* (39.5 Ω) and *CuO/GDL* (6.45 Ω). The latter is therefore the sample characterized by the lowest resistance to charge transfer.

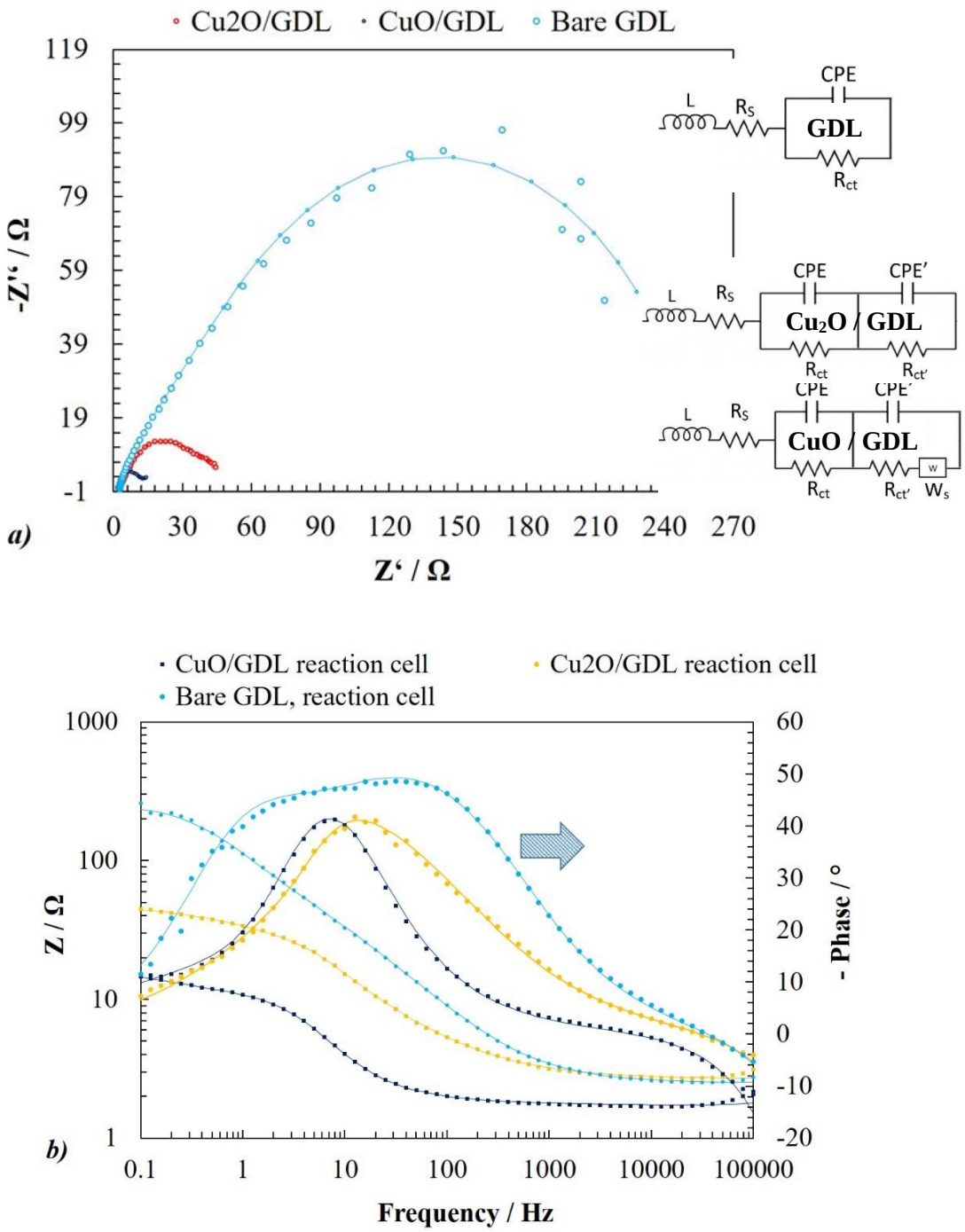

Figure 5.17 *a) Nyquist plots, equivalent circuits and b) Bode plot for GDL, Cu_2O/GDL and CuO/GDL modified electrodes acquired from EIS measurements in the System B.*

	R_s (Ω)	L (nH)	R_{ct} (Ω)	CPE		R_{ct} ' (Ω)	CPE'	
				Yo *10^{-3} ($\Omega^{-1}*s^N$)	N		Yo *10^{-3} ($\Omega^{-1}*s^N$)	N
Bare GDL	2.42	557	299	1.98	0.656	-	-	
Cu_2O/GDL	2.66	467	39.5	6.69	0.594	6.68	3.03	1.1
CuO/GDL	1.72	752	6.45	7.70	1	10.4	93.7	0.536

Table 5.2 *Equivalent electric circuit elements acquired from Nyquist fit and simulation.*

The maximum point of the Nyquist plot coincides with the relaxation frequency (when the relation ωRC = 1 is true), where the product R*C is the time constant τ. In the case of the *CuO/GDL* sample, the relaxation frequency occurs at lower values than the *Cu_2O/GDL* and *GDL* bare sample; therefore, to satisfy the previous relationship, the resistance must be greater than the other two, confirming the lower R_{ct} value. This lower value could justify the results obtained by the electrocatalytic CO_2 reduction tests. Lower resistances to charge transfers could therefore explain the higher ability to perform the CO_2 reduction reactions and therefore the higher productivity.

5.3.5 Elements for improving cell design

5.3.5.1 Evaluation of resistances within an electrochemical cell

The realization of an electrochemical prototype working in real conditions (i.e. at higher current densities and larger geometrical surface area of the electrodes) goes through the understanding and evaluation of the resistances within the device that can provide overpotential, thus limiting the electrocatalytic performance. Aim of this part of the work was to evaluate the origin of resistivity losses within a electrochemical device, by evaluating the contribution of resistances such as the electrolyte, the membrane and the electrodes.

In this direction, the series (Rs) and charge transfer (R1) resistances were measured through the Electrochemical Impedance Spectroscopy (EIS) using a conventional H-type electrochemical cell, flowing CO_2 into a 0.1 M $KHCO_3$ electrolyte. These independent resistances were measuring by varying the position of the reference electrode (RE, Ag/AgCl 3M), which was placed i) close to the working electrode (WE, Pt-rod) or ii) far from it (close to a Pt-rod counter electrode, CE), in different configurations (see Figure 5.18). Two different types of commercial proton exchange membranes were compared: the reinforced Nafion® membrane (N-324) and the thinner Nafion® NR-212 membrane, which provided different resistance contributions.

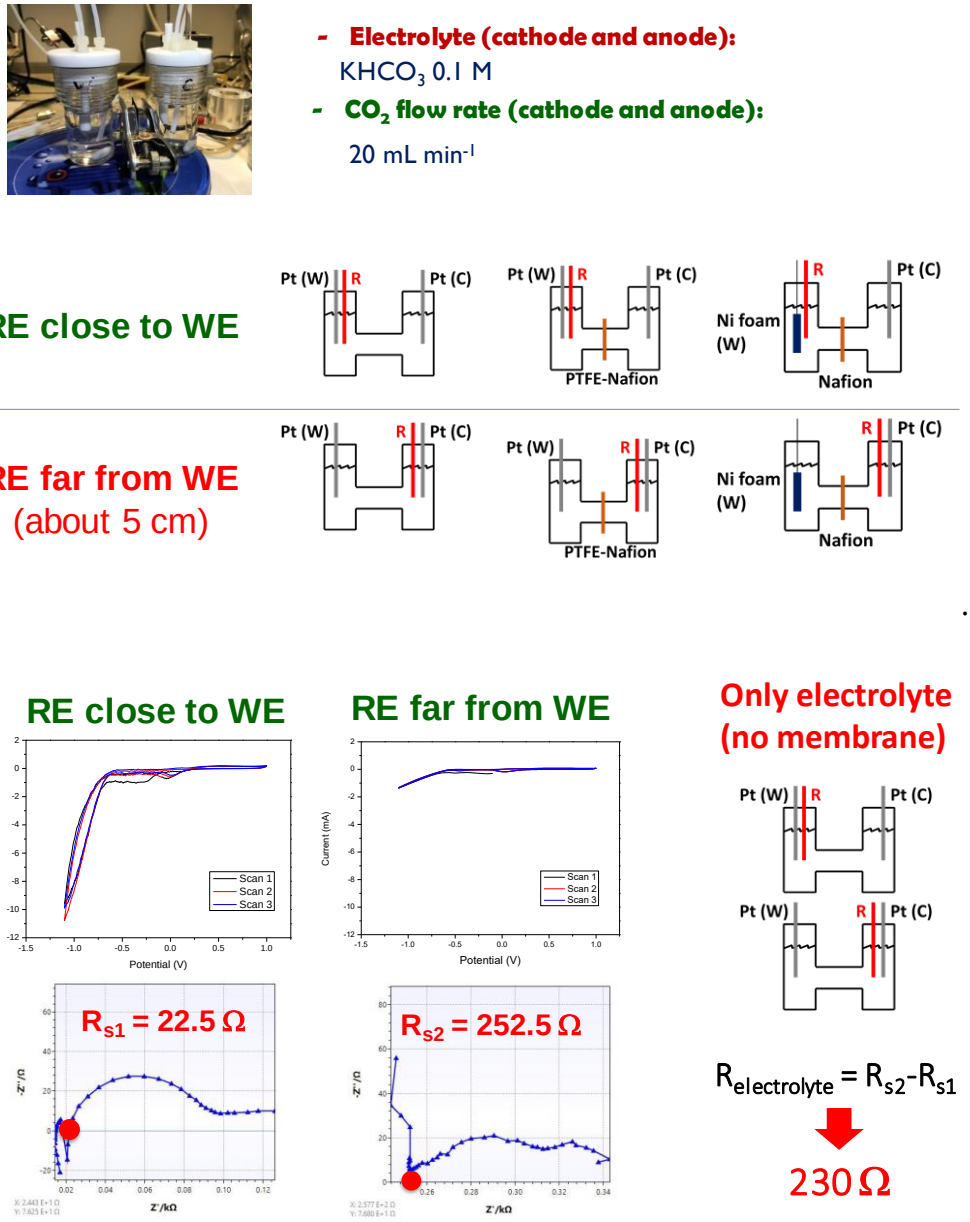

Figure 5.18 *Current density vs. potential and Nyquist plots when the RE is close and far from the WE electrode. The total electrolyte contribution to resistance is also reported.*

When the WE was close to RE, and keeping the Pt-road as WE, were measured the resistances without and with the membrane and a last measure only replacing the WE with a Ni-foam as WE. When the RE was placed far the WE (Pt-road), the resistances were evaluated with the same procedure, without and with the same membrane, and in the last case adding a Ni-foam as WE instead of the Pt-road. In the figure 5.19 is showed how the position of WE in respect to the RE affects substantially the current density, which turn from 1 mA cm^{-2} to 5 mA cm^{-2} respectively for the WE far from the RE and WE close to the RE, showing how the electrolyte plays a great contribution in total resistance; in the first case the Rs1 was

252,2 Ω and in the latter 22.5 Ω. Table 5.3 summarizes all the values of R_s and R_1. The electrolyte contribution was estimated as 230 Ω by (R_{s2}-R_{s1}) difference. Despite the PTFE-reinforced Nafion (N-234) resistance was higher than conventional Nafion® NR-212 (34 vs 13-25 Ω), this membrane allows in general to limit cross-over of species from the cathode to the anode, keeping the different pH between electrolytes in the two liquid compartments and avoiding that products obtained by reduction at the cathode migrate to the anode and oxidize. The most important result of this part of the work is the understanding that the electrolyte is the main cause of resistance within an electrochemical device. Working in gas-phase configuration or reduce the quantity of electrolyte between the electrode by using more compact devices (i.e. reducing the distance between the electrodes) are thus the possible solution to limit overpotential in an electrochemical device[32-34].

Electrolyte	RE close to WE	RE close to CE	R (Ω)
	R_s=22.5 Ω R_1=75.4 Ω J=-5.06mA	R_s=252.5 Ω R_1=89.9 Ω J=-1.01mA	230
PTFE-reinforced Nafion (N-324)	RE close to WE	RE close to CE	
	R_s=25.48 Ω R_1=309.8 Ω J=-3.34mA	R_s=286.7 Ω R_1=112.8 Ω J=-1.00mA	34
MEA (GDL + Nafion NR-212)	RE close to WE	RE close to CE	
	R_s=26.92 Ω R_1=123.5 Ω J=-8.01mA	R_s=291.3 Ω R_1=1E20 Ω J=-9.93µA	13-25
Gas phase simulation (GDL+ Nafion 212)		RE close to CE	
		R_s=118.9 Ω R_1=35.2 Ω J=-4.00mA	

Table 5.3 *Series resistance (Rs), charge transfer resistance (R1) and global cell resistance for each element within an electrochemical device.*

5.3.5.2 Electrode pH stability evaluation

The explorable pH range in both liquid compartments (cathode and anode) is limited by several factors, including the stability ranges of the respective electrodes. Figure 5.19 shows the E/pH diagram of Cu_2O, namely the phase Pourbaix diagram, evidencing all the Cu species in equilibrium at a defined potential and pH (in the same conditions of pressure and temperature). The explored areas for electrochemical CO_2 reduction in this work are highlighted in the diagram (see red and green squares), while the red and green lines correspond to the

pH/potential profiles for CO_2ERR and OER. Using a copper-based cathode, it should be taken into account its low stability due to a wide spectrum of reduction and/or corrosion phenomena, which can affect its performances causing leaching in the solution. The use of anode materials different from Pt or C (e.g. Ni-based electrodes), usually stable at higher pH values, should also be carefully considered, as an anolyte different from $KHCO_3$ aqueous solution should be used, because its solubility in water (3.6 M) allows to reach a maximum pH of 8.1. These considerations make necessary to work at different pH values in the two half-cells, in order to not compromise the performances of the two electrodes (cathode and anode) for the CO_2ERR and OER, respectively. As described in the previous sections, the use of a PTFE reinforced membrane can help to maintain a good separation of the two compartments minimizing crossover phenomena.

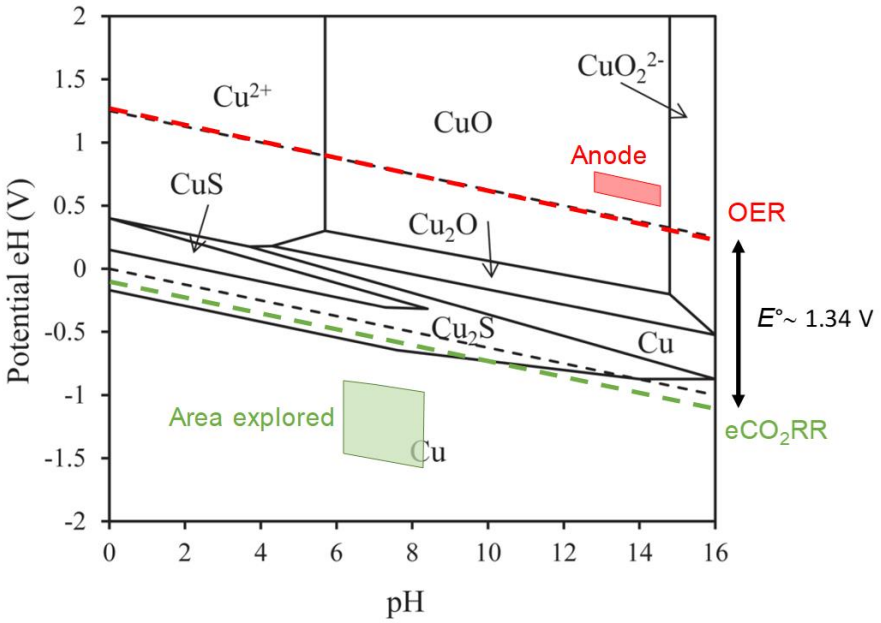

Figure 5.19 *Pourbaix diagram (Potential vs. pH) for Cu species in CO_2 electroreduction.*

5.3.5.3 Choose of the best working configuration

After the evaluation of resistance losses within the cell, a series of tests were performed, aimed at finding the best operating configuration in CO_2ERR process. In designing an electrochemical cell, three different compartments can be added: i) a gas chamber, to feed CO_2 and collect the gas products; ii) a liquid cathode compartment, with the catholyte in contact with the Cu-based catalyst on GDL; iii) a liquid anode for OER, separated from the cathode by a membrane.

Many operative cell configurations can be investigated. In this work, two configurations were explored: configuration n.1 and configuration n.2. They differ each other by the possibility or not to close the gas chamber exit, and leave the possibility to collect gases in the cathode.

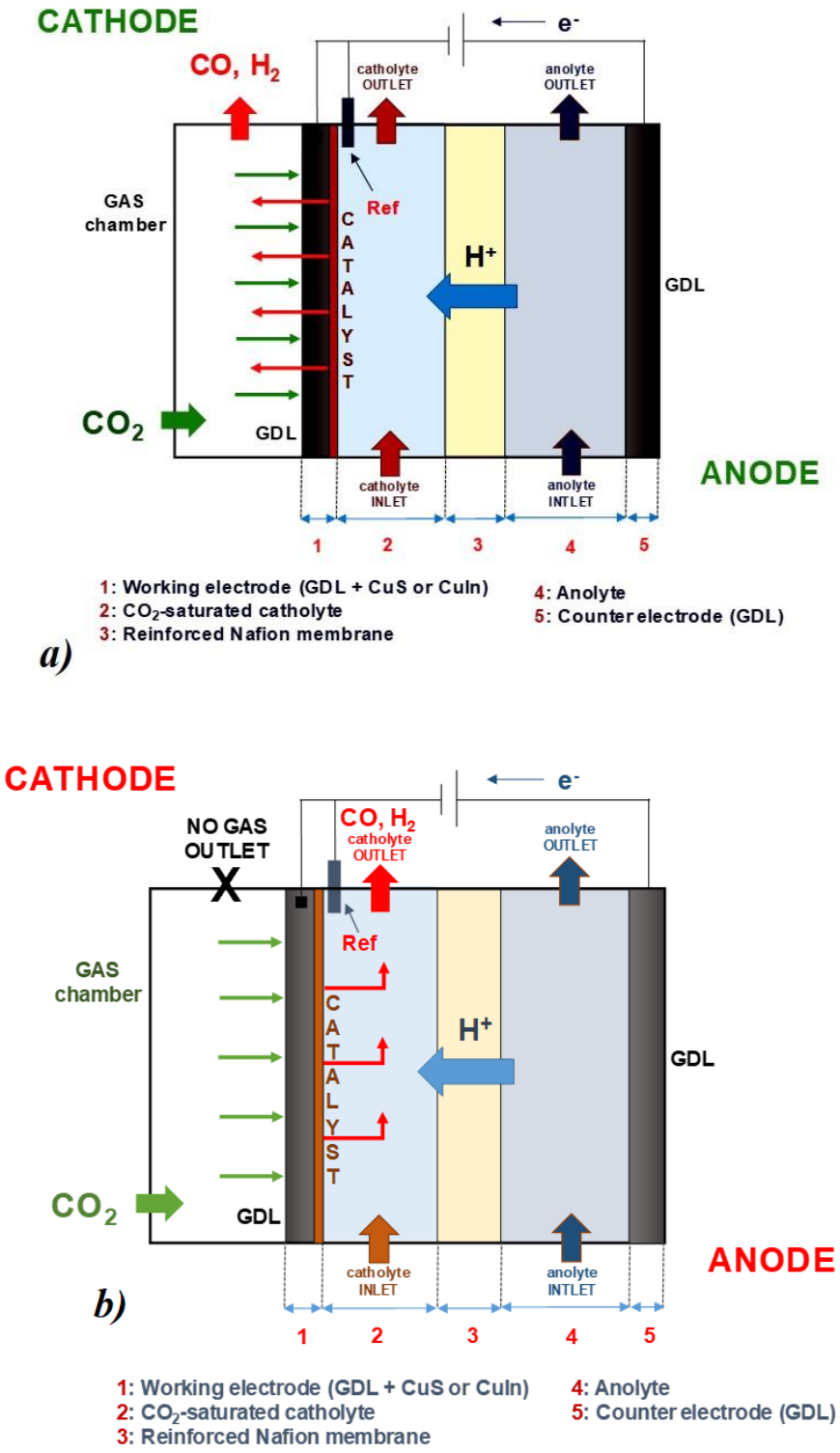

Figure 5.20. a) *Configuration n.1;* ***b)*** *Configuration n.2.*

In configuration n.1, CO_2 is introduced into the gas chamber and passes through the GDL reaching the catalyst (Figure 5.20a); the gas products (mainly CO and H_2) come back through the GDL and go out from the gas chamber. The liquid products, instead, (mainly formic acid) are collected in the cathodic compartments. The peculiarity of this configuration is the easy separation of gas and liquid product flows. For configuration n. 2 (Figure 5.20b), CO_2 is introduced into the gas chamber but, as the gas chamber outlet is closed, it is forced to cross through the GDL and exit from the liquid cathode compartment. The main advantage of this configuration is the increase of the local concentration of CO_2 directly on the catalyst surface, which is usually limited by the CO_2 solubility in an aqueous electrolyte. However, further resistances are added due to the pressure drop of gas CO_2 that must pass through the GDL.

These two configurations were realized and tested in lab-scale, using GDL both as WE and as CE, with 0.1 M $KHCO_3$ catholyte (saturated with CO_2), applying a potential of -0.8 V vs RHE, and flowing 20 mL min^{-1} in the cathode. The currents, due to the absence of an efficient electrocatalyst (i.e. Cu) were lower, in the order of -0.3 mA cm^{-2}, but CO and HCOOH were obtained (even if with low productivity), due to the presence of a carbon microporous layer on the commercial GDL, necessary for a better adhesion of the electrocatalytic powder on the GDL surface.

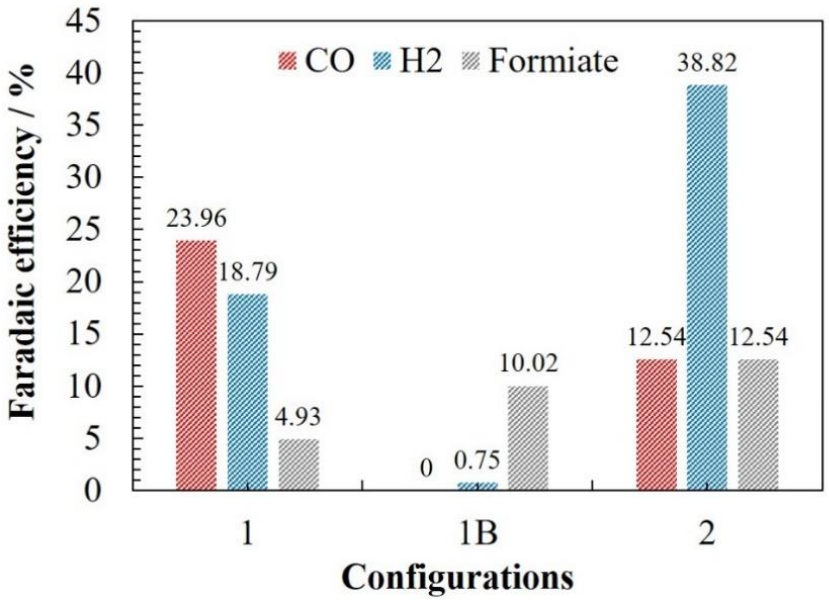

Figure 5.21 *Faradaic Efficiency (FE) % for different cell configurations.*

The gas products were collected both from the outlet of the gas chamber (see 1 configuration) and in the cathode compartment (see 1B configuration). The results show how most of the gas products were found in the gas-chamber outlet, ad only a small fraction of hydrogen was collected from the catholyte reservoir (Figure 5.21). This is a confirmation of the theoretical pathway illustrated in the Figure 5.20a. Moreover, the configuration n.1 allowed a higher collection of CO and less of H_2, if compared to the configuration n.2, at least when GDL bare foils are used as electrodes.

5.3.5.4 Optimal cathodic pH

An important prerequisite, before performing all the tests, is the evaluation of how the catholyte pH value can influence the current density and the Faradaic efficiency. Test aimed to obtain this information were made using CuS_x or *Cu-In* electrocatalysts (prepared as described in the experimental part) as the cathode, and GDL as the anode adopting the configuration n.1.

The use of commercial GDL electrodes as the anode allowed to focus only on the electrocatalyst behaviour excluding the contribution of a custom-prepared anode for OER, which can suffer of reproducibility issues. The tests were carried out at three different pH values (5.9, 6.8 and 8.1) obtained by CO_2-saturated 0.01, 0.1 and 3.6 M $KHCO_3$ aqueous solutions, respectively. A potential of -0.8 V vs RHE was applied at the working electrode (cathode), and two flow streams of CO_2 were fed into the cell: one into the gas-chamber and another into the cathode-compartment, both of 20 mL min^{-1}.

All the results are summarized in the Figure 5.22.

The current density increases with the pH in the all the tests. In the case of CuS_x (solid blue line), it was -0.79, -2.81, -44.7 mA cm^{-2} at pH 5.9, 6,8, 8.1, respectively. For the *Cu-In* sample (solid red line), the current density was -0.79, -5.26, 42.2 mA cm^{-2} at pH 5.9, 6,8, 8.1, respectively. The Faradaic efficiency to carbon products (CO and HCCOH) was estimated for both the catalysts, evidencing a maximum at pH = 6.8 and decreasing at pH 8.1. The maximum FE% was 46% for CuS_x and 42.1% for *Cu-In*. These preliminary results show that the optimal pH is 6.8 for both the catalysts.

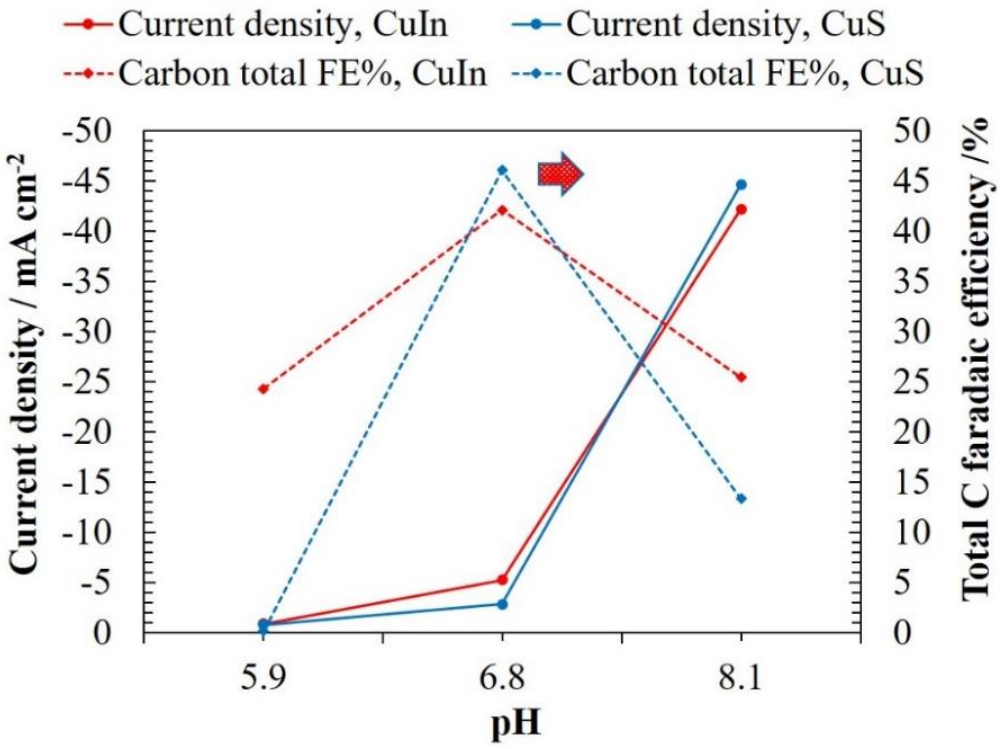

Figure 5.22 *Current density and Total Carbon Faradaic efficiency for different catholyte pH values and cell configuration.*

In the configuration n.2, as mentioned in the previous section, the CO_2 enters the gas chamber and flows through the GDL, while the gases products are detected from the cathode compartment. To choose the optimal CO_2 flow, several tests (90 min long) were performed flowing the CO_2 only into the gas chamber (from 5 to 20 mL min^{-1}).

A cathodic potential of -0.4 V vs RHE with GDL both as cathode and anode was applied in all these tests. It can be observed how the hydrogen concentration (expressed in ppm) increases with decreasing the inlet CO_2 flow (flows of 5 mL min^{-1}, green bars, exhibit the maximum values), reaching a plateau and stable value after 30 min (Figure 5.23). The FE% resulted similar for both the tests carried out at 20 and 10 mL min^{-1}. This consideration makes favourite the use of 10 mL min^{-1}, thus saving CO_2.

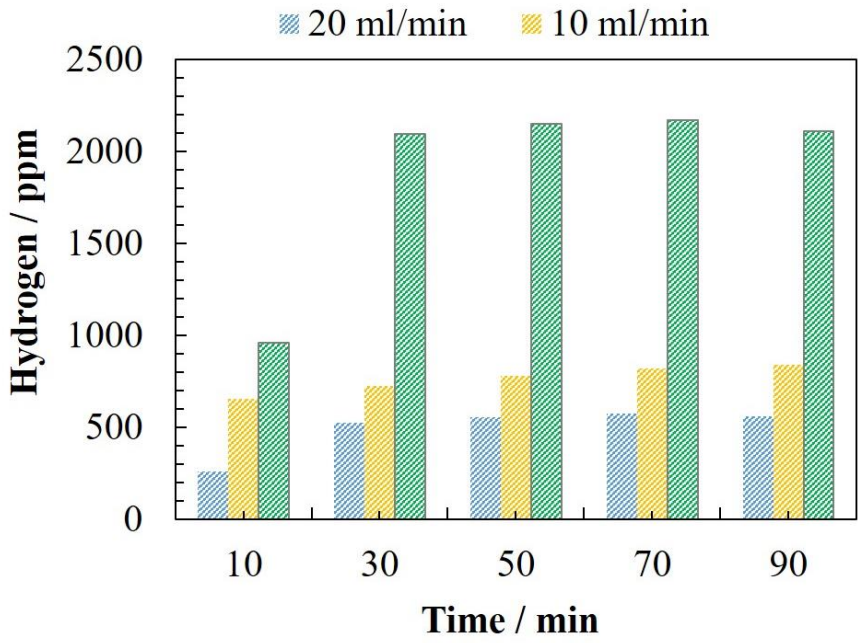

Figure 5.23 *CO_2 flow influence in hydrogen concentrations.*

5.3.6 *CuS_x* selectivity

Tests at different cell configuration

Once determined the optimal pH catholyte, a series of tests were carried out to analyse the performances of a *CuS_x* electrocathode, whose synthesis was described in the paragraph 5.3.1. These tests were performed, with both the configuration n.1 (Figure 5.24a) and n.2 (Figure 5.24b), at different cathodic potentials with 0.1 M $KHCO_3$ aqueous electrolyte in both the liquid compartments. In all the graphs, it is only reported formic acid (HCOOH) as the main carbon product because *CuS_x* acts like a selective electrocatalyst to formic acid[35]. For the configuration n.1, at -1 V vs RHE, the current density, FE and the EE were: 7.2 mA cm^{-2}, 57.9 % and 26.6 % respectively. EE represents the Energetic Efficiency and was calculated as $\frac{E^\circ \ FE}{E^\circ + \mu}$, where E° is the thermodynamic potential, FE the Faradaic efficiency and μ the cell overpotential. It expresses the ability to convert the electrical potential applied into the desired product.

For the configuration n.2 at the same potential, these values were 6,6 mA cm^{-2}, 39.6 % and 18.8 %. The values of FE% to CO, not reported in the graphs, were estimated as 1.62 and 0.84 for the configuration n.1, and 1.7 and 0.80 for the configuration n.2.

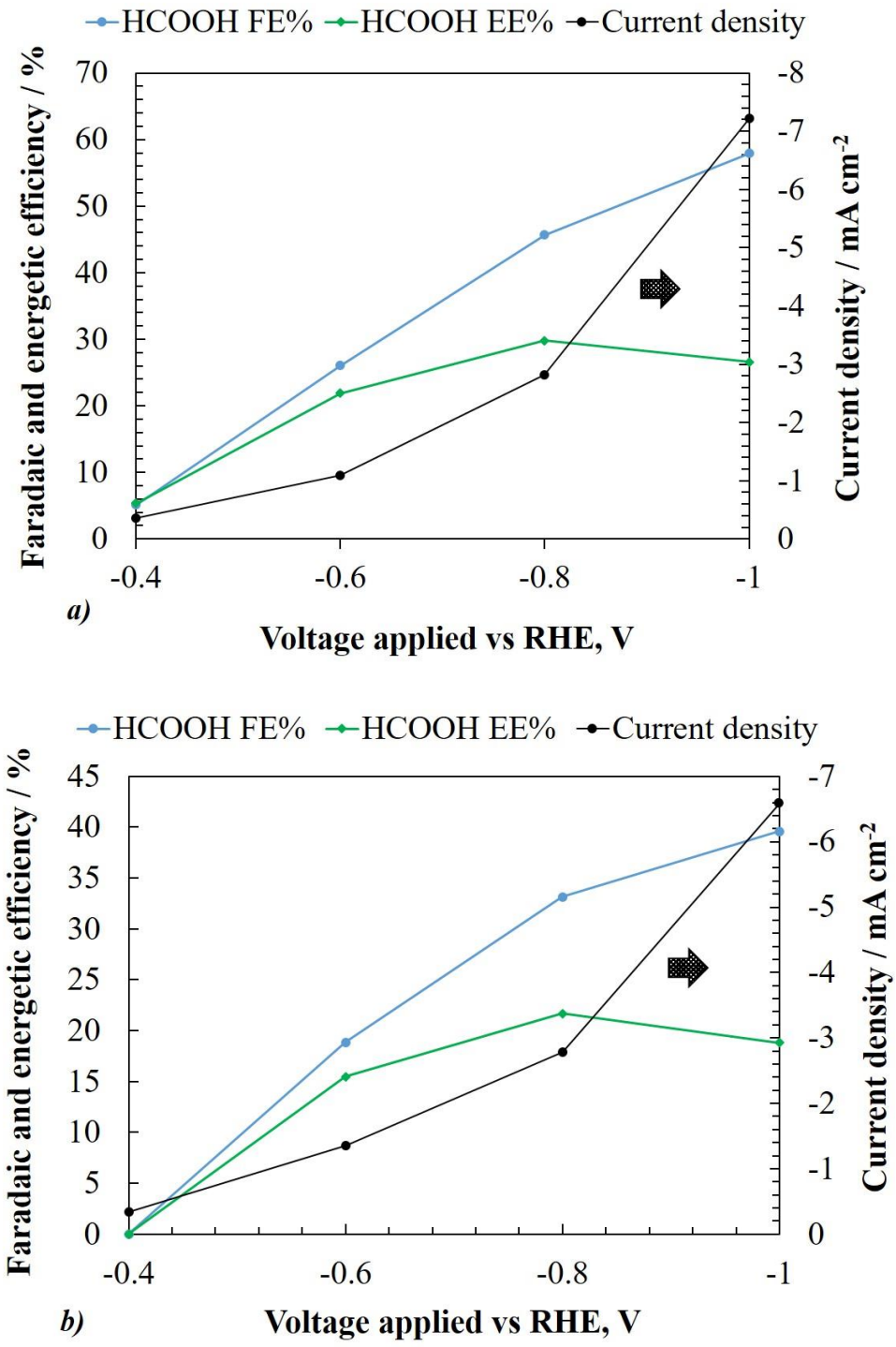

Figure 5.24 *Formiate FE / %, EE / %, J / mA cm^{-2}* ***a)*** *Configuration n.1* ***b)*** *Configuration n.2*

Figure 5.25 shows the profiles of FE% of H_2 (grey lines), HCOOH (green lines) and CO (red lines) for both the configurations (solid line for n.1 and broken for n.2) and for different cathodic potentials. It can be observed how the FE% values to formic acid and carbon monoxide, even with significate difference in the order of magnitude, increase with the potential while, on the contrary, the hydrogen FE% decreases. Except for hydrogen, all the values reported with the configuration n.1

are higher than that of configuration n.2. The formic acid FE% for the configurations n.1 and n.2 result 58.5 and 39.5 % at -1 V vs RHE, respectively, while for hydrogen FE% were 33.3 and 39.6%, respectively.

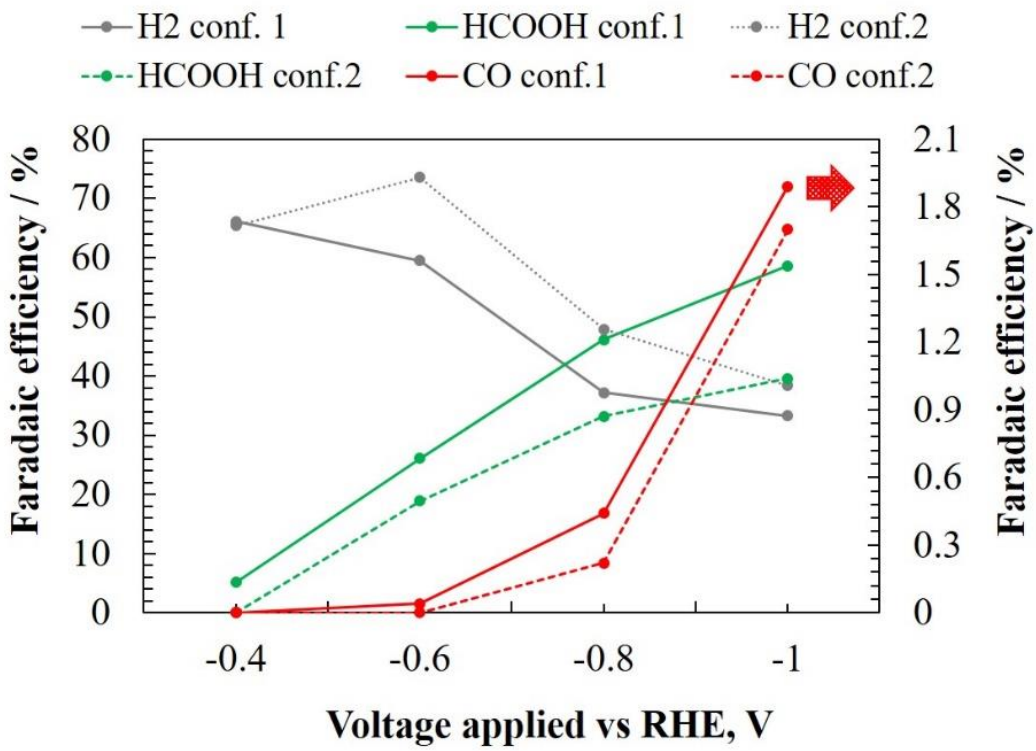

Figure 5.25 *Faradaic efficiency % profiles at different applied voltages for CuS_x tested at pH=6.8 in: conf. n.1 (solid line) and conf. n.2 (broken line).*

5.3.7 *Cu-In* selectivity

Tests at different cell configuration

In this section, the tests with *Cu-In* as electrocathode and GDL as anode are reported. These tests were carried out under the same conditions of the tests reported for CuS_x. The FE% and the current density were estimated for different potentials and for the configuration n.1 (Figure 5.26a) and n.2 (Figure 5.26b).

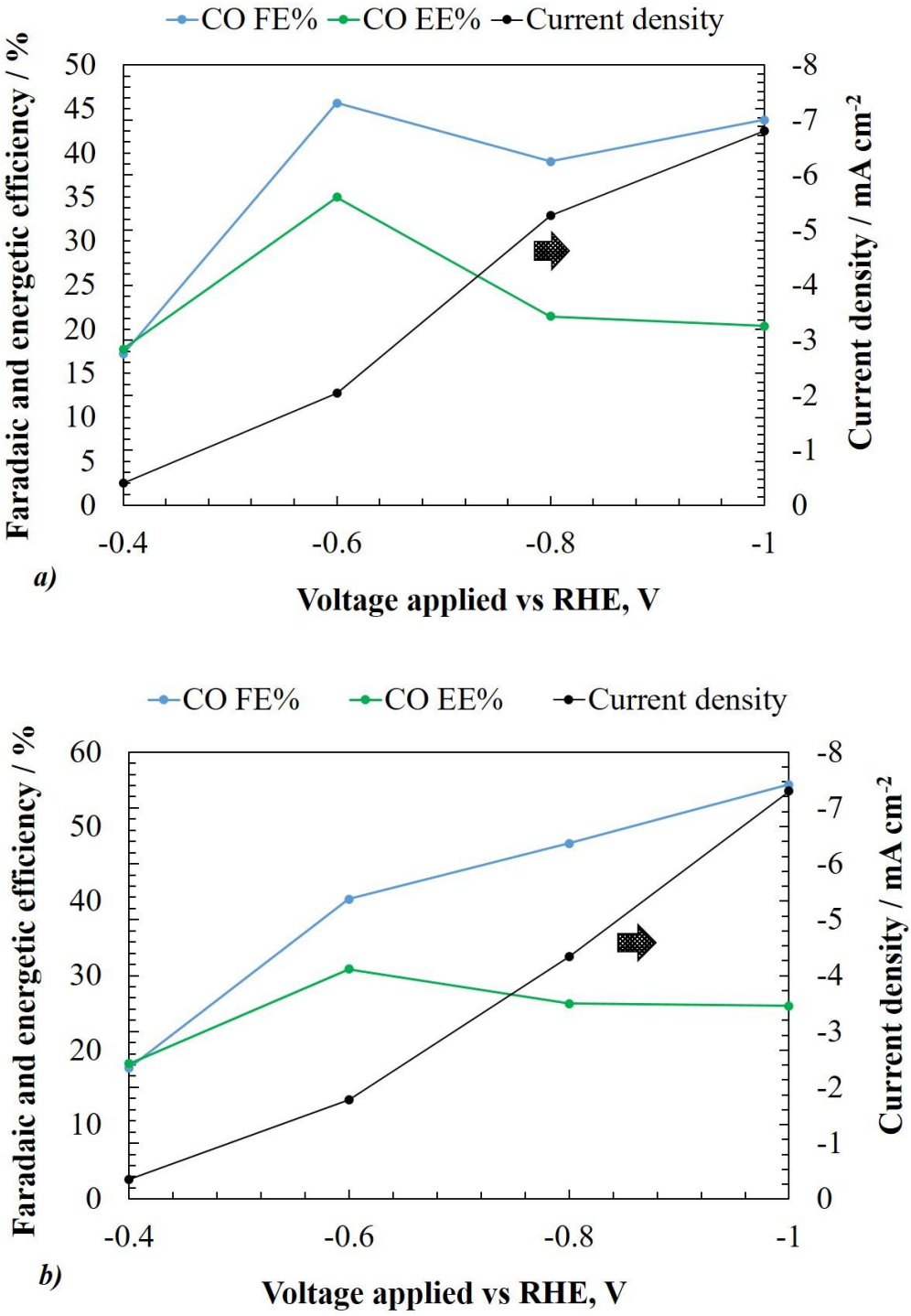

Figure 5.26 *CO FE / %, EE / %, J/ mAcm-2* ***a)*** *Configuration n.1* ***b)*** *Configuration n.2*

Figure 5.27 shows a plot of current density and the CO FE and EE for the two configurations, excluding the HCOOH. *Cu-In*, in fact, is an electrocatalyst selective to the formation of carbon monoxide, as reported by ETH et al.[36]. Current density values for the two configurations seem to be slightly different at -0.8 V vs RHE, while they are quite similar at the other two potentials. The carbon monoxide FE%

values for the configurations n.1 and n.2 result 43.73 and 55.62 % at -1 V vs RHE, respectively, while for hydrogen, FE% were 21.17 and 19.85%, respectively.

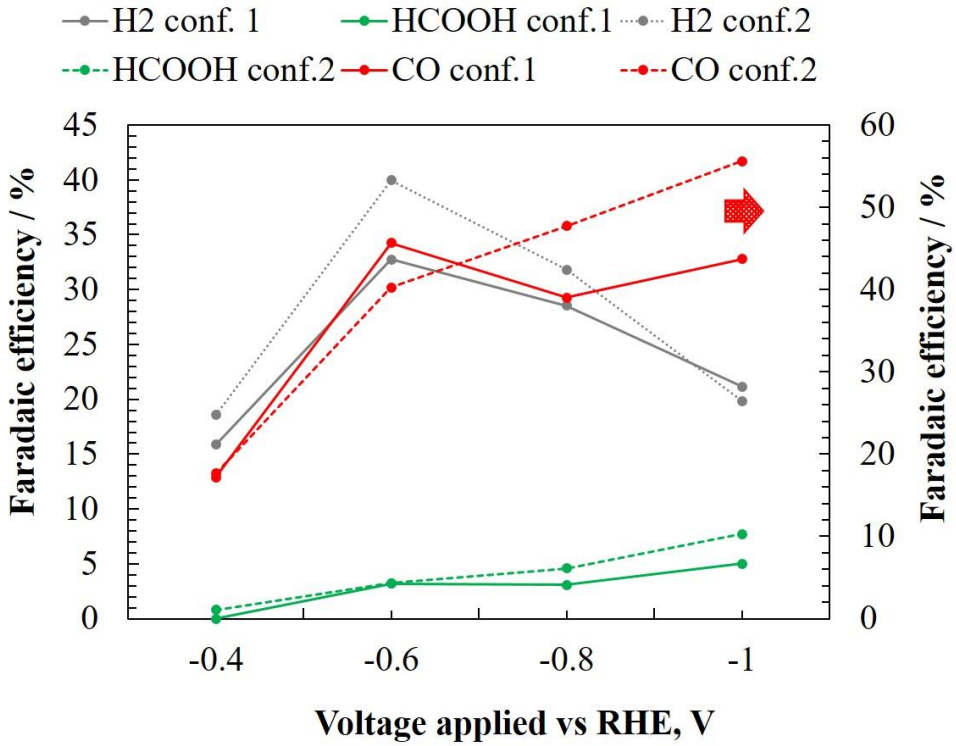

Figure 5.27 *Faradaic efficiency % profiles at different applied voltages for Cu-In in* ***a)*** *configuration n.1 (solid lines) and* ***b)*** *configuration n.2 (broken lines)*

5.3.8 Comparison between CuS_x and Cu-In

Cyclic voltammetry

In this section, the main cyclic voltammetry curve (CVs) profiles are reported for all the electrocatalytic tests. The CVs were performed in any case starting in the following range: from the OCP to the target final value in the first cycle and from 0.4 V vs RHE up to the same final value in the following cycles. The CV were made before (CV_1, solid lines) and after the CA (CV_2, broken lines) until stabilization of the curve, as described in the protocol for the electrochemical tests. The CV_1 and CV_2 for the tests with CuS_x as the cathode are reported in Figure 5.28a,b respectively. At -0.4 V vs RHE, the two CVs (green curves) have similar profiles, in both intensity and shape, with a current density of -0.5 mA cm^{-2}. They diverge at -1 V vs RHE, and the current density for the CV_1 and CV_2 resulted respectively -6.3 to -8.6 mA cm^{-2}. The two onset potentials at -0.4 and -1 V vs RHE

were -0.25 an -044 V vs RHE, respectively. The onset potential is an indication of the start of the reduction reaction at a significant rate.

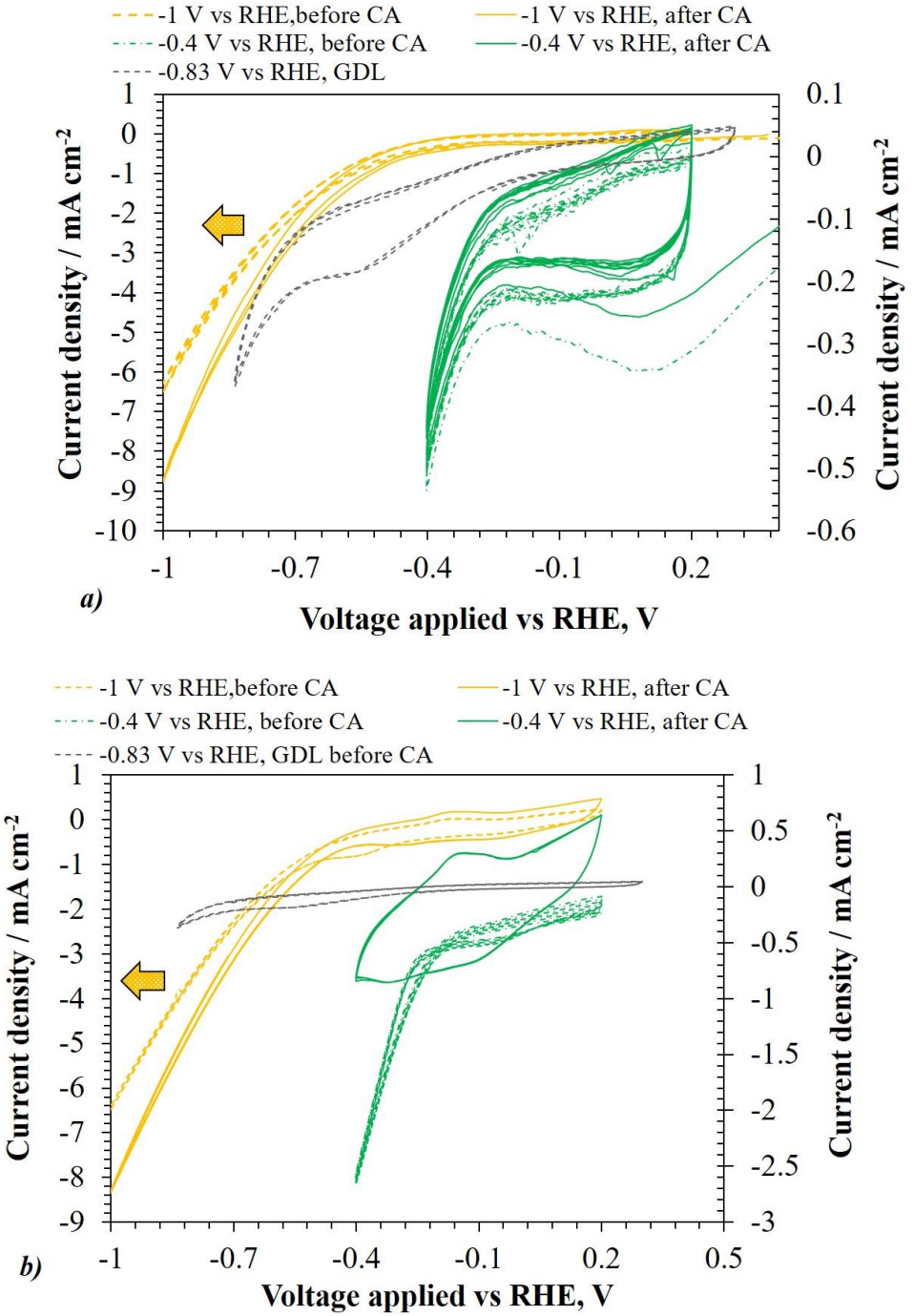

Figure 5.28 *CVs evaluated before (broken lines) and after the CA (solid lines) for a) CuS_x b) Cu-In compared with the CV using GDL as cathode (broken black lines).*

The CV_1 and CV_2 for the tests with *Cu-In* at -0.4 V vs RHE totally differ in intensity and shape, becoming flatter in the latter case. These modifications are not observed at -1 V vs RHE. At -0.4 V vs RHE, the current density values for the CV_1 and CV_2 resulted in the range from-6.3 to -8.6 mA cm^{-2}, respectively, while at -1 V vs RHE

they were from -6.3 to -8.2 mA cm^{-2}, respectively. The onset potential resulted -0.20 and -0.40 V vs RHE for -0.4 and -1 V vs RHE, respectively.

Energetic efficiency

The energetic efficiency (EE%), as calculated in the previous paragraphs, is here reported for carbon monoxide and formic acid for the tests carried out with *Cu-In* (green lines) and CuS_x (blue lines) as electrocatalysts (Figure 5.29).

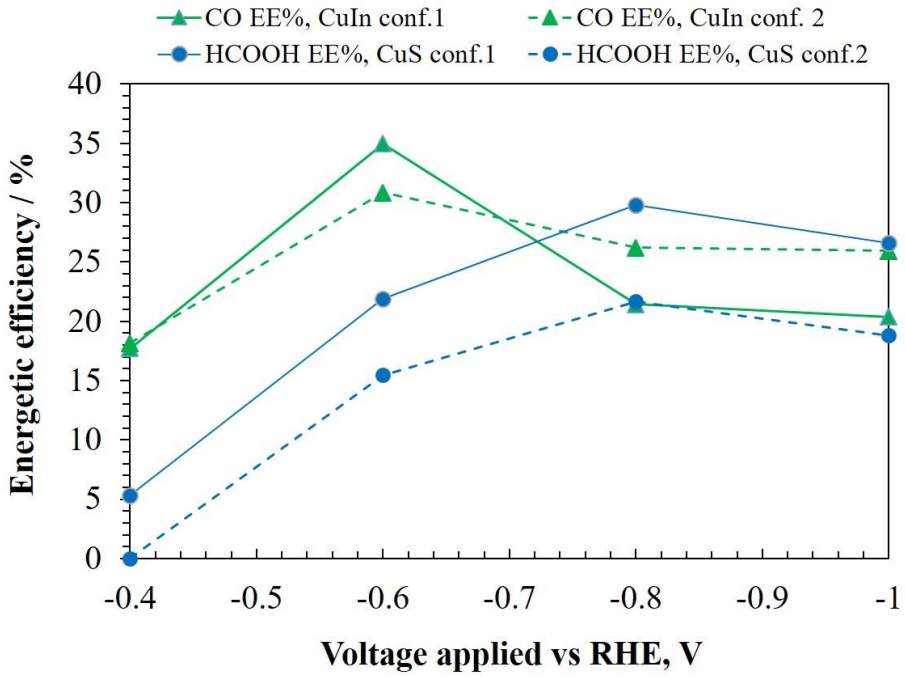

Figure 5.29 *Energy efficiency profiles at different applied voltages for CuS_x and Cu-In in: configuration n.1 (solid line) and configuration n.2 (broken line).*

The values are report for both the configuration n.1 (solid lines) and for the configuration n.2 (broken lines), and for the potentials from -0.4 to -1 V vs RHE. All the data collected so far indicate how in the adopted experimental conditions the test with *Cu-In* showed a higher FE% at -0.6 vs RHE, while the test with CuS_x provided the best performance at -0.8 V vs RHE, also confirmed by the EE calculations. For the test with *Cu-In* at-0.6 V vs RHE, the CO EE% is 34,9 % and 30,8 % for the configuration n.1 and n.2, respectively. For the CuS_x *test* the formate EE were 29.8 and 21.7% for the configuration n.1 and n.2, respectively.

From the analysis of these results, the following observation can be summarized: i) *Cu-In and* CuS_x based electrodes behaved as selective electrocatalysts for CO_2

reduction to carbon monoxide and formic acid, respectively; ii) the maximum total carbon FE% for both the electrodes was obtained at pH 6.8; iii) the maximum CO EE% with *Cu-In* as catalyst, was obtained with the configuration n.1 at pH 6.8 and -0.6 V vs RHE; iv) the maximum HCOOH EE% with CuS_x as catalyst, was obtained with the configuration n.1 at pH 6.8 and -0.8 V vs RHE.

Moreover, regarding the configuration n.2, a CO_2 flow of 10 ml min^{-1} resulted too high, causing a leaching of the catalyst. Thus, a lower CO_2 flow into the gas chamber (0.5-1.0 mL min^{-1}) could limit the detachment of the catalyst preserving the stability of the electrode.

5.3.9 Effect of the type of membranes

The behaviours of a series of commercial anionic and cationic membranes were evaluated in the electrocatalytic reduction of CO_2. In general, the use of a different membrane influences not only the total cell resistance, but can also modify the catalytic performances (e.g. formic acid productivity, minimization of H_2 production, total FE%, and crossover and osmosis phenomena). The following membranes were tested:

i) the anionic Fumapem FAA-3-30 membrane;

ii) the anionic Sustainion X37-50 membrane;

ii) the cationic (protonic) Nafion N324 membrane (Teflon reinforced);

iv) the non-reinforced protonic Nafion membranes (Nafion-212, Nafion-HP, Nafion-115 and Nafion-117);

v) the bipolar Fumasep FBM-PK.

All the anionic and bipolar membranes needed to be activated before every test, through the procedures described below:

Anionic Fumapem FAA-3-30

The membrane activation of anionic Fumapem FAA-3-30 was carried out at room temperature using a 0.5 M KOH aqueous solution. The membrane was wet for 1 hour, repeating this procedure three times. This operation allows to remove the 99.9% of the Br ion, used for storage. Once completed the activation, the membrane was washed with water to remove the base.

Anionic Sustainion X37-50

The membrane Anionic Sustainion X37-50 was soaked in 1 M KOH aqueous solution for 12-24 hours to allow the exchange of chloride ions with hydroxide ions. At the end, the membrane was rinsed with water before the use.

Bipolar Fumasep FBM-PK

The membrane Bipolar Fumasep FBM-PK was firstly put in an H-type cell, paying attention to mark the cathodic side of the membrane. Then, 0.5 M NaOH and 0.5 M H_2SO_4 solutions were added into the anode (in contact with the anion exchange membrane side) and into the cathode (in contact with the cation exchange membrane side), respectively. The membrane was left in contact with the two solutions for 12 hours. After that, the two liquids were replaced with MQ water and remained in contact with it for 1 hour (changing water every 20 min). At the end, the membrane was storage in Mili-Q water.

The Nafion membranes were instead directly activated in situ in the electrochemical device before testing of CO_2 reduction.

All the tests were carried out using a *CuS_x/GDL* (density. 1 mg cm^{-2}) as the cathode and a GDL as the anode. As catholyte and anolyte, CO_2 saturated 0.1 M $KHCO_3$ aqueous solution (pH 6.8) and 1 M KOH aqueous solution (pH 14) were used, respectively. The high OH^- concentration in the anolyte was necessary to not compromise the stability of the anodic catalyst, in the case of transferring results to the use of a real oxygen evolution catalyst (e.g. a Ni-based catalyst). Due to a considerable pH difference in the two half-cells, it was necessary to check any eventually osmotic effect, which could cause a water transfer from the less concentration to the more concentrate solution (from cathode to the anode in this case). Preliminary tests using thinner Nafion membranes (i.e. occurred for the

Nafion-212 and Nafion-HP), in fact, excluded their further use due to a considerable passage of liquid in the first 30 minutes. The non-reinforced thin anionic membranes, Fumapem FAA-3-30 and Sustainion X37-50, provided similar osmosis issues, which were instead limited with Nafion-115, Nafion-117 and bipolar membrane Fumasep FBM-PK membranes, and absent for the Teflon-reinforced Nafion membrane N324.

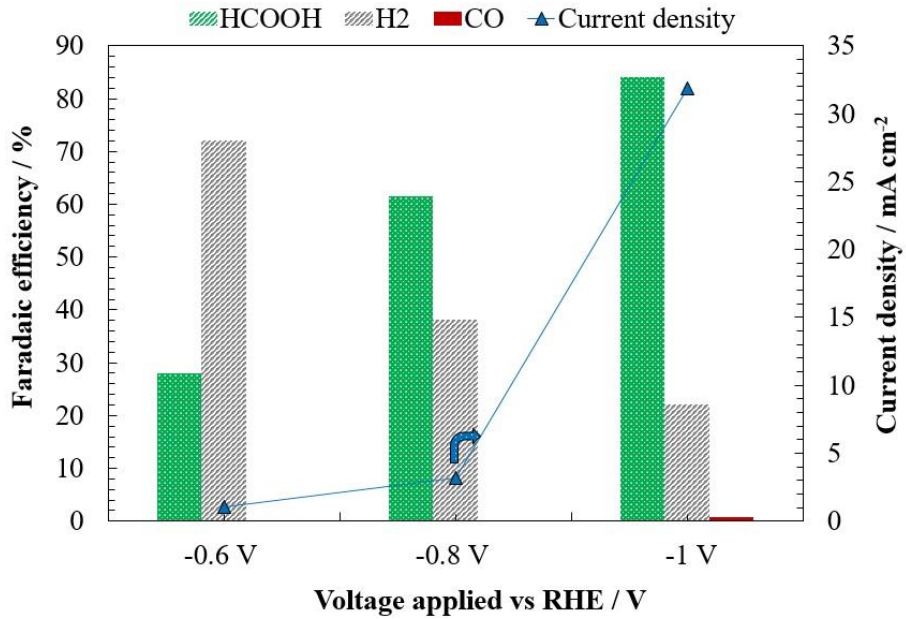

Figure 5.30 *Faradaic efficiency and current density for tests carried out with Bipolar Fumasep FBM-PK membranes.*

Figure 5.30 reports the Faradaic efficiency and the current density for tests performed at different voltages with the Bipolar Fumasep FBM-PK. The HCOOH FE at –0.6, -0.8 and -1 V vs RHE were 28%, 61.6% and 84%, respectively; the H_2 FE were instead 72%, 38% and 22%, respectively. Figure 5.31 reports the Faradaic efficiency and the current density for tests carried out with the two different membranes: the reinforced Nafion-324 and the Bipolar Fumasep FBM-PK, both applying -1 V vs RHE.

The FE for the tests with Nafion-324 and the FBM-P were: 73.6% and 84% for HCOOH, 2.93% and 0.85% for CO and 25.8% and 22% for H_2, respectively. The current density values were 14.20 and 31.8 mA cm^{-2}, respectively. Even if the behaviour of the bipolar membrane seemed better, the protonic Nafion-N324 membrane resulted more stable for many cycles of tests.

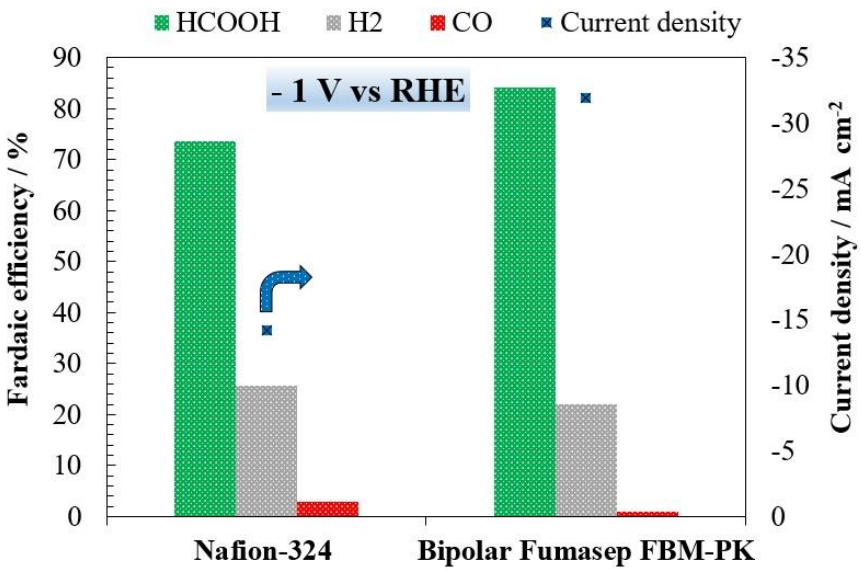

Figure 5.31. *Faradaic efficiency and current density for tests carried out with Nafion-N324 and Bipolar Fumasep FBM-PK membranes.*

5.3.10 Characterization

XRD

The crystallographic structure of the samples was investigated through X-ray diffraction of powders. All the analyses were performed from 10° to 80° through a PSD fast scan mode with these parameters: step size of 0.040° and a time per step of 165 s.

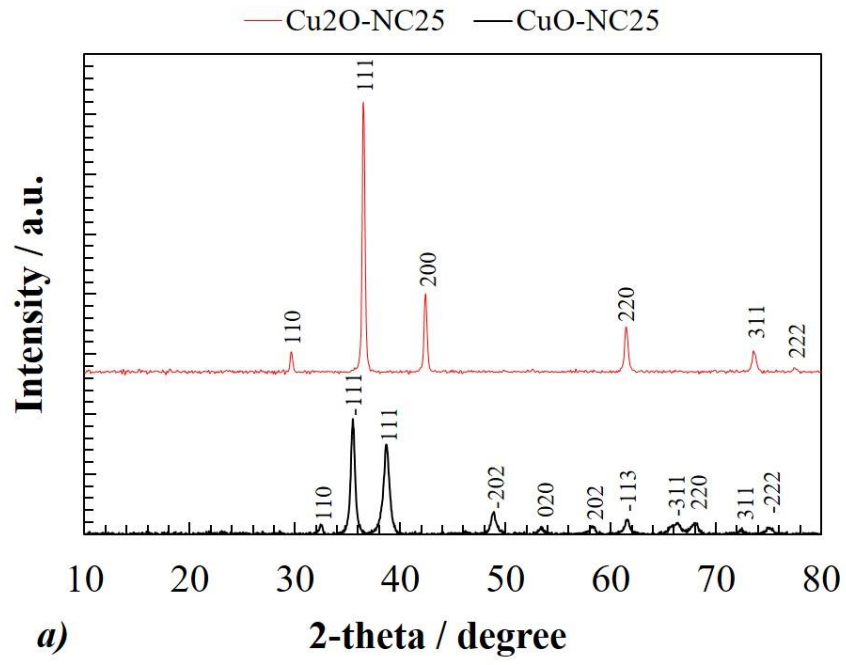

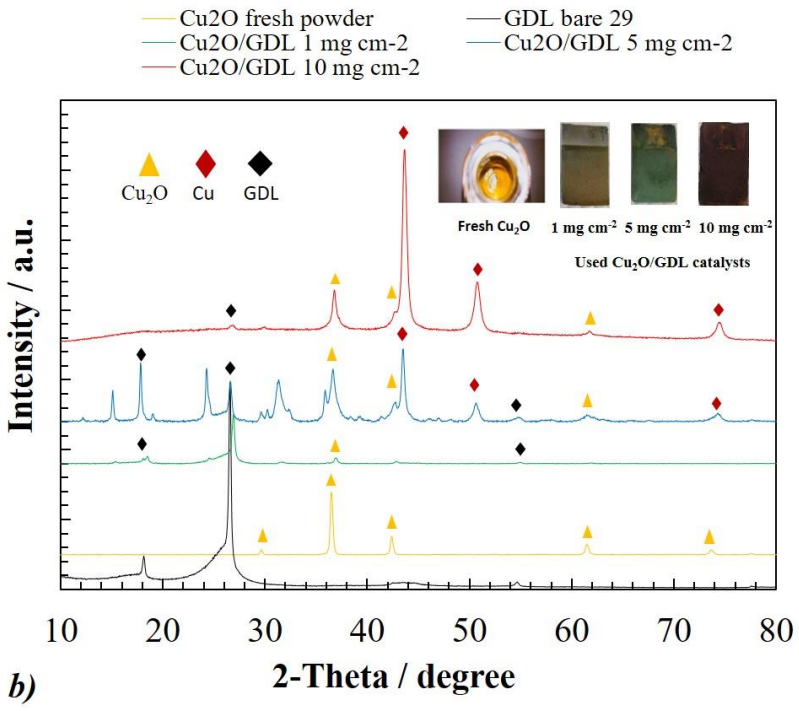

Figure 5.32 a) *Cu_2O-NC25 vs CuO NC-25 XRD;* ***b)*** *fresh Cu_2O-NC25 vs used catalyst with different loadings.*

The *Cu_2O-NC 25* (Figure 5.32, red line) was discussed in the Chapter 4. About the *CuO-NC-60*(Figure 5.32a, black line), the reflection planes at 32.6°, 35.5°, 38.7, 48.8°, 53.5°, 58.2°, 61.7°, 66.4°, 68.1°,72.4°, 75° are attributed to the (110), (-111), (111), (-202), (020), (202), (-113), (-311), (220), (311) and (-222) belonging to the copper oxide (II). In the Figure 5.32b, the XRD pattern of the fresh *Cu_2O-NC25* is compared with the used catalysts at different loadings after their processing at -0.8 V vs RHE. Metallic copper, as expected, is present in all the used catalysts due to the high negative voltage applied. Moreover, due to corrosion processes mediated by the carbonated species, some peaks of copper carbonate are present, and it is especially visible in the catalyst with 5 mg cm^{-2} loading (blue line).

Determination of the capacitance

In Figure 5.33, the double layer capacitance values, calculated for different catalyst loading, are reported. The double layer capacitance is an accumulation of electrical charges that occurs at the electrode/solution interface. The term double-layer refers to two electric layers of opposite charge, one relative to the surface of the polarized electrode and the second to a layer of solvated ions that are in the immediate vicinity of the electrode. These two layers are separated by a thin layer

(inner Helmholtz plane), varying from 0.1 to 1 nm, of solvent molecules adsorbed to the surface of the electrode, which acts as an insulator. A static electric field is formed between these two layers, and the system behaves like a capacitor, leading to an accumulation of these charges. The value of this capacitance depends on various factors, such as the applied potential, ionic concentration, temperature, adsorbed impurities, etc.

The capacitances were calculated by the procedure described in the paragraph 5.3.3.1. The indicated CP1 indicates the capacitance measured before the first CA (at -0.4 V vs RHE), while CP2 is the capacitance measured after the last CA (last test, -0.8 V vs RHE). It can be observed how the CP1 was very similar for all the different catalyst loadings, in a range varying from 2979 to 3557 µF cm^{-2} (vs 224734 µF cm^{-2} for the bare GDL at -0.4 V vs RHE). The high capacitance of the Cu_2O-based samples can consequently be attributed in part to the bare GDL. The CP2 resulted for every loading higher than CP1, and this difference increased with the catalyst loading. This behaviour can be determined by the following reasons: i) the increase in potential leads to an increase in the electric field between the two electric layers; ii) the reduction of the catalyst may lead to an accumulation of more charges. For 1, 5 and 10 mg cm^{-2}, the CP2 values were 4517, 8335 and 14347 µF cm^{-2}, respectively.

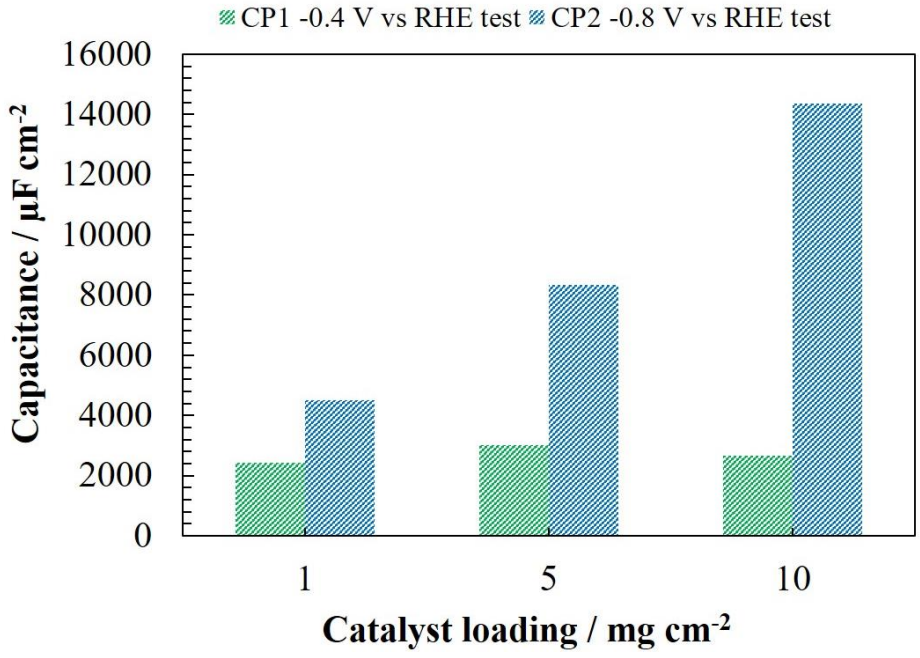

Figure 5.33 *DL capacitance for different test and loading.*

Catalyst morphology

The as prepared images of *Cu-In* and CuS_x SEM (reproduced from ETH group papers[26-27]) are showed and compared with the Cu_2O obtained with the same solvothermal synthesis, without any additional metallic precursor (Figure 5.34).

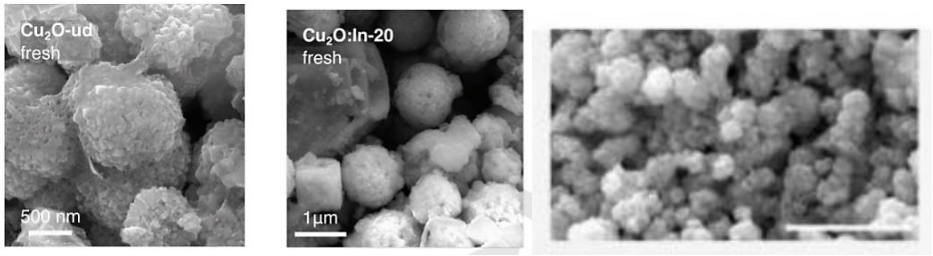

Figure 5.34 ***a)*** *Cu_2O* ***b)*** *Cu-In* ***c)*** *Cu-S*

fresh catalysts SEM images. Reproduced with permission from ref.[26-27]

The Cu_2O sample shows the presence of micrometric particles with the presence of dispersed cubes. The crystallite size for this sample, obtained through the Scherrer equation, ranges from 14 to 38 nm. Its morphology is characterized by a jagged surface made up of large irregular aggregates, with a size of about 1 µm (figure 2a). The introduction of indium causes the formation of cubes scattered on the surface and other micrometric aggregates (figure 2b). In the case of CuS_x (figure 2c) the morphology is similar, composed of irregular aggregates with dimensions in the sub-micrometric scale.

5.4 CONCLUSION

Electrocatalytic CO_2 reduction tests were carried out using Cu_xO-based catalysts as electrocathodes, both as pure oxides (+1 and +2 oxidation state) and doped with elements such as sulphur and indium, to address the selectivity towards formic acid and carbon monoxide, respectively.

Considering that the configuration of the reactor is of great importance in determining the total performance, various attempts have been made in this work to evaluate the best configuration to increase the Faradaic efficiency towards carbonaceous products improving the overall performances. These samples were deposited by spray-coating on gas diffusion layer (GDL), with various catalyst loadings. For the first test, a liquid-phase reactor, consisting of two chambers

(anode and cathode) separated by a proton exchange membrane (Nafion N324) was employed. In this configuration, tests processing Cu_2O and CuO as electrocatodes and GDL as anodes were carried out, in a potential range window from -0.4 to -0.8 V vs RHE. An operating protocol was identified for all the tests, consisting in the subsequent application of various procedures in order to standardize each operation and make the measurements comparable. Before the chronoamperometric (CA) measurement, for example, a series of CVs were carried out in order to stabilize the electrochemical system and work in steady-state. These electrocatalytic tests were aimed at evaluating i) the formed carbon-based products; ii) the influence of catalyst loading; iii) the influence of the oxidation state of copper.

The second part of the work concerned the optimization of the electrochemical cell. A gas chamber has been added to the reactor together with the anode and cathode compartments; this is an electrolyte-free chamber fed directly with a flow of pure CO_2, which then crosses the GDL-based catalyst, whose active sites are exposed to the cathodic chambers. The main tasks of the work were related to i) solving all the issues regarding the sealing of the three reactor compartments to avoid leakages, ii) setting all the electrical connections and the optimization of the chamber volumes and working-reference distance; iii) evaluating the best reactor configuration, cathodic pH, incoming CO_2 flow and membrane type to maximize the overall performances.

5.4.1 Effect of copper loading and oxidation state on performances

Results showed how an increase in the catalyst loading leads to an increase in the Faradaic efficiency towards formic acid and carbon monoxide, with the best performances at 10 mg cm^{-2}. Higher potentials than -0.6 V vs RHE, however, decreased the performances, due to catalyst deactivation phenomena. The CuO sample in general showed better Faradaic efficiencies and selectivity to CO compared to Cu_2O, with maximum values obtained at -0.6 V vs RHE. The testing results were supported by impedance measurements using electrochemical impedance spectroscopy (EIS). These measurements were made in two different electrochemical environments, called "system A" and "system B". The first is a solution in PBS and potassium ferrocyanide and the measurements were made by immersing the catalysts deposited on Screen printed carbon electrodes in these

solutions and applying a potential of 0.3 V. These measurements were carried out to study the behaviour of the sample in a reference system widely used in literature, especially in the field of sensors. The "B" system is instead the same electrochemical environment in which the CO_2 electro-reduction reactions were carried out. The measurements showed a lower value in the charge transfer resistance for the CuO sample (6.5 Ω against 39.5 Ω for Cu_2O/GDL).

5.4.2 Optimization of the electro-device

5.4.2.1 Evaluation of the reactor internal resistances

Preliminary tests were made to determine the internal elements of an electrochemical cell that contribute more to the overall resistance. The resistance contribution of the different parts of an electrochemical cell, including the electrolytes, electrodes and membranes, were estimated in an H-type cell. The experiments were carried out moving the working electrode close or far to the reference electrode, with and without a proton-exchange membrane and replacing the working electrode with a Ni based anode. The results showed how the major resistance contribution was determined by the electrolyte, estimated as 230 Ω, suggesting that a compact design and a gas phase reactor would provide a lower CO_2 overpotential. Moreover, a more specific anode (i.e. based on Ni) would reduce strongly the overpotential. The protonic exchange membrane Nafion N324 provided a good separation of the two chambers, without any pH modification.

5.4.2.2 Evaluation of the most performing configuration

About the best reactor configuration, two different configurations were proposed and studied. For this scope, electrochemical tests with GDL as working and counter electrodes were performed, under the application of -0.8 V vs RHE in 0.1 M $KHCO_3$ saturated with CO_2 as catholyte. The results showed in both the cases a good production of CO and HCOOH. However, when the gas chamber was kept open and the CO_2 flowed through the GDL catalyst, reacting and then coming out from the gas chamber (configuration n.1), HCOOH productivity was maximized and H_2 evolution was lower.

5.4.2.3 Effect of the best catholyte pH

For the evaluation of the optimal catholyte pH, several tests were performed processing CuS_x and Cu-In as electrocathodes and GDL as anode, with $KHCO_3$ water solution saturated with CO_2 at pH 5.9, 6.8 and 8.1. With both the catalysts, the current density increased with the pH, but in terms of Faradaic efficiency the best performances were obtained at pH 6.8.

5.4.2.4 Influence of the applied voltage on selectivity

The influence of the applied voltage was evaluated, from -0.4 to -1 V vs RHE, with both the electrocatalysts with a 0.1 M $KHCO_3$ water solution saturated with CO_2 at pH 6.8. The CuSx behaved as a HCOOH selective electrocatalyst, with the highest FE of 58.5 % reached at -1 V vs RHE. The results showed moreover how the configuration n.1 showed the best performances in terms of FE and lowest H_2 production, due to the higher gas-liquid capacity separation. The Cu-In electrode behaved instead like a CO selective electrocatalyst, with a maximum FE of 55.6 % at -1 V vs RHE and in this case the configuration n.2 provided the best performances. The energetic efficiency (EE) was calculated for both the electrocatalysts considering only HCOOH or CO as the main product contribution for the CuS_x and Cu-In, respectively. In both the configurations, the maximum EE % for C*u-In* was obtained at -0.6 V vs. RHE, while the maximum efficiency shifted to -0.8 V vs. RHE for CuS_x.

5.4.2.5 Influence of the membrane

Additional tests were performed with different protonic and anion exchange membranes, reinforced and not, processing CuS_x as electrocathode. Due to osmosis phenomena especially present for the thinner membranes, the comparisons were finally focused on the following two membranes: protonic reinforced Nafion N324 and bipolar Fumasep FBM-PK The performances of these two membranes were then compared in a test carried out at -1 V vs RHE employing 1M KOH solution as anolyte, processing the CuS_x cathode and a GDL anode. The performances in terms of HCOOH FE were comparable and no evident difference was detected, but the

Nafion N324 membrane allowed to limit cross-over phenomena and avoid oxidation of the reduction products at the anode.

As proved by the experimental results, the resistance of an electrochemical cell is mainly determined by the concentration, nature and volume of electrolyte present between the electrodes. A possible development in the future is to re-design the cell and minimize all the internal volumes in order to reduce these internal resistances. Finally, the use of a bimetallic copper-based system and adequate engineering of the reactor, in addition to the possibility of coupling the system with a renewable source of external energy (sunlight), represent a very promising way for future developments on the reduction of CO_2.

5.5 REFERENCES

1) Sánchez, O. G.; Birdja, Y. Y.; Bulut, M.; Vaes, J.; Breugelmans, T.; Pant, D. Recent Advances in Industrial CO_2 Electroreduction. *Current Opinion in Green and Sustainable Chemistry*. Elsevier B.V. April 1, **2019**, pp 47–56. https://doi.org/10.1016/j.cogsc.2019.01.005.

2) Nitopi, S.; Bertheussen, E.; Scott, S. B.; Liu, X.; Engstfeld, A. K.; Horch, S.; Seger, B.; Stephens, I. E. L.; Chan, K.; Hahn, C.; Nørskov, J. K.; Jaramillo, T. F.; Chorkendorff, I. Progress and Perspectives of Electrochemical CO_2 Reduction on Copper in Aqueous Electrolyte. Chemical Reviews. *American Chemical Society* June 26, **2019**, pp 7610–7672. https://doi.org/10.1021/acs.chemrev.8b00705.

3) Li, Q.; Rao, X.; Sheng, J.; Xu, J.; Yi, J.; Liu, Y.; Zhang, J. Energy Storage through CO_2 Electroreduction: A Brief Review of Advanced Sn-Based Electrocatalysts and Electrodes. *Journal of CO_2 Utilization* **2018**, *27*, 48–59. https://doi.org/10.1016/j.jcou.2018.07.004.

4) Shah, A. H.; Wang, Y.; Woldu, A. R.; Lin, L.; Iqbal, M.; Cahen, D.; He, T. Revisiting Electrochemical Reduction of CO_2 on Cu Electrode: Where Do We Stand about the Intermediates? *Journal of Physical Chemistry C* **2018**, *122* (32), 18528–18536. https://doi.org/10.1021/acs.jpcc.8b05348.

5) Nguyen, D. L. T.; Kim, Y.; Hwang, Y. J.; Won, D. H. Progress in Development of Electrocatalyst for CO_2 Conversion to Selective CO Production. *Carbon Energy* **2020**, 2 (1), 72–98. https://doi.org/10.1002/cey2.27.

6) Alfath, M.; Lee, C. W. Recent Advances in the Catalyst Design and Mass Transport Control for the Electrochemical Reduction of Carbon Dioxide to Formate. *Catalysts* **2020**, 10 (8), 1–20. https://doi.org/10.3390/catal10080859.

7) Sudhagar, P.; Roy, N.; Vedarajan, R.; Devadoss, A.; Terashima, C.; Nakata, K.; Fujishima, A. Hydrogen and CO_2 Reduction Reactions: Mechanisms and Catalysts. In *Photoelectrochemical Solar Fuel Production: From Basic Principles to Advanced Devices*; Springer International Publishing, **2016**; pp 105–160. https://doi.org/10.1007/978-3-319-29641-8_3.

8) Genovese, C.; Schuster, M. E.; Gibson, E. K.; Gianolio, D.; Posligua, V.; Grau-Crespo, R.; Cibin, G.; Wells, P. P.; Garai, D.; Solokha, V.; Krick Calderon, S.; Velasco-Velez, J. J.; Ampelli, C.; Perathoner, S.; Held, G.; Centi, G.; Arrigo, R. Operando Spectroscopy Study of the Carbon Dioxide Electro-Reduction by Iron Species on Nitrogen-Doped Carbon. *Nature Communications* **2018**, 9 (1), 1–12. https://doi.org/10.1038/s41467-018-03138-7.

9) Genovese, C.; Ampelli, C.; Perathoner, S.; Centi, G. Electrocatalytic Conversion of CO_2 on Carbon Nanotube-Based Electrodes for Producing Solar Fuels. *Journal of Catalysis* **2013**, 308, 237–249. https://doi.org/10.1016/j.jcat.2013.08.026.

10) Marepally, B. C.; Ampelli, C.; Genovese, C.; Tavella, F.; Quadrelli, E. A.; Perathoner, S.; Centi, G. Electrocatalytic Reduction of CO_2 over Dendritic-Type Cu- A Nd Fe-Based Electrodes Prepared by Electrodeposition. *Journal of CO_2 Utilization* 2020, 35 (June), 194–204. https://doi.org/10.1016/j.jcou.2019.09.017.

11) Marepally, B. C.; Ampelli, C.; Genovese, C.; Tavella, F.; Veyre, L.; Quadrelli, E. A.; Perathoner, S.; Centi, G. Role of Small Cu Nanoparticles in the Behaviour of Nanocarbon-Based Electrodes for the Electrocatalytic Reduction of CO_2. *Journal of CO_2 Utilization* **2017**, 21 (July), 534–542. https://doi.org/10.1016/j.jcou.2017.08.008.

12) Hori, Y.; Takahashi, I.; Koga, O.; Hoshi, N. Electrochemical Reduction of Carbon Dioxide at Various Series of Copper Single Crystal Electrodes. *Journal of Molecular Catalysis A: Chemical* **2003**, *199* (1–2), 39–47. https://doi.org/10.1016/S1381-1169(03)00016-5.

13) Raciti, D.; Wang, C. Recent Advances in CO_2 Reduction Electrocatalysis on Copper. *ACS Energy Letters* **2018**, 3 (7), 1545–1556. https://doi.org/10.1021/acsenergylett.8b00553.

14) Nitopi, S.; Bertheussen, E.; Scott, S. B.; Liu, X.; Engstfeld, A. K.; Horch, S.; Seger, B.; Stephens, I. E. L.; Chan, K.; Hahn, C.; Nørskov, J. K.; Jaramillo, T. F.; Chorkendorff, I. Progress and Perspectives of Electrochemical CO_2 Reduction on Copper in Aqueous Electrolyte. Chemical Reviews. *American Chemical Society* June 26, **2019**, pp 7610–7672. https://doi.org/10.1021/acs.chemrev.8b00705.

15) Wang, S.; Kou, T.; Baker, S. E.; Duoss, E. B.; Li, Y. Recent Progress in Electrochemical Reduction of CO_2 by Oxide-Derived Copper Catalysts. *Materials Today Nano* **2020**, 12. https://doi.org/10.1016/j.mtnano.2020.100096.

16) Montoya, J. H.; Peterson, A. A.; Nørskov, J. K. Insights into C-C Coupling in CO_2 Electroreduction on Copper Electrodes. *ChemCatChem* **2013**, *5* (3), 737–742. https://doi.org/10.1002/cctc.201200564.

17) Ren, D.; Ang, B. S. H.; Yeo, B. S. Tuning the Selectivity of Carbon Dioxide Electroreduction toward Ethanol on Oxide-Derived CuxZn Catalysts. *ACS Catalysis* **2016**, *6* (12), 8239–8247. https://doi.org/10.1021/acscatal.6b02162.

18) Roberts, F. S.; Kuhl, K. P.; Nilsson, A. High Selectivity for Ethylene from Carbon Dioxide Reduction over Copper Nanocube Electrocatalysts. *Angewandte Chemie* **2015**, *127* (17), 5268–5271. https://doi.org/10.1002/ange.201412214.

19) Gao, D.; Zegkinoglou, I.; Divins, N. J.; Scholten, F.; Sinev, I.; Grosse, P.; Cuenya, B. R. Plasma-Activated Copper Nanocube Catalysts for Efficient Carbon Dioxide Electroreduction to Hydrocarbons and Alcohols. *ACS Nano* **2017**, *11*, 4825–4831.

20) Kas, R.; Kortlever, R.; Milbrat, A.; Koper, M. T. M.; Mul, G.; Baltrusaitis, J. Electrochemical CO_2 Reduction on Cu_2O-Derived Copper Nanoparticles: Controlling the Catalytic Selectivity of Hydrocarbons. *Physical Chemistry Chemical Physics* **2014**, *16* (24), 12194–12201. https://doi.org/10.1039/c4cp01520g.

21) Zhu, W.; Tackett, B. M.; Chen, J. G.; Jiao, F. Bimetallic Electrocatalysts for CO_2 Reduction. *Topics in Current Chemistry*. Springer International Publishing December 1, **2018**. https://doi.org/10.1007/s41061-018-0220-5.

22) Wang, Y.; Cao, L.; Libretto, N. J.; Li, X.; Li, C.; Wan, Y.; He, C.; Lee, J.; Gregg, J.; Zong, H.; Su, D.; Miller, J. T.; Mueller, T.; Wang, C. Ensemble Effect in Bimetallic Electrocatalysts for CO_2 Reduction. *Journal of the American Chemical Society* **2019**, *141* (42), 16635–16642. https://doi.org/10.1021/jacs.9b05766.

23) Birhanu, M. K.; Tsai, M. C.; Kahsay, A. W.; Chen, C. T.; Zeleke, T. S.; Ibrahim, K. B.; Huang, C. J.; Su, W. N.; Hwang, B. J. Copper and Copper-Based Bimetallic Catalysts for Carbon Dioxide Electroreduction. *Advanced Materials Interfaces* **2018**, 5 (24), 1–34. https://doi.org/10.1002/admi.201800919.

24) Huang, J.; Mensi, M.; Oveisi, E.; Mantella, V.; Buonsanti, R. Structural Sensitivities in Bimetallic Catalysts for Electrochemical CO_2 Reduction Revealed by Ag-Cu Nanodimers. *Journal of the American Chemical Society* **2019**, 141 (6), 2490–2499. https://doi.org/10.1021/jacs.8b12381.

25) Espro, C.; Marini, S.; Giusi, D.; Ampelli, C.; Neri, G. Non-Enzymatic Screen Printed Sensor Based on Cu_2O Nanocubes for Glucose Determination in Bio-Fermentation Processes. *Journal of Electroanalytical Chemistry* **2020**, 873. https://doi.org/10.1016/j.jelechem.2020.114354.

26) Shinagawa, T.; Larrazábal, G. O.; Martín, A. J.; Krumeich, F.; Pérez-Ramírez, J. Sulfur-Modified Copper Catalysts for the Electrochemical Reduction of Carbon Dioxide to Formate. *ACS Catalysis* **2018**, 8 (2), 837–844. https://doi.org/10.1021/acscatal.7b03161.

27) Larrazábal, G. O.; Martín, A. J.; Krumeich, F.; Hauert, R.; Pérez-Ramírez, J. Solvothermally-Prepared Cu_2O Electrocatalysts for CO_2 Reduction with Tunable Selectivity by the Introduction of p-Block Elements. *ChemSusChem* **2017**, 10 (6), 1255–1265. https://doi.org/10.1002/cssc.201601578.

28) Suryanto, B. H. R.; Chen, S.; Duan, J.; Zhao, C. Hydrothermally Driven Transformation of Oxygen Functional Groups at Multiwall Carbon Nanotubes for Improved Electrocatalytic Applications. *ACS Applied Materials and Interfaces* **2016**, 8 (51), 35513–35522. https://doi.org/10.1021/acsami.6b14090.

29) Sheng, W.; Kattel, S.; Yao, S.; Yan, B.; Liang, Z.; Hawxhurst, C. J.; Wu, Q.; Chen, J. G. Electrochemical Reduction of CO_2 to Synthesis Gas with Controlled CO/H_2 Ratios. *Energy and Environmental Science* **2017**, 10 (5), 1180–1185. https://doi.org/10.1039/c7ee00071e.

30) Marques Mota, F.; Nguyen, D. L. T.; Lee, J. E.; Piao, H.; Choy, J. H.; Hwang, Y. J.; Kim, D. H. Toward an Effective Control of the H_2 to CO Ratio of Syngas through CO_2 Electroreduction over Immobilized Gold Nanoparticles on Layered Titanate Nanosheets. *ACS Catalysis* **2018**, 8 (5), 4364–4374. https://doi.org/10.1021/acscatal.8b00647.

31) Hernández, S.; Farkhondehfal, M. A.; Sastre, F.; Makkee, M.; Saracco, G.; Russo, N. Syngas Production from Electrochemical Reduction of CO_2: Current Status and Prospective Implementation. *Green Chemistry* **2017**, 19 (10), 2326–2346. https://doi.org/10.1039/c7gc00398f.

32) Genovese, C.; Ampelli, C.; Marepally, B. C.; Papanikolaou, G.; Perathoner, S.; Centi, G. Electrocatalytic Reduction of CO_2 for the Production of Fuels: A Comparison between Liquid and Gas Phase Conditions. *Chemical Engineering Transactions* **2015**, 43, 2281–2286. https://doi.org/10.3303/CET1543381.

33) Ampelli, C.; Genovese, C.; Perathoner, S.; Centi, G.; Errahali, M.; Gatti, G.; Marchese, L. An Electrochemical Reactor for the CO_2 Reduction in Gas Phase by Using Conductive Polymer Based Electrocatalysts. *Chemical Engineering Transactions* **2014**, 41 (Special Issue), 13–18. https://doi.org/10.3303/CET1441003.

34) Genovese, C.; Ampelli, C.; Perathoner, S.; Centi, G. A Gas-Phase Electrochemical Reactor for Carbon Dioxide Reduction Back to Liquid Fuels. *Chemical Engineering Transactions* **2013**, 32, 289–294. https://doi.org/10.3303/CET1332049.

35) García-Muelas, R.; Dattila, F.; Shinagawa, T.; Martín, A. J.; Pérez-Ramírez, J.; López, N. Origin of the Selective Electroreduction of Carbon Dioxide to

Formate by Chalcogen Modified Copper. *Journal of Physical Chemistry Letters* **2018**, 9 (24), 7153–7159. https://doi.org/10.1021/acs.jpclett.8b03212.

36) Larrazábal, G. O.; Shinagawa, T.; Martín, A. J.; Pérez-Ramírez, J. Microfabricated Electrodes Unravel the Role of Interfaces in Multicomponent Copper-Based CO_2 Reduction Catalysts. *Nature Communications* **2018**, 9 (1), 1–10. https://doi.org/10.1038/s41467-018-03980-9

6. GLUCOSE AMPEROMETRIC DETECTION

6.1 ENZYMATIC AND NON-ENZYMATIC GLUCOSE SENSORS

Great part of interest and efforts of the Biosensing industry has been aimed to the detection of glucose, especially nowadays in which blood continuous monitoring applications are widely spread. Clark and Lyons in 1962 introduced the first type of selective enzymatic glucose sensor, based on the quantification of oxygen consumed by glucose in a catalytic oxidation[1]. Among these, the 1-oxidase (GOx), for its characteristics of stability and selectivity, was defined by Wilson and Turner in 1992 as the ideal sensor[2]. Its redox centre, the FAD (flavin adenine dinucleotide), in contact with glucose, is reduced to ($FADH_2$), while glucose turns to glucolactone (reaction 1):

$$GO_x(FAD) + Glucose \rightarrow GO_x\,(FADH_2) + Glucolactone \qquad 1)$$

The next step involves the reoxidation of the $FADH_2$ into FAD, which can be achieved by: 1) reduction of the free oxygen present, producing hydrogen peroxide; 2) electroactive mediators; 3) electrochemical systems. These three ways represent in order first, second and third enzymatic sensor generations[3].

The reaction involving consumption of oxygen is showed below (reaction 2):

$$GO_x(FADH_2) + O_2 \rightarrow GO_x\,(FAD) + H_2O_2 \qquad 2)$$

The main disadvantage of this approach is that the free oxygen is considered like a catalytic mediator, and its quantification can be very difficult because the oxygen content can vary significantly making the measure affected by a considerable error. The mediators are electroactive species with the role to accept electrons from the $FADH_2$ centre, in order to be useful for this scope, they should have several characteristics like insoluble nature, low molecular weight, low redox-potential, high stability and toxicity. Their redox-potential should be suitable to provide

selective oxidation of the $FADH_2$ avoiding the oxidation of other interferents. As mediators, example of ferrocyanides and ferrocene derivates are reported in literature.

The third generation involves the use of solid electrodes to transfer the electrons to the redox-centre. Today, mesoporous materials with high porosity and surface area, which can interact in intimate way with enzymes allowing an easier electron transfer, are employed making possible to detect a reduction current only in correlation with the investigated process. Comparing with first and second generations, the third one allows to avoid the dependence of the oxygen content and the presence of mediators and other interfering species.

Another generation, raised in the last years, is the fourth generation, represented by non-enzymatic glucose sensors, introduced by Walther Loeb, involving electrocatalytic processes to speed up the reaction otherwise too slow to obtain significant currents[4]. The first type reported, and introduced before the oxygen electrode of Clark, was based on a lead anode used for the oxidation of glucose in sulphuric acid. The main disadvantages are related to the slow kinetics of glucose oxidation, poor selectivity, deactivation for adsorption of real sample constituents and poor pH stability range. In literature, the use of several classes of materials are reported, including nickel, platinum, copper, carbon electrodes. Electrocatalytic processes involve the formation of a bond between the electrode and the adsorbate, through the interaction of d-electrons and d-orbitals of the first. The oxidation state of the metal affects this bond strength, allowing a different adsorbate/electrode interaction which can causes in turn an easier desorption of the products. A concerted mechanism was proposed by Pletcher (Figure 6.1), proceeding with the simultaneous hydrogen extraction by the electrode and the adsorption of the organic molecules, the latter requiring then two adjacent metal sites [5]. These considerations make the engineering of geometry of the electrode surface.

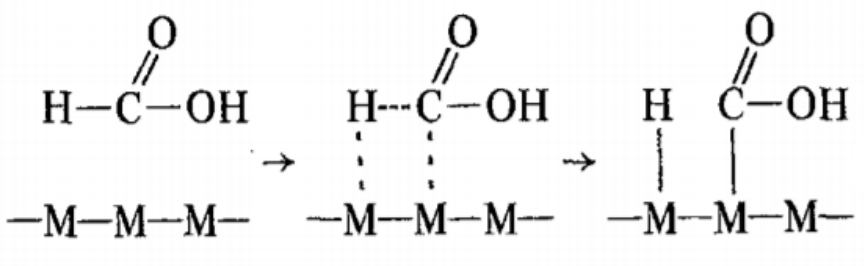

Figure 6.1 *Concerted mechanism proposed by Pletcher*[5]

It was reported that oxidation of glucose is possible for the presence of OH^- groups adsorbed on the metal surface, which provide a pre-oxidized layer that mediates the glucose oxidation, preventing the reduction of the electrode. This theory, whose mechanism is reported in the Figure 6.2, is called "Incipient hydrous oxide atom mediator" and was proposed by Burke[6].

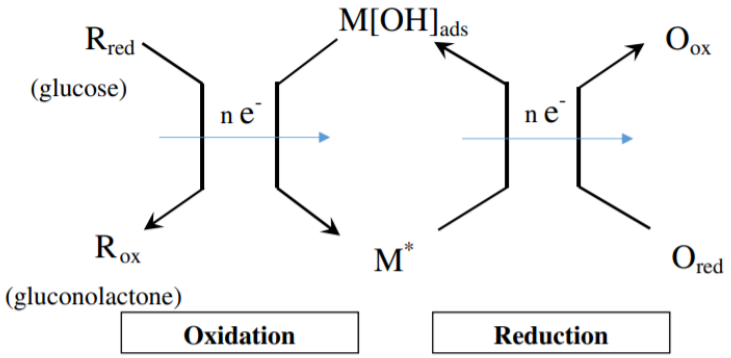

Figure 6.2 *Incipient hydrous oxide atom mediator model for oxidation of glucose*[6]

This model can be adapted for platinum, ruthenium, iridium, palladium and gold, while in the case of nickel and copper electrodes, the hydrous groups do not catalyse the reaction but affect the oxidation state of the surface-metal hydroxide. In the next paragraph, the amperometric detections by glucose oxidation in KOH water solution using cuprous oxide based sensors with different particle size, are reported.

6.2 STATE OF THE ART

In order to monitor the glucose concentration in many fields like the biofermentation processes or its physiological level in medicine field to contrast the diabetes (varying in the 3-9 mM range), a fast and cheap technique is required. The amperometric detection fits these requirements and is also characterized by high

selectivity and sensibility, low cost, easy-use and in general high reliability. Then, it is also required developing and engineering the biosensor and amperometric sensor.

Due to the numerous disadvantages that affect the enzymatic glucose sensors, like the high sensibility for the environment, the pH working range, the optimal temperature, the tricky immobilization operations and high cost, today non-enzymatic electrodes are being developed and widely spread. These consist in metal oxides like Cu_2O, NiO, TiO_2, CuO, ZnO, metal oxides deposited on carbon nanotube frameworks, and composite materials aimed to increase reliability and glucose oxidation selectivity[7-11].

In particular, cuprous oxide (Cu_2O) is a very promising material because of its low band bap (2.17 eV) and also a large surface area, and it is widely employed in several fields like electrode materials, lithium-ion batteries, gas sensors. It has been shown how this material offers good performances in terms of high selectivity in glucose detection[12-15]. Indeed, nowadays miniaturized solid electrodes using the screen printed technology (SPCE) are employed in the mass production because of several advantages. They are low-cost, characterized by an environmental friendly fabrication process, present good thermal conductibility and mechanical and electrical resistivity. These electrodes were employed also for the detection of various gasses, DNA, hydrogen, hydrogen peroxide, heavy metals and glucose[16-19].

6.3 SCOPE OF THE CHAPTER

In the following sections, all the chronoamperometry (CA) and voltammetry tests (CV) aimed to detect the glucose concentration, to establish the detection limit and the relative sensibility, are presented. As sensors, Cu_2O nanocubes prepared with different particle size by a facile wet precipitation method and deposited on screen-printed carbon electrodes (SPCEs) were employed[20]; they were characterized by UV/Visible spectroscopy, XRD and SEM analysis. This material was chosen because of its well know selectivity to glucose oxidation, easy and low-cost fabrication route and good stability.

6.4 TESTING

As mentioned above, Cu_2O nanocubes with different particles size were employed to prepare glucose sensors. For this scope, the performances of the samples Cu_2O NC-25 and NC-60 were evaluated. The wet precipitation synthesis of Cu_2O powder has been already described in Chapter 4. The samples, in the form of powders, were dispersed over commercial screen printed carbon electrodes (SPCEs), through the follow procedure: 5 mg of powder was dispersed in 100 µL of water, under sonication, to obtain a homogenous suspension. Then, 5 µL of this ink, were cast on the SPCE electrode by wet impregnation, and finally dryed. All the electrochemical experiments were carried out with a DropSens mStat 400 potentiostat. In Figure 6.3 the experimental setup is reported, focusing on the SPCE dipped into the solution, with the presence of a magnetic stirrer. The tests reported below refer to glucose amperometric detections and relative measurements of impedance.

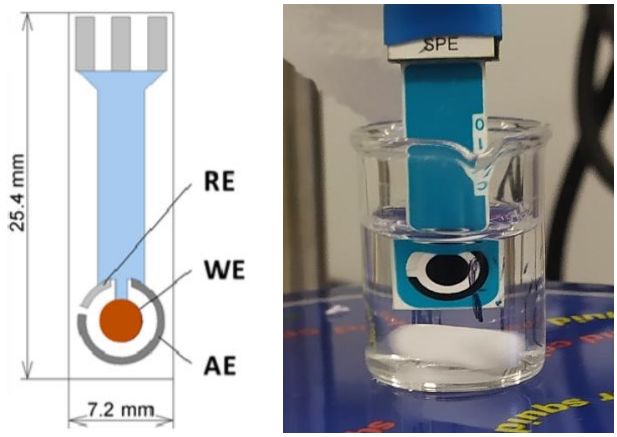

Figure 6.3 *SPCE electrode.*

Electrochemical Impedance Spectroscopy (EIS) tests, with a frequency range from 1 10^5 Hz to 0.1 Hz and amplitude of 0.01 VRMS, were carried out to test the electrochemical properties of the bare SPCE and the two Cu_2O NC/SPCEs in 5 mM potassium ferricyanide and 1 M PBS water solutions by applying a potential of 0.3 V. In figure 67, the Nyquist plot is showed, reporting in the X-axis and Y-axis the real and negative imaginary part of the system impedance[133]. It can be observed that for the three samples a semicircle profile is present at high frequencies (left portion of the graph), but in the case of the bare SPCE (blue line), it appears not defined with respect to the sample based on Cu_2O. In Table 6.1, all the values obtained are

reported, namely: the series resistance (Rs), which is the resistance due to the electrolyte and electrode combination, the charge transfer resistance (R_{ct}), calculated at infinite frequency and zero amplitude perturbation, due to the electronic transfer resistance at electrode/electrolyte interface, while W_s (Warburg diffusion resistance) is the ion diffusion resistance in the electrolyte, indicating if the reaction is controlled by diffusion. The R_{ct} is mostly used to check and compare the resistance properties of more systems, because for a given electrolyte/electrode Rs is constant and W_s is frequency dependent. The radius of the semicircle portion allows the calculation of the R_{ct}, and in the case of the SPCE resulted 10.5 kΩ, while the lower value was reported for the NC-25/SPCE, 4.85 kΩ. The higher value for the SPCE is related to its low conductivity, while the lower value of NC-25/SPCE (the semicircle is extended even for low frequencies) means that it can provide a higher electronic transfer in respect to NC-60/SPCE, whose value is 6.67 kΩ.

	Rs (Ω)	**R_{ct} (kΩ)**	**CPE**		**W_s**
			Y_O *10^6 (Ω^{-1}*s^N)	N	Y_O*10^6 (Ω^{-1}*$s^{1/2}$)
Bare SPCE	550	10.5	578	0.875	
NC-60/SPCE	420	6.67	19.1	0.795	190
NC-25/SPCE	610	4.85	24.9	0.686	

Table 6.1 *Resistances values for the bare SPCE, Cu_2O NC-25/SPCE and Cu_2O NC-60/SPCE*

In the Figure 6.4 a) and b) the equivalent electric circuit obtained through the EIS are reported, describing the electric behaviour of the electrochemical system investigated. The electrochemical system with bare SPCE and Cu_2O NC-25/SPCE sensors can be described by the model a) while the one with Cu_2O NC-25 by the model b). The first includes the CPE/R_{ct} parallel in series with the Rs, while the second differs only for the R_{ct}, which is in turn in series with the W_s. This indicates that the reaction is controlled by diffusion at low frequencies and this is also highlighted in the Nyquist plot, in which the points tend to diverge for Z' > 5 kΩ (red line), with the respect to the NC-25/SPCE (green line).

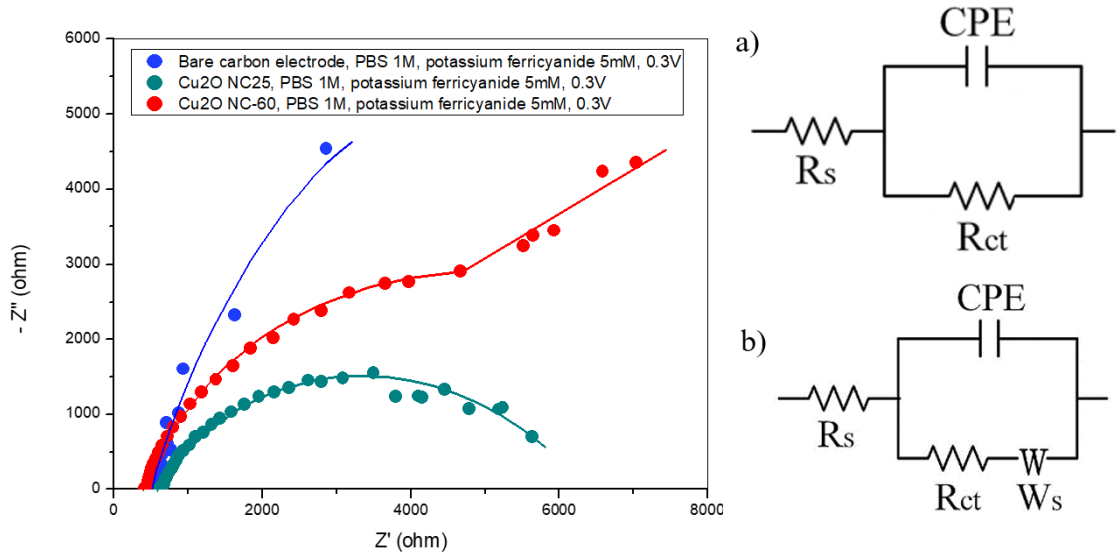

Figure 6.4 *Nyquist plot in 1 M PBS and 0.3 M potassium ferrocyanide and equivalent circuit for* ***a)*** *NC-60/SPCE;* ***b)*** *bare SPCE, Cu_2O NC-25/SPCE.*

The glucose amperometric detection tests were reported below, and consist essentially in chronovoltammetry (CVs) and chronoamperometric measurements performed under different conditions. In Figure 6.5 a), the CV curves for the Cu_2O NC-60 in KOH 0.1 M from 0.2 to 1 V with a scan range of 50 mV s^{-1} and different glucose concentrations in the 0-10 mM range, are reported. The redox couple Cu(II)/Cu(III), present in alkaline electrolyte, were reported to have a role even in absence and presence of glucose[21]; in its absence, the anodic and cathodic current peaks can be related to this redox couple, while in presence of glucose, Cu_2O is firstly oxidized to $Cu(OH)_2$, which in turn oxidizes the glucose to gluconic acid becoming CuOOH in the surface of the electrode. This is the active species that catalyses the oxidation since both Cu(I) and CuO have not been reported to be catalytically active[21].

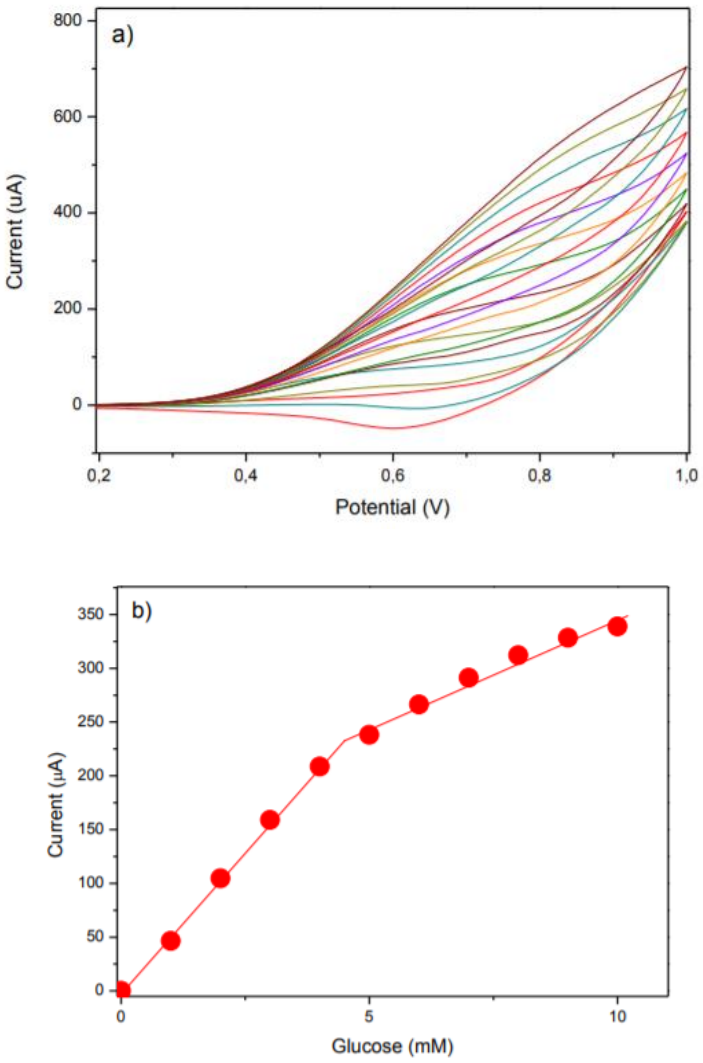

Figure 6.5 a) *CV curves in 0.1 M KOH in the 0.2-1 V range, 50 mV s^{-1} for different glucose concentration;* ***b)*** *relative calibration curves.*

Cyclic voltammetry measurements from 0 to 1 V with a scan rate of 50 mV s^{-1}, were performed for the bare SPCE, NC-25/SPCE and NC-60/SPCE in a 0.1 M KOH solution (Figure 6.6). It can be observed how the two Cu_2O based sensors show higher sensitivity in respect to the bare SPCE, especially for the NC-25/SPCE. This can be explained in relation with the particle size, lower for the latter sample, which provides a higher concentration of active sites. These results fit with the EIS measurements previously discussed and, in according to which, the NC-25/SPCE exhibits the lowest charge transfer resistance.

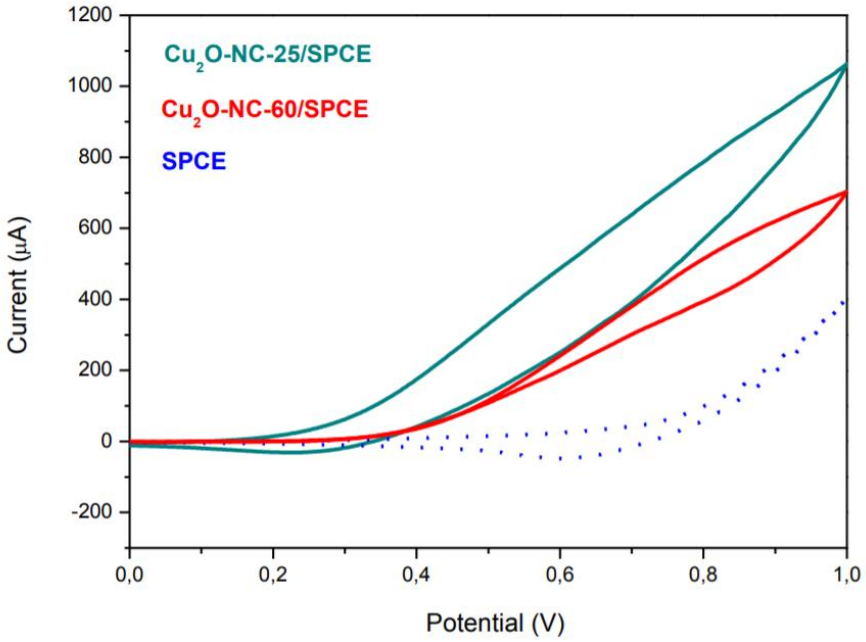

Figure 6.6 CV curves in 0.1 M KOH with a scan rate of 50 mV s^{-1} for bare SPCE, Cu_2O-NC25/SPCE, Cu_2O-NC60/SPCE.

Figure 6.7 reports a) the CV curves from 0 to 1 V with a scan rate of 50 mV s^{-1} for the NC-25/SPCE sensor, with 10 mM glucose and b) the relative oxidation and reduction peaks plotted vs the square root of the scan rate.

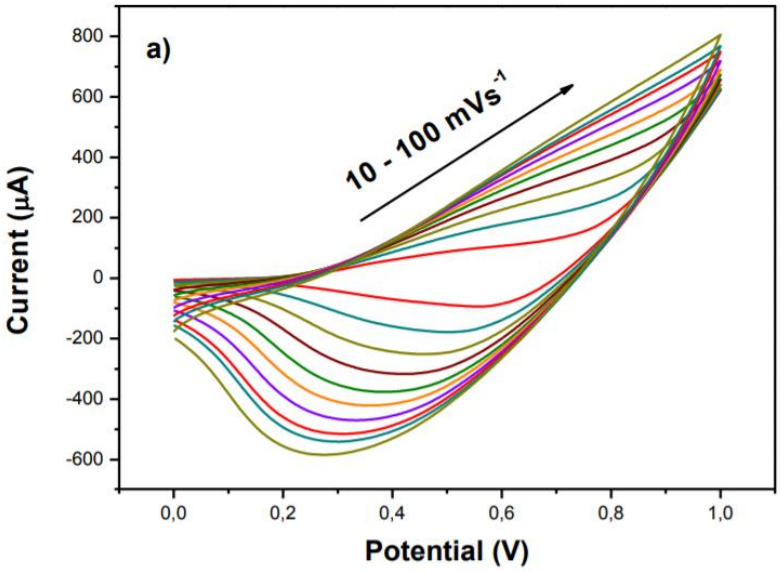

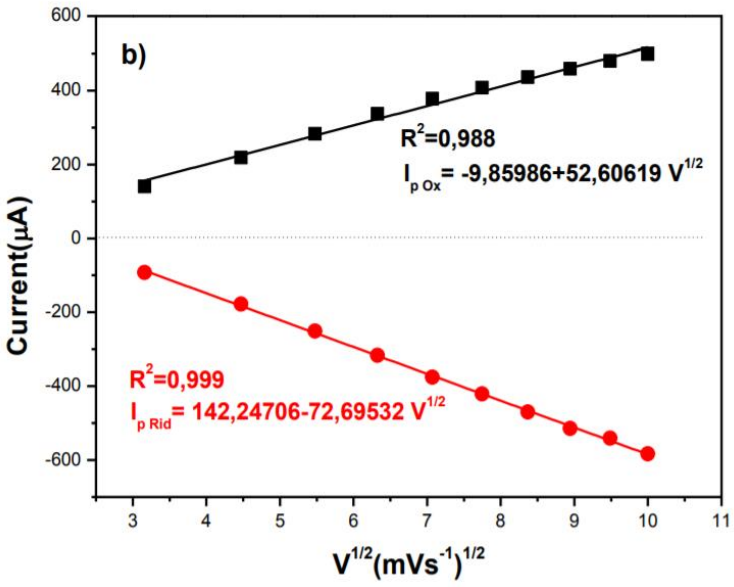

Figure 6.7 *a) CV curves with NC-25/SPCE from 0 to 1 V with 10-100 mV vs^{-1} scan rate range in 1 mM glucose; b) Oxidation and reduction current vs square rate of scan rate plots.*

This series of measurements were aimed to understand the kinetics of the investigated reactions, in order to know which of the two processes, namely the electrons transfer in electrode/electrolyte interface or the diffusion process through the electrolyte, are the limiting factors. It can be observed how the anodic and cathodic currents increase linearly with the square root of scan rate and this an evidence of a diffusion controlled kinetic, characterized by fast adsorption and surface reactions in the electrode. In the Figure 6.8 a), the calibration curve with the sensor NC-25 in a 0.1 M KOH solution is reported, applying three different potentials (0.50, 0,65 and 0.70 V) for different glucose solution concentrations, from 0 up to 2 mM. A linear response in the potentials and concentrations scanned range can be observed and the increment of the potential is followed by an increment of the current. Then, the higher sensitivity was obtained applying 0.7 V. Figure 6.8 b) shows the amperometric detection adding the glucose solution at regular interval of time, while the relative calibration curve is reported in Figure 6.8 c). For any addition of glucose, an interval time of 3 s elapses until reaching the 95% of the steady-state current value, with a quick response. It can also be noticed how the sensor keeps a stable response over a test of 2000 s, without showing significative decays of the signals during the voltage application. A value of 3.1 µA was reported as detection limit, while glucose concentrations over 5 mA cause a saturation in the signal. The sensitivity was estimated as 1040 µA/mM cm^{-2}.

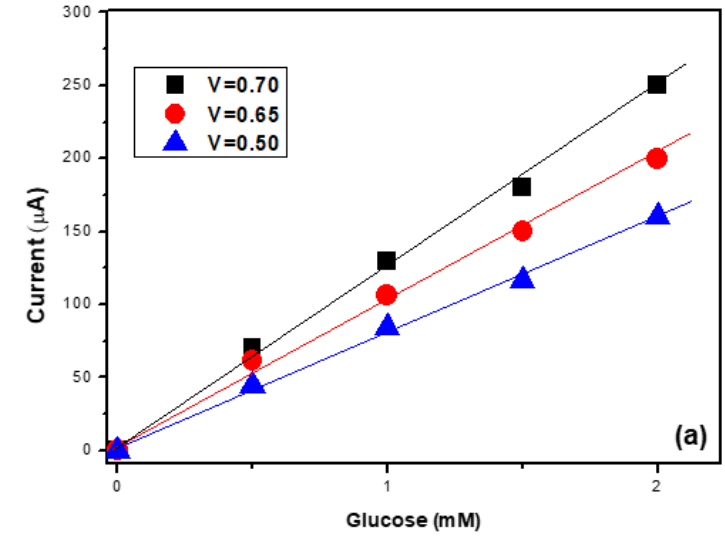

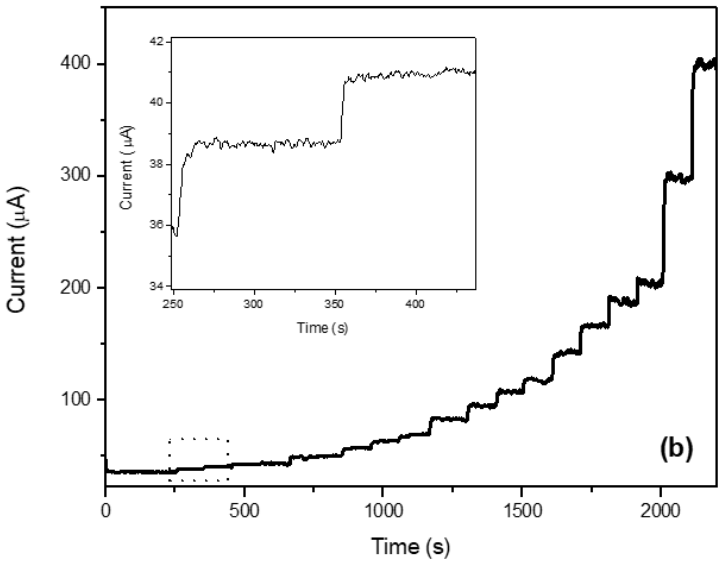

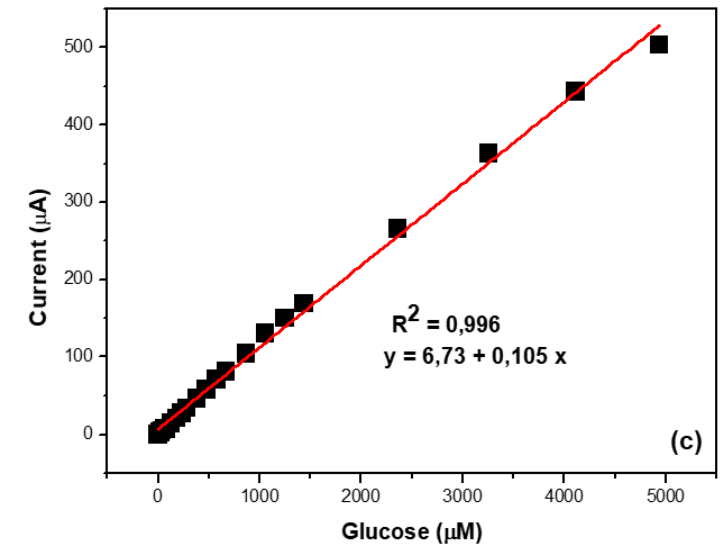

Figure 6.8 *Amperometric test a) at different potentials and glucose concentration; b) at constant voltage (0.7 V); c) Calibration curve.*

Real alcoholic mixture generally includes several compounds apart from glucose; thus, a series of tests were performed to check how these materials are selective in the respect to glucose and respond to other species. Amperometric detections, using the sensor *Cu_2O NC 60 SPCE*, were carried out applying a fixed potential of 0.7 V and adding subsequently the follow compounds: 1 mM glucose, 0.1 mM fructose, 0.1 mM sucrose, 0.1 mM mannose and 0.1 mM ethanol in 0.1 M KOH. Figure 6.9 a) reports how the sensor does not show sensitivity towards other sugars apart from glucose, while in Figure 6.9 b) the reproducibility over subsequent addition of glucose is reported.

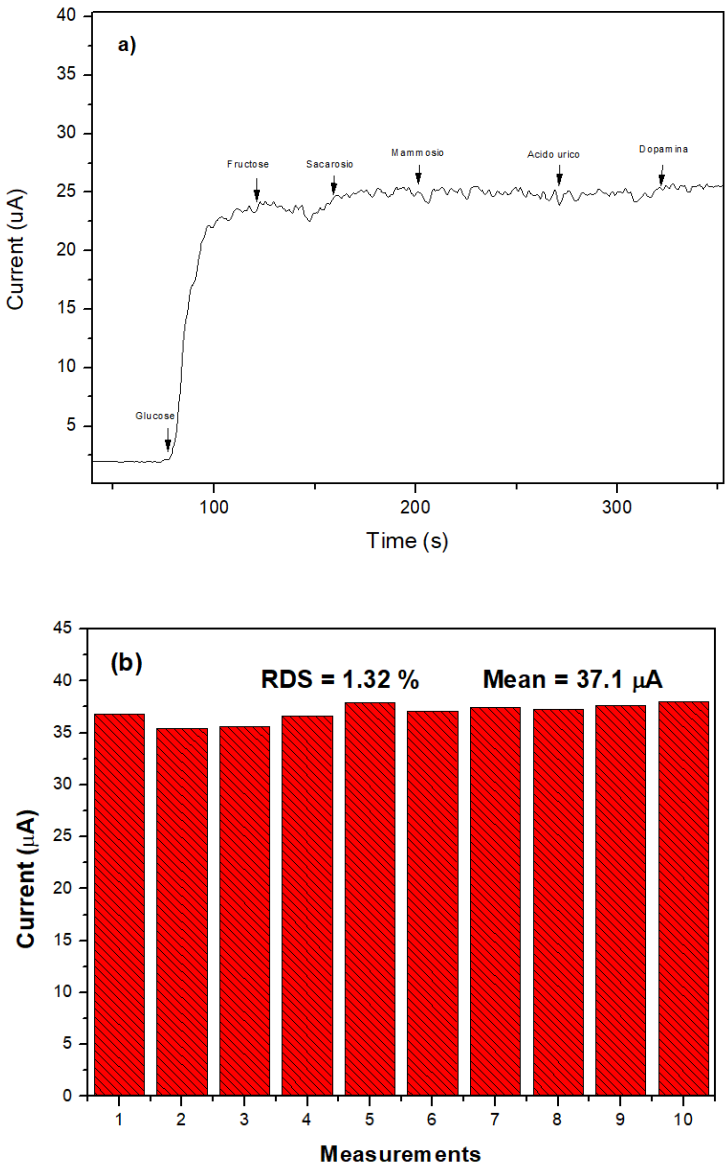

Figure 6.9 a) *Chronoamperometry test adding different compounds;* ***b)*** *reproducibility over subsequent addition of glucose.*

6.5 CONCLUSION

Cuprous oxide based sensors were prepared synthesizing Cu_2O in the form of powder by a facile precipitation method and then depositing the related water suspension on screen-electrode electrodes (SPCE) by drop casting method.

Two different Cu_2O particle size samples with the same nanocube morphology were prepared adjusting the temperature in one step of the synthesis. SEM analysis confirmed the different grain sizes of the two samples: the particles size distribution of Cu_2O NC-25, ranging from 150-200 nm, resulted lower than that of Cu_2O NC-60 varying from 200-900 nm.

The comparison between the two sensors in the amperometric detection of glucose was supported by Electrochemical Impedance Spectroscopy (EIS) measurements carried out in a PBS and in a potassium ferrocyanide solution. The sample Cu_2O NC-25 showed a lower charge transport resistance - R_{ct} (4.85 kΩ) than Cu_2O NC-60 (6.67 kΩ), confirming the higher sensibility of the first obtained in the amperometric tests. For the sample Cu_2O NC-25, the sensitivity for the glucose amperometric detection in KOH water solution was equal to 1040μA/mM cm^{-2} with a 0.007 to 4.5 mM response linear range and 31μM at S/N ratio as detection limit. Moreover, these Cu_2O-NC-SPCE sensors did not show interference from ethanol and other substrates, and are then promising candidates for glucose determination.

6.6 REFERENCES

1) Clark, L. C.; Lyons, C. Electrode Systems for Continuous Monitoring in Cardiovascular Surgery. *Ann N Y Acad Sci*. **1962**, 102, 29–45.

2) Wilson, R.; Turner, A. P. F. Glucose Oxidase: An Ideal Enzyme; 1992; Vol. 7.

3) Park, S.; Boo, H.; Chung, T. D. Electrochemical Non-Enzymatic Glucose Sensors. *Analytica Chimica Acta*. January 18, **2006**, pp 46–57. https://doi.org/10.1016/j.aca.2005.05.080.

4) Wang, G.; He, X.; Wang, L.; Gu, A.; Huang, Y.; Fang, B.; Geng, B.; Zhang, X. Non-Enzymatic Electrochemical Sensing of Glucose. *Microchimica Acta*. **2013**, pp 161–186. https://doi.org/10.1007/s00604-012-0923-1.

5) Pletcher, D. Electrocatalysis: Present and Future; **1984**; Vol. 14.

6) Tian, K.; Prestgard, M.; Tiwari, A. A Review of Recent Advances in Nonenzymatic Glucose Sensors. *Materials Science and Engineering* C. Elsevier BV August 1, **2014**, pp 100–118. https://doi.org/10.1016/j.msec.2014.04.013

7) Zhu, H.; Li, L.; Zhou, W.; Shao, Z.; Chen, X. Advances in Non-Enzymatic Glucose Sensors Based on Metal Oxides. *Journal of Materials Chemistry B. Royal Society of Chemistry* **2016**, pp 7333–7349. https://doi.org/10.1039/C6TB02037B.

8) Haghparas, Z.; Kordrostami, Z.; Sorouri, M.; Rajabzadeh, M.; Khalifeh, R. Fabrication of Non-Enzymatic Electrochemical Glucose Sensor Based on Nano-Copper Oxide Micro Hollow-Spheres. *Biotechnology and Bioprocess Engineering* **2020**, 25 (4), 528–535. https://doi.org/10.1007/s12257-020-0058-x.

9) Ahmad, R.; Khan, M.; Tripathy, N.; Khan, M. I. R.; Khosla, A. Hydrothermally Synthesized Nickel Oxide Nanosheets for Non-Enzymatic Electrochemical Glucose Detection. *Journal of The Electrochemical Society* **2020**, 167 (10), 107504. https://doi.org/10.1149/1945-7111/ab9757.

10) Ahmad, R.; Tripathy, N.; Ahn, M. S.; Bhat, K. S.; Mahmoudi, T.; Wang, Y.; Yoo, J. Y.; Kwon, D. W.; Yang, H. Y.; Hahn, Y. B. Highly Efficient Non-Enzymatic Glucose Sensor Based on CuO Modified Vertically-Grown ZnO Nanorods on Electrode. *Scientific Reports* **2017**, 7 (1), 1–10. https://doi.org/10.1038/s41598-017-06064-8.

11) Soomro, R. A.; Nafady, A.; Ibupoto, Z. H.; Sirajuddin; Sherazi, S. T. H.; Willander, M.; Abro, M. I. Development of Sensitive Non-Enzymatic Glucose Sensor Using Complex Nanostructures of Cobalt Oxide. *Materials Science in Semiconductor Processing* **2015**, 34, 373–381. https://doi.org/10.1016/j.mssp.2015.02.055.

12) Yu, X.; Zhang, J.; Tang, X.; Wei, Y.; Kou, S.; Niu, J.; Yao, B. Preparation and Performance of Non-Enzymatic Glucose Sensor Electrode Based on Nanometer Cuprous Oxide. *Nanomaterials and Nanotechnology* **2018**, 8. https://doi.org/10.1177/1847980418793526.

13) Lv, J.; Kong, C.; Hu, X.; Zhang, X.; Liu, K.; Yang, S.; Bi, J.; Liu, X.; Meng, G.; Li, J.; Yang, Z.; Yang, S. Zinc Ion Mediated Synthesis of Cuprous Oxide Crystals for Non-Enzymatic Glucose Detection. *Journal of Materials Chemistry B* **2017**, 5 (44), 8686–8694. https://doi.org/10.1039/c7tb01971h.

14) Liu, W.; Chai, G.; Zhao, X.; Dai, Y.; Qi, Y. Effect of Different Copper Sources on the Morphology of Cuprous Oxide and Its Application as a Non-Enzymatic Glucose Sensor. *Sensors and Actuators, B: Chemical* **2020**, 321 (January), 128485. https://doi.org/10.1016/j.snb.2020.128485.

15) Cao, H.; Yang, A.; Li, H.; Wang, L.; Li, S.; Kong, J.; Bao, X.; Yang, R. A Non-Enzymatic Glucose Sensing Based on Hollow Cuprous Oxide Nanospheres in a

Nafion Matrix. *Sensors and Actuators, B: Chemical* **2015**, 214, 169–173. https://doi.org/10.1016/j.snb.2015.03.026.

16) Pasakon, P.; Mensing, J. P.; Phokaratkul, D.; Karuwan, C.; Lomas, T.; Wisitsoraat, A.; Tuantranont, A. A High-Performance, Disposable Screen-Printed Carbon Electrode Modified with Multi-Walled Carbon Nanotubes/Graphene for Ultratrace Level Electrochemical Sensors. J*ournal of Applied Electrochemistry* **2019**, 49 (2), 217–227. https://doi.org/10.1007/s10800-018-1268-1.

17) Dorledo de Faria, R. A.; Messaddeq, Y.; Heneine, G. D.; Matencio, T. Application of Screen-Printed Carbon Electrode as an Electrochemical Transducer in Biosensors. *International Journal of Biosensors & Bioelectronics* **2019**, 5 (1), 9–10. https://doi.org/10.15406/ijbsbe.2019.05.00143.

18) Pilas, J.; Selmer, T.; Keusgen, M.; Schöning, M. J. Screen-Printed Carbon Electrodes Modified with Graphene Oxide for the Design of a Reagent-Free NAD^+-Dependent Biosensor Array. *Analytical Chemistry* **2019**, 91 (23), 15293–15299. https://doi.org/10.1021/acs.analchem.9b04481.

19) Antuña-Jiménez, D.; González-García, M. B.; Hernández-Santos, D.; Fanjul-Bolado, P. Screen-Printed Electrodes Modified with Metal Nanoparticles for Small Molecule Sensing. *Biosensors* **2020**, 10 (2), 1–22. https://doi.org/10.3390/bios10020009.

20) Espro, C.; Marini, S.; Giusi, D.; Ampelli, C.; Neri, G. Non-Enzymatic Screen Printed Sensor Based on Cu_2O Nanocubes for Glucose Determination in Bio-Fermentation Processes. *Journal of Electroanalytical Chemistry* **2020**, 873, 114354. https://doi.org/10.1016/j.jelechem.2020.114354.

21) Sridara, T.; Upan, J.; Saianand, G.; Tuantranont, A.; Karuwan, C.; Jakmunee, J. Non-Enzymatic Amperometric Glucose Sensor Based on Carbon Nanodots and Copper Oxide Nanocomposites Electrode. *Sensors* (Switzerland) **2020**, 20 (3). https://doi.org/10.3390/s20030808.

7.GENERAL CONCLUSION

In this PhD thesis, different electro- and photo-catalytic approaches have been studied for the reduction of CO_2 to organic compounds attractive in the energy field and chemical industry.

As regards the photocatalytic approach, a novel gas phase flow-through photoreactor operating at ambient pressure and temperature was designed and tested. The catalysts were fabricated in the form of perforated nanomembranes, representing an integral part of the whole photo-catalytic assembly. These nano-membranes were crossed by a CO_2/H_2O flow with an appropriate ratio thanks to their mesoporosity, allowing CO_2 to be adsorbed on the active sites present on the side exposed to light irradiation. Operation in gas-phase allowed obtaining considerable advantages compared to conventional applications, such as common photoelectrochemical (PEC) or slurry reactors, among which: i) increase the local concentration of CO_2 at the catalyst interface solving the issues of poor solubility of CO_2 in aqueous environments ii) avoid the diffusion limits due to transport phenomena in the double-layer electrode/solution; iii) favour different reaction pathways. The catalysts were based on Cu_xO, deposited in the form of thin films on various supports, including ordered arrays of titania nanotubes (TiO_2NTs), obtained by controlled anodic oxidation. Copper films were obtained by electrodeposition, in the form of a *p* or *n* semiconductor, by varying the electrolytic bath. This technique was chosen because it is cheap and allows to vary easily the morphology of the sample by acting on various parameters such as the pH of the electrolyte, the applied voltage, the deposition time and the temperature. The *Cu_2O/TiO_2NTs/Ti p-n,* obtained by assembling *Cu_2O p-type* and the *TiO_2NTs n-type,* allowed to obtain the most promising results such as a Faradaic efficiency (FE) of 44% for acetic acid and an Apparent Quantum Yield (AQY%) of 21.5% for methanol and acetic acid, among the highest values ever reported. These results could be explained by the formation of a *p-n* junction that modifies the Fermi energy levels of the two semiconductors and enables different reaction paths not previously present.

Although further studies are needed to validate this hypothesis, the reported characterizations, among which UV/Vis spectroscopy and photocurrents, may suggest this possibility. Furthermore, the electrocatalytic testing results showed a

different distribution of the products compared to those normally reported in the literature, in favour of C2-C3 compounds, and this can be ascribed in part to the novel configuration of the designed photo-reactor. Moreover, this can be explained by taking in account some factors including: i) the samples after the reaction were extracted with a few drops of diluted sulphuric acid to capture any products that remained adsorbed on the catalyst; ii) the low partial pressure of the water (approx. 4%) in the CO_2 flow made it possible to minimize all those reactions that involve the coverage of the active sites by H*. These results, considering the absence of a hole scavenger and the minimization of side reactions that lead to the formation of hydrogen and together with the novel design concept of continuous flow photoreactor operating in the gas phase, are very promising for future applications.

Regarding the electrocatalytic reduction of CO_2, Cu_xO-based electrodes, both in the form of pure oxides (at different oxidation states, I and II) or doped with other elements, such as S and In (CuS_x and Cu-In), have been fabricated by solvothermal synthesis and deposition and processed in different setup and cell configurations. All the catalysts were deposited by spray-coating on a carbon gas diffusion layer (GDL) at different catalyst loadings. The first tests were carried out in a two-chamber liquid-phase reactor, in which the two compartments were separated by a protonic-membrane, using pure Cu_2O and CuO as electrocathodes and GDL as anodes: the reaction products detected were mainly formic acid, CO and hydrogen, generally obtained with low efficiencies. It was evaluated how the influence of catalyst loading can affect productivity and it was shown how the CuO allowed to obtain the highest results in terms of Faradaic efficiency of carbonaceous products and CO selectivity at -0.6 V vs RHE. The results were supported by impedance measurements through Electrochemical Impedance Spectroscopy (EIS), which evidenced a lower resistance to charge transfer in CuO sample that can justify the testing results.

Most of the work was also dedicated to the optimization of the reactor and the choice of operating conditions, including the best configuration in order to detect most of the formed products, the cathodic pH, the choice of the inlet CO_2 flow and the type of membrane for the separation of the two compartments. The setup was modified and the new device was composed by three different compartments, including now a gas-chamber.

Prior to process the catalysts in this new setup, preliminary tests, with GDL both as electrocathode and anode, were conducted on an H-type cell with the aim of evaluating how the internal elements of a cell determine its overall resistance. EIS analysis was carried out, using two proton exchange membranes: the reinforced Nafion® membrane (N-324) and the thinner Nafion® NR-212 membrane, which provided different resistance contributions. The data cleared how the electrolyte represents the greatest contribution in terms of resistance, therefore the ways to minimize these terms are either to work in the gas phase or to decrease the distance between the electrodes in liquid phase. The Nafion® N-324 membrane was designated for successful testing as, despite its superior resistance, it allowed the pH of the two compartments to keep stable over time.

Subsequently, experimental tests were aimed to understand the best operating configuration of the cell. This configuration consists of three chambers, operating with different gas flows within the cell. Configuration n.1 was found to be the one that allowed to obtain the best results in terms of Faradaic efficiency to carbonaceous products. In this configuration, the CO_2 enters the gas chamber, through the GDL, adsorbs on the active sites of the catalyst, while the products formed come back to the gas chamber where they are collected and analysed.

Subsequent tests showed the best cathodic pH to maximize the FE. This was found to be equal to 6.8, with FE values to formic acid much higher than those obtained by working with pH 5.9 or 8.1. Subsequent tests were carried out using advanced electrodes based on CuS_x and Cu-In, reported in the literature to be selective for formic acid and carbon monoxide, respectively. Tests were carried out with GDL as anode and led to a maximum of 58.5% for formic acid in the case of CuS_x and 55.6% for carbon monoxide for Cu-In, with maximum energetic efficiency (EE) obtained at -0.8 V vs RHE for CuS_x (29.8%) and at -0.6 V vs RHE for Cu-In (35.0%).

Further tests were performed using a series of anionic, cationic and bipolar membranes to evaluate the effects on total performance in terms of current density and efficiency of the products. Among the screening of many commercial membranes, most of them (especially the thinner ones) caused osmosis problems. Thus, we focused on comparing the bipolar Fumasep FBM-PK and the reinforced protonic Nafion 324 membranes, obtaining similar results but no cross-over phenomena were observed for the latter.

These results are very promising and efforts should be concentrated on the possibility of limiting further the overpotential. Taking into account that the large contribution in the internal resistance has been identified in the electrolyte, the next step concerns the chance of minimizing the electrolytic compartments as much as possible.

The last part of the work focused on the use of copper samples, previously used for electrocatalytic purposes, as sensors for glucose detection, through amperometric tests. Cu_2O samples of different sizes, produced by wet precipitation, were deposited on commercial supports, screen printed carbon electrodes (SPCE), through the drop-casting technique. The sample with the smallest particle size (*Cu_2O NC-25*) offered the best results in terms of glucose sensitivity, 1040µA/mM cm^{-2} in aqueous KOH solution. The amperometric results were supported by impedance measurements, evidencing that this sample provided also the lowest resistance to charge transfer. These samples, whose production is particularly cheap and simple, are promising candidates for glucose detection, even considering that they do not show any interference with ethanol and other substrates.

LIST OF ACTIVITIES CARRIED OUT

RESEARCH PERIOD ABROAD

1) *ICIQ* (Institut Català d'Investigació Química), Tarragona 18/03/2019 -18/04/2019

2) *ETH* (Institute for Chemical and Bioengineering), Zurich 01/05/2019 - 01/07/2019

Motivation of the stay: During this period, he worked in a collaboration in the framework of the H2020 A-LEAF project n.732840 from the European Research Council (Research and Mobility ARCADIA Project), on the synthesis of different electrodes for CO_2 electroreduction and start-up tests of the electrochemical cell device.

ATTENDED SEMINARY

1) WebinarsAREA Science 24/06/2020
(Research Infrastructures + Open Innovation)

2) Fast Webinar Metrohm Italiana Srl

- Electrochemistry applied to Galvanics 25/06/2020
- Spectroelectrochemistry 30/07/2020

PUBLISHED PAPERS (in ISI Web of Science/Scopus)

1) Espro, C.; Marini, S.; **Giusi, D**.; Ampelli, C.; Neri, G. Non-Enzymatic Screen Printed Sensor Based on Cu_2O Nanocubes for Glucose Determination in Bio-Fermentation Processes. *Journal of Electroanalytical Chemistry* **2020**, *873,* 114354. DOI: https://doi.org/10.1016/j.jelechem.2020.114354.

2) **Giusi, D.**; Ampelli, C.; Genovese, C.; Perathoner, S.; Centi, G. A Novel Gas Flow-through Photocatalytic Reactor Based on Copper-Functionalized Nanomembranes for the Photoreduction of CO_2 to C1-C2 Carboxylic Acids and C1-C3 Alcohols. *Chemical Engineering Journal* **2020**, 127250. DOI: https://doi.org/10.1016/j.cej.2020.127250.

PAPERS TO SUBMIT (in ISI Web of Science/Scopus)

1) Title: *$BiVO_4$-TiO_2 nanotube heterostructures as photoanodes in a compact photo-electrocatalytic cell (PEC) for solar water splitting*; Corresponding Author: Prof.

Claudio Ampelli; Co-Authors: João Angelo Lima Perini; Francesco Tavella; Elias Paiva Ferreira Neto; Maria Valnice Boldrin Zanoni; Sidney José Lima Ribeiro; **Daniele Giusi**; Gabriele Centi; Siglinda Perathoner. **SUBMITTED**

2) Title: *Synergetic electrocatalytic effects of Cu_2O-TiO_2 heterostructures in a solar driven PEC device for CO_2 reduction to >C1 chemicals*; Co-Authors: **Giusi D**., Tavella F., Miceli M., Ampelli C., Centi G., Cosio D., Genovese C., Perathoner S. **SUBMITTED (Chemical Engineering Transactions)**

3) Title: *Electrochemical insight into the role of copper oxide deposited over carbon gas diffusion layer in CO_2 reduction*; Co-Authors: **Daniele Giusi**, Matteo Miceli, Claudio Ampelli, Chiara Genovese, Siglinda Perathoner, Gabriele Centi. **IN PREPARATION**

ABSTRACT PROCEEDINGS IN NATIONAL AND INTERNATIONAL CONFERENCES

1) F. Tavella, C. Ampelli, C. Genovese, **D. Giusi**, S. Perathoner, G. Centi. Water Photo-Electrolysis onto Highly Ordered Nanotube Arrays Based on TiO_2 and Ta-oxy-N, *XX Congresso Nazionale di Catalisi – XX Congresso Nazionale della Divisione di Chimica Industriale* (GIC-DiChIn2018), Book of abstracts, O06PP, Milan (Italy), 2-5 September 2016.

2) **D. Giusi**, F. Tavella, C. Genovese, C. Ampelli, S. Perathoner, G. Centi, Photocatalytic reduction of CO_2 over Cu_2O nanocubes prepared via solvothermal and precipitation methods, *EFCATS School on Catalysis*, Book of abstracts, Liblice (Czech Republic), 25-29 June 2018.

3) M. Miceli, C. Genovese, C. Ampelli, **D. Giusi**, S. Perathoner, G. Centi, Development of photoelectrocatalytic artificial-leaf type devices for CO_2 conversion, *Making Business with Green Chemistry & Sustainable Energy Summer School*, Sarteano (Italy), 22-26 July 2019.

4) **D. Giusi**, C. Ampelli, C. Genovese, S. Perathoner, G. Centi, Selective photocatalytic reduction of CO_2 to methanol in gas-phase over *p*-type Cu(I)-based semiconductor layers, *14th EuropaCat – European Congress on Catalysis*, Book of abstracts, Aachen (Germany), 18-23 August 2019.

5) **D.Giusi,** C. Ampelli, C. Genovese, S. Perathoner, G. Centi, Role of Cu(I) in addressing selectivity of CO_2 reduction by electrocatalytic or photocatalytic route, *4th edition of Avogadro Colloquia*, Rome (Italy), 17-18 December 2019.

ACCEPTED ABSTRACT FOR INTERNATIONAL CONFERENCES

1) **Giusi D**., Tavella F., Miceli M., Ampelli C., Centi G., Cosio D. Synergetic electrocatalytic effects of Cu_2O-TiO_2 heterostructures in a solar driven PEC device for CO_2 reduction to >C1 chemicals, *ICheaP15*, Naples, 23-26 May 2021.

ATTENDANCE IN NATIONAL AND INTERNATIONAL CONFERENCES

1) **Poster presentation** on *EFCATS School on Catalysis*, Liblice (Czech Republic), 25-29 June 2018

2) **Oral presentation** on *14th EuropaCat – European Congress on Catalysis*, Aachen (Germany), 18-23 August 2019

3) **Poster presentation** on *4th edition of Avogadro Colloquia*, Rome (Italy), 17-18 December 2019

ACKNOWLEDGEMENT

I thank my Supervisor, Prof.ssa Siglinda Perathoner, my Co-tutor, Prof. Claudio Ampelli, Prof. Gabriele Centi and the entire research group for their support. My appreciation goes also to Daniele Cosio for the reactors manufacturing and deep gratitude have to be reserved to Prof. Giovanni Neri for him willingness during the activities.

I also wish to acknowledge Prof. Javier Pérez-Ramírez (ETH), Prof. José Ramón Galán-Mascarós (ICIQ) for hosting me in their research groups within A-LEAF project, Dr. Martin Fernandez Antonio José (ETH) and Dr. Jesús González Cobos (ICIQ) with whom I led part of scientific activities in the laboratory and also all the other research group people. A final thank goes to Dr. Miguel García Tecedor (Universitat Jaume I) for collaboration on the study of the resistances inside the cell and the membranes behavior.